Study on the Spatial Distribution and Collimation of Photons in X-ray Fluorescence Imaging of Human-Sized Objects

Dissertation
zur Erlangung des Doktorgrades
an der Fakultät für Mathematik, Informatik und Naturwissenschaften
Fachbereich Physik
der Universität Hamburg

vorgelegt von

Regina Ute Garmatter

Hamburg

2026

Gutachter/innen der Dissertation:	Prof. Dr. Florian Grüner Prof. Dr. Gudrid Moortgat-Pick
Zusammensetzung der Prüfungskommission:	Prof. Dr. Florian Grüner Prof. Dr. Gudrid Moortgat-Pick Prof. Dr. Michael Potthoff Dr. Theresa Staufer Dr. Elisabetta Gargioni
Vorsitzender der Prüfungskommission:	Prof. Dr. Michael Potthoff
Datum der Disputation:	21.08.2026
Vorsitzender des Fach-Promotionsausschusses PHYSIK:	Prof. Dr. Johannes Haller
Leiter des Fachbereichs PHYSIK:	Prof. Dr. Markus Drescher
Dekan der Fakultät MIN:	Prof. Dr.-Ing. Norbert Ritter

Abstract

Nowadays, cancer is one of the world's most common causes of death, and the World Health Organization predicts that by 2050, the number of diagnosed cancer cases will increase by 77% compared to 2022. Imaging modalities are of essential importance for increasing the success of cancer treatment and reducing mortality. In addition to anatomical imaging modalities (e.g., computed tomography (CT)), which provide structural information about tumors, functional imaging modalities (e.g., positron emission tomography (PET)) provide valuable metabolic and molecular information that can be used to localize tumors and monitor treatment response. X-ray fluorescence imaging (XFI) is a type of functional imaging technique that relies on the use of markers (e.g., gold nanoparticles) within the object to be imaged. An externally applied X-ray beam irradiates the object, and its interaction with the marker causes the emission of fluorescence photons with element-specific energies, which are detected as the imaging signal. In contrast to the widely used imaging method PET, XFI can achieve a higher spatial resolution and a non-radioactive marker allows for longitudinal studies. Currently, however, XFI is only used in preclinical studies and imaging human-sized objects poses challenges. High background noise overlays the imaging fluorescence signal and makes the application of XFI on human-sized objects difficult. Approaches described in the literature to perform XFI on human-sized scales are currently associated with large and impractical setups or low sensitivities. This thesis therefore investigates the application of XFI on human-sized objects with a more compact and less expensive setup. The aim is to study the spatial distribution of photons and the collimation of background photons in this context. This is done using Monte-Carlo simulations and a model that numerically calculates photon path probabilities. Combining a backward-located detector and a lamellae-based collimator can reduce the background significantly. The lamellae-based collimators strongly restrict the field of view of the detector outside the signal-emitting target, thereby increasing the sensitivity of the target compared to the uncollimated case. To align the collimator, the target location is determined a priori by complementary anatomical imaging techniques, which is why this approach is considered in the context of multimodal imaging. This strategy achieves sensitivities within the range of values reported in the literature, for which, in some cases, a detector approximately three orders of magnitude larger was used, and could therefore represent a more practical and cost-effective alternative.

Zusammenfassung

Heutzutage ist Krebs eine der weltweit häufigsten Todesursachen und die Weltgesundheitsorganisation prognostiziert, dass die Anzahl der diagnostizierten Krebsfälle bis 2050 um 77% im Vergleich zu 2022 steigen wird. Zur Steigerung des Therapieerfolgs und Senkung der Mortalität bei Krebs sind Bildgebungsmethoden von wesentlicher Bedeutung. Neben anatomischen Bildgebungsverfahren (z.B. Computertomographie (CT)), die strukturelle Informationen über Tumoren liefern, bieten funktionelle Bildgebungsverfahren (z.B. Positronen-Emissions-Tomographie (PET)) wertvolle metabolische und molekulare Informationen, die zur Lokalisierung von Tumoren und zur Überwachung des Ansprechens auf eine Tumortherapie genutzt werden können. Die Röntgenfluoreszenz-Bildgebung (XFI) ist eine solche funktionelle Bildgebung, die auf der Verwendung von Markern (z.B. Goldnanopartikel) im Objekt basiert. Dabei wird ein Röntgenstrahl von außen auf das Objekt gerichtet, dessen Wechselwirkung mit dem Marker zur Emission von Fluoreszenzphotonen mit elementspezifischen Energien führt, die als bildgebendes Signal detektiert werden. Im Gegensatz zur weit verbreiteten Bildgebungsmethode PET, kann mit XFI eine höhere räumliche Auflösung erreicht werden und ein nicht-radioaktiver Marker ermöglicht longitudinale Studien. Derzeit wird XFI jedoch nur in präklinischen Studien eingesetzt und die Bildgebung von menschengroßen Objekten ist mit Herausforderungen verbunden. Ein hoher Untergrund überlagert das bildgebende Fluoreszenzsignal und erschwert die Umsetzung von XFI bei menschengroßen Objekten. Ansätze aus der Literatur, XFI an menschengroßen Objekten durchzuführen, sind derzeit mit großen, unpraktikablen Aufbauten oder niedrigen Sensitivitäten verbunden. In dieser Arbeit wird daher die Anwendung von XFI an menschengroßen Objekten mit einem kompakteren und kostengünstigeren Aufbau betrachtet. Das Ziel besteht darin, die räumliche Photonenverteilung und die Kollimation der Signal-überlagernden Untergrundphotonen in diesem Kontext zu untersuchen. Dazu wurden Monte-Carlo-Simulationen und ein Modell verwendet, das Pfadwahrscheinlichkeiten von Photonen numerisch bestimmt. Die Kombination aus einem in Rückwärtsrichtung positionierten Detektor und der Verwendung von lamellenbasierten Kollimatoren kann den Untergrund stark reduzieren. Die lamellenbasierten Kollimatoren schränken das Sichtfeld des Detektors außerhalb des signalgebenden Targets stark ein, wodurch sich die Sensitivität des Targets im Vergleich zum unkollimierten Fall erhöht. Zur Ausrichtung des Kollimators wird das Target vorab mittels komplementärer anatomischer Bildgebungsverfahren bestimmt, weshalb dieser Ansatz im Kontext multimodaler Bildgebung betrachtet wird. Diese Strategie ermöglicht Sensitivitäten im Größenbereich publizierter Literaturwerte, für die teilweise ein um ungefähr drei Größenordnungen größerer Detektor verwendet wurde, und könnte daher eine praktikablere und kostengünstigere Alternative darstellen.

Contents

1 Introduction **1**

2 Physical Background **4**
2.1 Interaction of Photons with Matter . . . 4
2.1.1 Photoelectric Effect . . . 4
2.1.2 Coherent Scattering . . . 6
2.1.3 Compton Scattering . . . 7
2.1.4 Attenuation of Photons in Matter . . . 9
2.2 X-rays . . . 11
2.2.1 Generation of X-rays . . . 11
2.3 X-Ray Fluorescence Imaging . . . 12
2.4 Radiation Dose . . . 13

3 Material and Methods **15**
3.1 Geant4 . . . 15
3.2 Statistics . . . 15
3.3 Numerical Photon Model . . . 17
3.3.1 Fluorescence Model . . . 17
3.3.2 Compton Model . . . 20
3.3.3 Numerical Model with a Pixelated Detector . . . 21
3.3.4 Numerical Model with a Collimator . . . 21
3.3.5 Limitations of the Numerical Model . . . 22
3.4 Detectors . . . 22
3.5 Gold Nanoparticles . . . 25

4 Numerical Analysis of Multiple Compton Background **27**
4.1 Setup . . . 27
4.2 Validation of the Numerical Model . . . 28
4.3 Spatial Distribution of Multiple Compton-Scattered Photons . . . 30
4.4 Spatial Distribution for Increased Detector Distance . . . 34
4.5 Discussion . . . 36

5 Uncollimated X-ray Fluorescence Imaging **37**
5.1 Setup . . . 37
5.2 Absorbed Dose within a Human-Sized Object . . . 38
5.3 Results . . . 40
5.3.1 Fluorescence Dependency on the Detector Angle and Signal Range 40
5.3.2 Background Dependency on the Detector Angle and Energy Range 41
5.3.3 Significance Dependency on the Detector Angle and Energy Range 44
5.3.4 Impact of Doppler Broadening . . . 46
5.4 Discussion . . . 47

6 Development of Collimator Designs **49**
6.1 Vertical-Lamellae Collimator . . . 49
6.1.1 Principle of the Collimator with Vertical Lamellae . . . 49
6.1.2 Setup . . . 51
6.1.3 Effect of the Ideal Collimator . . . 52
6.1.4 Effect of Lamella Material and Thickness on Collimator Performance 56
6.1.5 Spatial Resolution . . . 62
6.1.6 FOV and Sensitivity for Different Gold Target Positions . . . 65
6.2 Horizontal-Lamellae Collimator . . . 68
6.2.1 Principle and Setup of the Collimator with Horizontal Lamellae . . . 68
6.2.2 Field-of-View Volumes . . . 69
6.2.3 Impact of the Detector Displacement Outside the Beam Plane . . . 70
6.2.4 Impact of the Lamella Number . . . 75
6.2.5 Impact of the Lamella Length . . . 80
6.2.6 Sensitivity for a 150° Detector . . . 85
6.2.7 Sensitivity for a 180° Detector . . . 87
6.3 Comparison of Collimator Designs . . . 90
6.4 Discussion . . . 93

7 Test Measurement for Experimental Validation **102**
7.1 Setup . . . 102
7.2 Experimental Results . . . 104
7.3 Impact of the Alignment . . . 105

8 Conclusion and Outlook **108**

Bibliography **110**

A Appendix **122**
A.1 Compton1 and Compton3 Model . . . 122
A.2 Collimators Used for the Comparison in Section 6.3 . . . 126
A.3 Simulations for the Test Measurement . . . 129

List of Figures **132**

List of Tables **135**

1 Introduction

In 2022, about 10 million deaths worldwide were attributed to cancer. Therefore, cancer is one of the leading causes of death. In the same year, about 20 million people were diagnosed with cancer and the World Health Organization (WHO) even predicts a 77% increase to over 35 million cases by 2050 [1, 2]. The growing and aging human population is responsible for this increase. Other reasons for the predicted increase in cancer are, for example, overweight and decreasing air quality [2].
In general, cancer is a disease consisting of malignant cells that have developed from normal cells into abnormal cells during a multi-stage process which arises from several DNA damages in cells [1, 3, 4]. These malignant cells grow uncontrollably and invade surrounding tissues from a primary tumor within the body. Additionally, metastases can occur, which are secondary tumors formed by tumor cells that spread throughout the body to distant sites [1, 3]. The causes of cancer can be classified into several categories. Intrinsic factors include, for example, age and genetics, while the extrinsic factors are classified as chemical carcinogens (e.g. alcohol consumption), biological carcinogens (e.g. virus infections) and physical carcinogens (e.g. UV or ionizing radiation) [4, 1]. Overall, the aim becomes clear with respect to the statistics and prognoses for cancer cases, which is to further reduce the mortality, increase the healing probability and extend the lifetime as much as possible with an improved quality of life [1].
Nowadays, a cancer diagnosis is not necessarily associated with death and often, even healing is possible for some types of cancer while others, such as lung cancer, are still associated with a high mortality. Besides the type of cancer, the survival rate is mainly impacted by an early diagnosis and an efficient treatment [5, 1, 6]. In this context, imaging modalities play an important role, as they are used in all phases of cancer disease progression [6]. This includes the screening, when no symptoms have arisen yet, diagnosis and staging, as well as imaging for treatment planning and monitoring the treatment response to adjust the treatment therapy if necessary [7, 6]. There are different types of imaging modalities, which can be distinguished into anatomical and functional imaging methods. While anatomic imaging modalities provide structural information, such as tumor location and structural changes to surrounding tissues, functional imaging provides insight into the biological functions of tumors and surrounding tissues. Due to their different strengths, they are often combined which is called multimodal imaging [6, 8, 9, 10].
Anatomical information can be obtained using non-invasive radiography based on X-rays, which are ionizing radiation and were discovered in 1895 by Wilhelm Conrad Röntgen [11, 12, 13]. Due to their interactions with matter, the X-rays are attenuated differently depending on the material's properties (atomic number and density) and the incident energy of the X-rays. Consequently, for an inhomogeneous object, such as the human body, the intensity of the detected X-rays varies after passing through the object, resulting in contrast in the X-ray image [12, 11, 13]. However, radiography only provides a projected two-dimensional image, whereas computed tomography (CT) provides three-dimensional images. CT is based on the same principle as radiography, except that the object is irradiated from different locations, providing 3D information [13]. Therefore, CT imaging is well-established and associated with a high spatial resolution of approximately 0.5 mm in

conventional CT [14, 15]. The use of X-rays, however, can also cause DNA damage since they are ionizing radiation [13]. Furthermore, by CT imaging, no or barely functional information is provided [10].
In contrast, the non-invasive imaging modality magnetic resonance imaging (MRI) uses no ionizing radiation, but rather radio frequency pulses and magnetic fields to provide detailed images of organs and tissues. MRI often delivers superior soft-tissue contrast compared to CT imaging and is associated with a high sensitivity in many clinical applications. For instance, MRI achieves the highest sensitivity for breast cancer detection compared to other imaging modalities [13, 16]. Furthermore, specific MRI techniques can also provide functional information [13]. MRI typically has a spatial resolution of about 1 mm in anatomical scans and 2 mm in some functional imaging. However, with modern scanners, the resolution can be improved to 0.5 mm for anatomical imaging and to 1.0 mm for functional imaging [17].
To gain functional, molecular or metabolic information, single photon emission computed tomography (SPECT) or positron emission tomography (PET) are commonly used [7, 9]. These modalities are particularly relevant for monitoring the treatment response in, for example, molecularly targeted therapies [10]. Both SPECT and PET use intravenously injected radiotracers, which are gamma-emitting isotopes in SPECT and positron-emitting isotopes in PET [7, 9, 18, 10]. In PET, the radioactive tracer emits positrons that annihilate with electrons, producing two photons that are emitted in opposite directions and detected in coincidence [7, 19]. The advantages of these two imaging modalities are their high sensitivity compared to other methods, such as CT, since they can detect tracer concentrations down to 100 pM [10]. However, as with radiography and CT, ionizing radiation is used here, even from within the body, and the patient remains exposed beyond the imaging duration due to the tracer's half-life. Furthermore, the spatial resolution of PET is limited by the positron range before annihilation, resulting in a resolution of about 4-6 mm and about 15 mm for SPECT which is much lower compared to CT or MRI [11, 20, 18, 21].
Therefore, another imaging modality that provides functional, molecular and metabolic information with better spatial resolution would be useful. X-ray fluorescence imaging (XFI) is an option since it is able to perform qualitative and quantitative studies [22, 23]. This technique uses markers, such as nanoparticles or single atoms and it is based on the principle that an object to be imaged is irradiated by an X-ray beam and the markers within the object induce the emission of fluorescence photons, which serve as the detected signal [23, 24]. Unlike SPECT/PET, non-radioactive markers, such as gold nanoparticles (GNPs), are used, meaning that exposure to ionizing radiation occurs only during the XFI imaging procedure which reduces the exposure time [11, 24]. Furthermore, using a non-radioactive marker means that the marker does not decay, enabling longitudinal studies with XFI as long as the marker is present within the body [22, 25, 11, 24]. This may be helpful in the context of monitoring cancer treatment. Moreover, fluorescence photons are associated with element-specific characteristic energies [23]. Therefore, simultaneous detection of multiple elements is possible, whereas with PET only one single marker can be imaged [26, 11]. In XFI, the spatial resolution is defined by the beam diameter which typically lies in the sub-millimeter to millimeter range, resulting in a spatial resolution

higher than that of PET but lower than that of MRI or CT [27, 24, 11]. The sensitivity in XFI depends on the detected fluorescence counts relative to the underlying background within the signal's energy range and can achieve higher sensitivities than CT, though lower than in PET [25, 11, 10].
Nowadays, XFI is used preclinically at scales ranging from the single-cell scale up to small animals [25, 11]. However, imaging human-sized objects is challenging due to a large intrinsic background overlying the signal [28]. Grüner et al. provide a possible solution to overcome the "intrinsic background problem" by combining spatial and spectral filtering [28]. More precisely, they designed collimator leaves for a 4π detector and applied a spectral filtering algorithm that takes into account only the detector areas that increase the significance of the signal. However, such a detector would be extremely costly and technically challenging to realize [28]. Another research group studied a lung phantom with a detector in the backward direction [29]. However, the detector size they used, about $1600\,\mathrm{cm}^2$, is still relatively large, as detectors used in XFI commonly have an area of up to about $4\,\mathrm{cm}^2$ [29, 30, 31]. This raises the question whether XFI on human-sized scales is feasible with smaller, more practical detectors.
This thesis aims to examine the spatial distribution of the scattered photons in human-sized objects and to investigate collimator strategies as a potential solution to reduce the background by restricting the field of view (FOV) of the detector, thereby enabling XFI on human-sized objects with commercially available detectors. For the collimator designs presented in this thesis, it is assumed that XFI would be used in the context of multimodal imaging and that the location of the target is known a priori from other imaging modalities. Consequently, this approach can be applied to cancer treatment monitoring, for example, but not to pharmacokinetics, where the target locations are unknown.
Sec. 2 explains the physical background, including X-rays, photon matter interaction, the XFI-principle and radiation dose. The methods and materials used, are described in Sec. 3 which include Geant4 simulations based on a Monte Carlo code, statistics and a numerical photon model based on calculating photon path probabilities. The section about materials also includes detectors and gold nanoparticles. In Sec. 4, the background caused by multiple Compton scattering is studied numerically with respect to its spatial distribution and it is being validated by Geant4 simulations. Sec. 5 examines the uncollimated XFI energy spectra with respect to the background, fluorescence and significance for different detector angles and signal ranges. Subsequently, in Sec. 6, different collimator designs are investigated with respect to various configurations, as well as the detector's FOV and achieved sensitivities. Also, the presented collimators are compared with each other and their results are discussed and compared with different setups from the literature. A test measurement for experimental validation is performed in Sec. 7. Finally, the main results are summarized in Sec. 8 along with an outlook.
This thesis is based on the invention made by Dr. Theresa Staufer and Prof. Dr. Florian Grüner on the advanced collimation Ansatz for large objects using backward detection with optimized lamellae geometries for defining sufficiently small field-of-views as an effective way of spectral background reduction [32]. This invention was based on a detailed study on the manifold of possible photon paths in small as well as large objects, yielding the new collimation method.

2 Physical Background

2.1 Interaction of Photons with Matter

The interaction of photons with matter is an important aspect in medical imaging. This includes, for example, computed tomography and radiography, in which the attenuation of X-ray beams through matter is measured, but also the XFI imaging technique used in this thesis, which is explained in more detail in Sec. 2.3 [33]. Important interaction processes for XFI include the photoelectric effect, as well as coherent and incoherent scattering, which are described in more detail below. Another interaction process is pair production, which is the interaction between a high-energy photon and the Coulomb field of the nucleus or electrons. Through this interaction, a photon creates an electron-positron pair, thereby annihilating the photon [34]. However, since pair production only occurs at high energies, it is negligible in XFI.

2.1.1 Photoelectric Effect

The photoelectric effect is an interaction process in which a photon is fully absorbed by an inner shell electron, followed by the emission of this electron as a photoelectron [34, 35]. In this process, the incident photon needs to have an energy E_γ that is at least as large as the binding energy of the inner electron E_{b,e_i^-}. This energy E_{b,e_i^-} depends on the shell in which the electron is located before the photon is absorbed. If the photon energy is larger than the binding energy, the electron absorbs the entire energy of the photon and is ejected (Fig. 2.2a). As a result, the atomic shell is ionized and the ejected electron has a kinetic energy E_{kin,e^-} that is equal to the difference between the two energies E_γ and E_{b,e_i^-}:

$$E_{kin,e^-} = E_\gamma - E_{b,e_i^-}. \tag{2.1}$$

Here, low photon energies result in emitted electrons with a trajectory that is mostly perpendicular with respect to the incident photon, while higher energies result in emitted electrons moving in the forward direction [34, 35].
The probability of the photoelectric effect can be described by the photoabsorption coefficient μ_{pe}, which depends on the density ρ, the atomic number Z, and the energy E_γ [34]:

$$\mu_{pe} \propto \rho \frac{Z^n}{A E_\gamma^3} \approx \rho \frac{Z^{n-1}}{E_\gamma^3} \quad \text{for } E_\gamma << 511\,\text{keV}. \tag{2.2}$$

The exponent n depends on the atomic number, which is larger for electrons from the K-shell than for electrons from shells further outwards (L-, M-, ...shell). This is because electrons from the K-shell are closer to the nuclear charge and shield it, so that outer electrons experience a lower nuclear charge and Z therefore has a lower impact. For light elements, the power of Z for K-shell electrons is $n = 5$ and for outer shell electrons $n = 4.5$, whereas for heavy elements, $n = 4$ applies [34]. In addition, the electron density has an impact on the probability of the photoelectric effect, which is more likely at higher densities. These are found in particular in the inner K-shell of heavy atoms, where the electron binding is stronger [34, 35]. Thus, in the photoelectric effect, around 80% of

the photons are absorbed by K-shell electrons and only around 20% of the photons are absorbed by electrons from shells further out [34]. Finally, μ_{pe} also depends on the energy E_γ of the absorbed photon. It is an anti-proportional relation with a power of three, as can be seen in Eq. 2.2 [34]. This means that the photoelectric effect is especially important for low energies [35]. In Fig. 2.1, the mass-attenuation coefficient $\mu_m = \mu/\rho$

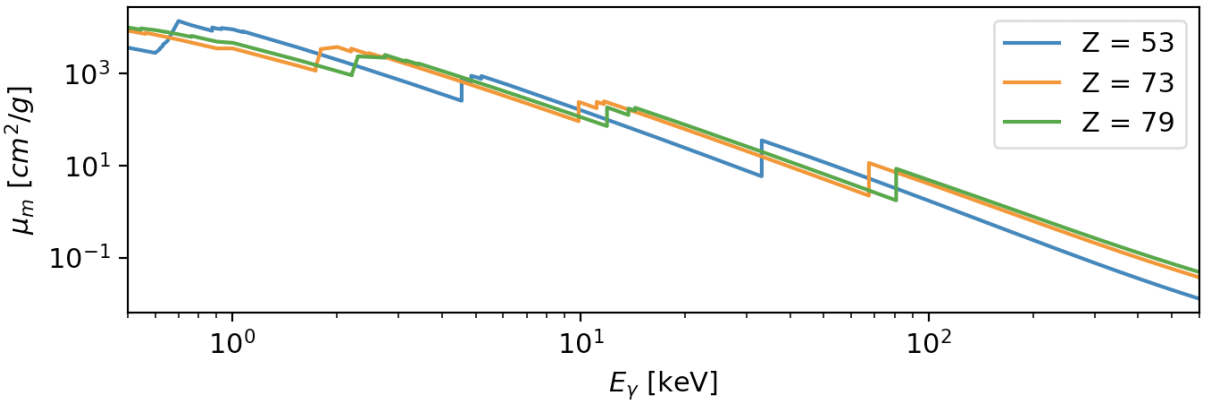

Figure 2.1: The mass-attenuation coefficient $\mu_m{=}\mu/\rho$ $[\frac{cm^2}{g}]$ of the photoelectric effect for the elements iodine (Z = 53), tantalum (Z = 73), and gold (Z = 79) is shown as a function of incident energy E_γ [keV]. The values were taken from the xraylib [36].

of the photoelectric effect is shown as a function of energy for different elements. Gold and iodine are shown as potential targets in XFI, while tantalum is a potential collimator material. It appears that the coefficient does not decrease continuously with increasing energies, but rather has several absorption edges at the specific binding energies of the electron shells ($E_\gamma = E_{b,e_i^-}$), at which the probability of the photoelectric effect suddenly increases. Gold, for example, has an absorption edge at an energy of $E_\gamma = 80.72\,\text{keV}$ [36]. This corresponds to the binding energy of an electron from the K-shell, which can be ejected from this energy upwards. For tantalum and iodine, these K-edges are at lower energies. There, an electron from the K-shell can be ejected at energies above either 67.42 keV for tantalum or 33.17 keV for iodine [36]. Less energy is required for the emission of an electron from the L-shell or even higher shells, which can be seen from the lower energy edges. Furthermore, Fig. 2.1 shows the relation of Eq. 2.2, as the coefficients decrease with higher energy, except for the absorption edges, and a higher atomic number results in a larger coefficient, which is particularly noticeable at energies above 81 keV. However, Eq. 2.2 only holds for photon energies with $E_\gamma << 511\,\text{keV}$. At higher energies μ_{pe} is less energy-dependent with only a power of one [34]:

$$\mu_{pe} \propto \rho\frac{Z^n}{AE_\gamma} \approx \rho\frac{Z^{n-1}}{E_\gamma} \quad \text{for } E_\gamma >> 511\,\text{keV}. \tag{2.3}$$

The ejected photoelectron, also called a secondary particle, creates an electron hole, which is refilled by secondary processes [34, 37]. In the Auger process, for example, the inner hole recombines with an electron from an outer shell e_o^-. The energy released in this process is absorbed by a so-called Auger electron, which is then emitted (Fig. 2.2b) [37].

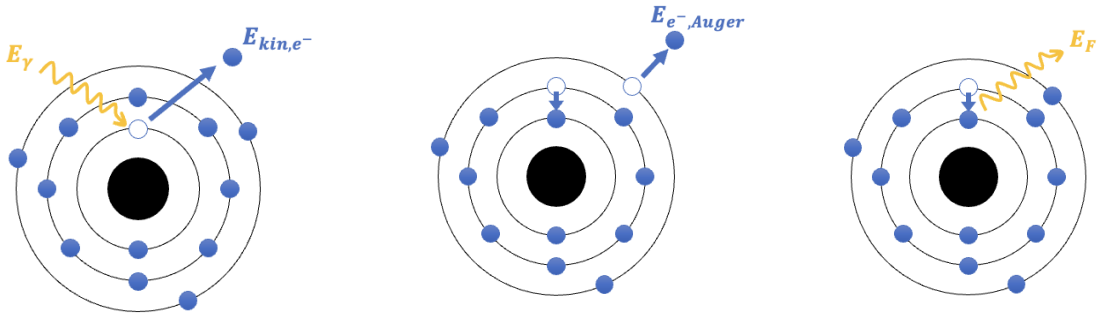

(a) Photoelelctric effect. (b) Auger process. (c) Fluorescence process.

Figure 2.2: An electron hole created in the inner shell by the photoelectric effect (a) is filled by an outer shell electron, resulting in either the emission of an Auger electron (b) or a fluorescence photon (c).

Another, more dominant secondary process is the emission of a fluorescence photon when the inner electron hole is filled by an electron from an outer shell (Fig. 2.2c). Consequently, the emitted photon has a characteristic energy E_F from the subtraction of both shell binding energies [34]:

$$E_F = E_{b,e_o^-} - E_{b,e_i^-} \tag{2.4}$$

These characteristic fluorescence lines are also written as $K_{\alpha 1}$, $K_{\alpha 2}$, $K_{\beta 1}$,.., $L_{\alpha 1}$... Here, the capital letter describes the shell of the electron hole (e_i^-) that is being refilled, and the Greek letter describes the shell from which the refilling outer electron originates (e_o^-) [37]. More precisely, the Greek letter describes the difference between these two shells. For example, if an electron from the L-shell refills a hole in the K-shell, the resulting fluorescence line is K_α [37]. The fluorescence photons are emitted isotropically in all directions. Additionally, the photoelectron ejected by the photoelectric effect can generate "Bremsstrahlung" due to its deceleration, which, like the characteristic fluorescence photons and the Auger-electrons, is categorized as tertiary radiation [34].

2.1.2 Coherent Scattering

When a photon is scattered at a free electron or weakly-bound shell electron without transferring any energy, the process is called Thomson scattering [34]. The incident photon drives the electron to oscillate at the same frequency as the incident photon. Afterwards, the oscillating electron directly re-radiates a photon with the same frequency and energy as the incident photon. Consequently, no ionization takes place. Since only the direction of the photon changes and not its energy, wavelength or frequency, this scattering process is called coherent [35, 34].
When the interaction of a low-energy photon takes place on an entire atom, this is referred to as Rayleigh scattering. It usually occurs when the ionization energy E_I (the minimum energy required to eject the least bound electron from a neutral atom [38]) is much higher

than the photon energy ($E_I >> E_\gamma$) [39, 40]. In Rayleigh scattering, the shell electrons of the atom oscillate coherently and subsequently photons with the same energy are re-radiated [34].
Like photoelectric absorption (Eq. 2.2) the coherent scattering coefficient μ_R depends on the density ρ, the atomic number Z and the photon energy E_γ, but with a weaker dependence [34]:

$$\mu_R \propto \rho \frac{Z^{2.5}}{AE_\gamma^2} \approx \rho \frac{Z^{1.5}}{E_\gamma^2} \quad \text{for } E_\gamma > 10keV. \tag{2.5}$$

However, Rayleigh scattering is not equally probable for all scattering angles, but instead is anisotropic. The angular dependence is described by the differential coefficient $d\mu_R/d\Omega$ [41]:

$$\frac{d\mu_R}{d\Omega} \propto (1 + \cos^2(\theta)). \tag{2.6}$$

Consequently, photons scatter predominantly in the forward or backward direction since Eq. 2.6 reaches its maximum for angles with $\theta = 0°$ or $\theta = 180°$, whereas perpendicular coherent scattering with $\theta \approx 90°$ is less probable [34].

2.1.3 Compton Scattering

Compton scattering is an interaction between a photon and a quasi-free electron, whereby the binding energy of the electron is smaller than the energy of the incoming photon $E_\gamma = h\nu$ [42, 43]. In this interaction, the photon transfers part of its energy and momentum to the electron, causing the electron to be ejected from the shell and thus ionization to occur, but also causing a change in the direction of the photon and thus scattering (Fig. 2.3) [34]. As a result, the photon loses some of its energy and its wavelength changes. Consequently, unlike Rayleigh or Thomson scattering, Compton scattering is not a coherent scattering process, but an incoherent one.

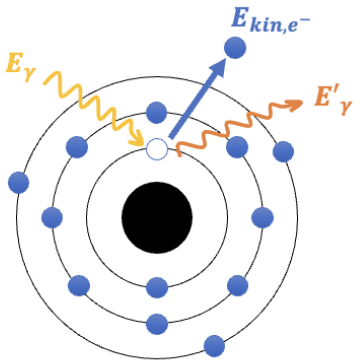

Figure 2.3: In Compton scattering, a photon with energy E_γ transfers part of its energy to an electron E_{kin,e^-} and afterwards has energy E'_γ.

The energy of the photon after Compton scattering $E'_\gamma = h\nu'$ can be derived from the conservation of energy and momentum of the photon and electron in which the electron

is approximated to be free and at rest [42, 35, 34, 44]:

$$E'_\gamma = \frac{E_\gamma}{1 + \frac{E_\gamma}{m_0 c^2}(1 - \cos(\theta))}. \tag{2.7}$$

As shown by Eq. 2.7, the energy of the Compton-scattered photon depends on the photon's scattering angle θ. A small scattering angle yields more energetic Compton-scattered photons. This means that less energy is transferred from the photon to the kinetic energy of the electron. However, scattering in the backward direction is associated with larger energy transfer to the electron and less energetic Compton photons (Fig. 2.4).

The Compton scattering is not isotropic, which means that the Compton probability

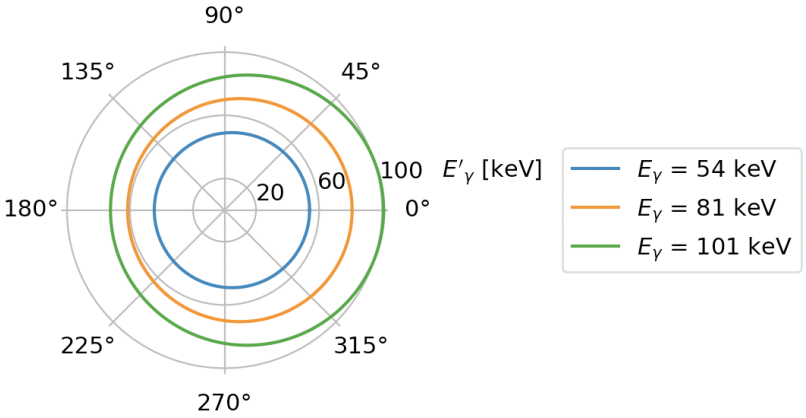

Figure 2.4: Energy E'_γ of Compton scattered photons for scattering angles θ with incident energies E_γ (calculated with Eq. 2.7).

depends on the scattering angle of the photon. This can be described by the differential cross section from the so-called Klein-Nishina equation, where the cross section σ, like the coefficient μ, is a measure of the interaction probability (it can be converted using Eq. 2.15) [45]:

$$\frac{d\sigma_{KN}}{d\Omega_\theta} = \frac{r_0^2}{2}\left(\frac{E'_\gamma}{E_\gamma}\right)^2\left(\frac{E_\gamma}{E'_\gamma} + \frac{E'_\gamma}{E_\gamma} - \sin^2\theta\right). \tag{2.8}$$

As shown in Eq. 2.8, the differential cross section per unit solid angle and per electron $d\sigma_{KN}/d\Omega_\theta$ for a photon with scattering angle θ also depends on the photon energy [45]. Possible angular distributions for different incident energies are shown in Fig. 2.5.
Most photons with high incident energies are scattered in the forward direction ($\theta < 90°$, $\theta > 270°$), while lower incident energies increasingly lead to more backscattering ($90° < \theta < 270°$). At an incident energy of 1 keV, the cross sections for the forward and backward scattering direction are even approximately equal. In addition, particularly few photons are scattered perpendicularly ($\theta = 90°$, $\theta = 270°$).

The total Compton cross section can be obtained by integrating the Klein-Nishina equation over all possible scattering angles [46]. It is clearly shown in Fig. 2.5 that in the range from 1 keV to 500 keV, a higher incident energy results in a lower total Compton cross section. Multiplying the total Compton cross section by the particle density provides the total Compton coefficient, as explained in more detail in Chapter 2.1.4 (Eq. 2.15).

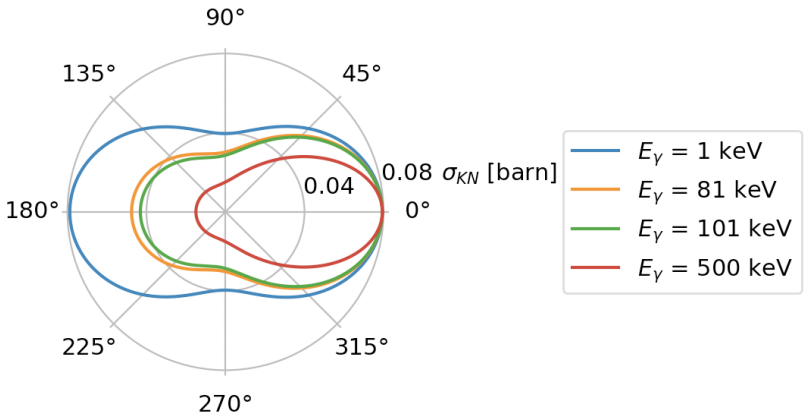

Figure 2.5: Klein-Nishina cross sections σ_{KN} [barn] = $[10^{-28}m^2]$ as a function of the scattering angle θ for unpolarized photons with incident energies E_γ between 1 keV and 500 keV (determined with the xraylib [36]).

2.1.4 Attenuation of Photons in Matter

When a monoenergetic photon beam penetrates through matter the photon intensity $I(x)$ decreases because some photons interact with the medium [47]. This intensity reduction $-dI/dx$ for a material thickness dx [cm] that the photons must penetrate depends on the linear attenuation coefficient μ [1/cm] [47, 48]:

$$-\frac{dI}{dx} = \mu I(x) \Leftrightarrow -\frac{dI}{I} = \mu dx. \tag{2.9}$$

By integrating Eq. 2.9 and subsequent transformations, the photon intensity I after penetrating through a medium with thickness $dx = l$ can be obtained, whereby this equation is also known as Beer-Lambert law [47, 49]:

$$\int_{I_0}^{I} \frac{1}{I} dI = -\mu \int_0^l dx \Leftrightarrow ln\left(\frac{I}{I_0}\right) = -\mu \cdot l. \tag{2.10}$$

$$I = I_0 e^{-\mu l}. \tag{2.11}$$

However, in XFI the number of photons N is often analyzed. Therefore, Eq. 2.11 can be transformed so that Eq. 2.12 can be used instead [34]:

$$N(l) = N_0 e^{-\mu l}. \tag{2.12}$$

The ratio of transmitted photons N to incident photons N_0 describes the transmission T [34]:

$$T = \frac{N(l)}{N_0} = e^{-\mu l}. \tag{2.13}$$

Consequently, the photon transmission decreases exponentially, which is illustrated in Fig. 2.6.

Photons interact much more often when penetrating heavy elements such as gold or tantalum compared to when passing through soft tissue or air. This is due to their larger

mass-attenuation coefficients μ/ρ (Fig. 2.7) and their high densities ρ. For example, gold has a density of 19.32 g/cm^3 and tantalum 16.65 g/cm^3, while soft tissue has a density of only about 1 g/cm^3 [50]. Consequently, 50% of the incident photons have already interacted after a short penetration depth of 0.0407 mm in gold and 0.0568 mm in tantalum. The highest transmission in Fig. 2.6 is in air, which, after a penetration depth of 30 cm, has a photon fraction of 99.4% that has not interacted with the air. In soft tissue, however, 99.55% of the photons have already interacted at this penetration depth, and the transmission there is therefore only T = 0.0045. These differences can be explained by the much lower density of air ($\rho = 0.0012$ g/cm^3) compared to soft tissue [50]. As already

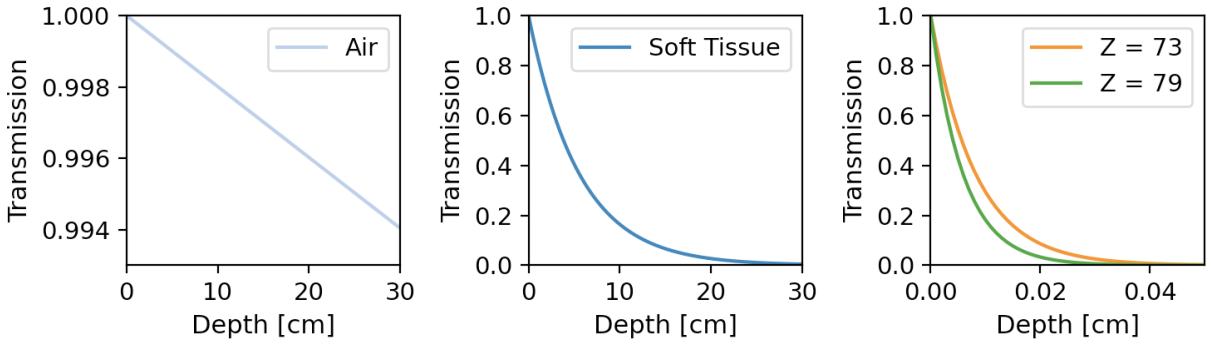

Figure 2.6: Transmission of photons with an incident energy of 81 keV in air and soft tissue, as well as in the elements tantalum (Z = 73) and gold (Z = 79). To determine the transmission, Eq. 2.13 is used, whereby Eq. 2.15 is used to calculate the required attenuation coefficient with μ/ρ from xraylib [36] and ρ from the NIST database [50].

mentioned, the number of photons is impacted by the linear attenuation coefficient μ, which results from all possible interactions of photons with matter, i.e., the photoelectric effect μ_{pe}, Rayleigh scattering μ_R, Compton scattering μ_C and pair production μ_{pp} [51, 52]:

$$\mu_{total} = \mu_{pe} + \mu_R + \mu_C + \mu_{pp}. \tag{2.14}$$

Pair production, however, only becomes relevant for energies above 1.022 MeV and therefore negligible in the considered energy range [43]. Furthermore, the linear attenuation coefficient μ is often also expressed by the mass-attenuation coefficient $\mu_m = \mu/\rho$ $[cm^2/g]$ and the density ρ $[g/cm^3]$ of the medium or by the cross section σ $[cm^2]$ and the number of particles per unit volume n $[1/cm^3]$ [53]:

$$\mu = \mu_m \rho = \sigma n. \tag{2.15}$$

However, the attenuation coefficients depend not only on the material density ρ, but also on the photon energy E_γ of the incident photons and the atomic number Z of the material [54, 36].
These total mass-attenuation coefficients and their various components for soft tissue and gold, taken from xraylib [36], are illustrated in Fig. 2.7.
Both axes are logarithmic, with the various μ_m values plotted as a function of energy E_γ between 0.1 keV and 600 keV. In both cases, the photoelectric effect is the dominant component of the total mass-attenuation coefficient at lower energies. In gold, it dominates

up to an energy of about 520 keV, while in soft tissue, Compton scattering is already more dominant at an energy of about 27 keV. The mass-attenuation coefficient of the photoelectric effect shows the absorption edges discussed in Chapter 2.1.1, which are caused by the binding energies of the electrons. In contrast to soft tissue, the absorption edges of gold lie at much higher energies, which is why the photoelectric effect is more important at higher energies. It is also shown that at low energies, Rayleigh scattering occurs more frequently than Compton scattering, which reverses after a certain energy. This is because for Compton scattering, the electrons must be quasi-free, which is rather achieved at high energies, whereas for Rayleigh scattering, the energy must be low enough to not cause ionization (Sec. 2.1.2 and 2.1.3). However, it seems that the Rayleigh mass-attenuation coefficient has only a minor impact on the total mass-attenuation coefficient anyway.

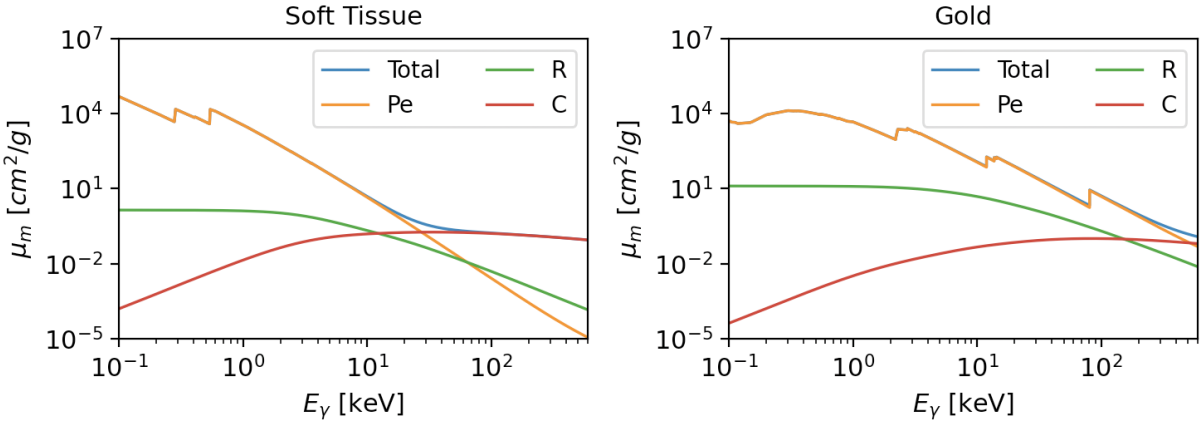

Figure 2.7: The total mass-attenuation coefficient μ_m (Total) and its various components from the photoelectric effect (Pe), the Rayleigh scattering (R) and Compton scattering (C) as a function of incident energy E_γ for soft tissue and gold.

2.2 X-rays

X-rays are electromagnetic radiation used in many imaging modalities and occupy the high-energy region of the electromagnetic spectrum. For example, the energies of visible light and UV radiation range from 1 eV to 40 eV, while X-rays usually have energies in the keV range [34]. Electromagnetic radiation consists of periodic waves with electric and magnetic fields that are perpendicular to each other [55, 56].

2.2.1 Generation of X-rays

X-rays share many similarities with gamma rays, as both are in the same energy range. Gamma rays are produced by the decay of unstable nuclei, however, X-rays are generated differently. To understand how X-rays are generated, it is useful to take a closer look at how an X-ray tube works, which is able to generate X-rays. Part of the X-ray tube is a cathode filament which is connected to an electrical circuit. The electrical resistance heats the cathode and induces the thermionic emission. As a result, some electrons are emitted from the cathode filament. The X-ray tube contains two electrodes (anode and

cathode) that are located in a vacuum and connected to high voltage. The negatively charged cathode is located on the side of the emitted electrons, which are accelerated towards the positively charged anode due to the applied voltage. Corresponding to the applied high-voltage, the electrons have a kinetic energy in the range of keV. X-rays are generated when the accelerated electrons interact with the anode atoms [55].
If the electron is deflected from its trajectory due to the Coulomb field of the anode nuclei, it undergoes acceleration (change in direction and/ or speed) [57, 55]. The energy released by this deceleration is emitted as electromagnetic radiation, which is known as Bremsstrahlung. In this process, the distance between the electron and the anode nuclei determines the strength of deflection and thus the energy of the Bremsstrahlung. The maximum deflection and hence the most energetic photons are produced if electrons hit the anode nuclei and convert all their energy into the Bremsstrahlung. However, this is relatively unlikely, and interactions at greater depths are more frequent, resulting in less energetic radiation. Finally, this distance dependence between the electron and the anode nuclei generates a broad energy spectrum [55].
Another possibility is that the accelerated electrons eject inner-shell electrons out of the anode atoms. After these electron holes have been refilled by other electrons from a more outer shell having a lower binding energy, characteristic X-rays are generated that correspond to the binding energy differences. Characteristic peaks then appear in the energy spectrum alongside the broad Bremsstrahlung spectrum [55].

Besides X-ray tubes, X-rays can also be generated using other sources. Synchrotron radiation, for example, is often generated by a storage ring in which charged particles with relativistic velocity are deflected and focused on a circular trajectory [58, 37, 37]. This transversal acceleration and focusing is enabled by either electrical or magnetic fields, whereby the use of deflection or curved magnets is technically easier for the generation of synchrotron radiation [37]. In synchrotrons, undulators are often used as insertion devices. Undulators force electrons onto a periodic trajectory by using a periodic magnetic field, thereby causing the emission of radiation [37]. As a consequence, quasi-monochromatic, highly collimated and brilliant X-rays can be generated [59]. In summary, X-rays are usually produced either by the acceleration of charged particles or by characteristic radiation.

2.3 X-Ray Fluorescence Imaging

This thesis focuses primarily on the imaging technique of X-ray fluorescence imaging (XFI), which is why XFI is explained in more detail in this chapter in terms of physics. XFI is a functional imaging technique based on the interaction processes between photons and matter described in Sec. 2.1 [60, 11]. An object of interest is scanned by an X-ray beam, inducing the photoelectric effect and the subsequent emission of characteristic fluorescence photons. These characteristic photons are element-specific and are detected as the signal in XFI, enabling the simultaneous identification of different elements [25, 60, 22, 61, 24]. For this reason, it is common practice in XFI to use specific markers (e.g., gold nanoparticles) to track certain targets in an object to be scanned [11, 24].
However, the incident X-rays not only generate fluorescence photons through the photo-

electric effect, but also interaction processes that overlap with the signal and are considered background noise. The background in the signal range limits the sensitivity of an XFI measurement [11]. Since Rayleigh-scattered photons scatter coherently and do not lose energy, they typically do not fall within the energy range of fluorescence photons. In contrast, Compton photons lose some energy due to their (single or multiple) scattering, depending on the scattering angle, resulting in a broad spectrum (Sec. 2.1.3). This means that Compton photons can overlap the signal range. As a result, many Compton photons are generated, especially in the case of large objects due to their increased penetration depths [28, 62]. Furthermore, the beam is attenuated, which has a particular impact on markers located deep inside the object. Fewer photons then reach the marker, resulting in fewer possible fluorescence photons being generated and thus a weaker signal (Sec. 2.1.4). Note that Compton photons dominate the intrinsic background [28].
The resolution achievable with XFI is thereby determined only by the beam size. This is why the synchrotron is the preferred choice, as it offers a monochromatic pencil beam with a small beam diameter and, in addition, a high flux and maximum sensitivity available today. For example, the P21.1 beamline from PETRA III (DESY, Hamburg) provides a diameter of about 1 mm [28, 22, 11, 25]. However, some setups with conventional X-ray sources are also being developed in order to perform XFI with more compact and cost-effective beam sources [11].
In summary, the fluorescence photons generated by the photoelectric effect represent the signal in XFI, while the other interaction processes represent the overlaying background noise, with Compton accounting for a particularly large proportion.

2.4 Radiation Dose

Many medical imaging methods, such as CT and XFI, use X-rays, which are ionizing radiation [63, 64]. Ionizing radiation is high enough in energy to remove electrons from atoms or molecules (Sec. 2.1). Consequently, DNA damage and cell mutations can occur as a result of the created ions and free radicals arising from direct and indirect ionization [63, 65]. Therefore, X-rays are associated with some health risks, and it is important to pay attention to the so-called radiation dose, a parameter that measures the impact of radiation when performing imaging with ionizing radiation, and to keep it "as low as reasonably achievable" [64, 63]. The radiation dose can be distinguished between the absorbed dose and the equivalent dose. While the absorbed dose measures the amount of energy absorbed per unit mass in Gray ($1\,\mathrm{Gy} = 1\,\mathrm{J/kg}$), the equivalent dose takes different types of applied radiation into account and describes the biological effects in the unit of Sievert ($1\,\mathrm{Sv} = 1\,\mathrm{J/kg}$) [64, 65, 66].
The absorbed dose D is generally defined as the absorbed energy dE_{abs} per unit of mass dm when irradiating a volume [65, 66]:

$$D = \frac{dE_{abs}}{dm}. \tag{2.16}$$

The absorbed dose at a depth l can be estimated using the incident energy E_0, the parameter Φ, which is the number of photons N relative to the radiated area A_D, and the mass-energy absorption coefficient μ_{en}/ρ. Taking the decreasing photon number N

for deeper depths into account due to attenuation, the absorbed dose $D(l)$ for N_0 incident photons is a function of the depth l [65, 67, 66]:

$$D(l) = E_0 \cdot \Phi(l) \cdot \left(\frac{\mu_{en}}{\rho}\right) \quad \text{with} \quad \Phi = \frac{N_0 \cdot e^{-\mu l}}{A_D}. \tag{2.17}$$

Note that Eq. 2.17 equals the so-called Kerma and that the absorbed dose can only be described by Eq. 2.17 as long as Kerma and absorbed dose are the same [65, 66]. For the X-ray energies typically used in medical imaging, however, this is the case, as stated in [66]. The average dose up to a depth l_{max} can be obtained by integrating the dose $D(l)$ over the depth interval from l_{min} to l_{max}:

$$\overline{D} = \frac{1}{l_{max} - l_{min}} \int_{l_{min}}^{l_{max}} D(l)\, dl. \tag{2.18}$$

Unlike the mass-attenuation coefficient, the mass-energy absorption coefficient considers that not all of the energy of interacting photons within an irradiated volume is deposited in that volume. More precisely, in Compton scattering, depending on the scattering angle (Eq. 2.7), scattered photons only deposit part of their energy in the considered volume [65, 67].

3 Material and Methods

3.1 Geant4

Interactions between photons and matter are simulated by the free software toolkit Geant4 (GEometry ANd Tacking4). Geant4 is an object-oriented software package written in C++ [68]. As its name implies, Geant4 provides the ability to create a wide variety of different and complex geometries, which can be optionally visualized via the Geant4 graphical user interface (GUI) [69, 68, 70, 71].
The software offers a variety of materials that can be assigned to these geometries, enabling the simulation of many different setups [71]. In this way, a detector can be created as well [70]. Not only can the geometry and materials be specified, but also the physical properties of the particles that interact with this setup. This includes the particle type; photons, electrons, and ions are a few examples of what can be simulated [72, 71]. The possible energies of the simulated particles range from meV to GeV, and in some cases, even up to TeV [71].
After defining, the incident particle type and energy, among other parameters, the interaction of particles with the predefined geometrical setup is simulated by a Monte Carlo code [69, 70]. This means that each modeled event and its computation are independent of each other [70]. The effects of physical particle interactions are taken into account by implementing one of the many different physics model variants [71, 68]. For example, possible electromagnetic processes for photons include the photoelectric effect, Compton scattering, Rayleigh scattering and pair production [73]. The "Livermore" model, used for the simulations in this thesis, is a standard electromagnetic physics list that considers unpolarized photons and describes interaction processes [74]. All particle tracks, including secondary particles arising from previous interactions (e.g., electrons from Compton scattering), can be recorded and visualized in the GUI [72]. Physical properties such as energy, momentum, position, and time are stored [75]. Finally, the information of the detected particles can be stored in root files [76].
Overall, Geant4's ability to simulate a wide range of complex scenarios makes the software attractive for many physical applications.

3.2 Statistics

The behavior of interactions between photons and matter can be described by Poisson's law, which is a limit of the binomial distribution for large sample sizes and low probabilities. The resulting Poisson distribution describes the probability $p_\mu(k)$ of observing k events when μ events are expected [77, 78, 79]:

$$p_\mu(k) = \frac{\mu^k}{k!} e^{-\mu} \quad \text{with} \quad k \in \mathbb{N}_0. \tag{3.1}$$

In Poisson's statistics, the variance $\mathbb{V}ar(k)$ is equal to the expectation value μ_k [77, 78, 79]. Consequently, the standard deviation, which represents the fluctuations of the variable k, is σ_k [78]:

$$\sigma_k = \sqrt{\mathbb{V}ar(k)} = \sqrt{\mu_k}. \tag{3.2}$$

In the imaging method XFI, the interaction processes of photons with matter are distinguished in two categories: on the one hand, the interactions generating the fluorescence signal, and on the other hand, all other photon interactions generating the background. To determine whether a peak observed in a photon spectrum originates from signal photons rather than background fluctuations, one must perform a statistical test [62, 80]. One example of such a test is a one-sided null-hypothesis test under normality assumptions - the Z-test. Z-tests attempt to compute a test characteristic that is standard normal under the test assumptions, this test statistic is also called the significance [80].
In the literature, the following equation is frequently used to calculate the significance Z based on a given background B and signal S (e.g., from simulations) [28, 81]:

$$Z = \frac{S}{\sigma_B} = \frac{S}{\sqrt{B}}. \tag{3.3}$$

Here, Z is the ratio of the signal relative to the background fluctuation $\sigma_B = \sqrt{B}$ (s. Eq. 3.2), and a signal is typically considered significant if it is at least three times larger than the background fluctuation ($Z > 3$) [28].
However, Eq. 3.3 does have some limitations. With small sample sizes, the significance may be underestimated or overestimated [80]. In particular, a low level of background causes issues when applying Eq. 3.3. In such cases, even a small number of signal photons could yield a high significance [80]. If, for example, the background was zero, a significance of infinity would be calculated even if only a single signal photon was present, although in this case the signal should not actually be considered significant. For this reason, Eq. 3.3 only holds for a sufficiently large sample size and when the background is much larger than the signal ($B >> S$) [80, 82, 83].

Note that the content of the following section is based on the reference [80], unless otherwise stated. Rather than using the naive estimator $\hat{\mu}_k = k$ one can use more sophisticated methods such as using a closed form gamma conjugate prior, which yields a signal to noise ratio of

$$Z = \frac{S}{\sqrt{2B + S + 2}}. \tag{3.4}$$

This signal to noise ratio attempts to capture the fidelity for tracer quantification. However, it can also be adapted into a one sided null-hypothesis test by adding the a priori assumption of $\mu_s = 0$, yielding

$$Z = \frac{S}{\sqrt{2B + 2}}. \tag{3.5}$$

This Z-score is the test statistic for the subtraction method in XFI. In some cases throughout this thesis, the number of incident photons is scaled from N' to N incident photons using the factor N/N', and the same applies to the concentration c of the signal-providing target, scaled by the factor c/c'. In this thesis, Eq. 3.5 is used to determine significances unless otherwise stated, and a signal is considered significant if the significance Z, including the standard deviation σ_Z exceeding a threshold of three

$$Z - \sigma_Z > 3. \tag{3.6}$$

The standard deviation σ_Z of the predicted significance is calculated using the following equation:

$$\sigma_Z = \sqrt{\mathbb{V}ar(Z)} = \sqrt{\left(\frac{dZ}{dF}\right)^2 \mathbb{V}ar(F) + \left(\frac{dZ}{dB}\right)^2 \mathbb{V}ar(B)}. \tag{3.7}$$

Here, the variances, $\mathbb{V}ar(F)$ for the fluorescence counts and $\mathbb{V}ar(B)$ for the background counts, are described by the negative binomial distribution:

$$\mathbb{V}ar(X) = \mu_X \cdot \left(1 + \frac{N'}{N}\right) \quad \text{with} \quad X \in [F, B]. \tag{3.8}$$

In an experimental context, the subtraction method, as used in [25], for example, is a useful way to determine the signal significance. This method involves two measurements. One measurement should include the entire setup of the scenario, including the signal-emitting fluorescence target, in order to record the total counts T. In a separate measurement, the background B should be measured without the fluorescence target. Then, the significance Z of a potential signal peak $(T - B)$ can be determined using the following equation:

$$Z = \frac{T - B}{\mathbb{V}ar(T - B)} = \frac{T - B}{\sqrt{T + B}} \quad \text{with} \quad T = B + F. \tag{3.9}$$

Since the background B and total counts T are two independent Poisson variables due to the two separate measurements, $\mathbb{V}ar(T - B) = \mathbb{V}ar(T) + \mathbb{V}ar(B) = T + B$ holds, and is used in Eq. 3.9 [79, 77].

3.3 Numerical Photon Model

Another way to study the behavior of photons is to numerically model the number of photons detected. In the numerical modeling, photon paths are discretized. The probability of each path is calculated, and then the expected number of detected photons is determined. Unlike Geant4 simulations based on the Monte Carlo algorithm, this model eliminates statistical fluctuations. Additionally, the numerical model provides insights into the predicted counts by analyzing specific parameters. In contrast, Geant4 takes relativistic effects, such as Doppler broadening, into account.
The following chapter explains the numerical model for estimating fluorescence and Compton photons, since in XFI, fluorescence photons are considered to be signal photons, while Compton photons are considered to be the dominant background. The foundation of the numerical model was first developed by Prof. Dr. Florian Grüner, and then expanded in this thesis to include, for example, fluorescence photons, a pixelated detector and the determination of the detector's field of view when using a collimator.

3.3.1 Fluorescence Model

The fluorescence model estimates the number of fluorescence counts expected to be detected when an incident beam interacts with a gold (Au) target. For the modeling purposes, a scenario involving an arbitrary object, such as a standing, human-sized cylinder

made of soft tissue, and a detector placed in the surrounding world is considered. The world should mostly consist of either air or vacuum. A beam source is placed on the surface of the object at $O_S = (0,0,z_S)$, whereby for a standing cylindrical object with a radius R_{Obj}, the relation $z_S = -R_{Obj}$ would hold.
The object contains a gold target located on the z-axis between $z_{Au_{min}}$ and $z_{Au_{max}}$, to which the incident beam is also aligned. Consequently, gold fluorescence generation is only possible within this z_{Au} interval. The numerical model simplifies that only fluorescence paths are considered where the fluorescence occurs within the target with a step size or distance of d_z. This means that there are a total of $n = \frac{z_{Au_{max}} - z_{Au_{min}}}{d_z}$ possible steps or different fluorescence paths i. To estimate the number of gold fluorescence photons F_i of path i, the probability p_{F_i} of each possible path is calculated and multiplied by the number of photons N_0 from the incident beam. Summing over all paths results in the number of photons expected to be detected:

$$F = \sum_i F_i = \sum_i N_0 \cdot p_{F_i} \quad \text{with} \quad i \in \left\{1, 2, \ldots, \frac{z_{Au_{max}} - z_{Au_{min}}}{d_z}\right\}. \tag{3.10}$$

The probability p_{F_i} of each of these photon paths is based on several parameters, such as the transmission T, the yield of generated fluorescence photons Y_F, the geometrical factor, or more precisely, the solid angle G and the projection P:

$$p_{F_i} = (T_{in} Y_F T_{out} G P)_i \quad \text{with} \quad i \in \left\{1, 2, \ldots, \frac{z_{Au_{max}} - z_{Au_{min}}}{d_z}\right\}. \tag{3.11}$$

The various factors from equation 3.11, which define the probability of a single fluorescence photon path, are explained in more detail in the following.
First, the photons of the incident beam traverse a distance r_{in} through the object from the beam source (0, 0, z_S) to any position within the gold target (0, 0, z_{Au}). During this penetration, interactions with the object material may occur, resulting in fewer photons reaching the gold target and thus fewer photons being able to generate fluorescence. The fraction of photons that finally arrive at the gold target without any interaction is described by the transmission T_{in}, which is an exponential function according to equation 2.13:

$$T_{in} = e^{-\mu_{in} r_{in}} = e^{-\mu_{m,in} \rho_{Obj} r_{in}} \quad \text{with} \quad r_{in} = z_{Au} - z_S. \tag{3.12}$$

The mass-attenuation coefficient $\mu_{m,in}$ depends on the material that the photons pass through and on the incident energy of the photons. It is taken from xraylib [36], and the required material density ρ_{Obj} of the object for determining the total linear attenuation coefficient μ_{in} is taken from the NIST database [50].
Subsequently, the photons transmitted to the gold-target location $z_{Au} = z_{Au_{min}} + i \cdot d_z$ may generate some gold fluorescence photons in the target. The fraction of these generated fluorescence photons within the step size d_z is described by the fluorescence yield Y_F:

$$Y_F = \mu_F \cdot d_z = \mu_{m,F} \cdot \rho_{Au} \cdot d_z. \tag{3.13}$$

Now, the density ρ_{Au} and the mass-attenuation fluorescence interaction coefficient $\mu_{m,F}$ of the target material gold must be used to determine the linear attenuation coefficient

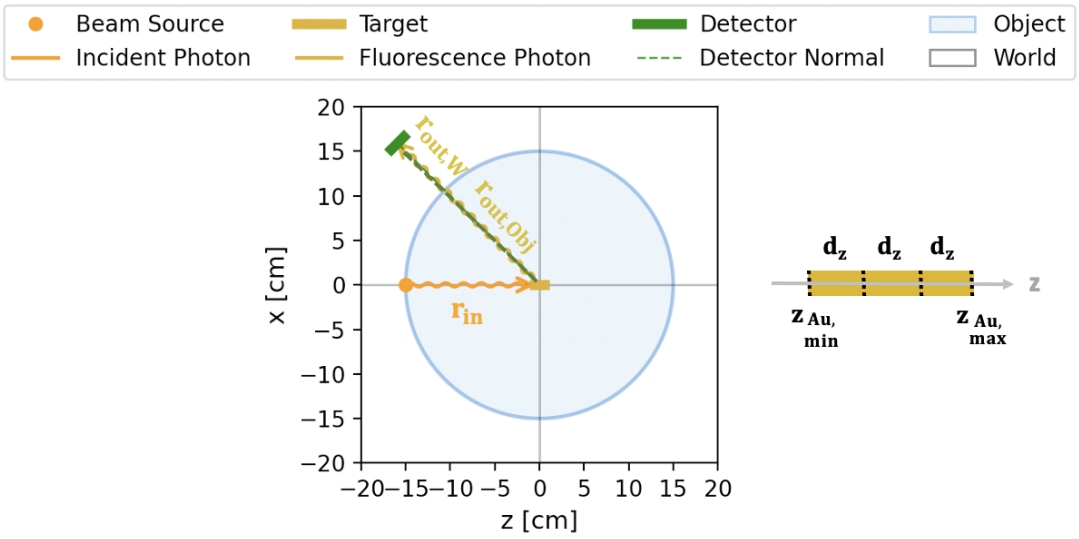

Figure 3.1: Principle of the Fluorescence Model in the beam plane ($y = 0$): A beam source on the z-axis at the edge of an object emits photons that travel a distance of r_{in} along the z-axis to the fluorescence target (0, 0, z_{Au}). In this case, the center of the target is at $z_{Au} = 0$. Subsequently, the fluorescence photons travel a distance of $r_{out,Obj}$ through the object, followed by an additional distance $r_{out,W}$ through the world, before reaching the detector. On the right, an enlargement of the target from $z_{Au,min}$ to $z_{Au,max}$ is shown, divided into sections with a step size of d_z for modeling purposes.

of the fluorescence μ_F. The factor $\mu_{m,F}$ can be determined using xraylib and depends on the atomic number Z of the fluorescence material, which is $Z = 79$ for gold, as well as on the incident energy E_{in} and the fluorescence line (K_α, K_β,...) [36]. As the object density, the density of the target can be taken from the NIST database [50].
Afterwards, the generated fluorescence photons traversing to the detector are considered. In doing so, the photons first transmit through the object and, after passing the object surface at any point (x_S, y_S, z_S), they transmit through the world. This results in a composite transmission from the object $T_{out,Obj}$ and the world $T_{out,World}$, which is described by T_{out}:

$$T_{out} = T_{out,Obj} \cdot T_{out,World} = e^{-\mu_{out,Obj} \cdot r_{out,Obj}} \cdot e^{-\mu_{out,World} \cdot r_{out,World}}. \tag{3.14}$$

The total linear attenuation coefficients $\mu_{out,Obj}$ and $\mu_{out,World}$ can be determined using Eq. 2.15 in the same way as the total linear attenuation coefficient μ_{in}. However, the characteristic fluorescence energies must be considered, which can be taken from xraylib [36], and the material must be set to air for the transmission outside the object. To calculate the distance to the detector, the simplified assumption that all fluorescence photon paths terminate at the center of the detector at (x_D, y_D, z_D) is made.
If, however, the detector is not a full solid angle 4π detector, not all fluorescence photons that transmit the distance $r_{out} = r_{out,Obj} + r_{out,World}$ are detected. The fraction of photons detected depends on the solid angle G of the detector area A_{Det} in terms of the distance

r_{out} of the location where the fluorescence photons come from:

$$G = \frac{A_{Det}}{4\pi r_{out}^2}. \tag{3.15}$$

Another parameter affecting the fraction of fluorescence photons to be detected or the fluorescence path probability is the alignment of the detector with respect to the fluorescence photon path, which is described by the projection P:

$$P = cos(\chi)cos(\psi). \tag{3.16}$$

The angle χ describes the angle within the equatorial or beam plane ($y = 0$) between the fluorescence path (from (x_D, y_D, z_D) to (0, 0, z_{Au})) and the detector normal, which are both projected onto the equatorial plane. In contrast, the angle ψ only describes the angle relative to the y-component of the fluorescence path to the detector center. In the case of a detector whose center lies in the equatorial plane and whose normal vector points to the center of the gold target, the angle of $\psi = 0°$ would apply to all modeled fluorescence paths, and the angle of $\chi = 0°$ would additionally apply to the fluorescence path originating from the center of the gold target. However, for a pixelated detector, which is described below, these angles would differ. Note that the fluorescence model can also be applied to other targets, and gold was chosen only because it is the marker of choice for human-sized XFI in this thesis, as will be discussed in Sec. 3.5.

3.3.2 Compton Model

The numerical Compton model, like the fluorescence model, considers an object and a detector within a defined geometry. The object in this modeled scenario is a vertical cylinder with a radius R_{Obj} and a height $H_{Obj} = \Delta y = 2R_{Obj}$. This geometry can be modified as needed. The center of the object is located at the origin (0, 0, 0) and a beam source is positioned on the z-axis at $z_S = -R_{Obj}$, so that the incident beam is aligned along the z-axis.

General Compton Model Estimating the number of multiple Compton-scattered photons to be expected is more challenging. Scattering then takes place not only on the z-axis, but can also occur anywhere in the entire cylinder for scattering orders greater than one due to previous Compton scattering. As in the models described above, the estimation of the detected multiple Compton-scattered photons is mainly influenced by the probability $p_{C_{j_i}}$ of a single photon path i and the incident photons N_0. Then, the number of j-times Compton-scattered photons C_j for n photon paths can generally be determined as follows:

$$C_j = \sum_{i=1}^{n} C_{j_i} = \sum_{i=1}^{n} N_0 \cdot p_{C_{j_i}}. \tag{3.17}$$

The probability of a single path i of a j-times scattered Compton photon depends on the incident transmission T_{in} from the beam source to the first scattering site, then on

the transmission values T_j from a Compton scattering site to either the next Compton scattering site or the detector, the Compton yield Y_{C_j}, the geometrical factor G_j with respect to the next Compton scattering site or detector, and finally also on the projection P:

$$(p_{C_j})_i = \left(T_{in} \left(\prod_{j'=1}^{j} Y_{C_{j'}} T_{j'} G_{j'} \right) P \right)_i . \tag{3.18}$$

To estimate the spectrum of photon energies E_j after j Compton scatterings, the angle θ of each Compton scattering c must be taken into account (Eq. 2.7):

$$E_j = \frac{E_0}{1 + \frac{E_0}{m_0 c^2} (\sum_{c=1}^{j} (1 - cos\theta_c))}. \tag{3.19}$$

Here, the electron is assumed to be free and at rest before interacting with the photon. Specific numerical models for Compton1 and Compton3 photons can be found in the Appendix A.1.

3.3.3 Numerical Model with a Pixelated Detector

Higher accuracy of the numerical model can be achieved by pixelating the detector and not just considering the center of the detector as the only destination of the photon path. Particularly with larger detector areas or short distances between the detector and the gold target, for example, the photon path lengths r_{out} would differ much more for different destination points on the detector compared to its center. The pixelation of the detector can then more accurately specify the different possible distances r_{out} of the photons when hitting the detector. Higher accuracy in transmission, solid angle, and projection is the result.
However, this also leads to more possible photons paths. In case of the fluorescence model, the fluorescence photon paths then no longer depend only on the index i or step size d_s of the gold target, but also on the number of detector pixels p or the detector pixel size $d_p \cdot d_p$.
In general, N_{path} photon paths are possible for a detector with p pixels and an object with a volume V and a length Z along the incident beam, with a step size d_s for an interaction order j:

$$N_{path} = \frac{Z}{d_s} \cdot \left(\frac{V}{d_s^3} \right)^{j-1} \cdot p \tag{3.20}$$

3.3.4 Numerical Model with a Collimator

In some scenarios, it may be necessary to consider the behavior of photons when a collimator consisting of lamellae is attached to the detector. This can be achieved by defining each lamella of the collimator by specific volumes. These would be located in the world in front of the detector, and then it is checked whether a photon path would cross any of these lamellae. If this is the case, the photon path is no longer considered to be detected. When modeling a collimator, the detector is divided into pixels to achieve greater

accuracy, since the collision of a photon path with a lamella depends on the angle of the photon path relative to the incident beam. If the detector was simplified to a single pixel instead of being divided into pixels, only one photon path per z-position would be possible. If, for example, this path did not hit a lamella, the detector would assume that this applies to all photons generated at this z-position, even if photons potentially hit a lamella at other detector positions. This is why a pixelated detector is mandatory when a collimator is used in front of the detector.

3.3.5 Limitations of the Numerical Model

The numerical model discretizes the photon paths, calculates the probability of each of those possible photon path and sums them all up. However, the model is limited by the step size because it only considers paths spaced by d_s, while paths at intermediate positions between steps are neglected. Therefore, it is important to choose a sufficiently small step size to decrease uncertainties and allow more accurate predictions regarding the expected number of detected photons.
Furthermore, at the end of the possible photon paths, the detector is simplified in the model as a point, which also limits the accuracy of the model. The pixelation of the detector increases the accuracy of the model. Nevertheless, the destinations of the photon paths on the detector are limited by a step size, like the possible scattering places.
However, a small step size would lead to a large number of possible photon paths and therefore also to enormous computation times, which represents a further limitation of the numerical model. For this reason, it is important to choose a step size (and pixel size) that represents a good compromise between computation time and accuracy. This is particularly challenging for triple Compton-scattered photons, as the number of paths is affected by seven dimensions due to their different scatter sites (Compton1 scattering place: d_{z_1} (or index k); Compton2 scattering place: dx_2, d_{y_3}, d_{z_2} (or indices l, m, n); Compton3 scattering place: dx_3, d_{y_3}, d_{z_3} (or indices r, s, t)). Concretely, this means that $i = k \cdot l \cdot m \cdot n \cdot r \cdot s \cdot t$ different paths must be calculated, and halving the step size leads to a $2^7 = 128$-fold increase in the number of paths, which would be further increased by a pixelated detector. To counteract this problem, the computation was parallelized by distributing the calculation across different Compton1 scattering locations. Then, each parallel process computed all possible higher-order Compton paths originating from a single Compton1 scattering location.

3.4 Detectors

In X-ray fluorescence imaging on human-sized objects, the choice of the detector is important. Due to the size of the object, the generated fluorescence photons may have to pass through a long distance within the object before they can be detected. To prevent too many fluorescence photons from being absorbed along the way, high-energy fluorescence photons are required, and consequently, a detector material with high efficiency at these high energies. Cadmium telluride (CdTe) offer a good option; unlike other materials such as silicon, which often exhibit a dramatic loss of efficiency in this energy range, these

materials can provide an efficiency of more than 90% at energies up to 65 keV and even 80% for energies around 80 keV for a thickness of 1 mm [84, 31, 85]. For this reason, the Amptek CdTe detector and the HEXITEC detector with a CdTe detector chip may be a good choice for recording signals from human-sized objects, and both are already widely used in the XFI research field [86, 87, 88, 89].

The XR100 CdTe detector from Amptek has its optimal energy range from 5 keV to 150 keV and consists of a single CdTe crystal with an area of 25 mm^2 and a thickness of 1 mm, combined with a cooling system and a preamplifier. In addition, a beryllium window (100 μm) is used to create a light- and vacuum-tight enclosure [31].

The detector's functionality is based on the generation of charges within the detector chip. The photons to be detected interact with the atoms of the detector material, and due to the high stopping power of cadmium and telluride at energies up to 100 keV, the photoelectric effect is probable [90]. Due to the interaction of photons with the CdTe atoms, electron-hole pairs are generated for every 4.43 eV [90]. Thus, the higher the energy of the incident photon, the more pairs are created [31, 85, 90]. However, the photoelectric effect also leads to an electron vacancy in the cadmium or telluride atom, which, when the vacancy is filled, causes the emission of a characteristic X-ray photon or an Auger electron [85, 34, 37]. Due to an applied bias voltage, the charges move, so that a current pulse can finally be measured, whose amplitude corresponds to the energy of the incident photon [85].

However, certain detector effects may occur during this measurement process, causing the recorded spectrum to differ from the ideal, true spectrum. As already mentioned, secondary characteristic X-ray photons might be emitted as a result of the photoelectric effect, more precisely due to the refill process of the electron vacancy [84]. These photons typically have energies of 23.2 keV and 26.1 keV, corresponding to the cadmium K_α and K_β lines, or 27.5 keV and 31.0 keV for telluride. These relatively high characteristic energies, compared to, for example, silicon with 1.7 keV or 1.8 keV, make it easier for characteristic CdTe photons to escape out of the detector. Thus, the escaped photon cannot be registered by the detector, and the actual measured energy is then the energy difference between the incoming photon and the escaped photons. Four additional so-called escape peaks can then be observed in the recorded spectrum along with the actual true peak [84].

Another effect that prevents the Amptek detector from being ideal is known as "hole tailing". The density of trapping sites in the crystal reduces the mobility of the charges and a fraction of them is trapped [85]. This results in incomplete charge collection and an asymmetric peak with a lower-energy tail [84, 85]. Furthermore, "pile-up" can occur. In this case, multiple photons are detected in a very short interval, so that they are registered as a single photon, meaning that all their energies add up. Even energies exceeding the original maximum incident energy can then be observed in the measured spectrum [91].

Lastly, electronic noise and Fano broadening lead to a Gaussian broadening, which determines the energy resolution of the detector. For example, at an energy of 60 keV, the full width at half maximum (FWHM) is between 0.5 keV and 0.6 keV, and the Fano factor is assumed to be 0.1 [84]. Meanwhile, an FWHM of 0.7 keV is estimated between 67 keV and 69 keV, and an FWHM of less than 1.5 keV is estimated for energies at 122 keV [92, 93, 31].

The CdTe-HEXITEC detector also uses a 1 mm thick CdTe detector chip and is based on the same detection method using the photoelectric effect as the Amptek detector explained above, and is therefore also affected by the detector effects mentioned [30]. However, with a size of 2 cm x 2 cm, the HEXITEC detector has a significantly larger detector area and is thus potentially a promising detector for human-sized objects, as it provides then higher statistics, allowing the dose to be reduced due to a shorter exposure time. Furthermore, the HEXITEC detector is a hyper-spectral high-energy X-ray area detector, which means that the detector area is divided in 80 x 80 pixels, each with a side length of 250 μm[30]. Consequently, the pixels provide 6400 spectra, which enable the behavior of photons at different detector positions to be mapped. Nevertheless, these pixels produce stronger detector effects. The small pixel size allows charge sharing, meaning that charge clouds are not only captured by a single pixel but can spread across multiple pixels [94]. As a consequence, there is a certain amount of energy loss per pixel. For readout, an ASIC microchip is used per pixel, which is linked to more noise due to the 6400 individual readouts, compared to the Amptek detector, which only has one preamplifier [94, 85]. Another difference is that the HEXITEC detector does not use cooling, which may result in higher thermal noise and leakage currents [31, 95]. Finally, the charge sharing, the ASIC noise and the absence of cooling result in lower energy resolution than with the Amptek detector. The literature reports a FWHM of 0.8 keV per pixel and 1 keV in total at 60 keV, for instance in [30].

In simulations, for example with Geant4, it is possible to distinguish between an ideal and non-ideal detector after creating any desired geometry. When defining an ideal detector, no detector effects are included, and the detected counts are declared as "True Counts", in contrast to the "Recorded Counts" where detector effects are taken into account. Like all objects detectors can also be defined as ideal absorbers. This means that after one photon interacts with the detector material, no further interactions can take place, since the photons are "killed" immediately afterwards. This is particularly interesting when comparing Geant4 simulations with numerical calculations or the numerical model. If a real detector with detector effects and the recorded counts is desired, the energy resolution must be set either by the Fano factor or the standard deviation, which can be derived from the FWHM [96]:

$$FWHM = 2\sqrt{2 \cdot ln(2)} \cdot \sigma. \tag{3.21}$$

For simulations modeling the Amptek detector, a FWHM = 0.6 keV at an energy E = 60 keV would result in a standard deviation of σ = 0.25 keV. In this thesis, however, the standard deviation of the Amptek detector is assumed to be σ = 0.3 keV, because the simulated energies exceed 60 keV, which corresponds to an FWHM of about 0.7 keV [92, 93]. When simulating the properties of the HEXITEC detector, a standard deviation of $\sigma \approx 0.425$ keV resulting from FWHM = 1.0 keV is used [30].
For example, Fig. 3.2 shows an energy spectrum simulated with an ideal and a realistic cadmium telluride detector. In this example, an 81 keV pencil beam with 10^{10} incident photons penetrates a human-sized soft-tissue cylinder with a diameter and height of 300 mm. Inside the cylinder, a gold-water mixture ($\rho_{Au} = 1.0 \frac{\text{mg}}{\text{ml}}$) with a length of 100 mm at a depth of 50 mm is located. The detector is located 225 mm away from the

center of the cylinder at a 10° angle with respect to the incident beam. It is simulated with an energy resolution of $\sigma = 0.3\,\text{keV}$ for the recorded counts. The effects of a realistic

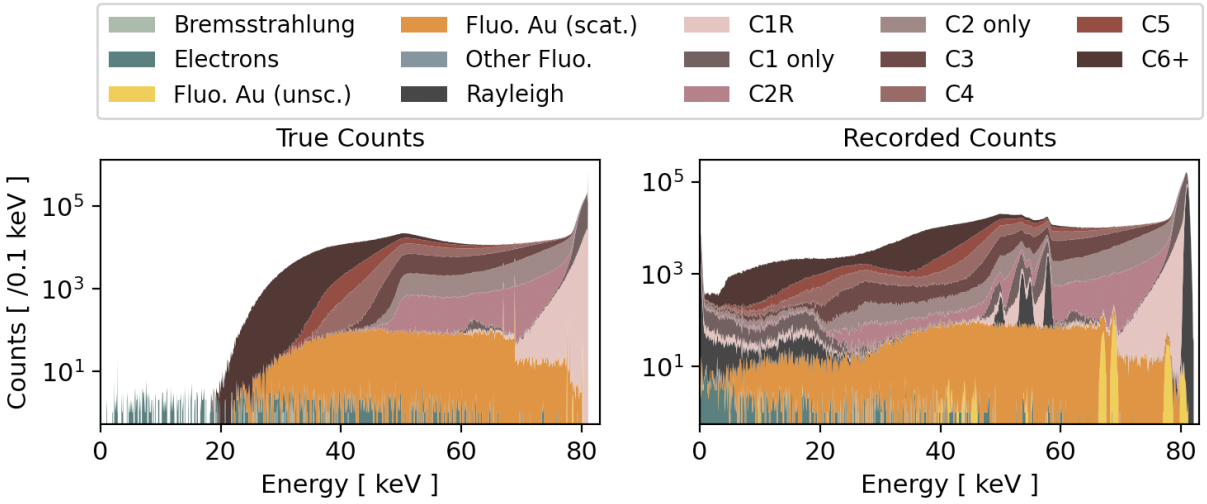

Figure 3.2: The true (left) and recorded (right) energy spectra of an 81 keV beam with 10^{10} incident photons penetrating a human-sized cylinder containing a gold-water mixture were simulated with Geant4. For the recorded counts, an energy resolution of $\sigma = 0.3\,\text{keV}$ was simulated. These spectra distinguish between possible interaction processes, such as Bremsstrahlung, electron emission, fluorescence, Rayleigh scattering, and Compton scattering of different scattering orders. In single or double Compton scattering, the photons are distinguished as "C only" or "CR" photons. This means that C1R photons, for example, undergo both Rayleigh scattering and a single Compton scattering.

detector become clear when considering the Rayleigh peak, which is prominent due to the small detector angle. In the energy spectrum of the true counts, Rayleigh photons are only detected at 81 keV (and therefore almost invisible), since this scattering process is coherent and associated with no energy loss (Sec. 2.1.2). However, the peak is broader in the recorded spectrum due to the detector's energy resolution. This is also evident in the unscattered gold fluorescence counts, which have line energies in the true spectrum as well. Furthermore, four additional Rayleigh peaks appear in the recorded spectrum at energies between 50 keV and 58 keV. These peaks are assigned to the four escape peaks due to the cadmium and telluride detector material. Additionally, due to the non-ideal detector, even many Compton photons with energies below 20 keV can be observed.

3.5 Gold Nanoparticles

In XFI, specific imaging markers are commonly used to generate fluorescence signals (Sec. 2.3). These markers can be functionalized by linking them to targeting molecules, enabling their delivery to the desired target region (e.g., a tumor) [62]. However, this requires a tracer that can be modified to bind to the desired target. Additionally, the tracer should be non-toxic since it is injected into the body of an animal or human. When performing XFI on human-sized scales, instead of on small animals for example, the photons must

traverse longer distances through the object, resulting in lower photon transmission (Eq. 2.13). Therefore, a marker or fluorescence target with a high atomic number that generates high-energy fluorescence photons should be chosen, enabling the fluorescence photons to leave the object.
Gold nanoparticles (GNPs) seem to be a promising choice which fulfill these properties. GNPs are associated with simple synthesis and modification of their size, shape, and surface, which is important for their functionalization [97, 98]. Since GNPs are also inorganic and not biodegradable, long-term tracking may potentially be possible without repeated injection of GNPs [97, 99]. Generally, GNPs are associated with low toxicity, which however, depends on factors such as the administered route or the properties of GNPs [62, 100, 97, 98]. For example, a tail vein injection shows lower toxicity than an oral injection in an experimental animal study [98]. Another study analyzed the toxicity of GNP concentrations using a physiologically-based pharmacokinetic model that extrapolates toxic values measured in small animals to humans. In that study, administered concentrations exceeding $0.005\,\frac{\mathrm{mg}}{\mathrm{kg}}$ were associated with gene expression changes in the liver of a 70 kg human [101]. However, since GNPs can be concentrated more strongly

Shell Transition	Siegbahn Notation	Line Energy	Energy Range Category
$L_3 \rightarrow K$	K_{α_1}	68.81 keV	K_α
$L_2 \rightarrow K$	K_{α_2}	66.99 keV	K_α
$M_3 \rightarrow K$	K_{β_1}	77.98 keV	K_β
$M_2 \rightarrow K$	K_{β_3}	77.58 keV	K_β
$N_3 \rightarrow K$	K_{β_2}	80.18 keV	K_γ
$N_5 \rightarrow K$	K_{β_4}	80.39 keV	K_γ

Table 1: The emitted fluorescence energies of gold for transitions from the L-, M-, and N-shells, which have different orbital quantum numbers, to the K-shell are listed [36]. The energy lines are classified into different "energy range categories" depending on the initial energy level.

locally than systemically in XFI imaging, the applicable toxicity thresholds may differ locally. These toxicological thresholds depend on the properties of the GNPs used, particularly their size, shape, and surface functionalization [102].
Moreover, gold is associated with the emission of high-energy fluorescence photons due to its high atomic number (Tab. 1) [36]. Note that the energies of the transitions from the M-shell to the K-shell are relatively close to each other and correspond to the K_{β_1} and K_{β_3} fluorescence lines in Siegbahn notation. With a non-ideal detector having an energy uncertainty of σ, distinguishing these lines would be challenging. This is why, unless otherwise stated, this thesis considers a "K_β" energy range with an uncertainty of $\pm 3\sigma$ around the energy lines from the M-shell to the K-shell. The same applies to the K_{β_2} and K_{β_4} lines, whose energy range is described by "K_γ" range in this thesis since they originate from the higher energy shell "N" instead of "M". The K_{α_1} and K_{α_2} lines are sometimes classified together as "K_α" energy range.

4 Numerical Analysis of Multiple Compton Background

Previous studies have shown that distinguishing a signal from the background is particularly challenging for human-sized objects [28]. These objects exhibit a large intrinsic background due to multiple Compton scattering within their large scattering volume. Furthermore, Grüner et al. reported that the Compton background is distributed anisotropically, and for an incident energy of 82.8 keV, the background within the signal range of the gold K_α fluorescence line, which has the highest fluorescence cross section among the gold fluorescence lines, can be minimized by choosing a detector angle of 60° with respect to the incident beam orientation [28, 36]. To understand the behavior of multiple Compton-scattered photons within large objects, the numerical model presented in Sec. 3.3.2 is used. This model allows Compton paths to be analyzed with respect to specific properties, such as their scatter origins. Since double Compton-scattered photons have been investigated in previous work [103], this thesis compares double Compton-scattered photons with triple Compton-scattered photons. Unlike the 4π-detector used by Grüner et al. [28], a smaller, commercially available detector size is chosen.

4.1 Setup

To study the intrinsic background when a human-sized object is irradiated by an X-ray beam, a water cylinder with equal diameter and height of 300 mm is considered. Further-

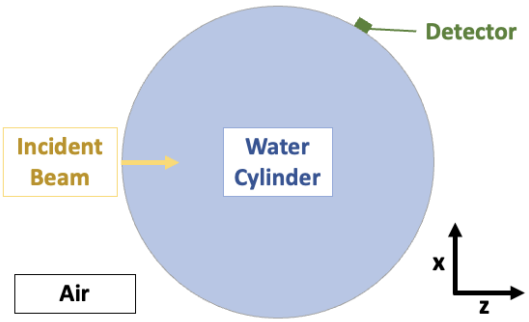

Figure 4.1: A water cylinder (blue, 300 mm diameter) located in air is irradiated by an incident pin beam (red) propagating along the z-axis and a detector (green, 5 mm × 5 mm area) is placed at a 60° angle with respect to the incident beam. Note that this schematic setup is not to scale, as the modeled detector and beam are shown larger than their actual size relative to the water cylinder for visibility.

more, a monochromatic incident beam of 85 keV is modeled, corresponding to the setup used by Grüner et al. [28]. A photon source is placed on the z-axis at (0, 0, -150) mm, directly in front of the cylinder, whose center is located at (0, 0, 0) mm. The 10^{10} incident photons propagate along the z-axis as an unpolarized pin beam through the cylinder,

meaning it has no extension in the x- and y-directions, which simplifies the use of the numerical model. Additionally, a detector with an area of 5 mm × 5 mm is located at a distance of 150 mm from the center of the cylinder and at an angle of 60° relative to the incident beam at (130, 0, 75)mm. Because of the small detector area compared to the large object size, the detector is treated as non-pixelated for simplicity in the numerical model. Furthermore, the detector is considered ideal in the following analysis.

4.2 Validation of the Numerical Model

The setup described in Sec. 4.1 was used to validate the numerical model with Geant4 simulations and the simulated total spectrum is shown in Fig. 4.2. Since most of the background is due to double Compton-scattered photons and triple Compton-scattered photons within the K_α signal range of gold, these Compton orders are considered for the subsequent analysis. Note that in the simulation, the detected Compton photons are distinguished between "C only" and "CR" photons for the Compton orders up to three. The "CR" photons include Compton-scattered photons that have undergone additional Rayleigh scattering, while "C only" photons have undergone only Compton scattering. For the comparison with the numerical model, "C only" photons are considered. Therefore, throughout Sec. 4, photons that have undergone only two Compton scatterings are referred to as "C2" photons and those with only three Compton scatterings as "C3" photons. The Compton model presented in Sec. 3.3.2 and as further explained in Appendix

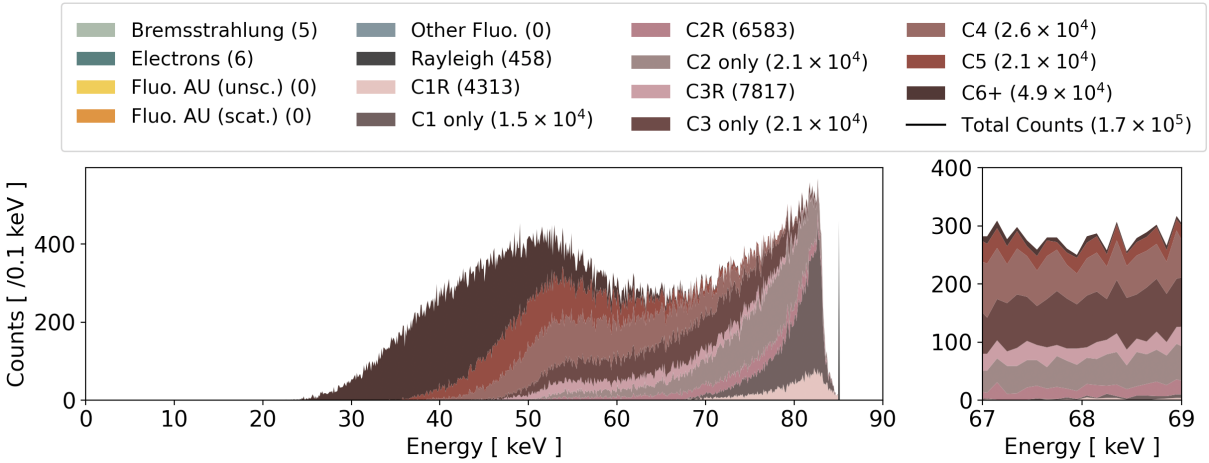

Figure 4.2: The true background spectrum of a human-sized object at a 60° detector angle is shown for 10^{10} incident photons across all energies (left) and within the K_α energy range of gold (right). More details about this setup are provided in Sec. 4.1.

A.1 is used to determine C2 and C3 photons numerically. As shown in Fig. 4.3 for the C3 photons, the number of modeled Compton counts depends on the chosen step size d_s, which was kept constant in the x, y and z dimensions ($d_s = d_x = d_y = d_z$). The model most closely agrees with the Geant4 simulation when the smallest investigated step size of $d_s = 5$ mm is used. Otherwise, a larger step size results in a stronger underestimation of the modeled counts compared to the simulated C3 counts. Therefore, the step size

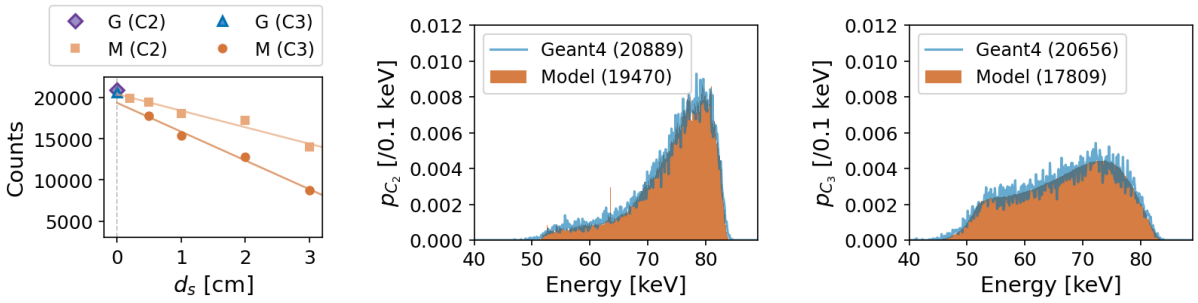

(a) (b) (c)

Figure 4.3: The number of numerically modeled Compton counts (M(C2), M(C3)) depends on the step size d_s. Extrapolating to $d_s = 0\,\text{mm}$ would result in discrepancies of 2.5% for C2 and 6.3% for C3 photons compared to the Geant4-simulated photons (G(C2), G(C3)) (a). The energy spectra of the double Compton-scattered normalized counts p_{C_2} (b) and the triple Compton-scattered normalized counts p_{C_3} (c), each normalized to their respective total count number, are computed by the numerical model (orange) with a step size of $d_s = 5\,\text{mm}$ and simulated by Geant4 (blue). The total number of simulated or modeled counts is written in the brackets. The simulated relative uncertainty is 0.7% (Eq. 3.2) for the simulated C2 and C3 photons.

should be as small as possible. However, due to computation time, especially for C3 photons (Sec. 3.3.5), the step size is limited. Hence, a minimum step size of $d_s = 5\,\text{mm}$ was chosen. Finally, a discrepancy of 13.7% remains for the C3 counts. One reason for this is the discretization of the modeled photon paths. Within a section of length equal to the step size d_z scattering locations are considered to have the same probability. This probability corresponds to the probability of a photon path scattering at the center of the section. This means that different attenuations, for example are not included within this section. Since the photons are attenuated exponentially (Eq. 2.13), this effect is especially pronounced for large step sizes. A step size d_z for a C3 photon has seven components: z_1, x_2, y_2, z_2, x_3, y_3, z_3. Consequently, inaccuracies accumulate more strongly than for C2 photons, which have only four components. For C2 photons, the discrepancy decreases to 6.8% when using a step size of $d_l = 5\,\text{mm}$, and using a step size of $d_l = 2\,\text{mm}$ further reduces the discrepancy to 4.5% (Fig. 4.3). When extrapolating the modeled photon counts to a step size of $d_s = 0\,\text{mm}$, a discrepancy of 2.5% for the C2 photons and of 6.3% for the C3 photons would remain. Despite a systematic investigation, the remaining discrepancy could not be attributed to a single dominant source and is likely due to a combination of several effects. For example, the detector is 0.2 mm thick in the simulation, as Geant4 requires a three-dimensional geometry, whereas the numerical model considers the detector as an ideal two-dimensional surface. Furthermore, a smaller step size achieves a smaller minimum distance between scattering locations and increases the maximum possible solid angle with respect to the detector nonlinearly (Eq. A.12). Additionally, the assumption that all paths end at the detector center further limits the accuracy with respect to the solid angle, the projection and transmission.
However, when considering the normalized count distributions p_T this uncertainty effect

disappears upon normalization (Fig. 4.3), and a good agreement is shown between the model and the Geant4 simulation for both the C2 and C3 normalized counts. The advantage of the numerical model is apparent, as there are no statistical fluctuations because the normalized count distributions reflect the calculated count probabilities, unlike the Geant4 spectra. The simulated Geant4 spectra represent the estimated probability distribution of detected photon counts. Therefore, they exhibit statistical noise, which becomes more pronounced when considering individual energy bins. For example, the bin with the highest count contains 112 C3 photons, corresponding to a statistical uncertainty of 9.5%, which is significantly larger than the 0.7% uncertainty in the total number of simulated C3 photons (Eq. 3.2). Therefore, the numerical model provides photon path probability distributions that are free of statistical fluctuations, making it advantageous compared to Monte Carlo simulations.
As shown in Fig. 4.3, C2 photons are associated with higher energies than C3 photons, whose spectrum is less pronounced at high energies but more prominent at lower energies. This can be explained by Eq. 3.19, which proves that an increase in scattering angles θ_C can more strongly decrease the photon's energy by increasing the denominator. Additionally, more combinations of Compton scattering angles are possible, resulting in the broad C3 photon spectrum. As a consequence, more C3 than C2 photons fall within the K_α signal range (67 keV$< E <$69 keV), even though more C2 photons are detected in total, as discussed in the following section.

4.3 Spatial Distribution of Multiple Compton-Scattered Photons

The distributions of the modeled C2 and C3 photons, depending on their last scattering location, are shown in Fig. 4.4. It is beneficial to first examine the C2 photons with a last scattering origin in the beam plane at $y = 0$ mm before considering the C3 photons and all the C2 photons. In the shown 2D histograms for C2 photons with $y = 0$ mm, each pixel corresponds directly to the probability of a single C2 path, whereas in the case of an unrestricted y-value or C3 photon probability histogram, the sum of the probabilities of multiple paths is contained within one pixel. Scatter origins close to the incident beam and the detector, located at (130, 0, 75)mm, are associated with larger detection probabilities. This is mainly due to the solid angle $G \propto 1/r^2$, which increases rapidly for small distances r and exhibits a stronger dependence on distance at small r than the other path probability factors, such as the transmission factor $e^{-\mu r}$ within water (Eq. 3.18), as demonstrated in Fig. 4.5.

Therefore, C2 scattering locations with short distances r_3 close to the detector are associated with large solid angles G_2 (Eq. A.10) and path probabilities. The same holds true for C2 scattering locations with a small distance r_2 to C1 scattering locations (Eq. A.7), which occur close to the beam axis because this is where the first Compton scattering takes place. However, fewer photons are detected directly from the z-axis since Compton scattering is associated with a minimum scattering angle that does not permit $\theta_s = 0°$ in the numerical model [36]. This means that the z-axis can only be the last scattering place for C2 photons if the photon undergoes 180° backward scattering as a first

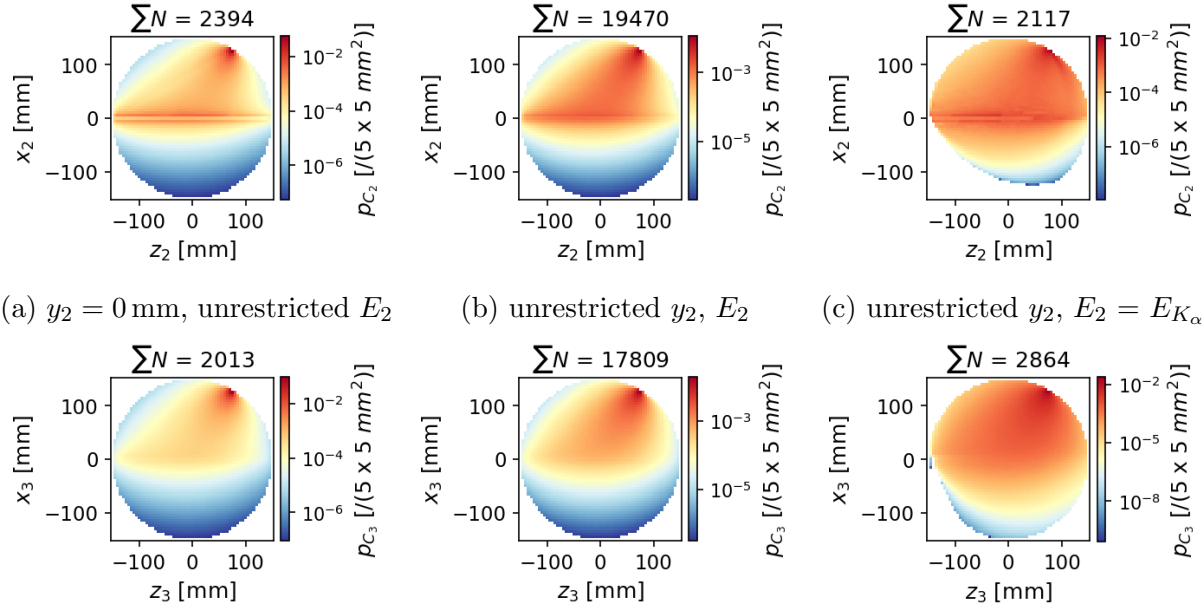

(a) $y_2 = 0\,\text{mm}$, unrestricted E_2 (b) unrestricted y_2, E_2 (c) unrestricted y_2, $E_2 = E_{K_\alpha}$

(d) $y_3 = 0\,\text{mm}$, unrestricted E_3 (e) unrestricted y_3, E_3 (f) unrestricted y_3, $E_3 = E_{K_\alpha}$

Figure 4.4: The probability distributions (p_C) of the C2 and C3 photons, modeled by Eq. 3.18 with a step size of $d_s = 5\,\text{mm}$, are shown as a function of their last scattering location (x_2, z_2) for the C2 photons and (x_3, z_3) for the C3 photons. The modeled total number of photons ($\sum N$) for $N_0 = 10^{10}$ incident photons is shown above. The distributions are distinguished by all modeled energies (a, b, d, e) and by the Au-K_α energy range only (c, f). Additionally, they are distinguished between the beam plane ($y = 0\,\text{mm}$) (a, d) and the projection over all y values (b, c, e, f). These distributions show that the probability of the last scattering location is non-uniform and depends on the Compton order.

Compton scattering event, which is less likely (Fig. 2.5). For scatter origins farther from the z-axis and the detector, the distances increase, causing the solid angle to decrease. This results in fewer photons being detected from these origins. In particular, when the last scattering event occurs at low x-values, with $x < 0$, the number of detected photons decreases drastically due to longer total pathways, which reduces both the solid angle and the transmission (Fig. 4.5). Additionally, scattering from this area is often linked to backscattering, which, as previously mentioned, also reduces the path probability.
Taking all C2 scatter origins into account, rather than only those with $y_2 = 0\,\text{mm}$, results in a more blurred probability distribution. Values of $x_2 = 0\,\text{mm}$ are less strongly associated with lower path probabilities, since, for photons with $y_2 \neq 0$, the scattering angles for $x_2 = 0\,\text{mm}$ are no longer only linked with a backwards scattering event. Furthermore, in the xz-planes with $y_2 \neq 0$, the shortest distances to the first Compton scattering site and the detector with $y_D = 0\,\text{mm}$ increase and thus the maximum solid angles decrease. Due to the various y-components, the photon probability distribution of the C2 scattering locations is blurred.
If only the K_α energy range of gold is taken into account, the distribution is even more

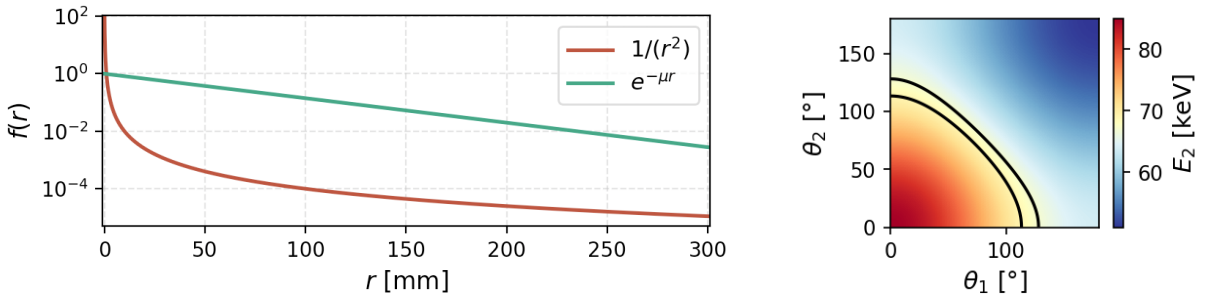

(a) (b)

Figure 4.5: (a): The functions $f(r)$ describing the solid angle $G \propto 1/r^2$ and the transmission $T \propto e^{-\mu r}$ are shown as a function of distance r. For the shown function $e^{-\mu r}$, a linear attenuation coefficient of $\mu = 0.0196\,\frac{1}{\text{mm}}$ was chosen, which corresponds to the coefficient for a photon with an energy of 67 keV within water. (b): The photon energy as a function of two scattering angles θ_1 and θ_2 is shown: The black lines show the Au-K_α energy range between 67 keV and 69 keV.

blurred and photons cannot be detected from all places within the cylinder. This can be attributed to the energy restriction, which does not permit the detection of all scattering angle combinations. For instance, for C1 photons, the scattering angles are only allowed to be between $113° < \theta_1 < 128°$ according to Eq. 3.19. Larger scattering angles result in energies below 67 keV, whereas smaller scattering angles cause energies above 69 keV (Fig. 4.5). This scatter angle restriction explains why C2 photons, with low x_2 and z_2 values at their last scattering location, are associated with no energies within the Au-K_α signal range at all y_2 scattering places. There, large scattering angles result in energies below 67 keV.

Contrary to the C2 photons, C3 photons have only a higher probability of being scattered last close to the detector, not close to the incident beam. This is because the previous scattering sites of the C3 photons, namely the second Compton scattering sites, are, unlike the first Compton scattering location, not restricted to the incident beam. Therefore, C3 scattering places close to the beam axis are farther away for many paths and are no longer mandatorily associated with a large solid angle. However, all modeled paths end at the detector, meaning that a large solid angle G_3 is achieved for all photon paths when the last scattering location is close to the detector. Consequently, the probabilities are larger there.
As with the C2 photons, comparing the probability distributions of the beam plane ($y_3 = 0\,\text{mm}$) and the projected case (all y_3) shows that the probability distribution is less focused when all y_3 scattering places are taken into account or when the Au-K_α signal range is considered. This is due to the same reasons as explained above for the C2 photons. However, since three Compton scatterings result in more scattering angle combinations, the C3 scattering locations are less geometrically restricted within the Au-K_α energy range. This enables scattering locations that would not be accessible with C2 photons, even though the total sum of scattering angles may be lower with C2 photons.

More precisely, C3 photons can achieve higher energies than C2 photons because the final Compton energy is a nonlinear function that can reach higher energy values with three moderate Compton scattering angles compared to one large scattering angle with C2 photons (Eq. 3.19). This energy dependency is illustrated in Fig. 4.5 as a function of two different scattering angles.

As also shown in Fig. 4.4, about 12% of the C2 and C3 photons originate from the beam plane when considering all photon energies. However, since the background within the Au-K_α signal is especially of interest, Fig. 4.6 shows the photon probability distributions within that energy range as a function of y_2 for the C2 photons and y_3 for the C3 photons. This provides information about how photons behave in the vertical direction. The probability distributions of both C2 and C3 photons exhibit similar behavior, with a

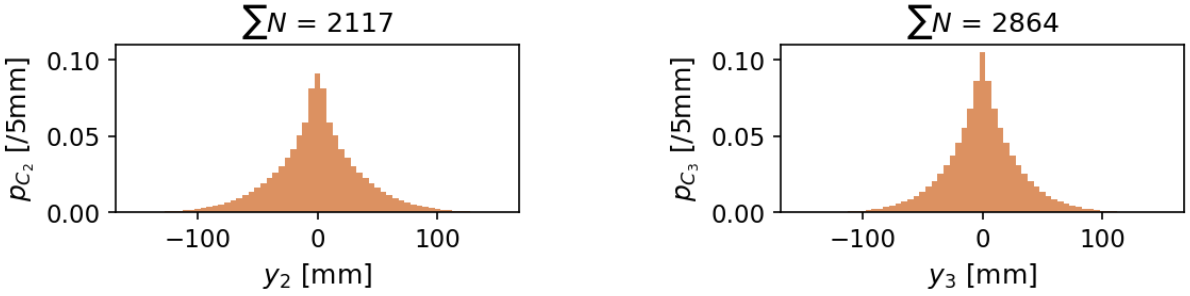

(a) (b)

Figure 4.6: The modeled path probabilities for C2 photons (a) and C3 photons (b) with a step size of $d_s = 5\,\text{mm}$ are shown within the Au-K_α signal range as a function of the last scatter y-component. The total number of modeled photons ($\sum N$) for 10^{10} incident photons is shown above. This plot shows that Compton photons originating from the beam plane ($y = 0\,\text{mm}$) are associated with the highest detection probability, accounting for about 10% of the total detected C2 and C3 photons.

peak at $y = 0\,\text{mm}$ and lower probabilities at greater distances from the beam plane. This means that the probabilities of the photon paths must differ for different y-components, since the number of modeled photon paths per y-component ($/5\,\text{mm}$) is the same. This can again be explained by the path length and distances r, which increase for scattering locations farther away, thereby decreasing the probability due to smaller solid angles and greater attenuation. Finally, 9.1% of C2 photons and 10.5% of C3 photons are expected to be detected from the beam plane. Since the detector is located in the beam plane, photons with scattering locations outside this plane require additional backscattering into the beam plane. This is associated with larger scattering angles and, therefore, mostly lower photon energy. Consequently, triple Compton-scattered photons, especially those with their last scattering location outside the beam plane, are associated with lower photon energies. Thus, the fraction of C3 photons that falls within the Au-K_α signal range is higher than that of the C2 photons within the beam plane. Conversely, this also means that nearly 90% of these background photons do not originate from the beam plane,

where fluorescence signal photons would occur. For example, in case of collimation, a major fraction of the background can be shielded in the y-direction with this setup.

4.4 Spatial Distribution for Increased Detector Distance

In this section, the spatial photon probability distribution is analyzed for a detector farther away, since a detector directly on the object surface is not practical. Furthermore, if a collimator, for example, was added in front of the detector, more space would be necessary between the detector and the imaging object. Therefore, a distance of $R_D = 300\,\text{mm}$ to the center of the object is chosen and the environment outside the object is set to air, while the rest of the setup remains as described in Sec. 4.1.
The probability distributions for the C2 and C3 photons are shown in Fig. 4.7. The high-

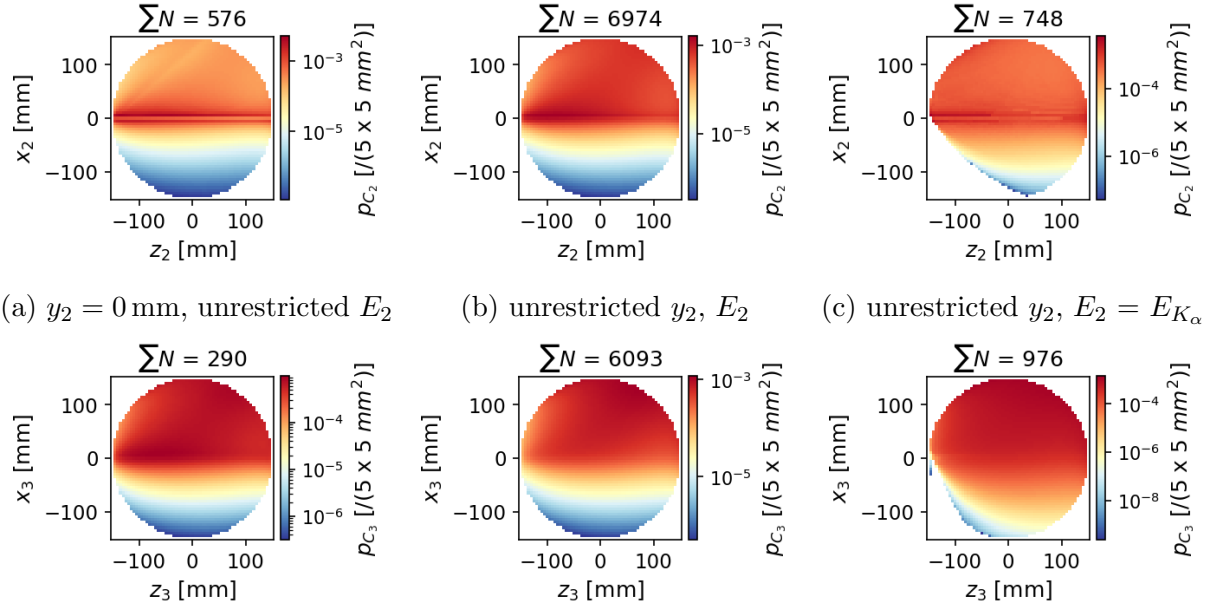

(a) $y_2 = 0\,\text{mm}$, unrestricted E_2 (b) unrestricted y_2, E_2 (c) unrestricted y_2, $E_2 = E_{K_\alpha}$

(d) $y_3 = 0\,\text{mm}$, unrestricted E_3 (e) unrestricted y_3, E_3 (f) unrestricted y_3, $E_3 = E_{K_\alpha}$

Figure 4.7: The probability distributions p_C of the C2 and C3 photons are modeled by Eq. 3.18 with a step size of $d_s = 5\,\text{mm}$ as a function of their last scattering position (x_2, z_2) for the C2 photons and (x_3, z_3) for the C3 photons. The modeled total number of photons for $N_0 = 10^{10}$ is shown above. The distributions are differentiated between all modeled energies (a, b, d, e) and the Au-K_α energy range only (c, f). There is also a differentiation between the beam plane ($y = 0\,\text{mm}$) (a, d) and all projected y values. This plot shows that for a more distant detector ($R_D = 300\,\text{mm}$) the probability distributions of C2 and C3 photons are less focused compared to a closer one (Fig. 4.4).

est probabilities of detecting C2 photons from the beam plane occur when they originate close to the incident beam, as in the case of a detector distance of $R_D = 150\,\text{mm}$. However, since the detector is no longer directly located on the object's surface, the photon

probability is now less pronounced close to the previous detector position (130, 0, 75)mm because there are no longer much larger solid angles due to especially short distances to the detector. Consequently, the photon probability distribution is broader and even more blurred when considering the probability distributions of all y_2 scattering locations or the Au-K_α signal range, for the same reasons as with $R_D = 150\,\text{mm}$.
For C3 photons, the probability distribution roughly divides the object into two halves, with scattering locations on the side of the detector associated with larger probabilities due to shorter path lengths. In contrast, scattering locations from the other side of the object with negative x_3 values are predominantly associated with backscattering, lower energy and a smaller Compton scattering cross section (Fig. 2.5) as well as greater attenuation (Eq. 2.13). Nevertheless, due to the smaller relative difference in path lengths, the photon probability distributions are less focused overall for a larger distance between the detector and the object.
Meanwhile, the number of detected background photons decreases to about 35% with the larger detector distance. This is mainly due to the smaller solid angle covered by the detector and the lower transmission. However, it should also be noted that the number of fluorescence photons is expected to decrease as well at larger detector distances.

The photon probability distribution in the vertical direction is shown in Fig. 4.8 as a function of the y-component of the last scattering location. Due to the longer distance

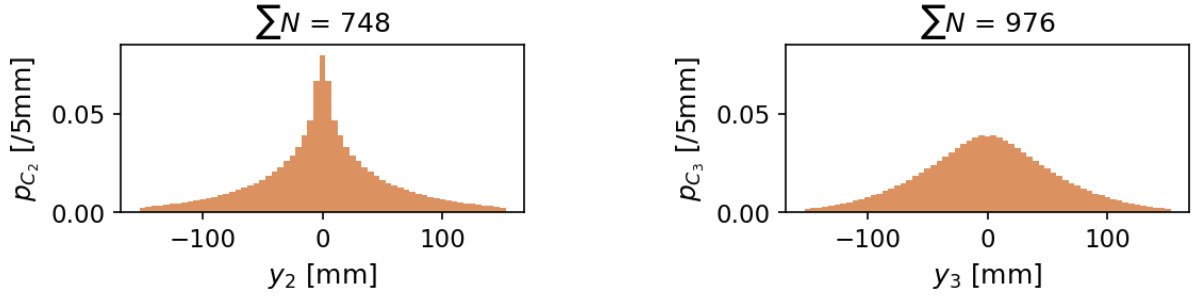

(a) (b)

Figure 4.8: The modeled path probabilities for C2 (a) and C3 (b) photons with a step size of $d_s = 5\,\text{mm}$ are shown within the Au-K_α signal range as a function of the last scatter y-component. The total number of modeled photons for 10^{10} incident photons is shown above. This plot shows that the probability of detecting photons originating from the beam plane decreases for a more distant detector ($R_D = 300\,\text{mm}$) compared to a closer one (Fig. 4.6).

between the detector and the object, the photon probability distribution broadens and the peak at $y_2 = 0\,\text{mm}$ decreases to 8% for C2 and 4% for C3 photons. This is particularly evident for C3 photons, where the peak is reduced by more than half compared to the case with a detector distance of $R_D = 150\,\text{mm}$. For many C2 photon paths, a second scattering location close to the beam plane is associated with especially large solid angles G_1, which increase the probability of detecting photons from there. However, there are

many more possible paths for C3 photons due to one additional Compton scattering and a smaller fraction of C3 paths experiences an additional Compton scattering event within the beam plane. More precisely, only 1.67% (1/60) of the modeled C2 photon paths have all scattering origins within the beam plane, whereas only 0.03% ($(1/60)^2$) of the modeled C3 photon paths have all scattering origins within the beam plane. Additionally, a detector farther away is associated with less differentiation in path lengths and solid angles, so that the path probabilities differ less and the probability distribution becomes much broader. To make it more explicit, when a distance of 5 mm between the last scattering location and the detector is elongated to 10 mm, the solid angle decreases by 75%, while it is only decreased by less than 6% when a distance of 155 mm is elongated by 5 mm.

4.5 Discussion

Overall, the numerical model enables studying the behavior of C2 and C3 photons in various scenarios, as presented here for two different detector distances. It was discovered that the probability distribution is often dominated by the impact of the solid angle, which can reach high values when the distance between scattering events or to the detector is short. For a detector close to the object, photon paths near the edge of the object are associated with high probabilities, but the photon distribution becomes broader for a detector farther away. Thus, the numerical analysis provides insight into the behavior of the multiple Compton scattering background, which overlays the fluorescence signal, highlighting the importance of the previous analysis.
In the context of XFI on human-sized objects, the numerical model shows that collimation in y-direction may be an option to reduce the multiple Compton-scattered background within the K_α energy range for a 60° detector angle. A more distant detector is associated with a broader probability distribution of C2 and C3 photons. For a distance of 300 mm from the detector to the center of the object, 96% of the C3 photons and 92% of the C2 photons would not originate from the beam plane ($y = 0 \pm 2.5$ mm). Since the signal fluorescence photons are generated along the incident beam, photons scattered outside the beam plane could be collimated, which would consequently reduce the background overlaying the fluorescence signal. However, when collimating all photons in the vertical direction but not those from the beam plane, it must also be considered that a collimator has a limited length, extending only at most to the object's edge. Consequently, a collimator cannot block all photons originating from a small, constant-height slice, but there would be an opening angle. Therefore, the detectable y-section of the object would be larger for object parts farther away from the collimator. This thesis presents some strategies for collimating the background, and the next section discusses whether this setup, considering the K_α signal range of gold for a detector at 60°, actually always is the best choice for imaging human-sized objects.

5 Uncollimated X-ray Fluorescence Imaging

The main goal of this thesis is to make XFI applicable to human-sized objects, which currently poses challenges due to the prominent background. Grüner et al. [28] demonstrated that the background of large objects behaves anisotropically depending on the detector angle and that the minimum background within the K_α fluorescence energy range of gold is achieved with an incident energy of 85 keV and a detector angle of 60°. They proposed a method to reduce the background using a pixel selection algorithm combined with large collimator leaves. However, this approach requires a large 4π detector, which would be highly cost-intensive [28, 62]. For this reason, in the following, a smaller detector area is considered to be studied in order to determine if an alternative, lower-cost approach is possible, with significant gold fluorescence signals still being detected.
Since other research groups have discovered that backward detection within the K_β energy range of gold is promising [104, 29], the behavior of photons, as well as the signal significance, will be systematically analyzed for different detector angles within the K_α and K_β energy range of gold. This will be done in order to develop a suitable collimation strategy in Sec. 6.

5.1 Setup

To analyze the photon distribution from a human-sized object without a collimator, simulations are performed using Geant4. For this purpose, a photon source is positioned at the coordinates (0, 0, -150.5) mm, generating unpolarized photons. The incident beam is a circular pencil beam with a diameter of 1 mm in this case. For statistical reasons, an initial number of $N_0 = 10^{10}$ incident photons is simulated. These photons propagate along the z-axis and enter at $z = -150$ mm in a standing soft-tissue cylinder having a diameter and height of 300 mm. Inside the cylinder is a 10 mm long cylindrical target containing a gold-water mixture with a diameter of 1 mm and a gold concentration of 1.0 mg/ml. The gold target is located at various positions (0, 0, z_{Au}) along the beam axis. In accordance with the gold target, whose absorption edge lies at 80.72 keV [36], a monochromatic input energy of 81 keV is selected, thereby maximizing the generation of gold fluorescence signal photons. To detect the photons, two cadmium telluride detectors, each 1 mm thick (corresponding to the common detectors described in Sec. 3.4) and with an area of 20 mm $\times$60 mm, are arranged at an angle α_D on either side of the beam source. The use of two detectors in mirrored positions allows more photons under the same conditions to be detected, thereby increasing the statistics. However, the total detector area is equivalent to six HEXITEC detectors, meaning it is much smaller than a 4π detector. For the recorded counts detected by a realistic detector, an energy resolution of $\sigma = 0.3$ keV is used. In addition, a distance of $R_D = 225$ mm from the center of the cylinder is chosen, which is a compromise.
On the one hand, there should be sufficient space to install a collimator, which cannot shield as many background paths if the length is too short; on the other hand, a small distance R_D is desirable to maximize the detector's solid angle and capture as many signal photons as possible (Sec. 4). A detector located too far away would also result in more

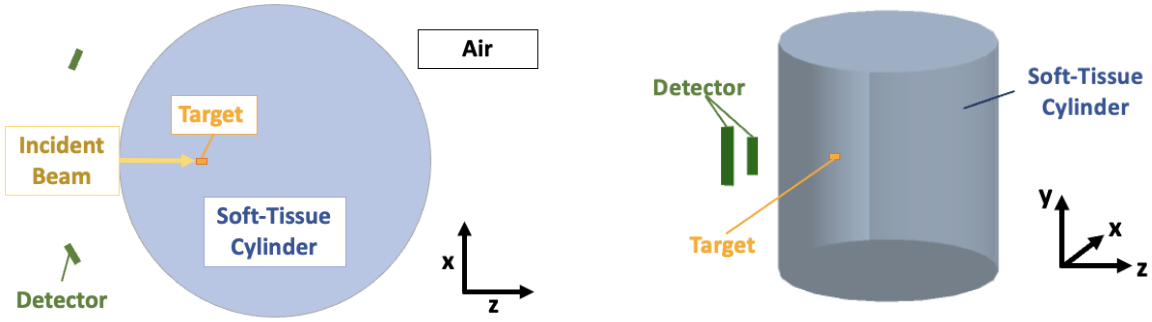

(a) Top View. (b) Side View.

Figure 5.1: A 10 mm long gold target (orange) is located inside a human-sized cylinder (300 mm diameter) made of soft tissue (blue), while the detector (green) is positioned at an angle of $\alpha_D = 150°$ to the incident beam (yellow). Note that this schematic setup is not to scale, as the modeled detector and beam in (a), as well as the target (a, b), are shown larger than their actual size relative to the water cylinder for visibility.

similar detection angles χ and ψ of the photons, so that precise collimation might also be more difficult in this case.
In addition to the Geant4 simulations, the numerical model described in Sec. 3.3.1 is used to study fluorescence photons. For this purpose, $N_0 = 1.3 \times 10^9$ incident photons are modeled by a pin beam with a step size of $d_s = 1$ mm. To improve accuracy and since the detector is now larger than in the previous Sec. 4, the detector in the model is pixelated, with the centers of the pixels spaced 1 mm apart.

5.2 Absorbed Dose within a Human-Sized Object

The main goal of this thesis is to enable XFI for human-sized objects. However, this requires considering the radiation dose (Sec. 2.4). Therefore, Eq. 2.18 is used to analyze the impact on the absorbed dose when using a lower energy of 81 keV instead of the 85 keV as used by Grüner et al. [28] and Blumendorf [105]. First, Eq. 2.18 is validated based on the average dose they simulated for 85 keV, since they used the same beam and object parameters described in Sec. 5.1 and only replaced the incident energy of 81 keV by 85 keV. Furthermore, they considered a soft-tissue sphere instead of a cylinder, but since the same diameter (300 mm) was used, the irradiated volumes along the incident beam are identical. With Eq. 2.18, the absorbed dose is calculated analytically to be 10.4 mGy for 85 keV, whereas an averaged absorbed dose of 10 mGy was simulated by Grüner et al. [28]. Accordingly, the doses are in good agreement, confirming that Eq. 2.17 reliably estimates the absorbed dose. Subsequently applying Eq. 2.17 to the same scenario, but with the lower energy of 81 keV, results in an average absorbed dose of 9.8 mGy (Fig. 5.2). This demonstrates that the absorbed dose is similar, reduced by only 0.6 mGy due to the larger mass-attenuation coefficient ($\mu_m(81\,\text{keV}) = 0.1810\,\text{cm}^2/\text{g}$,

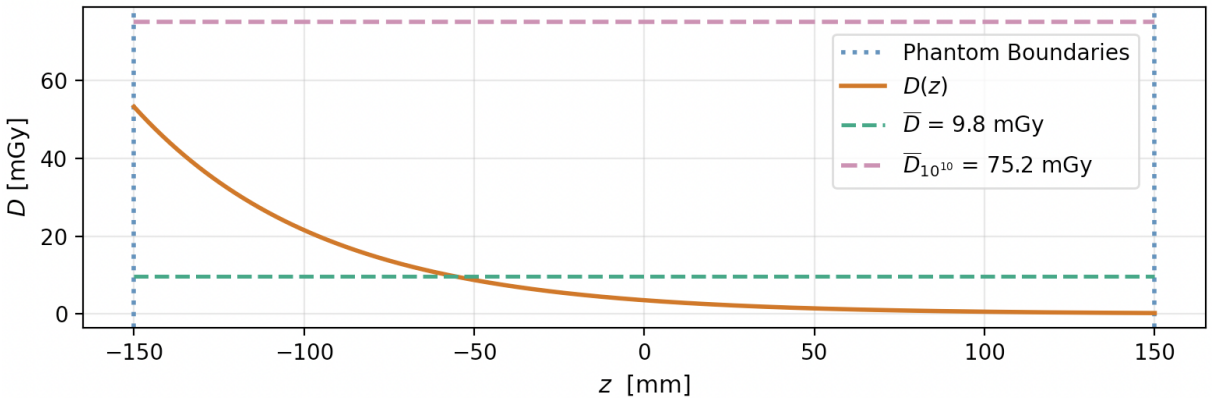

Figure 5.2: The absorbed dose D (orange) by a phantom volume (300 mm diameter) irradiated by a circular pencil beam with a diameter of 1 mm and an incident energy of 81 keV is shown for 1.3×10^9 incident photons as a function of the position within the human-sized phantom. The phantom borders are marked in blue. The averaged absorbed dose across the entire irradiated phantom volume is described by $\overline{D}$. Additionally, the average dose $\overline{D}_{10^{10}}$ for 10^{10} incident photons is shown (pink).

$\mu_m(85\,\text{keV}) = 0.1781\,\text{cm}^2/\text{g}$), which reduces the photon number, hence the value of Φ and the dose. Meanwhile, the energy-mass coefficient remains nearly identical in both cases ($\mu_{en} = 0.0248\,\text{cm}^2/\text{g}$). If 10^{10} incident photons, providing higher statistics, with an energy of 81 keV are used, an average dose of 72.2 mGy would be achieved. This is much higher than the absorbed dose of 10 mGy, which also corresponds to the dose used in other medical imaging modalities, such as in CT and PET [105]. Finally, 1.3×10^9 incident photons are also a good choice when using 81 keV to keep the dose low enough, because the dose barely changes compared to an incident energy of 85 keV and stays around 10 mGy. Nevertheless, understanding the behavior of photons may require high statistics to attribute their behavior to physics effects rather than statistical uncertainties in simulation studies. This is why in this thesis often 10^{10} photons are simulated but then scaled to 1.3×10^9 incident photons.

In contrast to the average absorbed dose integrated over all depths, the depth-dose curve provides insight into the locally absorbed dose at different depths within the irradiated volume (Fig. 5.2). The depth-dose curve decreases exponentially for larger z-values at deeper depths within the phantom. This is attributable to the attenuation of the beam. Consequently, the local dose is the highest at the phantom's edge at $z = -150$ mm with a value of 53 mGy and the average dose value of 9.8 mGy is achieved at a depth of 94 mm at $z = -56$ mm. In the center of the phantom the absorbed dose is only 3.5 mGy, while the lowest dose of 0.2 mGy is achieved at the other edge of the phantom at $z = 150$ mm.

5.3 Results

5.3.1 Fluorescence Dependency on the Detector Angle and Signal Range

At first, the fluorescence photons are examined without a collimator. Therefore, Fig. 5.3 shows the modeled fluorescence counts as a function of the detector angle for various positions (0,0,z_{Au}) of the gold target.

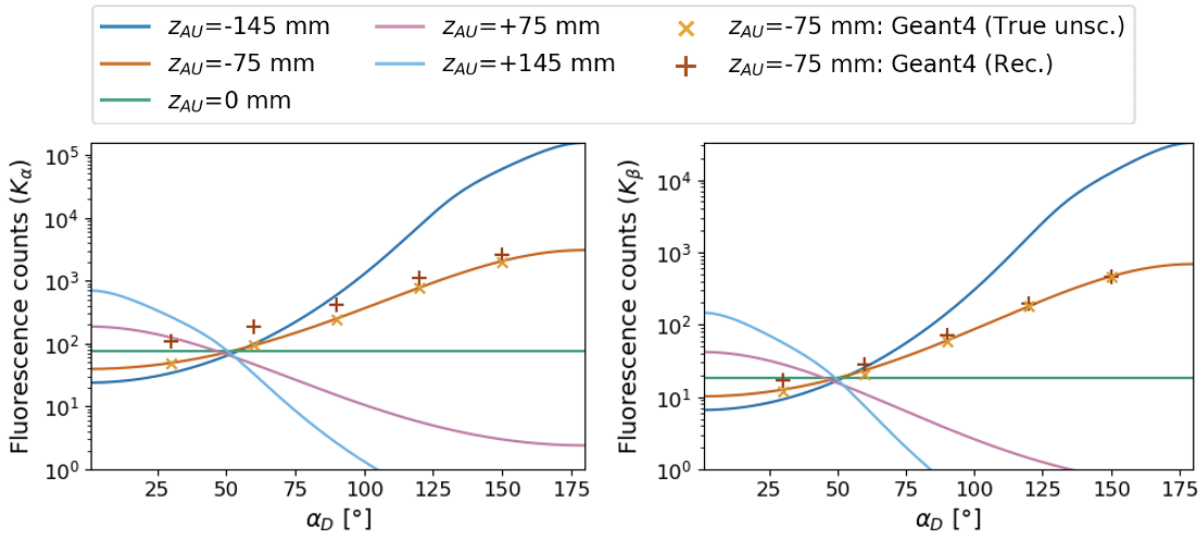

Figure 5.3: Modeled fluorescence counts for the K_α (left) and K_β (right) energies as a function of detector angle for different gold target positions z_{Au}. For comparison, Geant4-simulated unscattered (x) and total recorded (+) fluorescence counts are shown for $z_{Au} = -75\,\text{mm}$. The setup described in Sec. 5.1 was used with a gold concentration of 1 mg/ml and 1.3×10^9 incident photons.

In Fig. 5.3, the K_α and K_β fluorescence regions of gold are distinguished. In both regions, the most fluorescence counts are detected when the gold target is located near the beam source at $z_{Au} = -145\,\text{mm}$ and the detector is also positioned backwards at an angle of $\alpha_D = 180°$. This is due to the short path length of the incident photon to the target, which is associated with high transmission, as well as to the fact that the fluorescence photons generated there only have a short path to the detector, resulting in a large solid angle and thus in more detected fluorescence counts. However, a detector with $\alpha_D = 180°$ located in the beam plane could present difficulties in terms of practical feasibility, since the beam source is also located at 180°. Reducing the detector angle ultimately leads to a loss of fluorescence photons, since the photons to be detected must traverse longer distances and the fluorescence target with its center at $z_{Au} = -145\,\text{mm}$ is farther away. Consequently, the solid angle of the detector for the generated fluorescence photons decreases significantly. The small solid angle also explains why more fluorescence photons at small detector angles α_D <60° are detected for gold targets with higher z_{Au} values, even if the path length and thus the transmission do not differ significantly. However, the gold target with high z_{Au} values is closer to smaller detector angles in the forward direction, resulting in larger solid angles. For example, when using a detector with an angle of 10°,

the solid angles of fluorescence photons generated in a target with $z_{Au} = 145\,\text{mm}$ are about 1.5 orders of magnitude larger than those of a target with $z_{Au} = -145\,\text{mm}$, while the photon path lengths differ by only about 3%. Therefore, for targets located deeper within the object ($z_{Au} > 0\,\text{mm}$), a detector should be used in the forward direction to capture more fluorescence photons. Even better, the object should be rotated and irradiated from the opposite direction to maximize the detected fluorescence signal counts using a large detector angle. Otherwise, for a gold target at $z_{Au} = 145\,\text{mm}$, no K_α signal would be detected if a detector angle greater than 105° is used and the K_β signal would already be lost at a detector angle larger than 84°. In addition, at angles greater than 135° no K_β signal would be detectable anymore if the target would be at $z_{Au} = 75\,\text{mm}$. However, a depth of 150 mm is critical when the target is located at $z_{Au} = 0\,\text{mm}$, since this is the center of the object. At this point, all distances to the detector are equally independent of the detector angle, as is the fluorescence count number. This means that radiation from a different direction, caused for example by the object's rotation, would not increase the signal counts.
When comparing the fluorescence distributions for the different signal regions K_α and K_β, it is noticeable that the shape of the distribution does not really differ, but only the quantity of detected photons. This is due to the fact that they take the same paths, but vary in terms of fluorescence energy and cross sections. The fluorescence cross section for an incident energy of 81 keV is much smaller for the K_β line with $\sigma_{F,K_\beta} = 0.70\,\text{cm}^2/\text{g}$ than for K_α with $\sigma_{F,K_\alpha} = 5.07\,\text{cm}^2/\text{g}$ resulting in fewer fluorescence counts being generated in the K_β energy range, as shown in Fig. 5.3 [36]. Therefore, the conclusion can be drawn that the K_α region is more promising in terms of the fluorescence counts.
As a cross-check, the fluorescence counts simulated with Geant4 for a target at $z_{Au} = -75\,\text{mm}$ are also shown. These exhibit a good agreement with the numerically modeled counts, particularly for the simulated true unscattered fluorescence counts detected by an ideal detector. The recorded fluorescence counts, which include all gold fluorescence counts and detector effects, are slightly higher. This is because they also contain fluorescence photons that may have undergone additional scattering. These counts are however not included in the model, but they do slightly increase the total number of actual fluorescence photons.

5.3.2 Background Dependency on the Detector Angle and Energy Range

Besides the fluorescence counts for the signal, it is also essential to examine the background, as it may overlay the fluorescence signal, potentially making it challenging to distinguish the signal from the background. Therefore, Fig. 5.4 shows the backgrounds for different detector angles resulting from the setup described in Sec. 5.1.

As the gold target is relatively small compared to the human-sized object, the slight differences in the Compton cross sections of gold ($\sigma_{C,AU} = 0.1011\,\text{cm}^2/\text{g}$) and soft tissue ($\sigma_{C,ST} = 0.168\,\text{cm}^2/\text{g}$) have a negligible impact on the background [36]. Accordingly, the background does not change significantly when the gold target is shifted to different positions, which is why the background is analyzed independently of the gold target's position, unlike the detected fluorescence counts shown in Fig. 5.3.
The background spectra, which represent all detected photons except the gold fluorescence

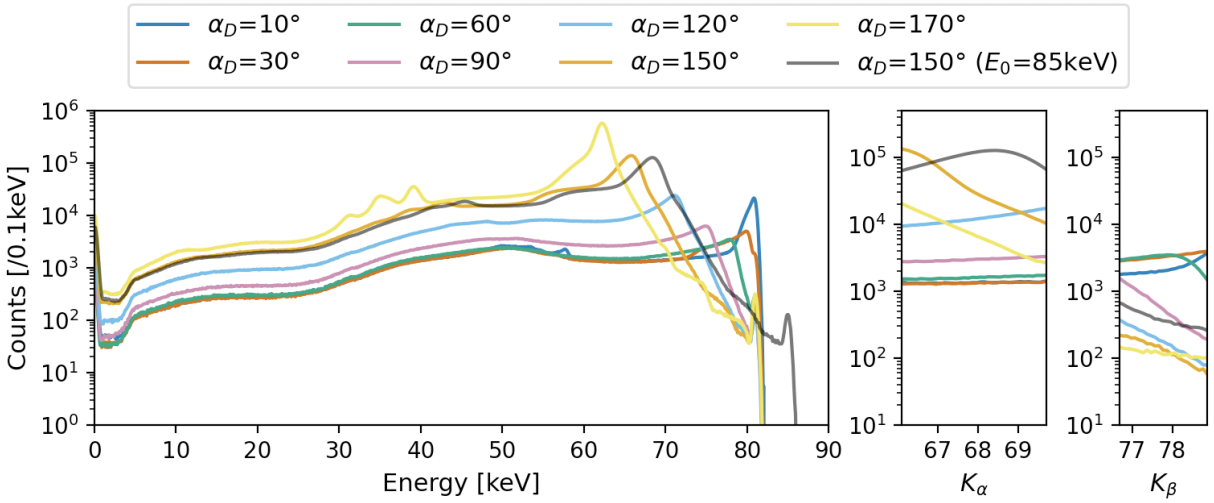

Figure 5.4: Simulated spectrum (recorded) of the background counts, scaled from $N_0 = 10^{10}$ to an incident photon number of $N_0 = 1.3 \times 10^9$, for various detector angles and an incident energy of $E_0 = 81\,\text{keV}$, with the exception of one scenario with $E_0 = 85\,\text{keV}$.

photons responsible for the signal, are shown in Fig. 5.4. Looking at the background spectra, it is clearly visible that the background is very broad due to Compton scattering, whereby photons lose a different amount of energy depending on the scattering angle.
As already explained in Sec. 2.1.4, at an incident energy of 81 keV, Compton scattering dominates in soft tissues, namely the material of the simulated cylinder, since the largest component of the total mass-attenuation coefficient is defined by the Compton mass-attenuation coefficient (Fig. 2.7). Furthermore, due to the dimension of the human-sized cylinder with a diameter or depth of 300 mm, the transmission is very low (Fig. 2.6). This means that interactions, particularly Compton scattering, between the photons and the soft tissue are highly likely. Therefore, after penetrating a depth of 300 mm, only 0.004% of the photons would pass through and leave the human-sized cylinder without any interaction, and even at a depth of 100 mm at $z = -50\,\text{mm}$, already 83.6 % would have interacted with the cylinder, causing the very broad Compton background.
The highest energy achievable by Compton-scattered photons is reached at the smallest scattering angles. Inside the cylinder, this occurs when photons are scattered only once directly when entering the cylinder at a shallow depth. For example, with an incident energy of 81 keV and a detector located at $\alpha_D = 10°$, the smallest scattering angle $\theta = 6.0°$ to the detector center would correspond to a maximum energy of 80.49 keV for C1 photons scattered within the object (Eq. 2.7). In contrast, only a minimum scattering angle of $\theta = 151.4°$, corresponding to a maximum energy of 62.4 keV, would be possible if the photon would hit the center of a detector located at $\alpha_D = 170°$. These maximum scattering energies, referred to the detector center, fall within the energy range of the background peaks for each individual detector angle, indicating that the C1 photons are responsible for these peaks. Moreover, Compton photons that have been scattered more than once are associated with more possible combinations of scattering angles, resulting in a broad spectrum and they often exhibit greater energy loss due to additional scatterings

(Fig. 4.5). Therefore, multiple Compton scattering is primarily associated with lower energies in the broad Compton continuum. Since the detector is not just a point but has a large detection area, smaller scattering angles and thus higher energies might also be detected. Additionally, the relativistic effect of Doppler broadening can cause slightly different energies to be detected (Sec. 5.3.4). Lastly, the Rayleigh-scattered photons also have a higher energy than the Compton-scattered photons because, in coherent scattering, the photons do not lose energy and retain the energy of the incident beam. Only due to the detector's energy resolution is the Rayleigh peak broadened. Note that using a non-ideal detector also causes low-energy photons to be detected, and with a 170° detector, for example, some of the C1 escape peaks are visible at energies between 30 keV and 40 keV. To sum up, the background peak is defined by C1 photons, whose energy is higher for smaller detector angles, as smaller scattering angles are possible in this case. In contrast, a larger detector angle causes the background peak and the Compton continuum to shift toward the lower energy range. Simultaneously, for detector positions with α_D >60°, more counts are detected overall, particularly in the C1 peak, since larger detector angles result in shorter photon path lengths within the object and, moreover, larger solid angles arise for detector angles greater than α_D >90°. However, a detector angle smaller than $\alpha_D = 60°$ is also associated with more detected counts across the entire spectrum, as the decreasing distance of the photons from the z-axis to the detector causes a larger solid angle of the detector and thus more counts are detected.
The shift of the background is a truly essential effect, as a large detector angle shifts the majority of the background out of the high-energy K_β signal region of gold, which is primarily dominated by C1 photons. This has also already been noted by Ahmad et al. [104] and Vernekohl et al. [29]. Although the total background is much higher when

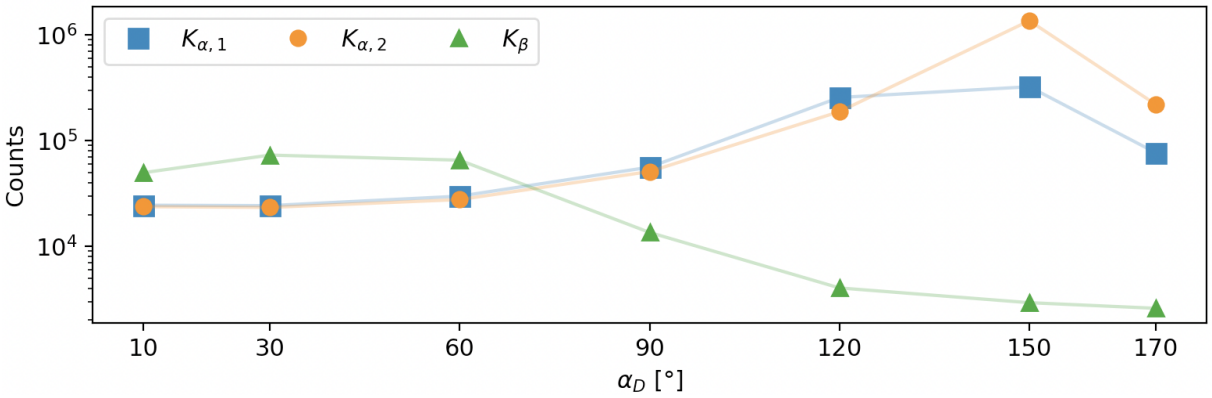

Figure 5.5: The recorded background counts of the setup described in Sec. 5.1 with 1.3×10^9 incident photons and an incident energy of 81 keV are shown in the $\pm 3\sigma$ intervals ($\sigma = 0.3$ keV) around the $K_{\alpha,1}$ (67.9 keV< E <69.7 keV), $K_{\alpha,2}$ (66.1 keV< E <67.9 keV) and K_β (76.7 keV< E <78.9 keV) lines.

integrated over all energies at a large detector angle, shifting the detector angle from 10° to 170° reduces the background in the K_β gold region by more than one order of magnitude, while it triples in the $K_{\alpha,1}$ gold region and even increases almost tenfold in the lower-energy $K_{\alpha,2}$ gold region, which is closer to the background peak (Fig. 5.5, 5.4).

In particular, the background is large since at $\alpha_D = 150°$, where the background peak of the C1 photons falls in the $K_{\alpha,2}$ gold region. Therefore, the number of background counts in the K_α region would be higher at backward detector angles. In Fig. 5.4, the incident beam energy of 81 keV at a detector angle of 150° is also compared with an incident energy of 85 keV, which was used in Grüner et al. [28]. Then, at an incident energy of 85 keV, the entire spectrum shifts to higher energies, resulting in more background in the K_β energy range. This shift in the spectrum for different incident energies is also why the minimum background within the K_α energy range occurs at an incident energy of 81 keV, not at 60° as in Grüner et al. [28], but rather at 30°. Nevertheless, the background in the K_α region is never lower than the background at backward detector angles in the K_β energy range, which is why large detector angles backwards seem promising.

5.3.3 Significance Dependency on the Detector Angle and Energy Range

After analyzing the fluorescence counts and the background separately, the key question remaining is how significant the fluorescence signal is in relation to the background. Therefore, Fig. 5.6 shows the significances for different detector angles α_D and gold target positions (0, 0, z_{Au}), when no collimator is used. Only significance values for the K_β en-

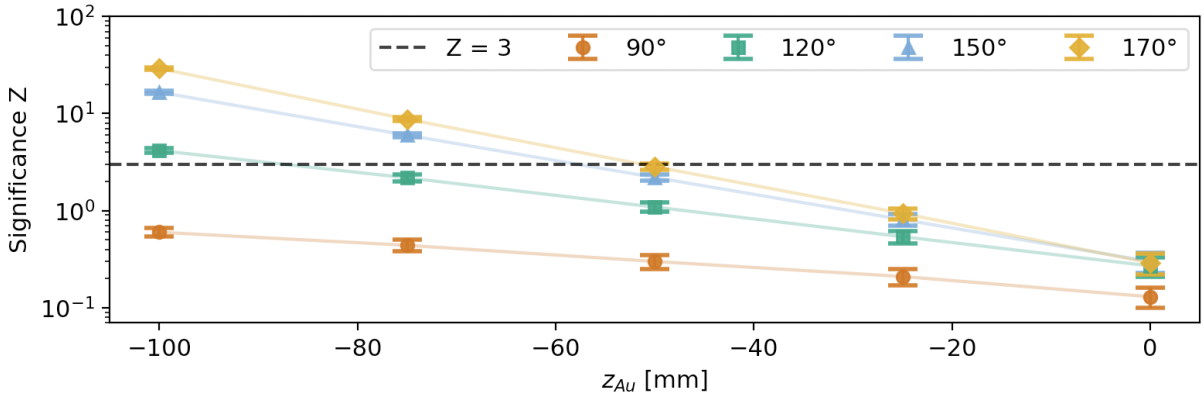

Figure 5.6: Based on the recorded counts with $N_0 = 10^{10}$ incident photons, the significances Z with their uncertainty ($\pm\sigma_Z$) are shown for $N_0 = 1.3 \times 10^9$ incident photons in the $\pm 3\sigma$ energy interval around the gold K_β line. These are shown for various gold target positions (0,0,z_{Au}) and detector angles α_D. The gold concentration is $c_{Au} = 1.0\,\mathrm{mg/ml}$.

ergy range of gold are shown in Fig. 5.6, since the background of the K_α range was much too high, resulting in no significant signals. Signals are typically considered significant if the significance is greater than three [28]. In this context, only gold targets at positions with $z_{Au} < -75\,\mathrm{mm}$ would achieve a significant signal, which is only possible at detector angles greater than 150° for $z_{Au} = -75\,\mathrm{mm}$ or 120° for $z_{Au} = -100\,\mathrm{mm}$.
A recorded spectrum with a significant signal is shown in Fig. 5.7. In this figure, the fluorescence counts are differentiated between non-scattered and scattered gold fluorescence. The unscattered counts primarily define the significance of a fluorescence signal, as they exhibit the known energies of the gold fluorescence lines, which are described in Sec. 3.5. However, due to the energy resolution of the detector, the recorded energy of the un-

scattered fluorescence photons may deviate slightly. In comparison, the gold fluorescence photons that undergo additional Compton scattering have lower energy, resulting in a continuum of scattered fluorescence photons. The number of gold fluorescence photons in the K_α region below 70 keV is much lower compared to the background, while the number of gold fluorescence photons in the higher-energy K_β region is higher than the background level, as shown in Fig. 5.7. The use of a realistic detector also causes some escape peaks

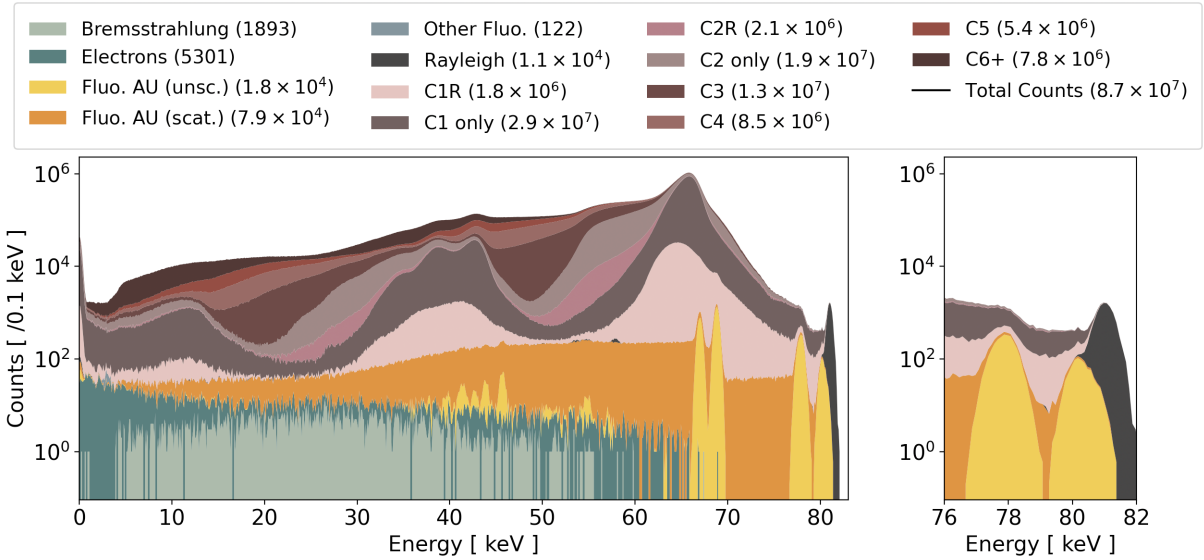

Figure 5.7: Recorded spectrum using $N_0 = 10^{10}$ incident photons, an incident energy of 81 keV, a gold target at $z_{Au} = -75$ mm with a concentration of 1.0 mg/ml and a detector at 150°. The total number of recorded photons is shown in the brackets.

of gold fluorescence photons due to the cadmium telluride detector material. These peaks appear in the energy range between 50 keV and 60 keV for the gold K_β fluorescence photons, while the escape peaks of the gold K_α fluorescence photons lie below 50 keV. The escape peaks are visible not only for the gold fluorescence in the stacked spectrum but also for the background peak, which is at 65.7 keV. Accordingly, escape peaks appear at lower energies between 34 keV and 43 keV, where the energy difference to the background peak corresponds to the K-energy lines of cadmium and telluride. This Fig. 5.7 confirms that, as explained above, the background peak is primarily defined by photons that have undergone a single Compton scattering, while the photons that have undergone multiple Compton scatterings define the Compton continuum in the lower energy range. Bremsstrahlung and electrons resulting from Compton scattering are also detected, but their proportion is very small compared to the other interactions, and their energies are lower than those of the gold fluorescence signals. Therefore, these are negligible. In contrast, Rayleigh-scattered photons are highly energetic, but only in the K_γ range of gold. Finally, in the promising K_β signal range of gold mainly single Compton-scattered photons appear as background.

5.3.4 Impact of Doppler Broadening

The simulations in Fig. 5.7 show that background photons, or more precisely, mainly C1 photons, are detected in the K_β signal region of gold. For cross-validation and to understand the behavior of the C1 photons, their energy spectrum was additionally estimated using the numerical model and compared with the simulations. For this purpose, the detector was pixelated with a distance of 0.5 mm between the pixel centers, and the beam axis within the cylinder was iterated with a step size of 1.0 mm. In this case, C1 photons, which did not undergo any other interaction apart from a single Compton scattering, were modeled and simulated. To enable a fair comparison, the true counts detected by an ideal detector with the same two-dimensional effective detector area as the model are considered to eliminate effects not taken into account in the numerical model.
As shown in Fig. 5.8, the simulated and numerically modeled energy spectra are in close agreement, with a difference of less than 1% in the total number of detected pure C1 photons. However, the energy spectrum in the simulation is broader than in the modeled one. While the peak in the modeled scenario is considerably higher, the simulation also detects some counts outside the numerically modeled energy range, resulting in a lower peak. More specifically, the model allows only energies between 61.8 keV and 67.1 keV, whereas the simulation detects photons in the range from 41.0 keV to 80.5 keV. This means that, numerically, no counts are expected in the K_β gold fluorescence energy range, yet some are detected in the simulated scenario. This is due to the Doppler broadening. In the

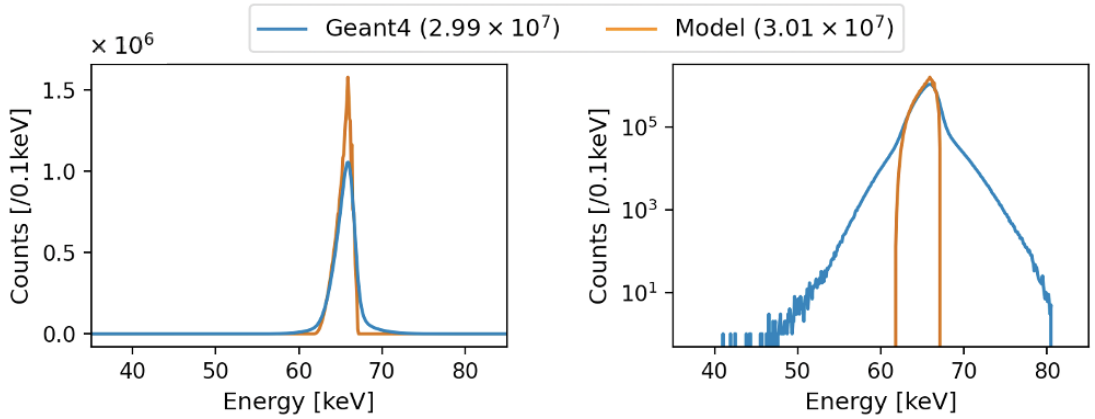

Figure 5.8: Single Compton-scattered photons (C1 only), simulated with an ideal detector with $N_0 = 10^{10}$ incident photons, an energy of $E_0 = 81$ keV, a gold target at $z_{Au} = -75$ mm with $c_{Au} = 1.0$ mg/ml, and a detector at $\alpha_D = 150°$ are compared with the modeled C1 only photons, plotted on a linear (left) and logarithmic (right) scale.

numerical model, the Klein-Nishina equation (Eq. A.3) is used to calculate the Compton energy, assuming that the electrons are free and at rest before the photon scatters [106, 107, 44]. In Geant4 simulations, however, the more realistic motion of the electron is taken into account, which results in an energy shift due to the electron's momentum when a photon is scattered off it. Consequently, the actual energy following a Compton scattering may be higher or lower than the energies calculated in the numerical model

using the Klein-Nishina formula, depending on the direction of the electron's initial momentum vector [106, 108].
Nevertheless, most of the C1 photons originate from the modeled energy range, which becomes particularly evident when using the linear scale for the count values. However, Doppler broadening causes background in the K_β signal energy range of gold, where, under the simplified assumption for the electrons in the numerical model, no background would otherwise be expected at all. This means that the numerical Compton model provides a good approximation of the expected total number of C1 photons, but cannot be used to estimate the C1 photons in the promising K_β signal energy range of gold.

5.4 Discussion

The previous results have shown that the lowest background within a gold fluorescence energy range can be achieved with the K_β energy range for large detector angles in the backward direction. Larger detector angles are related to larger minimum scattering angles, which decreases the energy of the detected Compton photons. For a detector in the backward direction, this phenomenon shifts the background peak to energies below the K_β signal energy range. An example is a 150° detector, which would only detect background photons caused by Doppler broadening. Consequently, the background is strongly reduced for this configuration and is much lower than that of any detector angle within the K_α energy range.
In fact, the background of a 60° detector within the Au-K_α energy range is larger than that of a backward detector within the K_β signal range. Even if the energy of the 60° detector were increased to 85 keV, corresponding to the configuration of Grüner et al. [28], and the spectrum were shifted to higher energies so that the K_α energy range would fall within the minimum of the Compton continuum, the background would still be associated with more background photons. This becomes obvious when considering the background of a 30° detector for 81 keV, which corresponds to the minimum background within the K_α range for 81 keV and is associated with a background that is still almost one order of magnitude larger compared to the minimum background within the Au-K_β energy range.
Contrary to the K_α energy range, for the K_β energy range, a lower incident beam energy of 81 keV seems more convenient than 85 keV. There are two main reasons for this. First, an incident energy of 81 keV results in lower-energy Compton photons than does 85 keV, meaning that the background peak is farther from the K_β energy range, resulting in less background. Second, the lower energy of 81 keV is closer to the gold absorption edge (80.72 keV), which increases the fluorescence cross sections. This is advantageous because K_β fluorescence cross-sections are already lower than those of K_α energy. While the K_β fluorescence cross section of gold is only $\sigma_{F,K_\beta} = 0.62\,\mathrm{cm^2/g}$ at an incident beam energy of 85 keV, it reaches a value of $\sigma_{F,K_\beta} = 0.70\,\mathrm{cm^2/g}$ at an incident beam energy of 81 keV [36].
Despite the fact that the fluorescence cross section of the K_β energy is much lower than that of the K_α energy ($\sigma_{K_\alpha} = 5.07\,\mathrm{cm^2/g}$), for certain target positions, more fluorescence photons are detected when considering the K_β energy range with a backward detector than the K_α range at 60°. This is mainly due to the larger achievable solid angles.

In contrast to backward detectors, a 60° detector detects nearly the same fluorescence counts regardless of the target position. This is advantageous because fluorescence counts are then detectable from all target positions, so rotation to radiate from the other side would be unnnecessary. However, the much smaller background and much larger number of fluorescence counts make the K_β energy range with a backward detector promising, which will be the focus in the following. Nevertheless, significant signals can only be detected from a few target positions, which is why a collimation system is necessary for further reducing the background.

6 Development of Collimator Designs

Based on the results presented in Sec. 5, some collimator designs are presented below to reduce the background problem when imaging human-sized objects within the Au-K_β energy range. These collimators are designed for a smaller detector compared to the 4π-detector used by Grüner et al. [28], making this approach more practical and economical. However, the collimator designs presented below are also limited by the requirement that the target location must be known from previous imaging using another imaging method in the context of multimodal imaging.

6.1 Vertical-Lamellae Collimator

6.1.1 Principle of the Collimator with Vertical Lamellae

The aim of the collimator with vertical lamellae, the "Vertical-Lamellae Collimator" is to shield all possible single Compton-scattered photons, since these have the highest energy and dominate the background in the gold K_β region, which, as discussed in Sec. 5.3, appears to be the most promising signal region for a significant gold signal. However, both the fluorescence signal photons and the C1 photons occur from the z-axis, which is the beam axis. Consequently, it is impossible to shield all C1 photons, otherwise no signal photons would be detected at all. In the following, a collimator design is presented in which only photons originating from the beam-axis section of the gold target are detected. This means that all C1 photons generated within the gold target would be shielded due to the collimator construction, which can be realized with some vertical lamellae in relation to the xz-plane. To understand the basic principle of the collimator, Fig. 6.1 schematically visualizes the structure and functionality of the collimator.

A gold target is located on the z-axis between (0, 0, $z_{Au,min}$) and (0, 0, $z_{Au,max}$). Then a detector (green) is added, and in this example, five lamellae (red) are used to shield photons from the z-axis out of the gold target. The lamellae L_1 to L_5 are spaced at a constant distance from each other at the detector and subdivide the detector in a sense, into four distinct areas D_1 to D_4. Each of these areas is only allowed to detect photon paths originating from the interval (0, 0, $z_{Au,min}$) to (0, 0, $z_{Au,max}$). This means that the detector sub-area D_3 has to be restricted by lamellae, which only allow photon paths with a certain minimum path angle relative to the beam. This corresponds to photons traversing from $z_{Au,min}$ to the upper edge at L_4 of the third detector region, as shown by the grey path in Fig. 6.1a. At the same time, the detector area must not detect photon paths with a too large path angle. The maximum path angle in the case of the detector sub-area D_3 then corresponds to the path from $z_{Au,max}$ to the lower edge of the detector sub-area L_2, shown by the blue path in Fig. 6.1a.

To restrict photon paths originating, for example, from z-values lower than $z_{Au,min}$ to the detector area D_3, a vertical lamella perpendicular to the xz-plane must be added, beginning at L_3 and ending at any point along the grey minimum path. Two possible lamellae (dotted red lines) are shown in Fig. 6.1b as examples. However, the option with the shorter lamella length would also shield the blue path with the maximum path angle originating from $z_{Au,max}$. This, in turn, would result in a lower number of detected

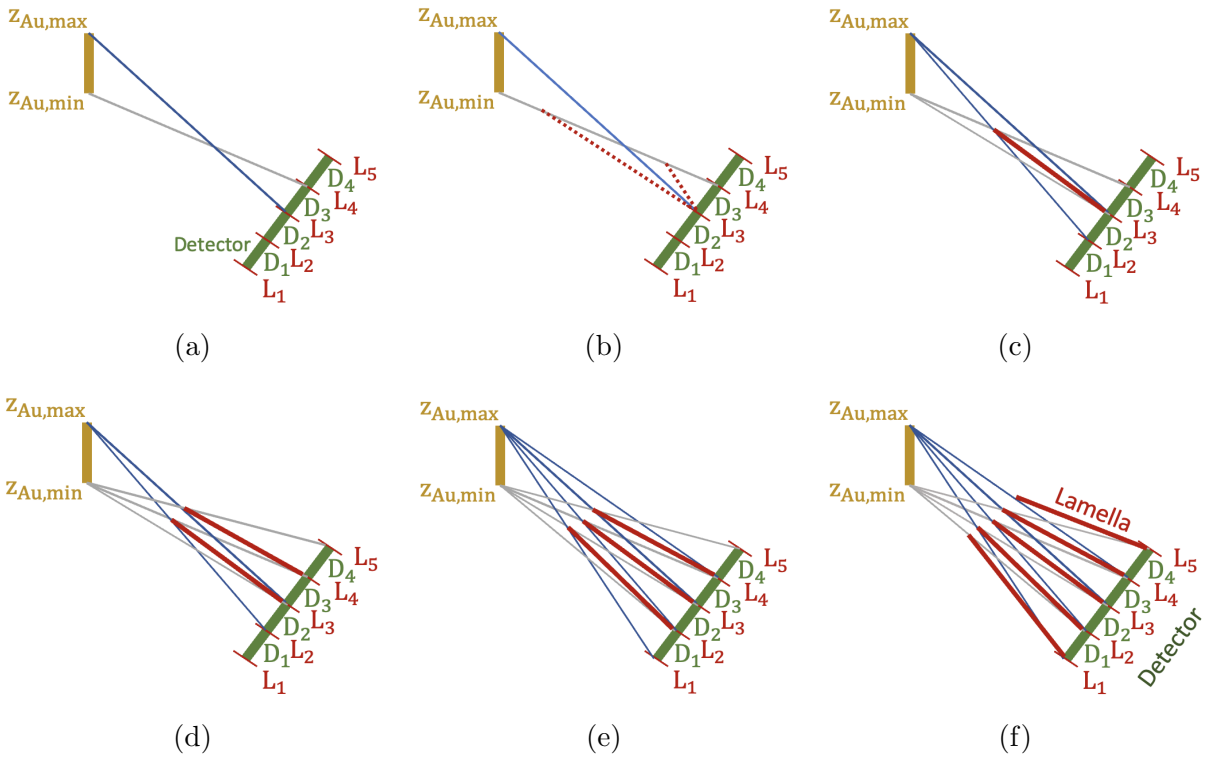

Figure 6.1: Structure and function of the collimator with lamellae (red) in front of the detector (green) to shield photons from the beam axis outside the gold target (gold) in the range from (0, 0, $z_{Au,min}$) to (0, 0, $z_{Au,max}$). The five lamellae L_1 up to L_5 divide the detector area into four distinct sub-areas D_1 to D_4. The grey lines correspond to the photon paths with the smallest permissible detection angle, while the blue lines correspond to the photon paths with the largest permissible detection angle for each detector sub-area.

counts, whereas for a high fluorescence count number, as many photons as possible from the target interval should be detected. Therefore, the other, longer lamella would be more appropriate.

However, if the minimum and maximum path angles of the additional detector sub-area D_2 are also taken into account, it turns out that the endpoint of the third lamella ultimately is defined by the path (blue) with the maximum angle required to reach the second detector sub-area (Fig. 6.1c). To sum up, the endpoint and thus the length of the middle lamella L_3 is determined by the intersection of two photon paths. One photon path extends from $z_{Au,min}$ to the upper edge of detector D_3, where lamella L_4 will be located, and the other photon path extends from $z_{Au,max}$ to the lower edge of the adjacent detector D_2, where lamella L_2 will be located. A longer lamella should not be used, as this would reduce the target's potential detection area, resulting in a lower number of detected fluorescence photons.

Subsequently, the endpoints of the other lamellae L_2 and L_4 are determined using the same principle, as shown in Fig. 6.1d and 6.1e. However, the endpoints of the outer lamellae L_1 and L_5 are not strictly defined, since they only need to shield one detector

area. More precisely, the first lamella L_1 only has to end somewhere along the grey path between (0,0,$z_{Au,min}$) and L_2, while the last lamella L_5 has to end somewhere along the path between $z_{AU,max}$ and L_4. One possible arrangement is shown in Fig. 6.1f. A way to determine an exact endpoint for the outer lamella is to imagine detector sub-areas D_0 and D_5 and calculate the endpoints using the same principle as for the middle lamellae, which is what is done in this thesis.
This principle of the collimator can also be applied to different configurations, such as different detector angles, target positions, or a larger number of lamellae. The advantage of using more lamellae and therefore reducing the distance between them is that shorter lamella lengths are achieved. This can be particularly useful when the lamella length is limited, for example due to the relatively large human-sized object, to avoid collisions between the object and the lamellae. Nevertheless, it should be noted that more lamellae also mean a higher proportion of lamella material, which may reduce the effective detector area and, consequently, the number of detected photons.
Note that, due to the maximized shielding of C1 photons, the detector's field-of-view (FOV) generated by the lamella alignment is severely restricted. For medical applications where the target region is already known, such as prostate imaging to assess residual tumor volume, this is not expected to be a problem. However, in pharmacokinetics, where the distribution of drugs is unknown, the collimator design would be unsuitable.

6.1.2 Setup

As in the scenario without a collimator, a cylinder made of soft tissue with a diameter and height of 300 mm is used as a human-sized object located in air. A gold-water mixture with a concentration of $c_{Au} = 1.0\,\mathrm{mg/ml}$, in a cylindrical shape with a length of 10 mm and a diameter of 1 mm is used as the signal target and is located at a depth of $z_{Au} = -75\,\mathrm{mm}$ along the z-axis. It should be noted that this position of the gold target is chosen to ensure a sufficient number of fluorescence counts in first proof-of-concept simulations regarding the developed collimator design. The gold target will also be shifted to other positions later in this chapter.
For the reasons described in Sec. 5, the two detectors, each with a detection area of 20 mm $\times$60 mm and a thickness of 1 mm, are arranged at a distance of $R_D = 225\,\mathrm{mm}$ from the cylinder center backward at an angle of $\alpha_D = 150°$ in order to reduce the background and increase the fluorescence counts due to the detector position. At the same time, the detector is aligned orthogonally to the center of the gold target. Cadmium telluride is used as the detector material with an energy resolution of 0.3 keV for the recorded counts.
The collimator design presented in Sec. 6.1.1 is used to shield the background along the beam axis outside the target. Due to the detector distance R_D used, nine lamellae are implemented to reduce the length of each lamella to approximately 67 mm to 72 mm and thereby avoiding collisions with the soft-tissue cylinder. As a result, the spacing between the outer lamellae at their ends is much smaller than the initial 20 mm at the detector. Furthermore, a kind of collimator housing is added by attaching a lamella to the base and on the top (Fig. 6.2) to reduce multiple Compton scattering outside the xz-beam plane, although this is less important for the gold K_β range. Note that nine vertical lamellae are chosen because fewer lamellae require a longer length to shield the entire z-axis outside the

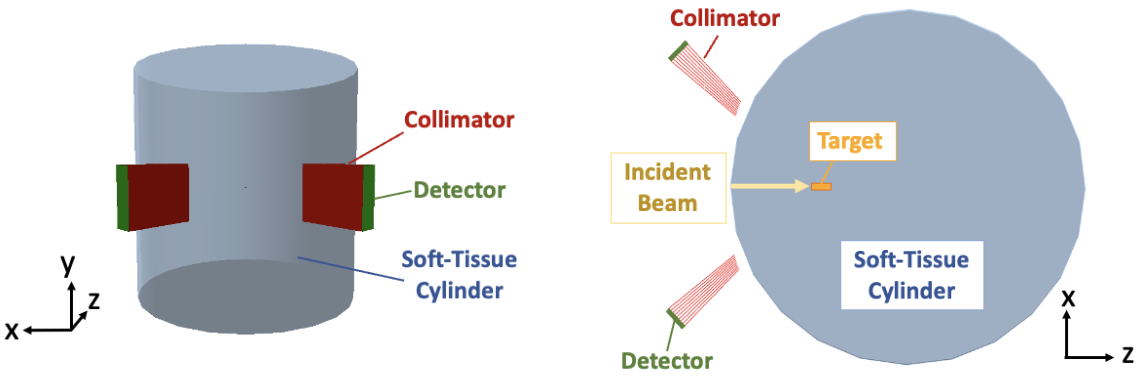

(a) Front View. (b) Top View.

Figure 6.2: A 10 mm long gold target (orange) is located inside a human-sized cylinder (300 mm diameter) made of soft tissue (blue), and the detectors (green) are arranged at an angle of $\alpha_D = 150°$ to the incident beam (yellow), with a collimator (red) placed in front of them. Note that while the relative proportions in (a) are to scale, the schematic setup in (b) is not to scale, as the target and the incident beam are shown larger than their actual size relative to the water cylinder for visibility.

target, which would cause the lamellae to collide with the object. However, more lamellae would block a larger area of the detector and hence reduce the fluorescence counts.
As the photon source, a monoenergetic pencil beam is used that provided photons with an energy of 81 keV and has a diameter of 1 mm, which corresponds to the diameter of the gold target. The beam source is located at $z_0 = -150.5$ mm. To ensure sufficiently high statistics in the simulations when verifying the collimator design, $N_0 = 10^{10}$ unpolarized incident photons with an energy of 81.0 keV are simulated. However, $N_0 = 1.3 \times 10^9$ incident photons, based on the results of Grüner et al. [28] and dose calculations (Sec. 5.2), are considered for calculating the significance.

6.1.3 Effect of the Ideal Collimator

To investigate the effectiveness of the collimator, the setup described in 6.1.2 is simulated using ideal absorbing lamellae with a thickness of 200 μm and compared with the scenario without a collimator (Fig. 6.3). Ideal absorbing lamellae mean that a photon is completely absorbed after interacting with a lamella, and no further effects or interactions can occur.

The impact of the collimator is illustrated in Fig. 6.3 by the fact that the number of detected photons (1.1×10^6) is significantly lower for the ideal collimator than in the initial scenario without a collimator, where 8.7×10^7 photons are detected. This means that the ideal collimator reduces the number of detected counts by a factor of almost 80. Photons of all energies are shielded, indicated by the decrease in counts across the entire collimated spectrum, meaning that photons of all Compton orders are absorbed by the detector. However, the shielding is not constant over all energies, since the background

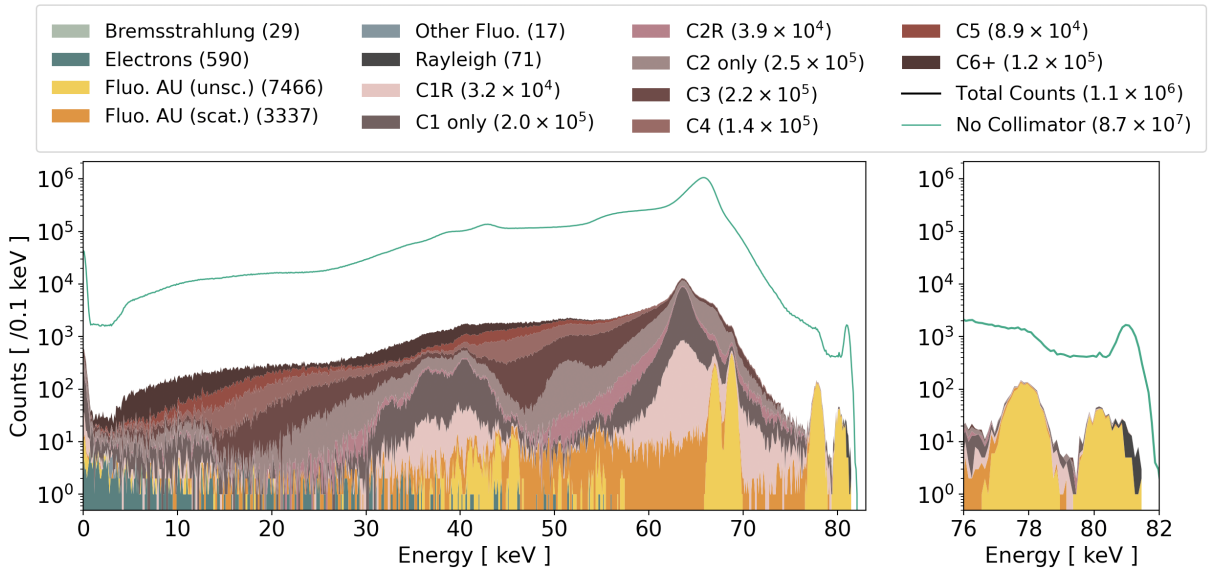

Figure 6.3: Simulated recorded spectrum with ideal lamellae in the collimator, each having a thickness of $t_L = 200\,\mu$m. For comparison, the total recorded counts without the collimator (green) are shown. $N_0 = 10^{10}$ incident photons are simulated with a gold concentration of 1.0 mg/ml, and the number of detected counts is indicated in the parentheses.

peak defined by C1 photons is at an energy of 65.7 keV in the uncollimated spectrum, but now at an energy of 63.6 keV in the collimated spectrum. The spectrum thus shows that the collimator shields C1 photons with higher energy in particular. According to Eq. 2.7, a higher energy for C1 photons also implies a smaller scattering angle, which is the case in the simulated scenario when the photons are scattered as early as possible after entering the soft-tissue cylinder. This means that the C1 photons, defining the background peak in the uncollimated spectrum at 65.7 keV, correspond to photons scattered at $z = -135$ mm with an angle of 118°. However, due to the design of the collimator, photons originating from the beam axis, such as pure C1 photons (declared as "C1 only" in the spectrum), can only be detected if they are generated within the gold target between $z_{Au,min} = -70$ mm and $z_{Au,min} = -80$ mm. Therefore, the collimator only accepts pure C1 photons with a scattering angle between 135.6°, scattered at $z_{Au,min} = -80$ mm, and 138.0°, scattered at $z_{Au,min} = -70$ mm. The consequence is that pure C1 photons can only reach energies between 63.46 keV and 63.69 keV if relativistic effects are not taken into account. This explains the reason why the background peak at 65.7 keV from the uncollimated spectrum disappears in the collimated spectrum, while the peak then appears at approximately 63.6 keV. However, due to the detector resolution and relativistic effects like Doppler broadening, Compton counts may be slightly higher or lower in energy, so a few C1 counts are still detected outside the expected energy range in the uncollimated spectrum.
In addition to the pure C1 photons, mixed scattering can also occur due to additional Rayleigh scattering. These photons can even be detected at energies higher or lower than

those expected for pure C1 photons. For example, if a photon undergoes a single Compton scattering event at a shallow depth ahead of the gold target, this is associated with a small scattering angle and therefore with high energy. Even though pure C1 photons would normally be absorbed by the collimator, it is still possible to detect the high-energy photon if it undergoes a further Rayleigh scattering, which alters the path of this photon such that it does not collide with the collimator but is instead detected. Since Rayleigh scattering is coherent, there would be no energy loss in a C1 photon. This also applies, of course, in cases where, for example, a Rayleigh scattering event is followed by a Compton scattering event and perhaps even another Rayleigh scattering event afterwards. However, the number of detected mixed scattered "C1R" photons is much lower compared to the pure C1 photons "C1 only", since the cross section of Rayleigh scattering is smaller in contrast to Compton scattering (Fig. 2.7). This is related with a lower probability of Rayleigh scattering.
Moreover, Fig. 6.3 shows that many of the twice Compton-scattered "C2 only" photons have higher energies than the C1 photons, whose peak is broader and ranges from 65 keV to 66 keV, compared to the sharper peak of the "C1 only" photons at 63.6 keV. Predominantly, the lower-energy C2 photons are shielded, since the C2 peak without a collimator is at 63.3 keV. The energy distribution for C1 and C2 photons as a function of the scattering angle θ, based on Eq. 3.19 from the numerical model, is illustrated in Fig. 6.4. It confirms that larger scattering angles θ_1 are associated with lower photon energies

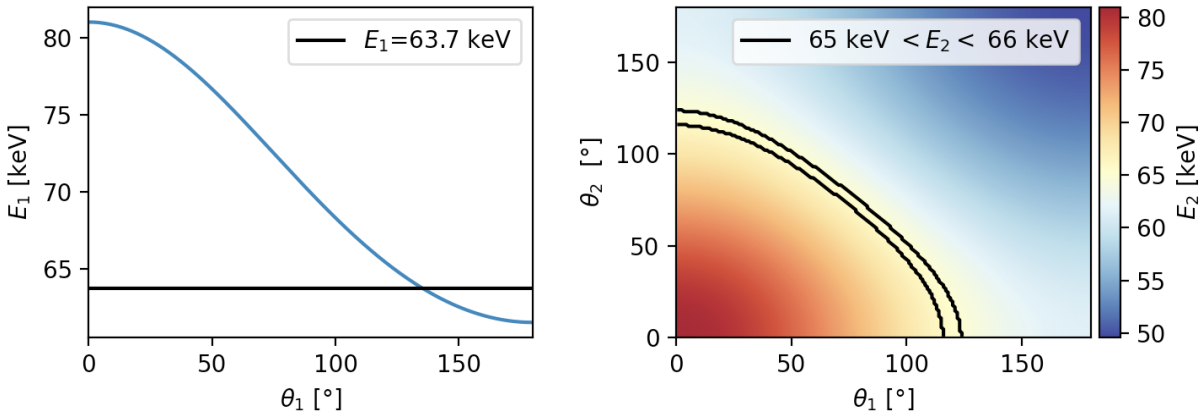

Figure 6.4: Modeled energy distribution based on Eq. 3.19 for single Compton-scattered "C1 only" photons (left) and for double Compton-scattered "C2 only" photons (right) as a function of the scattering angles θ_1 and θ_2. For C1 photons, the energy E_1 of the peak is marked in black at 63.7 keV when using the collimator, and for C2 photons, the peak energy range is indicated in black between 65 keV and 66 keV.

after the scattering process. However, due to the term $cos(\theta)$ in Eq. 3.19, the decrease is smaller for forward scattering at angles θ_1 close to 0° or for backward scattering at angles close to $\theta_1 \approx 180°$. When using the collimator described above at a detector angle of 150°, the C1 peak occurs at an energy of 63.6 keV, which corresponds to an angle $\theta_1 = 135.5°$. In contrast, the "C2 only" photons depend on two scattering angles for each Compton scattering event. However, due to the two Compton scatterings, even higher energies of

the twice Compton-scattered photons are possible, although the sum of both scattering angles $\theta_1 + \theta_2$ for C2 could be greater than for a C1 photon scattered directly by $\theta_1 + \theta_2$. For example, double-scattered photons with an energy of 65.0 keV, corresponding to the energy of the C2 peak with a collimator, might scatter first by $\theta_1 = 35°$ and than by $\theta_2 = 112°$. This would result in a total scattering angle of $\theta_1 + \theta_2 = 147°$, which, however, would only yield an energy of 62.7 keV, if this was the scattering angle of a photon that had undergone a single Compton scattering. Consequently, this phenomenon allows the detection of photons with higher energy that undergo double Compton scattering than photons undergoing single Compton scattering, even at larger total scattering angles overall, which also explains the higher energy of the C2 peak compared to the C1 peak. Note that the energy function is commutative and therefore the order of the scattering angles has no effect on the resulting energy.

Considering the Compton continuum below the C1 peak in Fig. 6.3, which is caused by photons that have undergone multiple Compton scatterings, there is almost no difference in shape compared to the uncollimated spectrum. The background is reduced by nearly a constant factor, meaning that photons of a higher Compton order are less spatially focused and, unlike the C1 photons, originate from a larger region. Before being detected, they have already been Compton-scattered several times, with no restrictions on the scattering angle, resulting in broad energy distributions for the Compton photons. Ultimately, only the location of the last scattering and the scattering angle decide whether the photon is absorbed by the collimator or being detected, resulting in the Compton continuum.
By focusing on the gold signal, the collimator is able to isolate the K_β gold line at approximately 77.8 keV and the K_γ line at approximately 80.3 keV. Almost no background remains, even the Rayleigh peak coinciding with the K_γ peak disappears almost completely. Finally, the signal in the K_β gold region for $N_0 = 10^{10}$ photons has a significance of $Z = 69.0 \pm 4.6$, based on 1278 gold fluorescence photons and only 170 background photons detected in this region. For $N_0 = 1.3 \times 10^9$ photons, a significance of $Z = 24.4 \pm 3.3$ is still expected. This is clearly higher than the significance of the signal without a collimator, which is only $Z = 16.6 \pm 0.4$ for $N_0 = 10^{10}$ photons. With no collimator, 22530 background photons and 3527 fluorescence photons are recorded. However, even though the fluorescence yield is roughly twice as high in the uncollimated scenario, the background is also more than two orders of magnitude larger. This strong reduction in background caused by the collimator, ultimately results in a much more significant gold signal. Even with 1.3×10^9 incident photons, the significance of $Z = 24.4 \pm 3.3$ in the collimated case is significantly higher than $Z = 6.0 \pm 0.3$ in the uncollimated case.
The signals in the gold K_γ region are now even significant. While the significance for 1.3×10^9 incident photons without a collimator with $Z = 2.0 \pm 0.2$ is not significant, it increases to $Z = 8.8 \pm 1.8$ through to the use of the collimator and becomes significant. The same applies to the $K_{\alpha 1}$ region of gold between 67.1 keV and 69.1 keV, where the significance reaches a value of $Z = 6.3 \pm 0.3$ instead of $Z = 1.8 \pm 0.1$. However, the signal from the $K_{\alpha 2}$ gold fluorescence line in the lower energy range remains insignificant in both scenarios, since it is closer to the C1 peak and the background is already too high.

In summary, the collimator appears to be a powerful tool for reducing background noise and thereby isolating fluorescence signals. This enables more significant gold signals in the K_β energy range of gold and also causes fluorescence signals in the K_γ and $K_{\alpha 1}$ ranges to become visible, which were previously insignificant.

6.1.4 Effect of Lamella Material and Thickness on Collimator Performance

In the previous section, the lamellae were considered to be ideal absorbers, but this only applies for simulations, not to reality. Therefore, a suitable material and lamella thickness have to be chosen to function as an absorber in the collimator.

Analysis of the Lamella Material For practical purposes, the absorbing material in the collimator should be non-toxic and mainly exhibit a high shielding effect, i.e., a high absorption coefficient in the relevant energy ranges. Common materials are tungsten or tantalum due to their high atomic number [109]. However, tungsten emits K_{β_1} fluorescence photons with an energy of 67.2 keV, very close to the emitted gold signal photons of the K_{α_2} line (67.0 keV) [36]. Due to the detector's energy resolution, distinguishing between these fluorescence photons would be impossible. Therefore, tungsten is less suitable as shielding material when gold is used as the target. Another material that has been used for shielding in the past is molybdenum. For example, Ungerer et al. [62] used collimator leaves made of molybdenum to shield background photons, which were also caused by a human-sized object but with an incident energy of 85 keV. Therefore, a comparison study of 200 μm thick lamellae made of tantalum and molybdenum is conducted below.

The stacked spectrum of the recorded counts from the simulation of the setup described in Sec. 6.1.2 is shown in Fig. 6.5. For comparison, also the total spectra of molybdenum lamellae, ideal lamellae, and the case without a collimator are shown. First of all, all collimators drastically reduce the number of detected counts. The total number of detected counts is decreased by more than one order of magnitude, even with the non-ideal materials. However, the tantalum lamellae appear to be more efficient, as they are able to reduce the total number of counts to a fraction of 1.95% compared to the uncollimated scenario, whereas the molybdenum collimator achieves only a reduction to 2.64%. To understand the greater count suppression achieved by tantalum lamellae, the spectrum with a tantalum collimator in Fig. 6.5 is analyzed in more detail.
In contrast to ideal lamellae, the simulated spectrum with tantalum exhibits two C1 peaks. One peak is located at 63.6 keV and the other at 65.7 keV. The peak with lower energy corresponds to the position of the C1 peak as when using ideal lamellae and thus arises due to the design of the collimator, which restricts the origin of the C1 photons (Sec. 6.1.3). The other, higher-energy peak is at the same energy as the C1 peak when no lamellae are used, implying that not all C1 photons are collimated outside the permitted gold target range, but still transmit through the non-ideal tantalum collimator. This phenomenon can also be observed in the case of a molybdenum collimator. There, however, the higher-energy C1 peak at 65.7 keV is even more prominent, indicating that

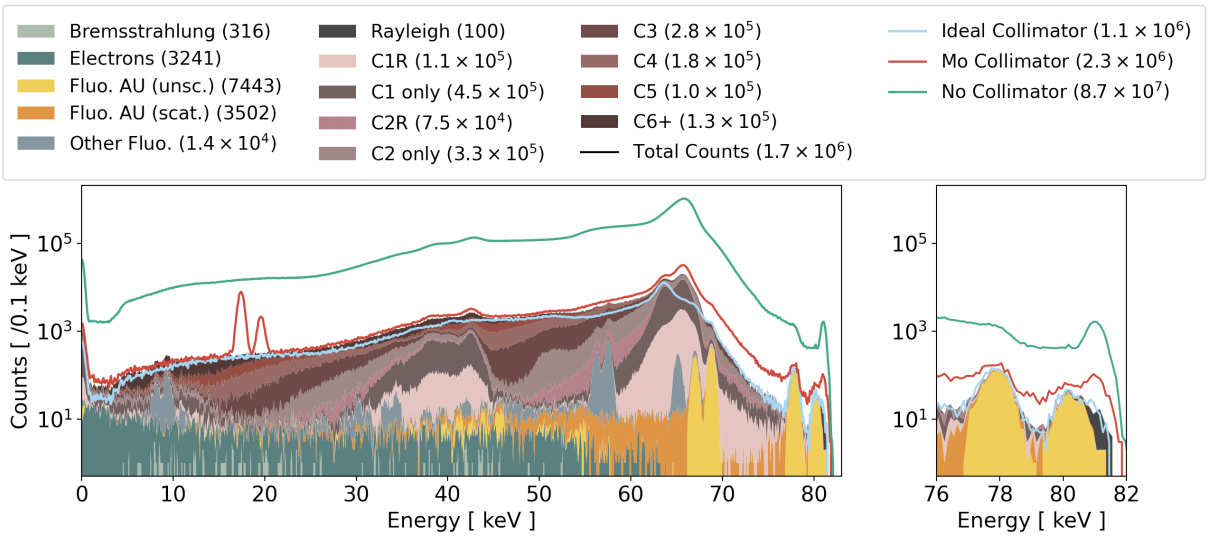

Figure 6.5: The recorded stacked spectrum for a tantalum collimator with a thickness of $t_L = 200\,\mu$m is compared with the total recorded spectra of the ideal absorbing collimator ($t_L = 200\,\mu$m) (blue), a molybdenum collimator ($t_L = 200\,\mu$m) (red), and the uncollimated case (green). $N_0 = 10^{10}$ incident photons are simulated.

molybdenum has a lower mass-attenuation coefficient. At higher energies, where the gold fluorescence signals K_α and K_β can be found, the discrepancy between the spectra collimated with molybdenum and tantalum increases. While tantalum lamellae, particularly at energies above approximately 68 keV, exhibit significantly fewer counts and thus lower shielding effectiveness, with their spectrum being nearly identical to that of the ideal lamellae, the background is reduced to a lesser extent with molybdenum lamellae. This can be explained by the mass-attenuation coefficients of molybdenum and tantalum.
As illustrated in Fig. 6.6, photoabsorption is the most prominent process in both materials, rather than scattering, thereby defining the total mass-attenuation coefficient. However, when comparing the mass-attenuation coefficients of tantalum and molybdenum, it becomes immediately apparent that tantalum displays a sharp increase at 67.4 keV, which corresponds to tantalum's K-absorption edge. Above this energy, electrons are able to transition from the K-shell to a higher energy level, resulting in the absorption of more photons at these high energies. Finally, the mass-attenuation coefficient rises from $\mu_m = 2.7\,\mathrm{cm}^2/\mathrm{g}$ to $\mu_m = 11.8\,\mathrm{cm}^2/\mathrm{g}$ at 67.4 keV, causing a huge reduction in the background above these energies. As a consequence of photoabsorption, secondary processes occur, such as fluorescence. Tantalum fluorescence photons occur in addition to the gold fluorescence signal and are visible in Fig. 6.5 under the category "Other Fluo". For example, the K_α energies are 57.5 keV and 56.3 keV, while the K_β line energy of tantalum is 65.2 keV. Unlike tungsten, this energy is fortunately still distant enough from the K_α fluorescence line energy of gold. However, with increasing energies above the absorption edge, the mass-attenuation coefficient decreases continuously. Nevertheless, in the K_β signal range of gold at 78 keV, $\mu_m = 8.1\,\mathrm{cm}^2/\mathrm{g}$ still holds.
In contrast, molybdenum only has an coefficient of $\mu_m = 2.1\,\mathrm{cm}^2/\mathrm{g}$ at 78 keV. The K-

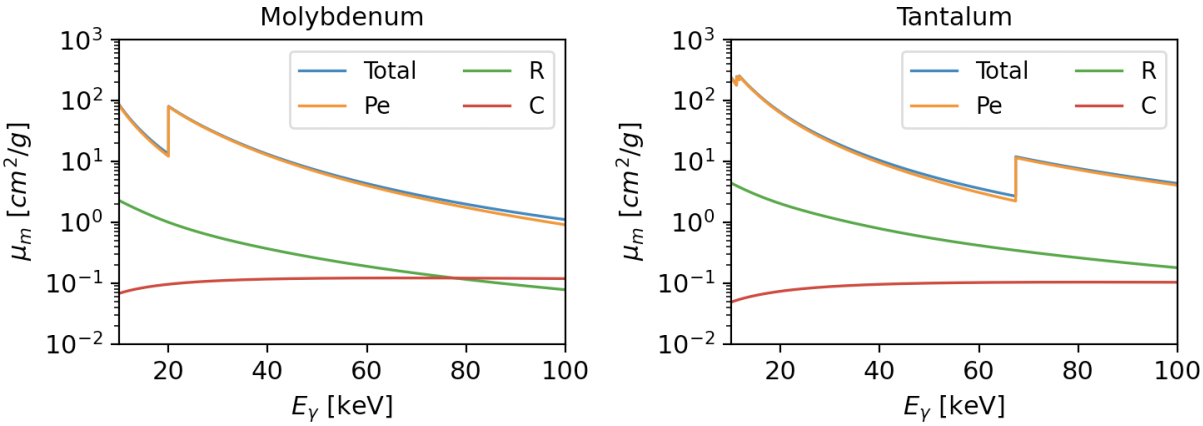

Figure 6.6: Total mass-attenuation coefficients μ_m and their components due to the photoelectric effect (pe), Rayleigh scattering (R), and Compton scattering (C) as a function of energy E_γ for molybdenum and tantalum (calculated with xraylib).

absorption edge is at much lower energy (20 keV), which explains the low mass-attenuation coefficient in the gold signal energies, even though its value at its K-edge is much higher ($\mu_m = 79.5\,\mathrm{cm}^2/\mathrm{g}$). Finally, in the recorded spectrum, two distinct molybdenum fluorescence peaks appear at 17.4 keV and 19.6 keV, while fewer photons are absorbed in the high-energy range. This means that more photons reach the detector and explains the discrepancy between the two materials and why tantalum is more suitable than molybdenum in case of the setup under consideration.
The fact that tantalum is a more suitable material than molybdenum is also reflected in the significance values of the gold signals shown in Table 2 and 3.

		K_{α_1}			K_{α_2}		
		F	B	$Z(1.3\times10^9)$	F	B	$Z(1.3\times10^9)$
Material	Ta	3795	22390	6.5±0.3	2379	160333	1.5 ±0.1
	Mo	3860	66956	3.8±0.2	2559	248925	1.3±0.1
	Ideal	3620	21397	6.3±0.3	2466	64612	2.5±0.1
	Air	11039	2.5×10^6	1.8±0.1	9124	10.5×10^6	0.72±0.02

Table 2: Simulated fluorescence (F) and background (B) counts for 10^{10} incident photons, as well as the corresponding significance values Z for 1.3×10^9 incident photons are listed. An energy interval of $\pm3\sigma$ is considered for the fluorescence lines K_{α_1} and K_{α_2}.

In Tab. 2 and 3 the simulated fluorescence and background counts in the different energy ranges for gold fluorescence are listed, as well as the significance Z for $N_0 = 10^{10}$ and $N_0 = 1.3\times10^9$ incident photons for the various collimator materials. Note that the material "Air" corresponds to the scenario without a collimator. The significance of a gold signal is higher in all cases when tantalum is used as the material instead of molybdenum, while the absence of a collimator is always associated with the lowest significance values. This means that both materials enhance the signal's significance and thus improve its visibility, with tantalum being nearly as efficient as ideal lamellae in some energy ranges. While,

		K_β			K_γ		
		F	B	$Z(1.3 \times 10^9)$	F	B	$Z(1.3 \times 10^9)$
Material	Ta	1214	179	22.6±3.1	342	132	7.4±1.5
	Mo	1298	1111	9.9±0.9	367	844	3.2±0.5
	Ideal	1278	170	24.4±3.3	364	103	8.8±1.8
	Air	3527	22530	6.0±0.3	920	13853	2.0±0.2

Table 3: Simulated fluorescence (F) and background (B) counts for 10^{10} incident photons, as well as the corresponding significance values Z for 1.3×10^9 incident photons are listed. An energy interval of $\pm 3\sigma$ is considered for the fluorescence lines K_β and K_γ.

for example, in the most promising gold region K_β the molybdenum collimator increases the significance of the gold signal from 6.0±0.3 to 9.9±0.9 for 1.3×10^9 incident photons, the tantalum collimator even achieves a significance of 22.6±3.1. This is more than twice as high as with molybdenum and nearly as high as when using an ideal collimator, where the significance is 24.4±3.3. This can be explained by the much stronger background with molybdenum, as discussed above, which is more than six times higher in the K_β region. At the same time, the number of detected fluorescence photons hardly differs when using different collimator materials and is only slightly higher for molybdenum, due to its lower absorption efficiency. When tantalum is used, more fluorescence photons are usually detected due to its lower absorption coefficient compared to an ideal absorbing material. This even results in some cases, as with K_{α_1}, where the significance is actually slightly higher than with ideal lamellae, despite the higher background. Nevertheless, surprisingly more fluorescence photons are simulated for ideal lamellae in the K_{α_2} and K_β fluorescence ranges of gold. This cannot be explained physically but is attributed to statistical uncertainties caused by the Monte Carlo simulation (Eq. 3.2).
Overall, even with non-ideal collimators made of molybdenum or tantalum, it is still possible to achieve a significant signal in the K_{α_1} and K_γ ranges for 1.3×10^9 incident photons, which is not the case without a collimator. In addition, the gold peak in the K_β region now exhibits much higher significance, while the K_{α_2} signal remains insignificant for 1.3×10^9 incident photons due to the strong background. Furthermore, tantalum is the most promising material for a collimator in this setup, as it shields the background more effectively than molybdenum in the considered gold fluorescence regions and is therefore associated with higher significance levels.

Analysis of Lamella Thickness Since the previous section established that tantalum appears to be the most suitable absorber material and exhibits properties that are nearly ideal for the setup described in Sec. 6.1.2, the impact of tantalum thickness on this setup is analyzed to determine the optimal lamella configuration. For this purpose, simulations are performed with tantalum thicknesses of 5 μm, 50 μm, 200 μm and 500 μm. The resulting spectra are shown in Fig. 6.7. In contrast to the previously analyzed scenario with 200 μm thick tantalum lamellae, only a single C1 peak remains when using the thicker 500 μm lamellae. This appears at 63.6 keV, where the lower-energy C1 peak of the 200 μm thick lamellae and the C1 peak of ideal lamellae are also located. It is therefore defined

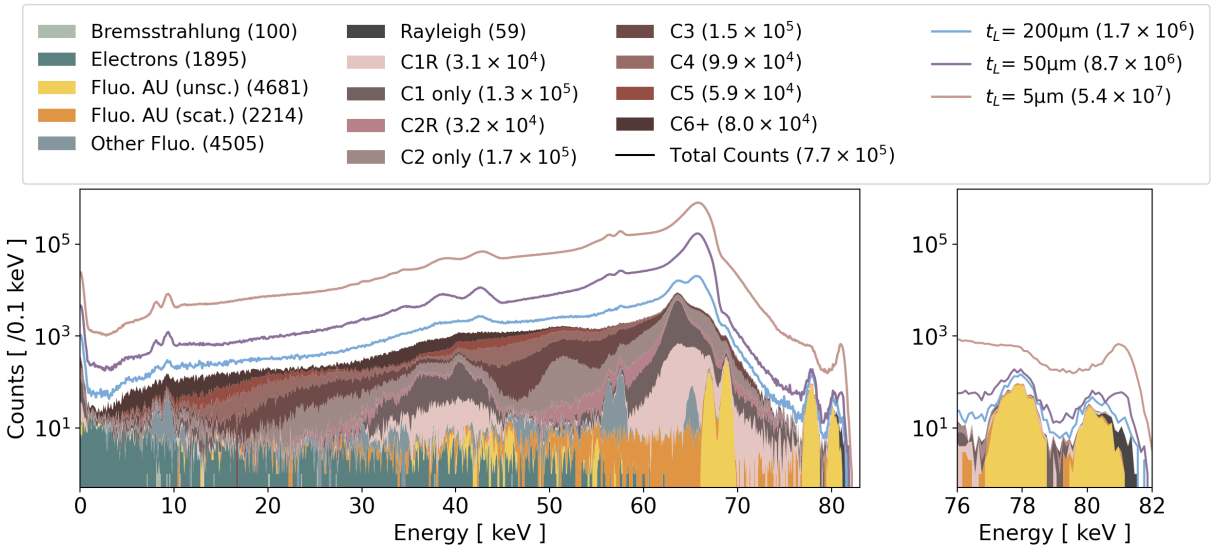

Figure 6.7: The spectrum of the recorded counts when using tantalum as the absorber material with a thickness of $t_L = 500\,\mu$m is compared with spectra for tantalum thicknesses of $t_L = 200\,\mu$m (blue), $t_L = 50\,\mu$m (purple) and $t_L = 5\,\mu$m (beige). $N_0 = 10^{10}$ incident photons are simulated.

by the collimator's design and the corresponding C1 restrictions, as explained in detail earlier. In other words, the lamella is ultimately thick enough to shield most C1 photons outside the gold target. The use of thinner lamellae, on the other hand, results in higher transmission through the lamellae and consequently leads to more detected photons outside the gold target, as can be seen in the spectra when using $50\,\mu$m or $5\,\mu$m. In these cases, the proportion of C1 photons outside the gold target is clearly higher, causing a background peak at 65.7 keV, which corresponds to the higher-energy C1 peak observed with $200\,\mu$m thick lamellae and, hence, also to the peak observed when no collimator is used. This lower absorbing efficiency is also reflected in a higher total count number for thin lamellae. A $5\,\mu$m collimator is linked to 5.4×10^7 detected photons, whereas a thickness of $200\,\mu$m allows only 1.7×10^6 photons to be detected and $500\,\mu$m even only 7.7×10^5 photons. This means that using $500\,\mu$m thick lamellae instead of $5\,\mu$m reduces the number of detected photons by nearly two orders of magnitude.
However, when the shape of the spectra is taken into account, it becomes clear that there is no constant shielding across all energies. It is conspicuous that at energies above 67.4 keV, in particular with $50\,\mu$m thick tantalum lamellae, the number of detected counts decreases more rapidly than with $200\,\mu$m thick lamellae. The reason for this phenomenon is the K-absorption edge of tantalum being at 67.4 keV and the Beer-Lambert law. The K-absorption edge is responsible for the fact that, for energies below the absorption edge, the mass-attenuation coefficient is lower than for energies above this edge, so that the absorption is less efficient at lower energies. At the same time, the Beer-Lambert law describes the number of transmitted photons through an exponential decrease (Sec. 2.1.4) with the mass-attenuation coefficient in the exponent, meaning that the decrease in transmitted photons is not constant for different thicknesses. At a high mass attenuation

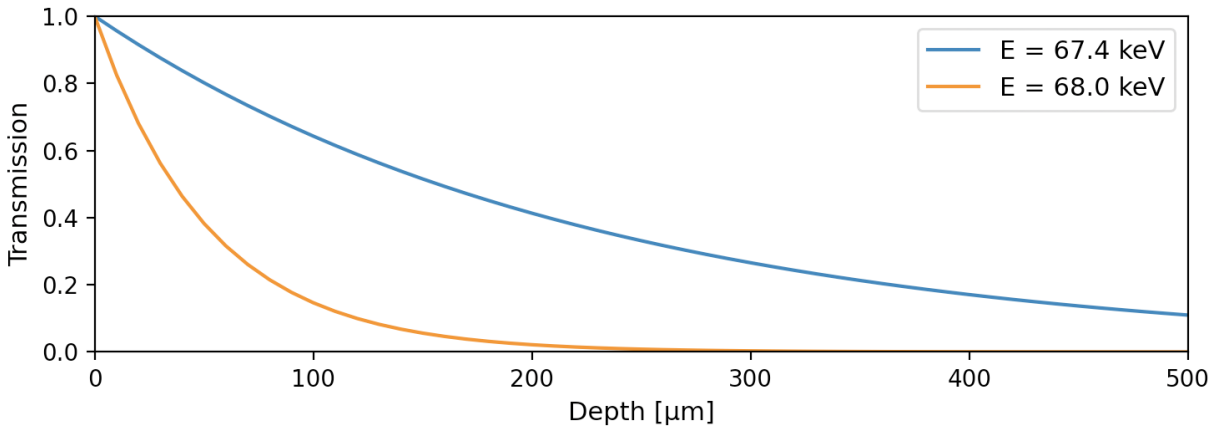

Figure 6.8: The exponential decrease ($e^{-\mu_m \rho_{Ta} d}$) of transmission according to the Beer-Lambert law is plotted for tantalum with a density of $\rho_{Ta} = 16.65\,\mathrm{g/cm^3}$ as a function of depth d for energies of 67.4 keV and 68.0 keV, where these define the mass-attenuation coefficient μ_m.

coefficient, the exponential decline is much steeper, resulting in much lower transmission even at relatively shallow depths. For example, while the transmission for photons with an energy of 68 keV is still 91.3% at a depth of 5 μm, it is already only 38.5% at a depth 50 μm and even only 2.2% at a depth of 200 μm. Since the transmission is already quite low at a thickness of 200 μm, there is hardly any difference in the spectrum between the 200 μm and 500 μm thick lamellae, which both have a transmission of nearly zero. In contrast, for photons with a lower energy of 67.4 keV directly at the K-edge, the decrease in transmitted photons is much smaller. Therefore, a depth of 50 μm is still associated with a transmission of 80.2%, which is more than 40% higher compared to photons with an energy of 68 keV, explaining the pronounced K-absorption edge. At a depth of 5 μm, the K-absorption edge is less pronounced in the spectrum, since the transmission for energies below and above the absorption edge is similar in both cases and still above 90%. It should be noted that the lamella thickness is of course not always equal to the possible transmission depth of the photons. This would only be the case if the photons hit the lamellae perpendicularly. Otherwise, the photons encounter even greater depths, and hence lower transmission occurs. Nevertheless, the transmission values mentioned above, provide a useful indication for understanding the spectra in Fig. 6.7.

As has already become clear in the preceding sections, the K_β gold fluorescence line is most promising, a result that is also confirmed by the spectra shown in Fig. 6.7. In particular, when using 500 μm thick lamellae, the K_β peak appears to be well isolated around 78 keV and stands out clearly from the background. Nevertheless, this lamella thickness is not associated with the most significant signal, as shown in Fig. 6.9. Even though 500 μm thick lamellae clearly yield the lowest background compared to the other thicknesses, the significance of the K_β signal is still lower than when using a thickness of 200 μm due to a lower fluorescence count value. In the simulation involving $N_0 = 10^{10}$ incident photons, only 830 fluorescence photons are detected for 500 μm thick lamellae,

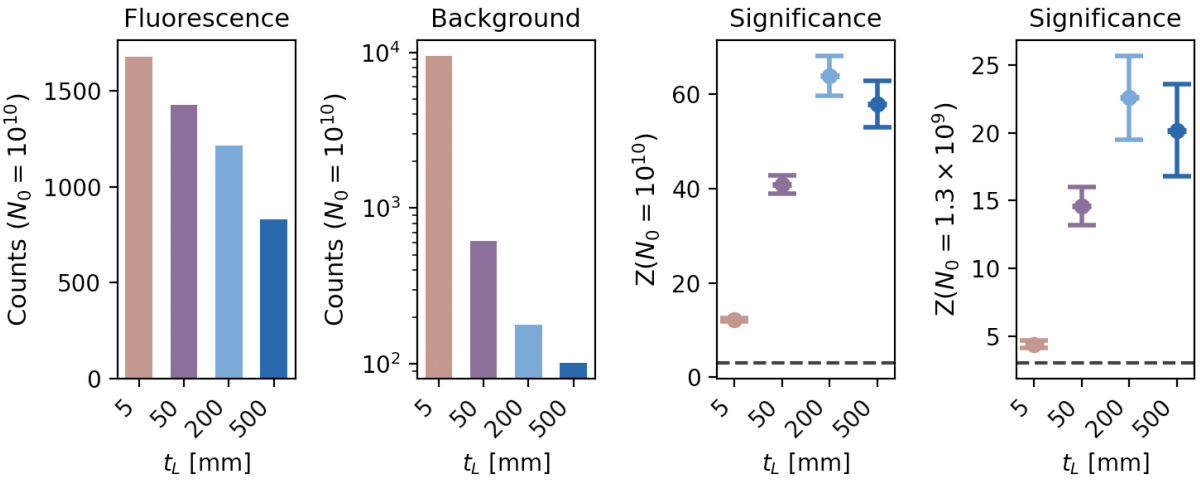

Figure 6.9: Four thicknesses t_L (5 μm (salmon), 50 μm (purple), 200 μm (bright blue), 500 μm (dark blue)) of tantalum lamellae are compared. The leftmost plot shows the simulated fluorescence counts and the second plot the background counts for $N_0 = 10^{10}$ incident photons within the Au-K_β interval. The third plot shows the significance values and their uncertainties based on the fluorescence and background counts shown in the first two plots and the fourth plot shows the estimated significance for $N_0 = 1.3 \times 10^9$ photons. A line at $Z = 3$ has been added, since the signals are considered significant above this value.

whereas 1214 are detected for 200 μm thick lamellae. This is, on the one hand, due to the lower transmission through the thicker lamella material according to the Lambert-Beer law and, on the other hand, due to a smaller effective detector area. The nine vertical lamellae, each 500 μm thick, which together would add up to 4.5 mm, are positioned directly in front of the detector, so that 22.5% of the 20 mm wide detector cannot be used for the detection of fluorescence photons. In comparison, the unusable detector area for 200 μm thick lamellae is only 9%.
However, while thinner lamellae are associated with more fluorescence counts, the background is also stronger. Therefore, thicknesses below 200 μm are not recommended for achieving high significance, even if the signals are significant in all cases with $Z > 3$ (Fig. 6.7). Finally, for 200 μm thick lamellae, a significance of 63.9±4.2 can be achieved for the 10^{10} simulated incident photons, which corresponds to a significance of $Z = 22.6 \pm 3.1$ with 1.3×10^9 incident photons for an acceptable dose. Therefore, lamellae made of tantalum with a thickness of 200 μm are considered the best realistic lamellae configuration and are selected for the following analyses.

6.1.5 Spatial Resolution

In XFI, spatial resolution can be distinguished between a longitudinal and a transverse component. As the name implies, the transverse spatial resolution describes the spatial resolution in the plane perpendicular to the incident beam, the xy-plane. This transverse component is defined by the diameter of the incident beam, which is 1 mm in the anal-

ysis scenario (Sec. 6.1.2). In contrast, the longitudinal component describes the spatial resolution along the beam axis. Common tools for restricting the beam axis and thus for obtaining information about the longitudinal origin of the photons are hole collimators placed between the beam and the detector [92, 110, 111]. In the analyzing setup described in Sec. 6.1.2, a collimator with nine vertical lamellae is used instead, whose primary function is to suppress a large part of the background while simultaneously restricting the possible origins of the photons. To determine the longitudinal spatial resolution provided by this collimator, the FOV of the detector is analyzed.
This is done by moving a gold target along the z-axis, the beam axis, to determine the number of detected fluorescence photons with and without the collimator, followed by determining the proportion of fluorescence photons that passed through the collimator without any interaction. This fraction is referred to as the collimator transmission T_C hereafter. The collimator used is the design described in Sec. 6.1.1 and Sec. 6.1.2, with 200 μm thick lamellae, focused on a 10 mm long section of the beam axis between $z = -70$ mm and $z = -80$ mm. This means that, due to the collimator's design, no photons are expected to be detected outside this interval along the beam axis. In order to obtain the photon distribution detected in this interval with a finer accuracy than only 10 mm, in accordance with the previously used gold target length (Sec. 6.1.2), a smaller gold target with an actual length of 0.5 mm is chosen instead and shifted by this length along the beam axis. Meanwhile, the collimator focus is maintained on the beam axis between $z = -70$ mm and $z = -80$ mm. This is analyzed in a vacuum environment in which the human-sized cylinder is removed to eliminate other superimposed effects such as scattering outside the gold target and thus determine only the effect of the collimator. The detector position at 150° and all other components of the setup remain as described in Sec. 6.1.2. Finally, the FOV is determined using Geant4 simulations, taking into account the recorded counts for tantalum lamellae to ensure a more realistic scenario, as well as the true counts for ideal lamellae, in order to avoid effects from the detector and the lamellae material that could distort the FOV. On the other hand, it is also modeled using the numerical model (Secs. 3.3.1 and 3.3.4), in which the lamellae and the detector are assumed to be ideal absorbers. For this, a step size of $d_z = 0.05$ mm along the gold target is used and a step size of $d_{Det} = 0.05$ mm for the detector pixelation, which is a compromise between a sufficiently high spatial resolution for the modeling and a reasonable computational time.
The modeled and simulated FOVs, particularly for the ideal absorber taking into account the true counts without detector effects, agree well for unscattered gold fluorescence photons within the K_β signal range, as can be seen in Fig. 6.10. There are only minor differences, which are most likely attributable to statistical fluctuations in the Geant4 simulations (Eq. 3.2) and to the resolution chosen in the numerical model (Sec. 4.2). In the simulation of tantalum lamellae, however, the proportion of detected unscattered fluorescence counts is slightly higher, since tantalum, unlike ideal lamellae, has a non-zero transmission. As shown in Fig. 6.10, no photons are detected outside the expected range between $z = -70.0$ mm and $z = -80.0$ mm. Therefore, the collimator's design successfully shields photons on the beam axis outside this focused section. However, this also reveals that photons within this section are partially shielded, since the collimator

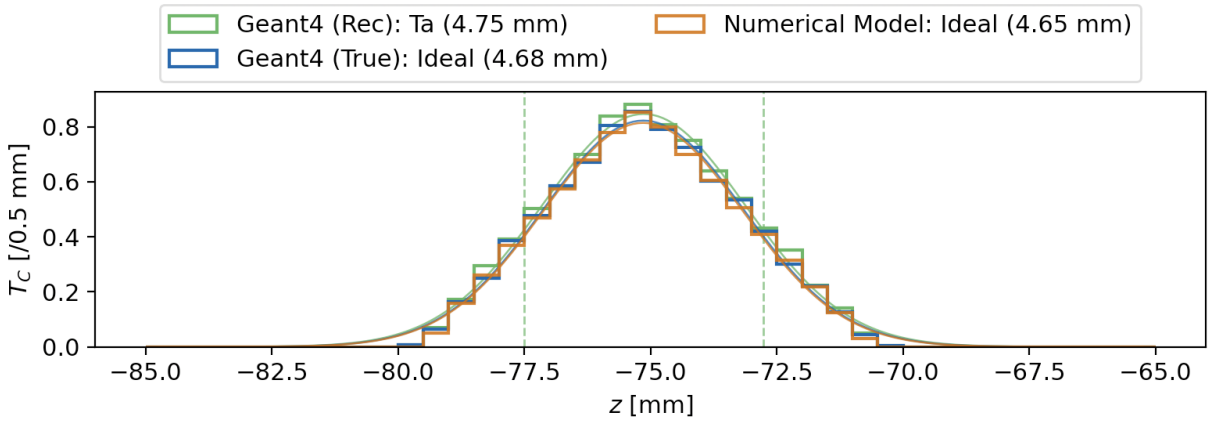

Figure 6.10: The collimator transmission values T_C for the detected, unscattered fluorescence photons, when using a collimator that focuses a 10.0 mm section of the beam axis between −80.0 mm and −70.0 mm, are plotted as a function of z, representing the FOV. Results from the numerical model are shown in orange, while Geant4 simulations distinguish between tantalum lamellae with recorded counts (green) and ideal lamellae with true counts (blue). A fitted Gaussian curve is included for each case, from which the FWHM is determined and indicated in brackets. For the recorded tantalum lamellae scenario, the FWHM boundaries are indicated as green dotted lines.

transmission is less than one. This means that, due to the design, the collimator is associated not only with the shielding of photons outside the focused beam-axis section, but also with a loss of the desired fluorescence signal counts. More precisely, the collimator transmission is roughly 60% across all target positions within the 10 mm long focus range. In particular, at the boundaries close to $z = -80.0$ mm and $z = -70.0$ mm, the loss of fluorescence photons due to the collimator is high, since more photons collide with the lamellae. For example, for a gold target between $z = -79.5$ mm and $z = -79.0$ mm, only about 5-7% of the fluorescence photons can be detected. In contrast, for a gold target located near the center between $z = -75.5$ mm and $z = -75.0$ mm, more than 85% of the fluorescence photons are detected, meaning that less than 15% of the photon paths collide with the collimator. As a consequence, the FOV distribution within the beam section accepted by the collimator between $z = -80.0$ mm and $z = -70.0$ mm can be well described by a Gaussian curve, yielding a full width at half maximum (FWHM) of approximately 4.7 mm for ideal lamellae and a slightly higher value when using tantalum lamellae. This is due to the higher transmission and thus higher detected fluorescence fraction for tantalum.

Finally, these collimator transmission distributions show that, as expected, all photons outside the focus section are blocked by the collimator. However, even fluorescence photons within this interval are partially collimated with a spatial resolution defined by the FWHM of about 4.7 mm. Note that this collimator transmission applies not only to unscattered fluorescence photons, but to all photons originating from the beam axis and then following a path toward the detector, such as the C1 photons. Thus, the determined FOV confirms that no C1 photons scattered outside the target reach the detector.

6.1.6 FOV and Sensitivity for Different Gold Target Positions

After analyzing the effect of the collimator for a gold target located between −80 mm and −70 mm on the z-axis, the effect of the collimator is analyzed for different depths of the 10 mm long gold target with a concentration of 1.0 mg/ml. A different target position is also associated with a different detector and lamella orientation. This results in different required lamellae lengths, which are determined by the principle described in Sec. 6.1.1. However, as the distance to the target increases, so do the necessary lamellae lengths. This is problematic for target positions with $z_{Au} > -50$ mm since the required lamellae to shield all C1 photons outside the beam axis would extend into the cylinder object. Consequently, the lamellae are shortened. Specifically, the length is reduced to 85%, 72% and 62% of the theoretically required length for target positions of $z_{Au} = -50$ mm, −25 mm and 0 mm.
As shown in Fig. 6.11 for the Au-K_β energy range of the gold target, a different target position and collimator orientation is associated with different detected count values for the background and fluorescence. The count value of the detected fluorescence photons

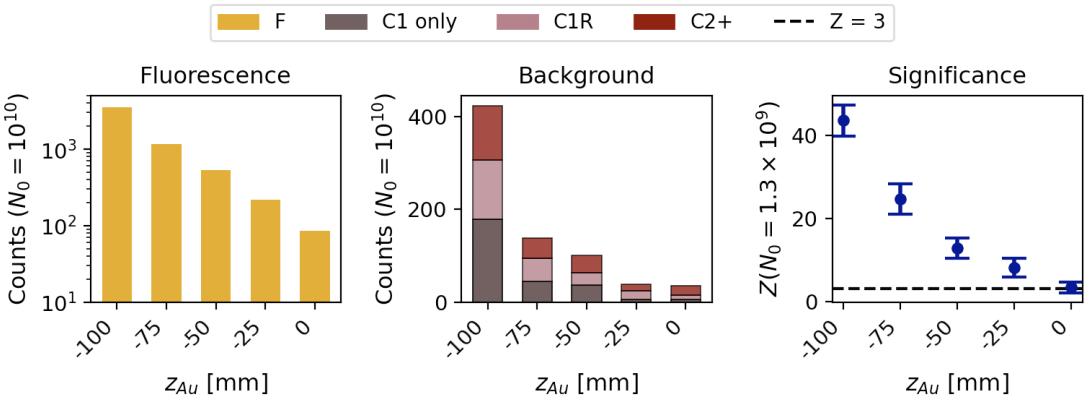

Figure 6.11: The simulated recorded fluorescence counts (gold) are shown on the left, the background counts (C1 only (brown), C1R (pink), C2+ (red)) in the center, and the significance Z (blue) on the right, for different target positions z_{Au} along the z-axis for a gold target of 10 mm length and concentration of 1.0 mg/ml. Fluorescence and background counts are shown for $N_0 = 10^{10}$ incident photons, while the significance is shown for $N_0 = 1.3 \times 10^9$ incident photons in the Au-K_β signal range.

is much higher for targets located at shallow depths, thus low z_{Au} values, than for targets located deeper in the object. Therefore, the detected fluorescence counts for a target at a depth of 50 mm and $z_{Au} = -100$ mm are almost seven times higher than for a target at a depth of 100 mm, corresponding to $z_{Au} = -50$ mm, where the collimator is also oriented. The higher number of detected fluorescence counts at lower depths is primarily caused by two factors: lower attenuation due to shorter path lengths from the beam to the target and then to the detector, and the larger solid angles of the detector due to the shorter distance from the target to the detector. For example, the photon path to the detector center with a generated fluorescence photon at $z = -100$ mm has a numerically modeled solid angle of $G = 0.0029$ (Eq. 3.15) and a transmission of about $T_{in} \cdot T_{out} = 0.1161$ based

on a path length of $r_{in}+r_{out} = 197\,\text{mm}$ (Eq. 3.12 and 3.14). Meanwhile, for a path with a generated fluorescence photon at $z_{Au} = -50\,\text{mm}$, the numerically modeled transmission is only about $T_{in} \cdot T_{out} = 0.0204$, based on a longer path length of $r_{in}+r_{out} = 283\,\text{mm}$, and the solid angle is additionally only $G = 0.0019$. However, according to these modeled factors, even fewer counts would be expected to be detected for a gold target at $z_{Au} = -50\,\text{mm}$. This can be explained by taking the FOVs into account.
Fig. 6.12 shows the FOV and corresponding FWHM for five different collimator orientations $z_{L,F}$, each corresponding to a 10 mm gold target at that position. However, to

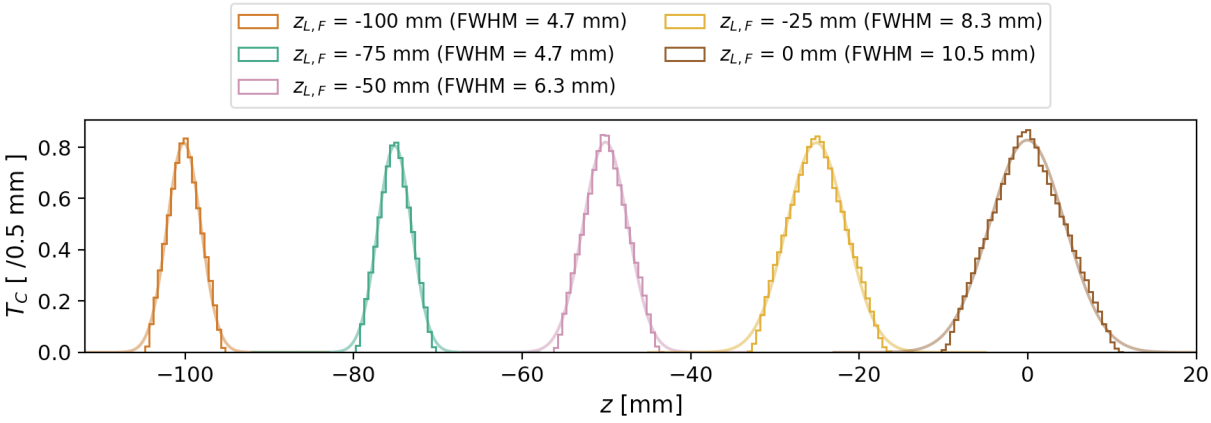

Figure 6.12: The collimator transmission T_C, indicating the FOV, is shown for five different collimator focus positions $z_{L,F}$: −100 mm (orange), −75 mm (green), −50 mm (pink), −25 mm (yellow), 0 mm (brown). A 0.5 mm long gold target is simulated and shifted along the z-axis to determine the transmission. The FWHM of the fitted Gaussian curves is indicated in the brackets.

determine the FOV, a gold target size of only 0.5 mm is simulated and shifted along the z-axis, while the collimator orientation is kept fixed for each scenario ($z_{L,F} = -100\,\text{mm}$, $-75\,\text{mm}$, $-50\,\text{mm}$, $-25\,\text{mm}$, $0\,\text{mm}$). The FOVs show that, for a collimator oriented to $z_{L,F} = -50\,\text{mm}$, the FWHM is 6.3 mm, and the maximum collimator transmission T_C= 0.849, which is larger than for a collimator oriented to $z_{L,F} = -100\,\text{mm}$. The latter only has an FWHM of 4.7 mm and $T_C = 0.835$, thus counteracting the transmission and solid angle factor. The larger FWHM is caused by the shortened lamellae for deep focus positions, starting from values larger or equal to $z_{L,F} = -50\,\text{mm}$, to prevent lamellae from extending into the cylindrical human-sized object. This also explains why the FWHM is identical for $z_{L,F} = -100\,\text{mm}$ and $z_{L,F} = -75\,\text{mm}$, but increases for deeper target positions, where the proportion of the required lamella length decreases, as described above. Consequently, the collimator transmission T_C due to the collimator design counteracts the decreasing transmission, $T_{in} \cdot T_{out}$, through the object and the world more strongly. However, the collimator transmission factor has a weaker effect on the detected fluorescence counts than the other factors since the fluorescence counts still decrease for the deeper simulated target positions with higher z_{Au} values. Therefore, a larger FOV at deeper target depths is beneficial for counteracting fluorescence loss, which would otherwise be associated with even more loss at a smaller FOV.

In contrast to the fluorescence counts, the background does not originate only from a 10 mm target section but from the entire beam axis for C1 photons and from the entire cylinder when experiencing additional Rayleigh scattering (C1R) or additional Compton scatterings (C2+). As shown in Fig. 6.11, the background exhibits a notable decline at deeper positions within the object, attributable to the previously mentioned reasons (solid angle, transmission). However, starting from the point at which the lamellae lengths are shorter than required, the larger FOV enables the detection of background photons from a larger region. This finally results in an almost identical background for the cases $z_{Au} = -25\,\text{mm}$ and $z_{Au} = 0\,\text{mm}$.
Overall, the background count values are low for these deep positions, as are the detected fluorescence count values, resulting in lower significance for deeper target positions due to the low fluorescence counts detected. Therefore, at $z_{Au} = 0\,\text{mm}$, the signal in the K_β range is insignificant for 1.3×10^9 incident photons. However, with a gold concentration of 1.360 mg/ml instead of 1.0 mg/ml, a significance of $Z = 4.5\pm1.5$ of the signal would be expected according to Tab. 4, which lists the minimum concentrations for the different target locations. In contrast, a target located at $z_{Au} = -25\,\text{mm}$ is already associated with

Setup	c_{min} [mg/ml] for z_{Au} [mm]				
	-100	-75	-50	-25	0
vertical lamellae	0.085	0.161	0.316	0.713	1.360
no collimator	0.194	0.538	1.466	3.986	>5

Table 4: The minimum detectable gold concentration c_{min} is shown for different target positions z_{Au} and a 150° detector, both with and without the Vertical-Lamellae Collimator. Here, 10^{10} incident photons are simulated with a gold concentration of 5.0 mg/ml and scaled to 1.3×10^9 incident photons. The minimum detectable concentration is determined as the concentration at which the significance of the simulated recorded counts fulfills Eq. 3.6.

a significant gold signal, $Z = 8.1\pm2.3$, for 1.3×10^9 incident photons. This is much greater than the insignificant signal of $Z = 0.8\pm0.1$ obtained when no collimator is used (Fig. 5.6), and it corresponds to a minimum detectable gold concentration of 0.713 mg/ml. The highest significances and thus the lowest minimum detectable gold concentration are achieved when the target is positioned close to the beam source, such as at $z_{Au} = -100\,\text{mm}$. In this case, a significance of $Z = 43.6\pm3.8$ is expected for 1.3×10^9 incident photons, which is much higher than $Z = 16.6\pm0.5$ without a collimator (Fig. 5.6). Therefore, only a gold concentration of 0.085 mg/ml is sufficient. Nevertheless, the collimation is more efficient for higher values of the target position, as there the minimum detectable concentration is reduced by a greater factor. For example, at $z_{Au} = -100\,\text{mm}$, the minimum concentration required for detection without the collimator is 2.2 times higher, whereas at $z_{Au} = -25\,\text{mm}$, it is 5.6 times higher. This is due to the large background at low depths, which is less collimated when the target is also located there.

6.2 Horizontal-Lamellae Collimator

Another collimator configuration consists of lamellae that are oriented horizontally instead of vertically with respect to the xz-beam plane, aiming to increase the sensitivity. In the following, this "Horizontal-Lamellae Collimator" is considered at a detector angle of 150° and 180°. At an angle of 180°, more fluorescence photons are expected to be detected from targets located not deeper than the center of the object (Fig. 5.3).

6.2.1 Principle and Setup of the Collimator with Horizontal Lamellae

In the Horizontal-Lamellae Collimator, the lamellae focus on the target. More precisely, they are aligned radially along the fluorescence paths to reduce the number of fluorescence photons being absorbed by the collimator (Fig. 6.13). Moreover, a vertical lamella

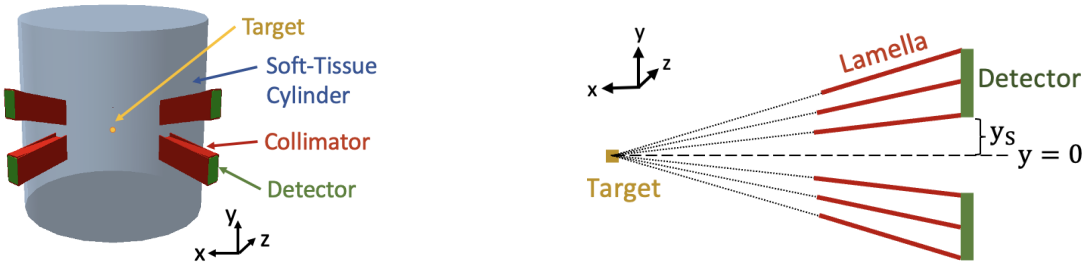

(a) (b)

Figure 6.13: (a) A soft-tissue cylinder (blue) with detectors (green) at α_D=150° and shifted in y-direction is shown, with a collimator attached in front of them. Note that the target is shown larger than its actual size relative to the water cylinder for visibility. (b) Schematic principle of the horizontal lamellae: The horizontal lamellae (red) start at the detector (green), which is divided and shifted by the component y_S out of the beam plane and converge along the fluorescence paths (thin, dotted black lines) towards the gold target (gold).

is added to each side of the detector along the horizontal lamellae to further restrict the origin of the detectable photons, thereby creating a kind of collimator housing. Based on the results from Sec. 6.1.4, all lamellae are made of tantalum and are 20.0 mm wide, corresponding to the width of the detector. The inner horizontal lamellae are designed to be 0.2 mm thick, while the outer lamellae and side lamellae are 2.0 mm thick to maximize shielding of photons outside the fluorescence target. The detector is divided in height and shifted out of the beam plane by y_S along the y-direction (Fig. 6.13). This means that the detector area of $20 \times 60\,\mathrm{mm}^2$ is divided into two $20 \times 30\,\mathrm{mm}^2$ detectors. This splitting is necessary to restrict the FOV, as will be analyzed in the next sections, and to enable detection by a detector located at 180°. Additionally, the number and length of the horizontal lamellae are varied and analyzed below, since unlike in the previous collimator design with vertical lamellae, the length of the lamellae is no longer limited by specific conditions in this collimator design. For the analysis, the distance between the horizontal lamellae at the detector remains constant.

For the following analysis of the Horizontal-Lamellae Collimator, the same setup as described in Sec. 6.1.2 is used unless otherwise specified. The only modifications are the replacement of the collimator with the Horizontal-Lamellae Collimator and the separation of the detector by a shift of y_S.

6.2.2 Field-of-View Volumes

To analyze the impact of different collimator configurations, such as the length or the number of the lamellae, the FOV volumes restricted by the collimator can be used to gain information for different scenarios. The FOV volumes consist of a horizontal FOV area component in the xz-plane that specifies the width of the volume and a vertical FOV area component that specifies the height. The FOV is defined by the most oblique trajectories that can still be detected without colliding with the collimator. More precisely, it is defined by the paths extending from the back edge of a lamella at the detector to the front edge of the neighboring lamella. This is illustrated schematically in Fig. 6.14 for the horizontal FOV due to the parallel vertical lamellae. On the other hand, the height of

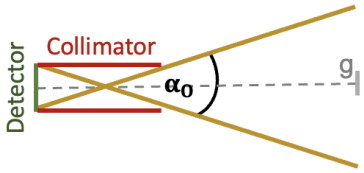

Figure 6.14: The FOV extends from the detector (green) along the detector normal to a length g and is defined by the opening angle α_O. The opening angle is defined as the angle between the two extreme photon paths (gold) that can reach the detector without hitting the collimator (red).

the vertical FOV area is determined by the vertical opening angle $\alpha_{O,H}$ in height, due to the maximum possible paths that are restricted by the horizontal lamellae. Finally, the projected FOV areas, A_C, for the horizontal and the vertical components, extended to a length of g, are provided by the opening angle α_O:

$$A_C = g^2 \tan\left(\frac{\alpha_O}{2}\right). \tag{6.1}$$

The total FOV volume V is calculated based on the assumption that its shape corresponds to a pyramid with a rectangular base G, whose width W and height H are determined by the opening angles and a FOV length g, which corresponds to the height of the pyramid:

$$V = \frac{1}{3} gHW \quad \text{with} \quad W = 2g \tan\left(\frac{\alpha_{O,W}}{2}\right),\ H = 2g \tan\left(\frac{\alpha_{O,H}}{2}\right). \tag{6.2}$$

The FOV of different collimator configurations can additionally be analyzed with respect to the collimator transmission T_C along the z-axis. In this context, the collimator transmission is modeled numerically and describes the fraction of photon paths that originate from the 1 mm long beam intersection and reach the detector without hitting the

collimator, compared to the number of detected photon paths when the collimator is not used. In the numerical model, possible paths begin within the 1 mm long beam section with a distance of $d_z = 0.2\,\text{mm}$ and end at the detector area, which pixelated with a pixel distance of $d_{Det} = 0.2\,\text{mm}$. The advantage of the numerical model is that it avoids the statistical uncertainties that may occur in Geant4. Furthermore, Geant4 is associated with longer computing times for FOV determination. For example, a step size of 1 mm along the beam axis results in 300 target positions that must be simulated, which quickly sums up to a long computation time when 10^{10} incident photons are simulated per position.

6.2.3 Impact of the Detector Displacement Outside the Beam Plane

The collimator with vertical lamellae aims to detect only photons originating from the 10 mm long fluorescence target, which, for the setup considered in Sec. 6.1.6, is possible for target depths lower than $-100\,\text{mm}$ ($z_{Au} < -50\,\text{mm}$). For targets with greater depths, the FOV along the beam increases up to a FWHM of 10.5 mm, where the collimator focuses on a target at $z = 0\,\text{mm}$. However, when using a collimator with only horizontal lamellae, photons from the entire beam axis would be detected without side lamellae for a detector in the beam plane ($y = 0\,\text{mm}$). Even with two vertical lamellae attached to the detector sides, the FOV along the z-axis, defined by the most oblique detectable paths without hitting the collimator, is expected to be larger. This is due to the greater spacing between the vertical lamellae corresponding to the detector width. However, a larger FOV along the z-axis is associated with a larger range of origins for background photons, particularly C1 photons, which originate from the z-axis. This may result in lower significant signals because a large fraction of the background in the Au-K_β signal range of gold is composed of the high-energy C1 photons, as discussed in Sec. 5.3.
To counteract this, the detector is divided, and each half's edges are shifted out of the beam plane by a component of y_S, as described in Sec. 6.2.1. The impact of shifting the detector, and thereby the Horizontal-Lamellae Collimator, is analyzed for a detector angle of $\alpha_D = \pm 150°$ relative to the incident beam, as in the scenario with the Vertical-Lamellae Collimator. The considered Horizontal-Lamellae Collimator consists of seven horizontal lamellae and two vertical side lamellae, each with a length of 70 mm, similar to the Vertical-Lamellae Collimator. A minimal shift of $y_S = 2\,\text{mm}$ is chosen to ensure that when this collimator is used for a detector angle of 180°, the distance between the incident beam and the detector is large enough to prevent the incident beam from colliding with the detector before entering the object to be imaged. This is because both the beam source and the detector are located at 180°.
The scenario is simulated with Geant4 to include Doppler broadening responsible for the background in the K_β signal range of gold. The simulated fluorescence and background photons, as well as the significances within the Au-K_β signal range of a 10 mm long gold target located at $z_{Au} = -75\,\text{mm}$ are shown in Fig. 6.15 for different detector offsets y_S. For this analysis, the simulated true counts are used to exclude distortions caused by detector effects and to isolate the impact of the collimator. The number of detected fluorescence photons decreases differently with a larger offset y_S than the background does. This behavior can be explained by taking the visualized FOV volumes into account, as shown in Fig. 6.16 for a length of $g = 220\,\text{mm}$.

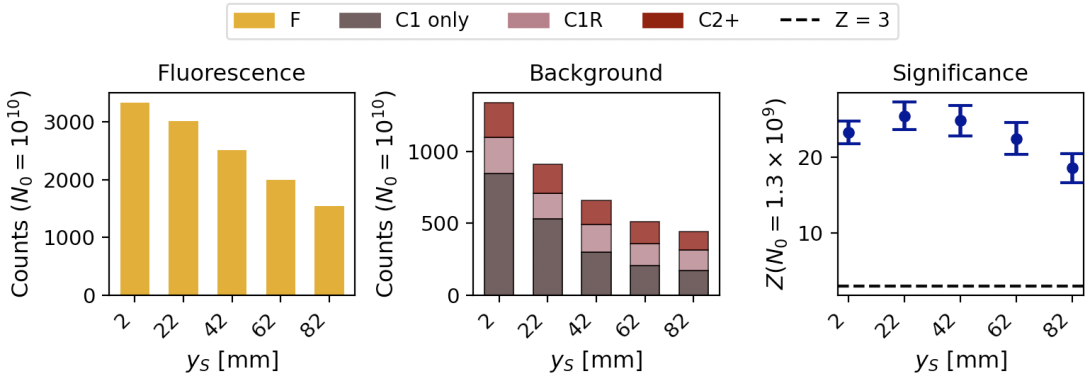

Figure 6.15: The simulated true fluorescence counts (gold) are shown on the left, the background counts (C1 only (brown), C1R (pink), C2+ (red)) in the center, and the significance Z (blue) on the right, for different detector shifts y_S for a collimator focused on $z_{Au} = -75\,\text{mm}$ on the z-axis. Fluorescence and background counts are shown for $N_0 = 10^{10}$ incident photons, while the significance is shown for $N_0 = 1.3 \times 10^9$ incident photons in the Au-K_β signal range, where the minimum significance of Z = 3 for a detectable signal is indicated by the black dashed line.

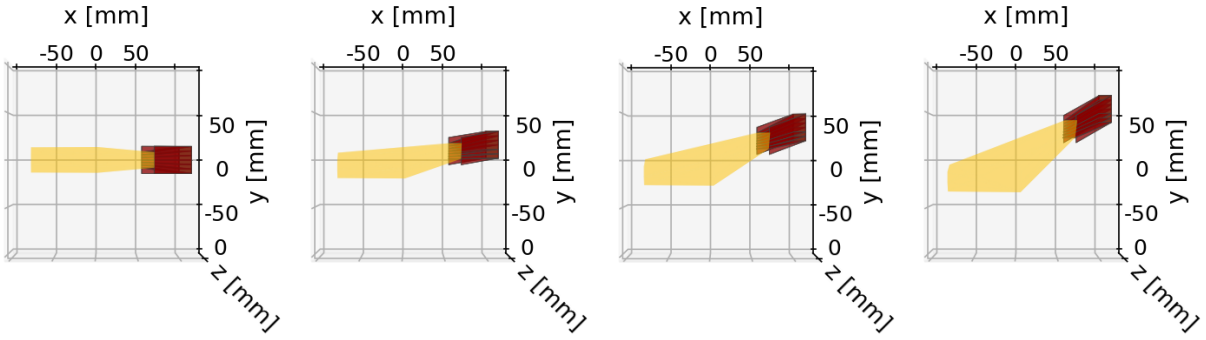

(a) $y_S = -15\,\text{mm}$ (b) $y_S = 2\,\text{mm}$ (c) $y_S = 22\,\text{mm}$ (d) $y_S = 42\,\text{mm}$

Figure 6.16: The FOV volumes (yellow), with a length of $g = 220\,\text{mm}$, are shown for different shifts y_S of the collimator (red). The z-axis is oriented out of the plane and points toward the observer.

For a detector with its center in the beam plane ($y_S = -15\,\text{mm}$), the vertical FOV component covers $y = 0\,\text{mm}$ for all FOV lengths g symmetrically. However, shifting the detector out of the beam plane results in a tilt of the FOV volume with respect to the xz-beam plane. This tilt increases with larger shifts and is associated with smaller intersections with the xz-beam plane and the z-axis, from which the fluorescence counts and single Compton-scattered photons originate, as shown in Fig. 6.17a. The intersections of the FOV volumes in the xz-beam plane show that the FOVs differ only in length along g for different detector shifts. Meanwhile, the horizontal opening angle $\alpha_{O,W} = 33.5°$ defining the width, stays constant for all variations of the shift. If the detector is shifted

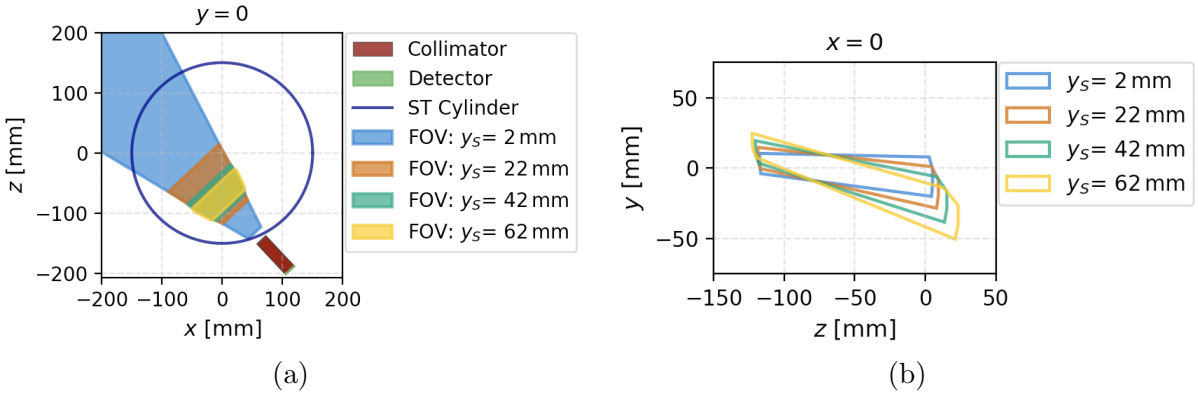

(a) (b)

Figure 6.17: The intersections of the FOV in the xz-beam plane at $y = 0$ (a) and in the yz-beam plane at $x = 0$ (b) are shown for different collimator shift values y_S. The edge of the soft-tissue (ST) cylinder is indicated by the blue circle.

out of the beam plane to $y_S = 2\,\text{mm}$, the FOV in the xz-beam plane within the soft-tissue cylinder, is restricted almost solely by the width opening angle and only a small length section directly in front of the detector remains uncovered. However, increasing the value of y_S results in a reduction in the FOV length within the xz-beam plane due to the steeper tilt of the FOV volumes, so that smaller areas of the object are captured from $y = 0$. In particular, when the detector is shifted from $y_S = 2\,\text{mm}$ to $y_S = 22\,\text{mm}$, the FOV covers a much smaller area of the object. As a consequence, fewer photons from the xz-beam plane are detected. In contrast, the FOV area in the yz-beam plane changes less significantly with increasing the detector shift (Fig. 6.17b). There, the detector shift is reflected in the FOV areas that appear to be rotated around (0, 0, -75) mm, causing the FOV regions to become more asymmetric with respect to the z-axis. Responsible for this phenomenon is the combination of the increased tilt of the FOV volume relative to the xz-plane at larger detector offsets and the varying distance along the z-axis to the detector, since the detector and the collimator are not aligned orthogonally to the z-axis. Accordingly, the yz-beam plane intersects the FOV volume at different extension lengths g, meaning that at positions closer to the detector, such as small z-values on the beam axis, the height is lower than at larger z-values, which are further away from the detector and have greater lengths g. While the opening angle in the height $\alpha_{O,H}$ remains nearly constant (decreasing only from 6.1° to 6.0° when the detector is moved from $y_S = 2\,\text{mm}$ to 42 mm), the tilt of the FOV with respect to the xz-beam plane increases (Fig. 6.16). Consequently, at shorter distances, such as for smaller z-values on the z-axis, the FOV is less extended. Thus, for a detector with $y_S > 0$, the y-component of the FOV has to be larger than it would be at a longer distance to the detector, such as for larger z-values on the beam axis. This explains the "FOV rotating effect" in the yz-beam plane when the detector is shifted and has as the effect of further restricting the FOV along the z-axis when the detector shift exceeds a certain value, in this case $y_S > 22\,\text{mm}$.
The FOVs visualized so far only consider the most oblique possible paths. Based on these FOVs, only the loss of the multiple scattered background, not the loss of fluorescence photons or C1 photons for detector shifts up to $y_S > 22\,\text{mm}$, could be explained, where

the FOV covers smaller areas of the object in the beam plane, but not smaller z-sections. Therefore, the collimator transmissions along the beam axis are determined using the numerical model and are shown in Fig. 6.18. There, the collimator attached in front of the detector focuses to $z_{L,F} = -75\,\text{mm}$, corresponding to the Geant4-simulated target location. Unlike with the Vertical-Lamellae Collimator, it is noticeable that with the

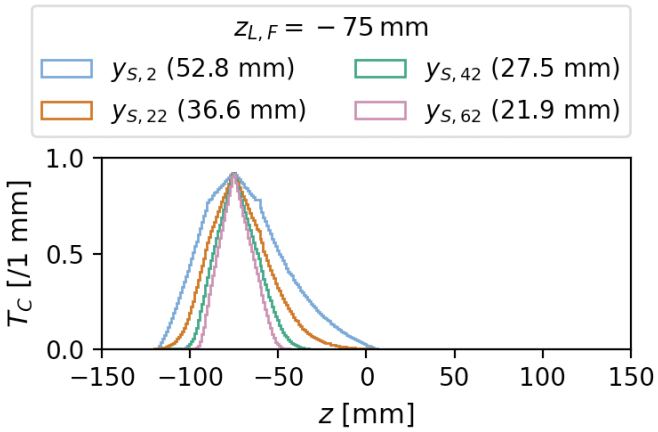

Figure 6.18: The modeled collimator transmission T_C along the z-axis is shown for different collimator shifts y_S, where the number in the index corresponds to the shift along the y-axis in millimeters. The FWHM values of the collimator transmission distribution are indicated in brackets and the collimator is focused on $z_{L,F}$ on the z-axis.

Horizontal-Lamellae Collimator, consisting of seven horizontal lamellae, the detectable beam volume is larger than the target length of 10 mm, depending on the shift of the detector. Since the collimator transmission T_C is not uniformly distributed across the maximum detectable z-section and only a few photon paths are detectable in the tail regions, the FWHM is a more reasonable way to describe the FOV of the detector. Shifting the detector out of the beam plane reduces the FWHM from 52.8 mm for an offset of $y_S = 2\,\text{mm}$ to 27.5 mm for $y_S = 42\,\text{mm}$. This means that more photon paths from the incident beam collide with the collimator and are absorbed due to the geometric change caused by the detector shift. Independent of the detector offset, a transmission of up to $T_C = 92\%$ can be achieved when the origin of the fluorescence photons z_{Au} equals the lamella focus $z_{L,F}$ on the beam axis at $z = -75\,\text{mm}$. The radially aligned lamellae, focused on $z_{L,F} = -75\,\text{mm}$ on the z-axis, achieve this high transmission value since their orientation corresponds to the fluorescence paths originating from z_{Au}=−75 mm, resulting in rare collisions. However, since the lamellae are not infinitely thin, but instead have a thickness of 0.2 mm, the effective detector area is reduced by the horizontal lamellae to 96% and a few paths strike along some lamellae expansions, explaining the transmission being lower than 100% at the lamellae focus. For photon paths originating from the beam axis farther from $z = -75\,\text{mm}$, more photon paths collide with the collimator as a consequence of being farther from the lamella focus and the collimator transmission T_C decreases.
Different strong slopes appear in the collimator transmission distributions, especially for a detector offset $y_S = 2\,\text{mm}$. This causes edges at around $z_{Au} = -90\,\text{mm}$ and $z_{Au} = -60\,\text{mm}$.

Regarding the numerical model, this interval corresponds to the beam section where only the horizontal lamellae are collimating, not the vertical side lamellae, so the collimation is weaker. It is also worth mentioning that the FOV curves appear asymmetrical, with a longer tail for larger depths associated with higher z_{Au} values. This can be explained by the detector's non-symmetrical alignment to the beam axis.These two phenomena, however, are less prominent for a larger detector offset, since the FOV curves become sharper due to the shift.
The average collimator transmission over all paths along the beam volume within the object is $T_C = 0.172$ for a detector shift of $y_S = 2\,\text{mm}$, $T_C = 0.119$ for $y_S = 22\,\text{mm}$ and $T_C = 0.085$ for $y_S = 42\,\text{mm}$, while the collimator transmission is considered to be $T_C = 1.000$ in the absence of a collimator. Thus, shifting the detector by 20 mm from $y_S = 2\,\text{mm}$ to $y_S = 22\,\text{mm}$ reduces the collimator transmission by 30.8%, whereas another shift from $y_S = 22\,\text{mm}$ to $y_S = 42\,\text{mm}$ would reduce the collimator transmission by 28.5% for photons originating from the beam axis.
A similar loss, but slightly larger than the average collimator transmission, of 37.4% in the "C1 only" counts is simulated for a shift from $y_S = 2\,\text{mm}$ to $y_S = 22\,\text{mm}$ (Fig. 6.15). This discrepancy can be attributed to the fact that the collimator transmission T_C only describes the fraction of paths which is not collimated. The actual number of detected photons also depends on the transmissions T_{in} and T_{out}, the Compton yield, the projection and the solid angle of the detector. Finally, shifting the detector further away from the beam plane increases the path length of the photons, as they must traverse an additional distance outside the beam plane. This is associated with lower transmissions T_{out} from the Compton event to the detector, as well as a lower projection and smaller solid angle of the detector, which explains a further reduction in detected background counts. For instance, the solid angle decreases by about 3.8% for paths going from $z = z_{L,F} = -75\,\text{mm}$ to the detector center when the detector is shifted from $y_S = 2\,\text{mm}$ to $y_S = 22\,\text{mm}$. Meanwhile, the projection decreases by about 1.9% (Eq. 3.15, 3.16). Additionally, the inhomogeneous photon distribution without a collimator along the z-axis results in more counts at small depths due to the solid angle. Therefore, reducing the collimator transmission at low z-values is linked with a larger fraction of collimated photons.
Along with the C1 photons, the background includes C1R and C2+ photons, as shown in Fig. 6.15. However, these background counts are less reduced for larger detector offsets, as demonstrated by the increased fraction of multiple-scattered background relative to the "C1 only" counts. This is because they can originate from the entire FOV and not only the z-axis. In contrast to the FOV section on the z-axis, the FOV volume in the cylinder barely changes. As previously mentioned, the horizontal opening angle remains constant and the vertical opening angle changes only slightly. While the vertical opening angle has a value of $\alpha_{O,H} = 6.1°$ for $y_S = 2\,\text{mm}$, it has a value of $\alpha_{O,H} = 5.6°$ for $y_S = 62\,\text{mm}$ and decreases only due to the farther position of the horizontal lamellae with respect to the focus point. Consequently, the loss is smaller than that of the "C1 only" photons.
The fluorescence counts decrease differently than the "C1 only" counts, since in the Geant4 simulation, the fluorescence target is only 10 mm long and generates fluorescence photons between $z_{Au} = -80\,\text{mm}$ and $z_{Au} = -70\,\text{mm}$, unlike the "C1 only" photons, which are generated along the entire beam axis within the object. Therefore, a target located around

$z_{L,F} = -75\,\text{mm}$ experiences higher average collimator transmissions: $T_C = 0.899$ for a detector with $y_S = 2\,\text{mm}$, $T_C = 0.867$ for $y_S = 22\,\text{mm}$, $T_C = 0.840$ for $y_S = 42\,\text{mm}$ and $T_C = 0.818$ for $y_S = 62\,\text{mm}$. Consequently, the average collimator transmission T_C decreases by only about 3.6% when the detector is shifted from $y_S = 2\,\text{mm}$ to $y_S = 22\,\text{mm}$, which is much lower than the 30.8% reduction when considering the entire beam axis. For further shifts the collimator transmission reduces less, however, the longer pathways occurring due to the detector shift cause a decrease in path probability and counteract the smaller loss in the collimator transmission. For a shift $y_S = 22\,\text{mm}$, the transmission T_{out} (Eq. 3.14) decreases by 3.1%, the solid angle by 3.8% (Eq. 3.15) and the projection by 1.9% (Eq. 3.16) for a fluorescence photon generated at $z = -75\,\text{mm}$ that traverses to the detector center. When the detector is shifted further to $y_S = 42\,\text{mm}$, the path lengths increase again, especially reducing the solid angle due to the power of two ($G \propto 1/r_{out}^2$), which is stronger by 6.1% and therefore responsible for a slightly larger fluorescence loss, as reflected in the simulated counts.
Finally, significant signals occur for all detector shifts y_S in the K_β signal range of gold (Fig. 6.15). The maximum significance occurs at $y_S = 22\,\text{mm}$ due to the larger background for $y_S < 22\,\text{mm}$. Conversely, for $y_S > 22\,\text{mm}$, the significance decreases due to weaker background loss compared to the fluorescence loss.

6.2.4 Impact of the Lamella Number

After analyzing the impact of altering the collimator's position outside the beam plane in the previous section, this section examines the impact of the collimator for varying numbers of horizontal lamellae. The same setup is used, with a detector shift of $y_S = 22\,\text{mm}$ based on the results of Sec. 6.2.3, as well as the same collimator configuration, whereby only the number of horizontal lamellae varies. The horizontal lamellae are spaced at equal intervals with a distance d_L, which depends on the number of the lamellae N_L and the detector height $H_D = 30\,\text{mm}$ in the considered scenario:

$$d_L = H_D/(N_L - 1). \tag{6.3}$$

To investigate the impact of the lamellae number only and to eliminate distortions caused by detector effects, the true counts and their significance simulated with Geant4 are shown in Fig. 6.19. The fluorescence and background counts decrease with a higher number of horizontal lamellae. However, the fluorescence counts decrease almost linearly when more lamellae are added, whereas the background decreases more sharply at lower lamellae numbers. Approximately half of the background is determined by the "C1 only" counts, which originate from the z-axis, while the remaining background undergoes at least one additional interaction (Fig. 6.19). This means that their last scattering event does not occur on the beam axis before they are detected. To gain insight into the behavior of the photons, Fig. 6.20 illustrates the FOV volumes for different numbers of lamellae.
The height and width of the FOV volumes in Fig. 6.20 are defined by the most oblique detectable paths that can pass through the collimator. A small number of lamellae, such as $N_L = 3$, results in a large FOV, especially in height, whereas four more lamellae ($N_L = 7$) strongly reduce the FOV height.

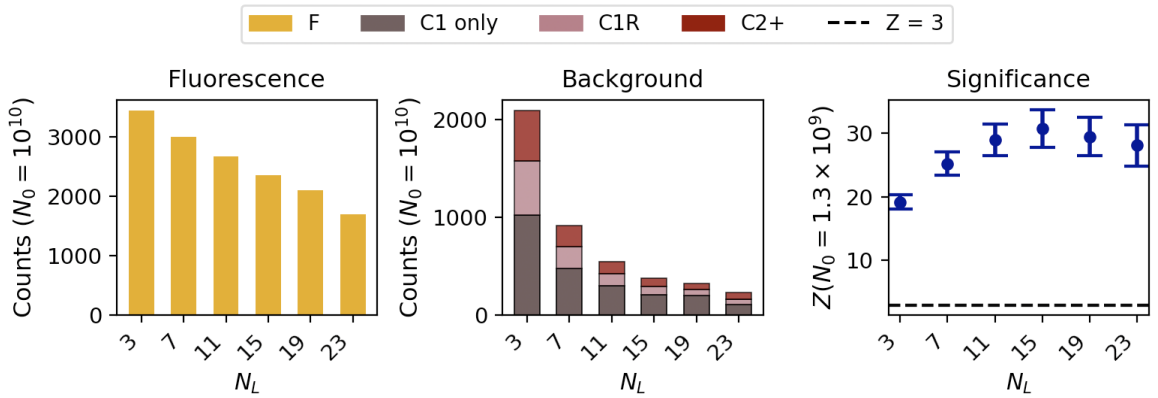

Figure 6.19: The simulated true fluorescence counts (gold) are shown on the left, the background counts (C1 only (brown), C1R (pink), C2+ (red)) in the center, and the significance Z (blue) on the right, for different lamella numbers N_L for a collimator focused on $z_{Au} = -75\,\text{mm}$ on the z-axis. Fluorescence and background counts are shown for $N_0 = 10^{10}$ incident photons, while the significance is shown for $N_0 = 1.3 \times 10^9$ incident photons in the Au-K_β signal range, where the minimum significance of $Z = 3$ for a detectable signal is indicated by the black dashed line.

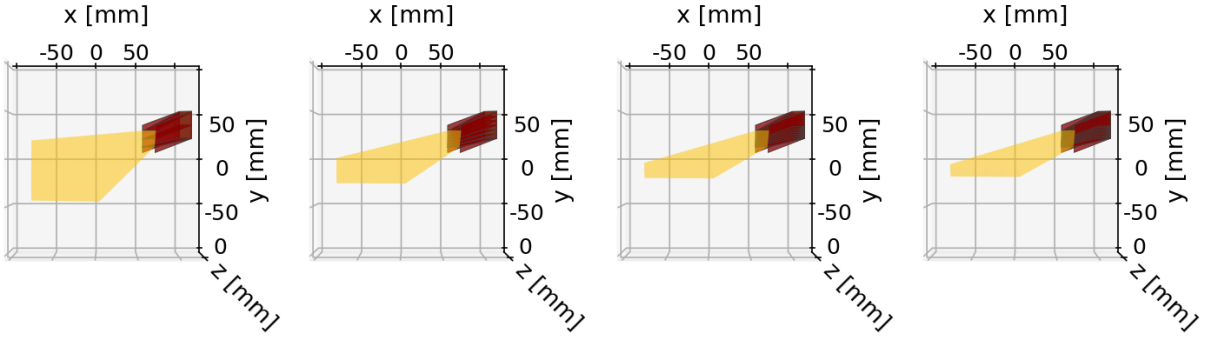

(a) $N_L = 3$ (b) $N_L = 7$ (c) $N_L = 15$ (d) $N_L = 23$

Figure 6.20: The FOV volumes (yellow) with a length of $g = 220\,\text{mm}$ are shown for different numbers of used horizontal lamellae N_L in the collimator (red). The z-axis is oriented out of the plane and points toward the observer.

After that, further additions of lamellae have almost no noticeable impact on the absolute height of the FOV and the volumes decrease less. Hence, the FOV volume with 23 lamellae is nearly identical to that with 15 lamellae, as illustrated by the intersection of the FOV volume with the yz-beam plane at $x = 0$ (Fig. 6.21). This behavior arises from the change in spacing d_L between the lamellae when the number of horizontal lamellae in the collimator varies. Calculated with Eq. 6.3, the spacing between three lamellae is $d_{L,3} = 15.0\,\text{mm}$, while the spacing of seven lamellae is only $d_{L,7} = 5.0\,\text{mm}$. Then, the spacing for 11 lamellae decreases to $d_{L,11} = 3.0\,\text{mm}$ and for 15 lamellae, it decreases by only 0.9 mm to $d_{L,15} = 2.1\,\text{mm}$. These spacings directly determine the vertical opening

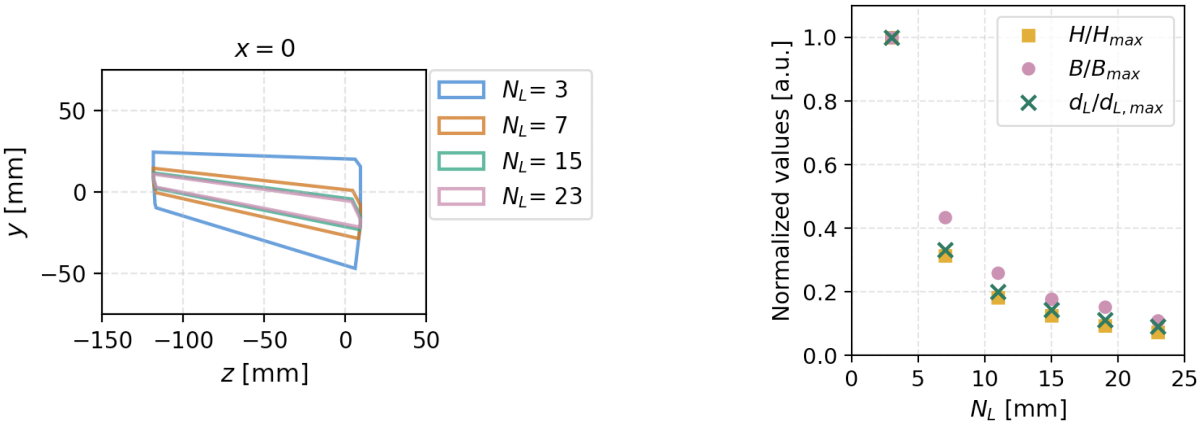

Figure 6.21: Left: The intersections of the FOV volumes in the yz-beam plane at $x = 0$ are shown for different numbers of horizontal lamellae N_L, indicated by different colors. Right: The lamellae spacings $d_L/d_{L,max}$ (green), the FOV height H/H_{max} (gold) and the simulated background B/B_{max} (pink) are normalized to their respective maximum values and shown for different lamella numbers N_L.

angle $\alpha_{O,H}$ in the y-direction, which is defined by the most oblique trajectories that are still detectable in height (Sec. 6.2.2). Accordingly, decreasing the spacing between horizontal lamellae, which occurs when more lamellae are added, correlates with a smaller vertical opening angle and, subsequently, a smaller height (Eq. 6.2).
The relation between the lamellae spacing and the height of the FOV is reflected in Fig. 6.21, where the normalized values are shown for varying lamellae numbers. The loss in the FOV volume height is almost equal to the spacing loss between the horizontal lamellae, so they are nearly proportional to each other. However, the normalized FOV heights are slightly lower than the lamellae spacings, and the difference increases with more lamellae. For example, increasing the number of lamellae from three to seven results in a 67% loss in the lamellae spacing and a 68% loss in the FOV height. However, using 23 lamellae instead of 19 results in a 19% spacing loss and a 22% FOV height loss. This discrepancy is due to the horizontal lamellae not aligning parallel to each other, but instead converging because they are all oriented toward the same reference point. Additionally, they are tilted due to the offset of the detector in y-direction. As a consequence, longer lamellae deviate more from a parallel arrangement, causing a more pronounced decrease in relative height. For parallel ones, the FOV height H would be directly proportional to the lamellae spacing d_L, following the lateral magnification relation for a lamella length l_L and a length l_{NC} outside the collimator [112]:

$$\frac{H}{d_L} \propto \frac{l_{NC}}{l_L}. \tag{6.4}$$

Contrary to the horizontal lamellae, the vertical side lamellae are parallel to each other. Thus, the lateral magnification in Eq. 6.4 holds when the FOV height H is replaced by the width W of the FOV and when the spacing of the horizontal lamellae d_L is replaced by the spacing of the vertical lamellae, corresponding to the detector width D_W. However, since the vertical lamellae are fixed and only the spacings of the horizontal lamellae

varies, the FOV volumes change only in height, not in width, and have a constant width opening angle $\alpha_{O,W}$ (Fig. 6.22a). Consequently, only the vertical FOV component affects the background loss when the number of horizontal lamellae is varied. According to Fig. 6.21, the background decreases by an amount similar to that of the height, but slightly less strongly. This implies that paths shielded by additional lamellae have a lower path probability than the average background paths. The addition of more lamellae reduces the FOV height in the yz-plane by blocking photon paths originating farther from $y = 0$ (Fig. 6.21), which are associated with longer path lengths and thus lower path probabilities.
Contrary to the multiple scattered background, fluorescence and "C1 only" counts can only occur along the incident beam, i.e., along the z-axis. Therefore, the possible detectable section of the incident beam directly corresponds to the intersection of the FOV area in the beam plane and the z-axis. As shown in Fig. 6.22a, the FOV in the xz-beam plane changes with the number of horizontal lamellae. Since there is no projection over all y-values, but only the intersection of the FOV volume in the beam plane at $y = 0$, the FOV areas differ in length. A higher number of lamellae is associated with smaller spacings between them and, consequently, a smaller FOV in y-direction. This results in smaller sections when crossing the beam plane and decreases the length of the FOVs.
As previously mentioned, variations in the FOV areas in the beam plane for different numbers of horizontal lamellae are due to different vertical opening angles. With three or seven lamellae, the FOV areas are large enough to cover the full z-section set by the horizontal opening angle due to the vertical lamellae. However, with more than seven lamellae, the smaller vertical opening angles result in smaller FOV areas that cover less of the z-axis. This is also represented in Fig. 6.22b, where the modeled collimator trans-

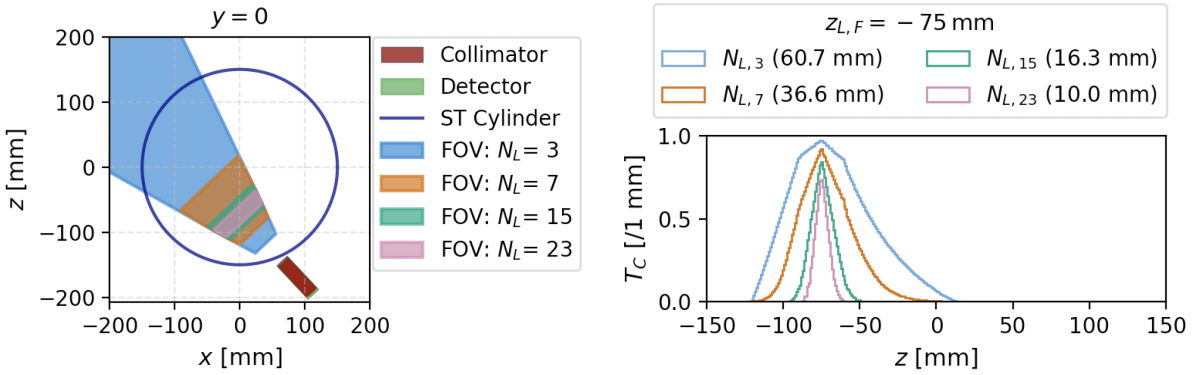

(a) (b)

Figure 6.22: The intersections of the FOV volume in the xz-beam plane at $y = 0$ (a) and the modeled collimator transmission T_C along the z-axis (b) are shown for different collimator lamella numbers N_L. The blue circle in (a) represents the soft-tissue (ST) cylinder edge. The number in the index corresponds to the number of horizontal lamellae. The FWHM values of the collimator transmission distributions are indicated brackets, and the collimator is focused on $z_{L,F}$ on the z-axis.

missions along the z-axis are shown and the collimator transmission is $T_C = 0$ when the

z-axis is outside the FOV area. However, it is notable that the collimator transmissions differ when using seven instead of three lamellae, even though the same z-axis section is covered by their FOV area in the beam plane. The collimator transmission distribution is less broad with seven lamellae compared to three lamellae, as demonstrated by the FWHM being 24 mm smaller. With seven horizontal lamellae, the collimator shields more photon paths from the outer z-ranges so fewer reach the detector from there. Therefore, the FWHM should also be considered, not just the maximum detectable z-axis section defined by the FOV volume.
Additionally, as opposed to adjusting the collimator position along the y-component (Sec. 6.2.3), the peak of the collimator transmission decreases with more lamellae. Specifically, the peak of the collimator transmission is at 97.4% for three lamellae and only at 74% for 23 lamellae. The peak occurs at the collimator's focus point $z_{L,F} = -75\,\text{mm}$, and is expected to be 100% due to the alignment. However, the lamellae are not ideally thin, as they have a thickness of 0.2 mm. Consequently, the effective detector area decreases with more lamellae since they are placed directly in front of the detector. This blocks some areas of the detector, preventing counts from being detected there. For example, three horizontal lamellae block only 1.3% of the detector area, whereas 23 lamellae block 14.7%. Furthermore, using more of the 0.2 mm thick lamellae reduces the free space between them. This causes more photon paths to collide with them, further reducing the collimator transmission peak.
Fluorescence photons originate from only the 10 mm long target along the z-axis in the simulated Geant4 scenario, resulting in different photon transmission compared to C1 photons, as shown in Fig. 6.19. Therefore, only the z-axis section between $-80\,\text{mm}$ and $-90\,\text{mm}$ is relevant for the fluorescence count behavior. Within this fluorescence target interval, collimator transmissions differ less than when considering the entire z-axis or FOV volume. For example, the average collimator transmission and thus the fraction of possible paths that can be detected with a collimator compared to without, is modeled to be 95.6% for three horizontal lamellae across the entire target, whereas it is still 86.7% for seven lamellae. This means there is only a reduction by 9.3% in the collimator transmission. Finally, this explains the lower count loss for fluorescence photons compared to the background, since the whole z-axis must be considered for the "C1 only" photons and the whole FOV volume for the multiple scattered photons. Note that the actual simulated count decrease is slightly larger, since the collimator transmission only takes the fraction of photon paths into account and not the actual count probability, which depends on factors such as the transmission T_{out} through the object material. Fluorescence photons generated at a lower depth within the target are closer to the detector and beam source and due to shorter path lengths, there is a higher path probability. However, regarding the collimator transmission, particularly for photons originating from the edges of the target, there is more prominent shielding. This slightly alters the fluorescence count loss compared to the collimator transmission loss when varying the number of lamellae. Therefore, the reduction of T_C is 15.9% when using 15 lamellae instead of seven, whereby the fluorescence counts in the simulations decrease by 19.4%. Nevertheless, the collimator transmission provides good insight into understanding the fluorescence behavior for different collimator settings.

In Fig. 6.19, the signal significances for the different numbers of lamellae are shown. The figure clearly shows that the significance of only three horizontal lamellae is much lower compared to more horizontal lamellae (19.2±1.1 for three lamellae but 25.3 ± 1.8 for seven lamellae) due to the large background caused by the large FOV volume, as discussed before. Using more lamellae increases the significance of the signal up to 15 lamellae. Beyond that, the significance decreases for further lamellae. This means that the loss of the background, which scales the significance with the factor $1/\sqrt{2B+2}$, is no longer large enough compared to the fluorescence loss. As explained above, the change in the FOV volume height, is too low compared to the fluorescence loss, which is affected by the lower collimator transmission peak due to the 0.2 mm thick lamellae. In the simulations, the background of the collimator with 15 and 19 horizontal lamellae is nearly the same, despite the expectation of a lower background for 19 lamellae. This can be attributed to statistical fluctuations due to the Monte Carlo code in Geant4. Finally, 15 horizontal lamellae are used in further considerations of the Horizontal-Lamellae Collimator as this lamella number is associated with maximum significance.

6.2.5 Impact of the Lamella Length

Another configuration parameter of the collimator is the length of the lamellae. Therefore, the same scenario as in Sec. 6.2.3 and Sec. 6.2.4 is simulated with Geant4, whereby the collimator has a shift $y_S = 22$ mm and consists besides the two vertical side lamellae of 15 horizontal lamellae. The true fluorescence and background counts, simulated with 10^{10} incident photons, as well as their significances for 1.3×10^9 incident photons, are shown in Fig. 6.23 for different lamellae lengths. Note that, as in the previous sections,

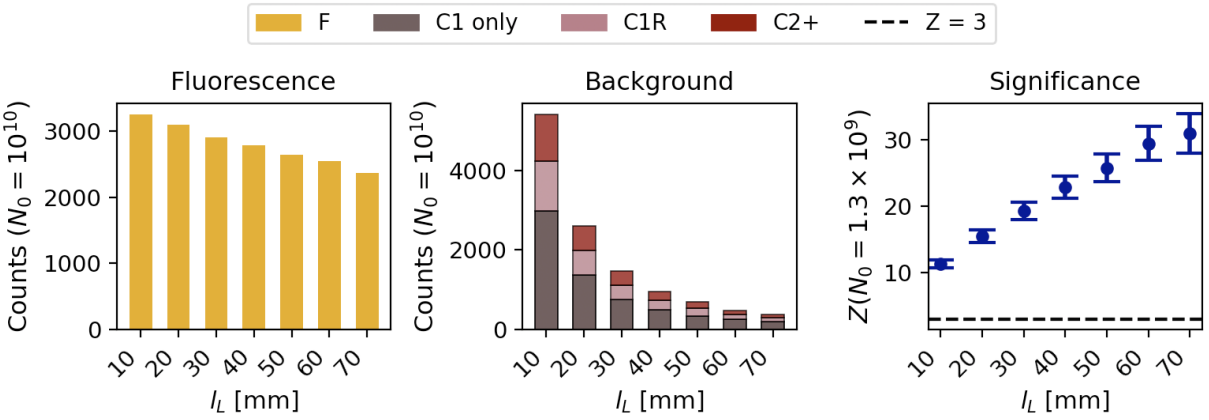

Figure 6.23: The simulated true fluorescence counts (gold) are shown on the left, the background counts (C1 only (brown), C1R (pink), C2+ (red)) in the center, and the significance Z (blue) on the right, for different lamella lengths l_L for a collimator focused on $z_{Au} = -75$ mm on the z-axis. Fluorescence and background counts are shown for $N_0 = 10^{10}$ incident photons, while the significance is shown for $N_0 = 1.3 \times 10^9$ incident photons in the Au-K_β signal range, where the minimum significance of $Z = 3$ for a detectable signal is indicated by the black dashed line.

the true counts are considered, to exclude distortions by detector effects. The length of the lamellae is described by l_L, which represents the length of both the horizontal and vertical lamellae. A maximum lamellae length of $l_L = 70\,\text{mm}$ is chosen to avoid collisions between the collimator and the soft-tissue cylinder.
As shown in Fig. 6.23, the behavior of the fluorescence counts differs from the background counts when the length l_L is varied. While the fluorescence counts decrease almost constantly when the lamellae length is extended by 10 mm, the background initially decreases strongly and then less strongly as the lamellae are elongating. Meanwhile, the significance for 1.3×10^9 incident photons increases up to $Z = 31.0 \pm 3.0$ at the maximum lamella length of 70 mm, meaning that the fluorescence loss remains low compared to the background loss.
This behavior can be interpreted by taking the FOV volumes for the different lamellae lengths into account (Fig. 6.24). The FOV volumes are much larger for shorter lamellae

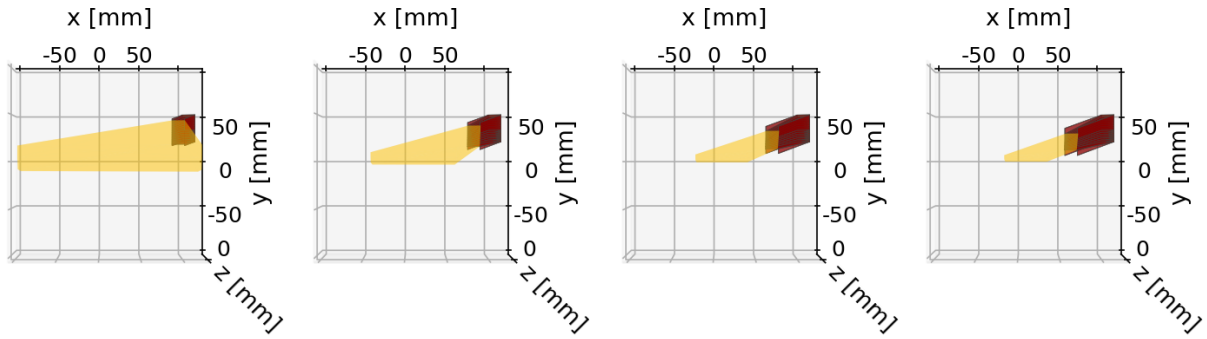

(a) $l_L = 20\,\text{mm}$ (b) $l_L = 40\,\text{mm}$ (c) $l_L = 60\,\text{mm}$ (d) $l_L = 70\,\text{mm}$

Figure 6.24: The FOV volumes (yellow) with a length of $g = 220\,\text{mm}$ are shown for various lamella lengths l_L in the collimator (red). The z-axis is oriented out of the plane and points toward the observer.

than for longer ones. In contrast to varying the number of lamellae, where the horizontal FOV width stays constant, the FOV volumes now change notably in width. As mentioned earlier, the width of the FOV is determined by the vertical lamellae and can be described by the opening angle $\alpha_{O,W}$, which is the sum of the maximum acceptance angles $\alpha_{P,S,max}$ for both collimator sides. More specifically, the maximum acceptance angles are defined by the paths extending diagonally from one vertical lamella on the detector to the other vertical lamellae at the end of the collimator relative to the vertical lamellae's orientation (Fig. 6.25a). These angles can be determined numerically and geometrically. In the numerical case, the angle between each possible path and the vertical lamellae is verified and the largest angle is considered to be the maximum acceptance angle. In the geometric case, the maximum acceptance angle is determined by the relation between the detector width W_D, corresponding to the spacing between the vertical lamellae, and the lamella length l_L:

$$\alpha_{O,W} = \alpha_{P,S1,max} + \alpha_{P,S2,max} \quad \text{with} \quad \alpha_{P,S,max} = \arctan\left(\frac{W_D}{l_L}\right). \tag{6.5}$$

Since the vertical lamellae have the same length, are parallel to each other and perpendicular to the detector, the maximum acceptance angle $\alpha_{P,S,max}$ at the collimator side is the same on both sides, resulting in a horizontal opening angle $\alpha_{O,W} = 2 \cdot \alpha_{P,S,max}$. According to the function of arctan(), a larger angle is reached for a larger value of the argument W_D/l_L, which increases as the lamella length l_L decreases. Conversely, longer lamellae are associated with smaller opening angles, as shown in Fig. 6.25b. However, since the arctan() function is nonlinear, the opening angle decreases less for long lamellae lengths.

Additionally, the FOV volumes change in the vertical direction in height, as shown in

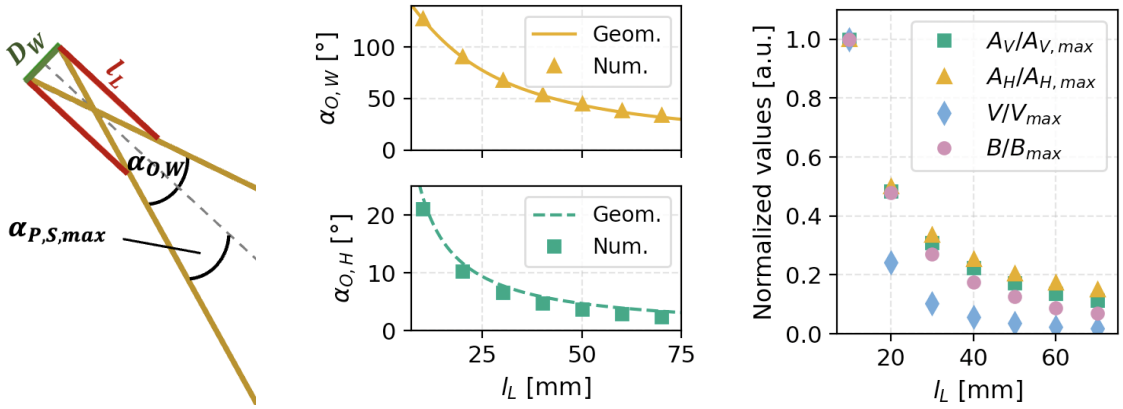

(a) (b) (c)

Figure 6.25: (a) The relation between the maximum acceptance angle in width $\alpha_{P,W,max}$ and the opening angle $\alpha_{O,W}$ of the paths (gold), which are set by the width W_D of the detector (green) and the length l_L of the vertical lamellae (red), is illustrated. (b) The opening angles in width $\alpha_{O,W}$ (gold) and height $\alpha_{O,H}$ (green) are shown as a function of lamella length l_L. The numerical determination is compared with the geometric estimation by Eq. 6.5, in which the opening angle in height $\alpha_{O,H}$ is estimated using the spacing between the horizontal lamellae d_L instead of the detector width W_D. (c) The vertical FOV area $A_V/A_{V,max}$ (green) and horizontal FOV area $A_H/A_{H,max}$ (gold), calculated by Eq. 6.1, as well as the FOV volume V/V_{max} (blue, Eq. 6.2) and the simulated background B/B_{max} (pink) are normalized to their respective maximum values and shown for different lamellae lengths l_L.

Fig. 6.24. This means that the height is affected not only by the spacing between the horizontal lamellae, as in the previous section, but also by the length of the lamellae. However, the vertical FOV is already strongly restricted at small lengths, as shown by the relatively tight height compared to the width of the horizontal FOV. This means that the opening angle in height $\alpha_{O,H}$ is already much lower at a lamella length of 10 mm, reflected in Fig. 6.25b. This phenomenon can be understood with a strongly simplified approximation where the horizontal lamellae are assumed to be parallel and perpendicular to the detector, rather than tilted and focused on the same point on the z-axis. This allows us to geometrically approximate the opening angle in height using Eq. 6.5, in which the detector width W_D has to be replaced by the spacing l_L between the lamellae, as they restrict the paths in the vertical direction. Finally, this geometric estimation appears

to be still a reasonable approximation, according to Fig. 6.25b. However, due to the assumption of parallel lamellae instead of converging ones with a tilt, the opening angles are slightly overestimated compared to the angles determined numerically. Nevertheless, this simplified geometric approximation depicts the impact factors of the height opening angles, namely the lamella length l_L and the horizontal lamella spacings d_L and explains their relation, which is described by the arctan() function.
The FOV volumes and their vertical and horizontal components can be calculated using Eq. 6.2 and Eq. 6.1 with the opening angles. These are shown in Fig. 6.25c for different lamella lengths l_L and are normalized to their maximum, which occurs at $l_L = 10\,\text{mm}$. For the calculations, the opening angles are determined numerically, whereby the vertical FOV area A_V is determined by the height opening angle $\alpha_{O,H}$ and the horizontal FOV area A_H by the width opening angle $\alpha_{O,W}$. Comparing the vertical FOV area with the horizontal FOV area confirms their similar behavior, as previously discussed. However, the vertical FOV decreases at a slightly stronger rate due to the non-parallel, converging horizontal lamellae with smaller openings for longer lamellae. The FOV volume consists of both the vertical and horizontal FOV component. Consequently, the decrease in the FOV volume for longer lamellae is the product of both components and is much stronger than it would be for one component alone. Including the background, which is also normalized to its maximum, it appears that the normalized background is larger than the normalized FOV volume. This is especially evident when extending the lamella length from 10 mm to 20 mm, where the loss in the FOV volume is much stronger than that of the background. While the FOV volume decreases to 24%, the background only decreases to 48%. This can be attributed to the fact that the horizontal FOV is very large for short lamellae. Even with a lamella length of 20 mm, it covers almost the entire cylinder, which is mainly responsible for the background, in the beam plane (Fig. 6.26a). More precisely, for 20 mm-long lamellae and a FOV extension length of $g = 170\,\text{mm}$, corresponding to the distance between the detector and target at $z_{Au} = -75\,\text{mm}$, the width of the FOV is still $W = 342\,\text{mm}$ (Eq. 6.2). Meanwhile, the vertical FOV is significantly smaller, covering only a small part of the 300 mm high cylinder. Lamellae with a length of 10 mm and the same FOV extension length $g = 170\,\text{mm}$ are only associated with a height of 63 mm, while the height is only $H = 31\,\text{mm}$ for a lamellae length of 20 mm. Therefore, the impact of the vertical FOV must be larger than that of the horizontal FOV, which barely changes when elongating 10 mm-long lamellae to 20 mm within the soft-tissue cylinder.

However, as the lamellae are extended further, the impact of the horizontal FOV increases. This is visible by the smaller differences between the normalized background and the normalized FOV volumes. Then, the smaller width opening angles restrict the FOV mainly within the object, as visualized for the beam plane in Fig. 6.26a. The small remaining differences between the FOV volumes and the background can be attributed to different path probabilities, which are especially large for paths close to the beam source. However, the FOV volumes seem to be mainly responsible for the background behavior overall.

As shown in Fig. 6.23, the simulated fluorescence counts behave differently than the total background counts when reducing the lamellae length, since they originate only from a smaller section of the incident beam axis and not the whole cylinder. The FOV in the

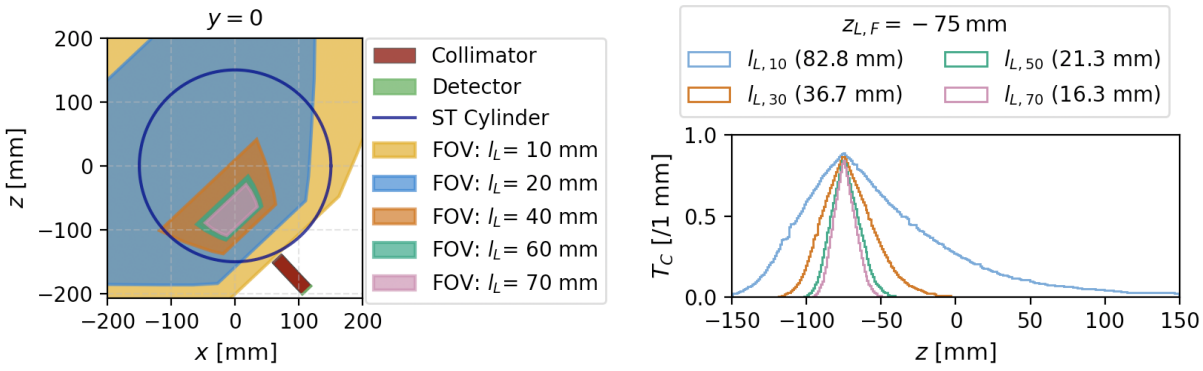

(a) (b)

Figure 6.26: The intersections of the FOV volume in the xz-beam plane at $y = 0$ (a) and the modeled collimator transmission T_C along the z-axis (b) are shown for different lamella lengths l_L. The blue circle in (a) represents the soft-tissue (ST) cylinder edge. The number in the index corresponds to the length of horizontal lamellae. The FWHM values of the collimator transmission distributions are indicated in brackets, and the collimator is focused on $z_{L,F}$ on the z-axis.

xz-beam plane is shown in Fig. 6.26a and demonstrates that, as previously discussed, the FOV decreases in width due to a smaller horizontal opening angle $\alpha_{O,W}$. However, the FOV also decreases in length due to a smaller vertical opening angle $\alpha_{O,H}$, resulting in a smaller area of the beam plane being covered by the FOV volume. This results in smaller FOV sections along the z-axis, as also reflected in Fig. 6.26b, which shows the collimator transmission T_C along the z-axis. For all lamella lengths, the collimator transmission is the highest at the focus point z_{Au}, but the average collimator transmission decreases for longer lamellae because of the smaller opening angles in width and height corresponding to Eq. 6.5. However, for long lamellae such as $l_L = 50\,\text{mm}$, the collimator transmission changes less, as reflected by the FWHM. This is due to the behavior of the arctan() function decreasing the opening angles for long lamellae less strongly (Fig. 6.25b). While the entire collimator transmission distribution applies to the "C1 only" background and explains the strong "C1 only" loss when enlarging small lamellae, only the interval between $-80\,\text{mm}$ and $-70\,\text{mm}$ on the z-axis is important for the simulated fluorescence counts in Fig. 6.23. There, the collimator transmission distributions differ less than they do along the entire beam axis. Thus, the average collimator transmission within the target, based on the distribution shown in Fig. 6.25b, amounts to a 4% reduction in each case when the lamellae are extended by 20 mm. In contrast, the average collimator transmission over the entire z-axis decreases much more significantly. For example, the average collimator transmission decreases from 28.8% to 11.4% when the length is extended from $l_L = 10\,\text{mm}$ to 30 mm.

In summary, the simulated fluorescence counts in Fig.6.23 decrease linearly and by a much smaller amount than the background counts since they originate from a small volume that is fully covered by the FOV, which is determined by the maximum detectable paths. Only the collimator transmission differs slightly for different lengths, resulting in a decrease in

the simulated fluorescence counts. Conversely, the background originates from the whole soft-tissue cylinder, which, particularly in height, is not fully covered by the FOV. Therefore, it is much more sensitive to FOV changes due to the lamellae and the FOV volume decreases by a power of two in the factor tan() due to the decreasing opening angle in width and height for longer lamellae. This results in increased significances for longer lamella lengths up to 70 mm.

6.2.6 Sensitivity for a 150° Detector

To determine the impact of the collimator, as well as the minimum detectable gold concentrations c_{min} for different target positions with a detector located at $\alpha_D = 150°$, the same setup as described in Sec. 6.2.1 is considered. Based on the previous analyses, a collimator with 15 horizontal and two vertical lamellae, each with a length of 70 mm, is chosen, and the collimator and detector are shifted by $y_S = 22$ mm. Here, changing the target position along the z-axis also involves changing the focus of the detector and collimator, ensuring that $z_{L,F} = z_{Au}$ always holds for the target center.
In Fig. 6.27, the different simulated recorded counts are shown for various target positions, with and without a collimator. Note that true counts were considered only to analyze the impact of the collimator in the previous sections. For the sensitivity, however, detector effects should also be taken into account. The fluorescence counts decrease exponentially with increasing the depth of the target, which is associated with larger z_{Au} values. This occurs in both cases, with and without the collimator, due to the longer path lengths described by the Beer-Lambert law (Eq. 2.12) and smaller solid angles. Accordingly, the number of fluorescence counts is reduced by about 60% when using a collimator compared to not using one. As previously mentioned, the non-infinitely thin lamellae and the partially shielded paths of fluorescence photons that do not originate directly from the center of the target target, to which the lamellae are aligned, are responsible for this. However, the background is much more reduced due to the collimator. While the background remains almost constant with no collimator and only slightly changes with different target positions due to the adapted detector orientation to the target, it behaves differently with the collimator attached. The collimator restricts the FOV along the z-axis, resulting in fewer photons being detected from there. Then, the collimator reduces the background to 3.4% for a target $z_{Au} = -100$ mm up to 0.22% for $z_{Au} = 0$ mm. The different behavior of the collimated background, especially the "C1 only" counts, for different target positions is due to their restricted origin. A target with a larger z_{Au} value and thus a collimator focus farther away is correlated with a longer path and fewer counts. Nevertheless, larger z_{Au} values are associated with lower significance due to the additional loss of fluorescence counts, as shown in Fig. 6.27 for 1.3×10^9 incident photons and a gold concentration of 1.0 mg/ml. However, the signals have much higher significances than they would without the collimator and for targets with values up to $z_{Au} = -25$ mm significant values with $Z > 3$ are achieved. With the collimator removed, targets located at $z_{Au} = -75$ mm already have insignificant signals.

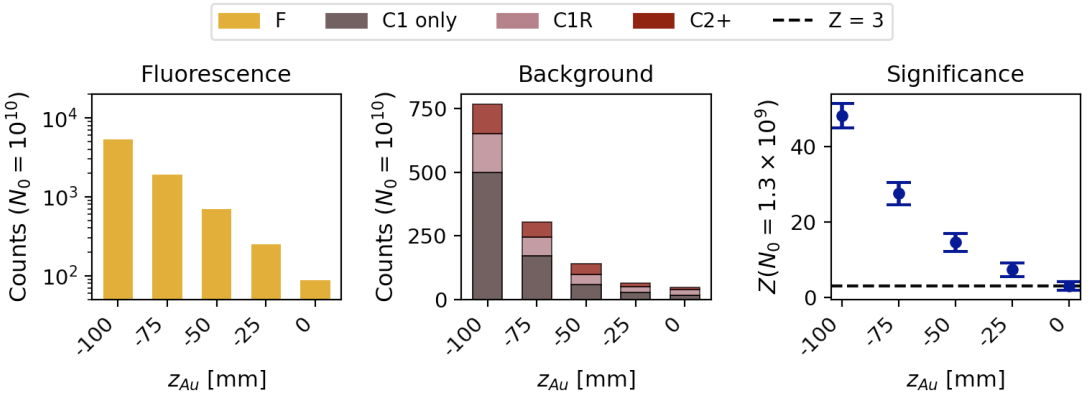

(a) Collimator

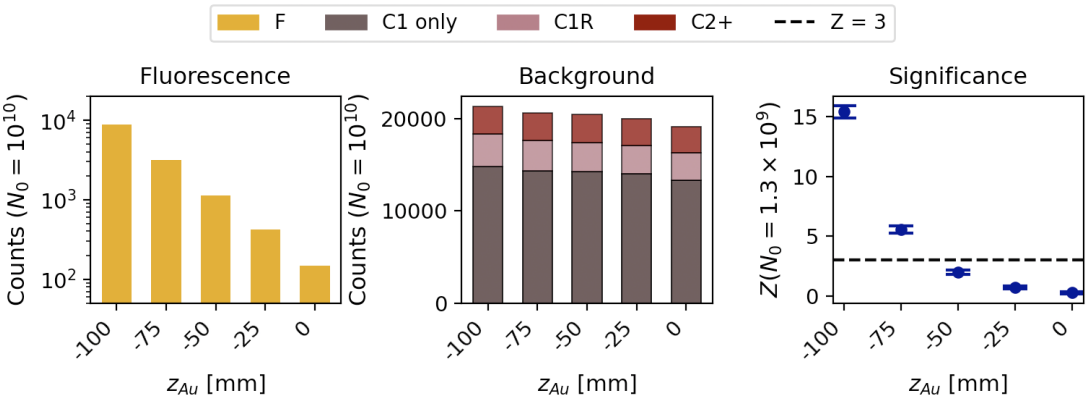

(b) No collimator

Figure 6.27: The simulated recorded fluorescence counts (gold) are shown on the left, the background counts (C1 only (brown), C1R (pink), C2+ (red)) in the center, and the significance Z (blue) on the right, for different target positions z_{Au} and a detector at 150°, with the collimator focused on the respective target position (top) and without a collimator (bottom). Fluorescence and background counts are shown for $N_0 = 10^{10}$ incident photons, while the significance is shown for $N_0 = 1.3 \times 10^9$ incident photons in the Au-K_β signal range, where the minimum significance of $Z = 3$ for a detectable signal is indicated by the black dashed line.

Furthermore, the resulting significances and their standard deviations are presented for 1.3×10^9 incident photons. In Tab. 5, the minimum detectable concentrations are shown for 1.3×10^9 incident photons. To determine them, 10^{10} incident photons and a gold concentration of 5.0 mg/ml are simulated with Geant4 and the recorded counts, taking detector effects into account, are then scaled to a minimum detectable concentration, so that Eq. 3.6 holds. When using a collimator, the minimum detectable concentrations are much lower than without a collimator, especially for deeper targets. For instance, a target at $z_{Au} = -25$ mm requires a minimum gold concentration of 4.30 mg/ml without a collimator, while the collimator reduces this concentration to 0.58 mg/ml to achieve significant signals, which is only 13.4% of the concentration without collimation. However, the difference between the minimum concentrations is smaller for targets with smaller z_{Au}

Setup	c_{min} [mg/ml] for z_{Au} [mm]				
	-100	-75	-50	-25	0
With collimator	0.074	0.136	0.271	0.575	1.460
Without collimator	0.210	0.580	1.608	4.297	>5

Table 5: The minimum detectable gold concentration c_{min} is shown for different target positions z_{Au} and a 150° detector, both with and without the Horizontal-Lamellae Collimator. Here, 10^{10} incident photons are simulated with a gold target of 5.0 mg/ml concentration and scaled to 1.3×10^9 incident photons. It is determined as the concentration at which the significance of the simulated recorded counts fulfills Eq. 3.6.

values, since the fluorescence photons cover a larger fraction of the detected counts due to the short pathways. Hence, even in the uncollimated case, the achievable minimum concentration is relatively low compared to the collimated case.

6.2.7 Sensitivity for a 180° Detector

In the previous sections, the collimator was attached to a detector located at an angle of $\alpha_D = 150°$. Now, the collimator is attached to a detector located at 180°. For this, detectors are used that are shifted out of the beam plane by $y_S = 22\,\text{mm}$ in the positive and negative y-direction, as with the 150° detector. At a detector angle of 180°, however, two detectors are considered instead of four, as was done for 150°. Each detector has a width of 40 mm and a height of 20 mm, and thus, the total detector area is equal to that of the 150° detector scenario. Correspondingly, the horizontal lamellae also have a width of 40 mm and the vertical lamellae are located at each detector side. As in the previous section, the collimator has 15 horizontal lamellae, each 70 mm long, with the lowest lamella focused on the shallowest target edge at $z_{Au,min} = z_{Au} - 5\,\text{mm}$ and the highest lamella focused on the farthest edge at $z_{Au,max} = z_{Au} + 5\,\text{mm}$, in order to detect more fluorescence photons.
In Fig. 6.28, the simulated recorded counts for the fluorescence and the background are shown with and without the collimator. As in the case of a detector at 150° (Fig. 6.27), the fluorescence counts decrease exponentially in both cases, with and without a collimator, due to the longer pathways for targets farther from the beam source, which correspond to larger z_{Au} values. When the target is located at $z_{Au} = -100\,\text{mm}$, the number of fluorescence counts is larger than that of a 150° detector, which detects 18% fewer fluorescence counts. The shorter distance between the target and the beam source and the 180° detector explains this difference. For the 180° detector, the distance between the target and the detector center is 130 mm, whereas for the 150° detector, it is 152 mm. However, this discrepancy decreases with deeper target depths and the simulated fluorescence counts are equal at $z_{Au} = 0\,\text{mm}$, where the distances are the same.
The collimator has a similar effect on the background as for the 150° detector. Without the collimator, the background remains nearly constant for all target positions. In this case, there are about 23,000 background counts and attaching the collimator drastically reduces the background, depending on the target position.

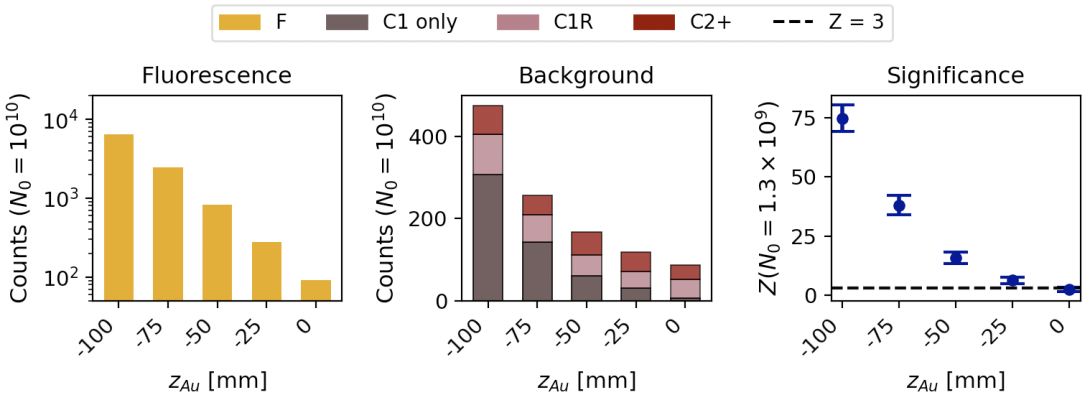

(a) Collimator

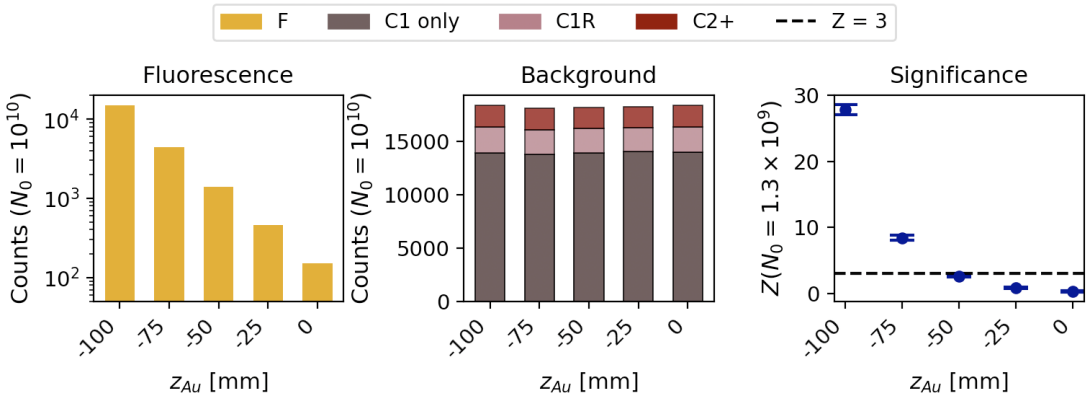

(b) No collimator

Figure 6.28: The simulated recorded fluorescence counts (gold) are shown on the left, the background counts (C1 only (brown), C1R (pink), C2+ (red)) in the center, and the significance Z (blue) on the right, for different target positions z_{Au} and a detector at 180°, with the collimator accordingly (top) and without a collimator (bottom). Fluorescence and background counts are shown for $N_0 = 10^{10}$ incident photons, while the significance is shown for $N_0 = 1.3 \times 10^9$ incident photons in the Au-K_β signal range, where the minimum significance of $Z = 3$ for a detectable signal is indicated by the black dashed line.

Note that, unlike with the 150° detector, the background without a collimator does not decrease slightly for larger z_{Au} values because the orientation of the 180° detector to the target does not change with different target positions. Furthermore, the uncollimated background is smaller than it would be with a 150° detector. For example, a target at $z_{Au} = -100\,\text{mm}$ detects 23,240 background counts for the 180° detector, while the 150° detector detects 26,875 counts. This difference can be attributed to the larger scattering angles associated with a 180° detector resulting in a lower probability of fluorescence photons having enough energy to fall within the K_β energy range of gold. Considering the collimated background counts, it appears that the fraction of the "C1 only" photons is smaller compared to the uncollimated case and also decreases with larger z_{Au} values. This means that the Compton counts originating from the z-axis are especially collimated. For a target deep within the object, such as at $z_{Au} = 0\,\text{mm}$, the collimator focuses on

it, thereby shielding photon paths originating from low depths. These shielded paths are associated with high path probabilities due to the short path length, causing a stronger background loss. However, even though the background for the 180° detector is lower than that for the 150° detector when focusing on shallow depths or low z_{Au} values, the decrease is less pronounced. For a gold target at $z_{Au} = -100\,\text{mm}$, the background of the 180° detector is only 63% of that of the 150° detector, which is due to the smaller FWHM of the collimator transmission, which is numerically modeled to only 7.2 mm instead of 14.1 mm. However, the background of the 180° detector is already 1.2 times larger for a target at $z_{Au} = -50\,\text{mm}$ and it doubles for $z_{Au} = 0\,\text{mm}$. This indicates that the collimator shielding is less efficient for targets farther away compared to the 150° detector, especially for the "C1R" and "C2+" photons not originating from the beam axis. Consequently, the signal significance is higher for the 180° detector at low target depths, but lower than for the 150° detector at large target depths. More precisely, the collimator achieves

Setup	c_{min} [mg/ml] for z_{Au} [mm]				
	-100	-75	-50	-25	0
With collimator	0.049	0.100	0.249	0.639	1.715
Without collimator	0.116	0.386	1.223	3.750	>5

Table 6: The minimum detectable gold concentration c_{min} is shown for different target positions z_{Au} and a 180° detector, both with and without the Horizontal-Lamellae Collimator. Here, 10^{10} incident photons are simulated with a gold target of 5.0 mg/ml concentration and scaled to 1.3×10^9 incident photons. It is determined as the concentration at which the significance of the simulated recorded counts fulfills Eq. 3.6.

higher significances with the 150° detector when the targets are located deeper than $z_{Au} = -25\,\text{mm}$. For shallower depths, collimation is more efficient with the 180° detector, which is also reflected in the lower minimum detectable concentrations. These concentrations are only larger with the 180° detector when $z_{Au} \geq -25\,\text{mm}$ applies (Tab. 6, 5). Nevertheless, even at $z_{Au} = -25\,\text{mm}$, the 180° detector reduces the minimum detectable concentration by 83% compared to without a collimator, from 3.75 mg/ml to 0.64 mg/ml. Overall, collimation with both detector angles greatly improves the significance of the signal and decreases the minimum detectable concentrations compared to the collimator.

6.3 Comparison of Collimator Designs

In a prior study, the research group of Jayarathna et al. used a "Parallel-Hole Collimator" with a HEXITEC detector [88]. To allow a comparison of the effectiveness of the collimator strategy used in that study and the lamellae collimators presented in this thesis, the HEXITEC detector area is considered and the lamellae collimators are adjusted accordingly. This thesis also considers a converging Cone-Hole Collimator with cone holes that focus on the target in order to determine whether focusing holes or lamellae perform better as collimators. Additionally, the comparison includes a collimator with horizontally aligned parallel lamellae. Details on each collimator setup can be found in Tab. 7 and in Appendix A.2.

Collimator	alignment	t [mm]	d_{xz} [mm]	d_y [mm]	α_D [°]	y_D [mm]
$C_{H,P,7}$	parallel	1.0	2.0	2.0	150	0.0
$C_{H,P,9}$	parallel	0.2	2.0	2.0	150	0.0
C_C	non-parallel	0.2	2.0	2.0	150	0.0
$C_{L,\parallel}$	parallel	0.2	20.0	2.0	150	0.0
$C_{L,h}$	non-parallel	0.2	20.0	2.0	150	0.0
$C_{L,h,s}$	non-parallel	0.2	20.0	2.0	150	32.0
$C_{L,h,180°}$	non-parallel	0.2	20.0	2.0	180	32.0
$C_{L,v}$	non-parallel	0.2	2.3	20.0	150	32.0

Table 7: The parameters of the different hole collimators are listed, including whether the holes or lamellae are parallel or converging. Listed parameters: the thickness t of each lamella or the minimum distance between neighboring holes; the size of the openings defined by the holes or neighboring lamellae at the detector side is described by d_{xz} in the xz-plane and by d_y in the vertical direction; the detector angle α_D in the beam plane; the component y_D of the detector with respect to the y-axis (y_D corresponds to the sum of the detector shift y_s and half the detector height). The compared collimators are the Parallel-Hole Collimators with 7×7 ($C_{H,P,7}$) and 9×9 ($C_{H,P,9}$) holes, the Cone-Hole Collimator C_C with 9×9 converging holes, the Parallel-Lamellae Collimator $C_{L,\parallel}$, the Horizontal-Lamellae Collimator $C_{L,h}$, the shifted Horizontal-Lamellae Collimator $C_{L,h,s}$, the Vertical-Lamellae Collimator $C_{L,v}$ and the shifted Horizontal-Lamellae Collimator $C_{L,h,180°}$ at a detector angle of 180° instead of 150°.

In Fig. 6.29, the detected fluorescence and background counts, as well as their corresponding significances, are shown for the different collimator designs. For the comparison, a target located at $z_{Au} = -75\,\text{mm}$ is considered and all collimators are attached to a detector placed at 150°. Additionally, based on the results of Sec. 6.2.7, the shifted Horizontal-Lamellae Collimator is also shown for a detector angle of 180°. It should be noted that two Parallel-Hole Collimator designs are considered. One follows the original design with 7×7 holes, while the other is an adjusted design with 9×9 holes and a smaller septum thickness, allowing for a fairer comparison with the lamellae collimators. Nevertheless, neither the Parallel-Hole Collimators nor the Parallel-Lamellae Collimator show significant signals when uncertainties are taken into account (Eq. 3.6). This is

because their parallel alignment does not follow the paths of the isotropically emitted fluorescence photons. Consequently, besides the background, many fluorescence photons are blocked. Additionally, the effective detector area for a Parallel-Hole Collimator is reduced by the septum thicknesses of the collimator directly in front of the detector to only 38.5% when 7×7 holes (1.0 mm septum thickness) are used, and to 63.6% when 9×9 holes (0.2 mm septum thickness) are used. This causes a further reduction in detected photons compared to the Parallel-Lamellae Collimator, which achieves an effective detector area of 85%. These collimators are located in the beam plane, meaning that, for the Parallel-Lamellae Collimator, there is only a restriction of the maximum detectable paths along the z-axis due to the vertical side lamellae, which are spaced 20 mm apart. A wider FOV range compared to the parallel holes results, which have smaller openings due to a hole diameter of 2 mm (Fig. 6.30).

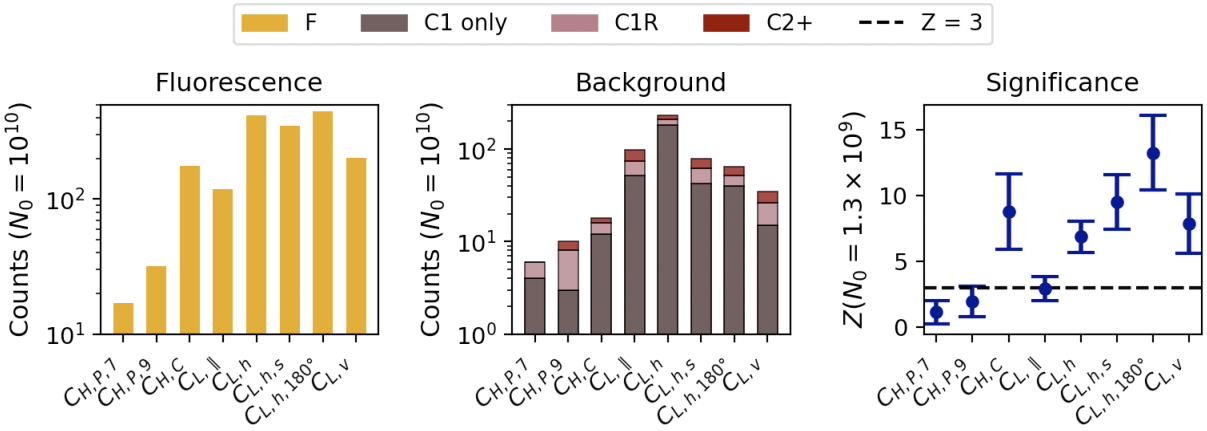

Figure 6.29: The simulated recorded fluorescence counts (gold) are shown on the left, the background counts (C1 only (brown), C1R (pink), C2+ (red)) in the center, and the significance Z (blue) on the right, for a target position $z_{Au} = -75$ mm, with each collimator oriented toward z_{Au}. Fluorescence and background counts are shown for $N_0 = 10^{10}$ incident photons, while the significance is shown for $N_0 = 1.3 \times 10^9$ incident photons in the Au-K_β signal range, where the minimum significance of $Z = 3$ for a detectable signal is indicated by the black dashed line. At a detector angle of 150°, the following collimators are considered: Parallel-Hole Collimator with 7×7 ($C_{H,P,7}$) and 9×9 ($C_{H,P,9}$) holes, Cone-Hole Collimator C_C, Parallel-Lamellae Collimator $C_{L,\parallel}$, Horizontal-Lamellae Collimator $C_{L,h}$, shifted Horizontal-Lamellae Collimator $C_{L,h,s}$, Vertical-Lamellae Collimator $C_{L,v}$. At a detector angle of 180°, the Shifted Horizontal-Lamellae Collimator $C_{L,h,180°}$ is considered. The shifted collimators have an offset of $y_S = 22$ mm.

Unlike the Parallel-Hole Collimators, the holes of the Cone-Hole Collimator focus on the fluorescence target. Thus, even if the hole radius at one end of the cone is smaller, fewer fluorescence paths are collimated while the background remains relatively low compared to the lamellae collimators. This can be understood by considering the FOV by the collimator transmission curve, which is much less broad and associated with higher transmission at $z_{Au} = -75$ mm for the Cone-Hole collimator due to its focused alignment

on z_{Au} compared to collimators with parallel alignment (Fig. 6.30). Therefore, a significant signal with $Z = 8.8 \pm 2.9$ is achieved.

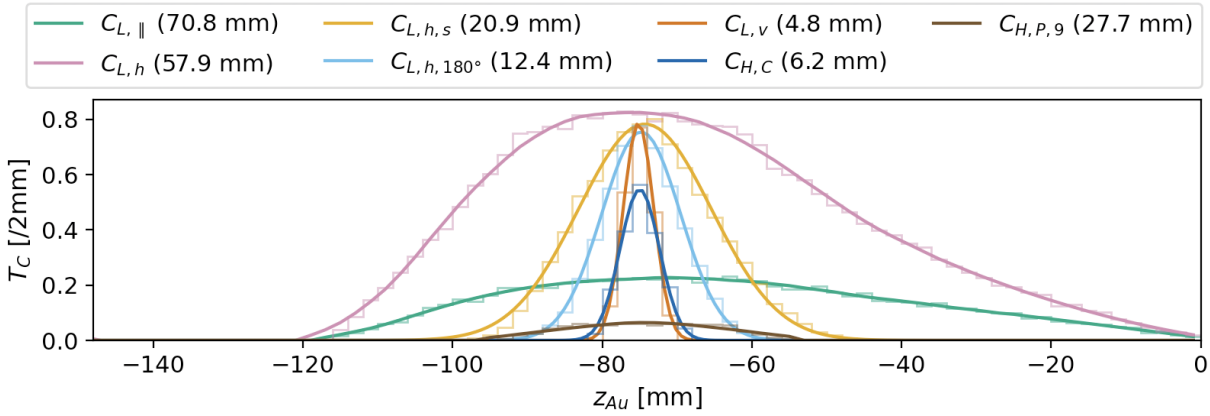

Figure 6.30: The simulated collimator transmissions T_C are shown for z-axis bins of 2 mm width for various collimators attached to a 150° detector: Parallel-Hole Collimator with 9×9 ($C_{H,P,9}$) holes, Cone-Hole Collimator C_C, Parallel-Lamellae Collimator $C_{L,\parallel}$, Horizontal-Lamellae Collimator $C_{L,h}$, Shifted Horizontal-Lamellae Collimator $C_{L,h,s}$, Vertical-Lamellae Collimator $C_{L,v}$. At a detector angle of 180°, the Shifted Horizontal-Lamellae Collimator $C_{L,h,180°}$ is considered. The shifted collimators have an offset of $y_S = 22$ mm. The FWHM values of the collimator transmission curves are indicated in brackets. This plot shows the dependence of the collimator transmission on the hole and lamellae alignment, revealing that hole-based collimators are associated with lower collimator transmissions, including the target focus range between −80 mm and −70 mm.

However, the number of detected fluorescence photons using the Cone-Hole Collimator is still low compared to collimators with non-parallel lamellae. With the Horizontal-Lamellae Collimators, approximately twice as many fluorescence photons are detected. The 150° detector counts the most fluorescence photons with the non-shifted Horizontal-Lamellae Collimator in the beam plane because the FOV along the z-axis is less restricted than with a collimator shifted out of the beam plane (Sec. 6.2.3) and the lamellae focus on the target, contrary to the Parallel-Lamellae Collimator. Consequently, the highest collimator transmission is achieved with the Horizontal-Lamellae Collimator in the beam plane, for which the maximum detectable section along the beam axis is equal to the detectable beam-axis section with the Parallel-Lamellae Collimator. This is set by the spacing of the vertical side lamellae (Fig. 6.30). Furthermore, the Horizontal-Lamellae Collimator in the beam plane is associated with lower attenuation and larger solid angles than the Horizontal-Lamellae Collimator shifted out of the beam plane, where the photon path lengths increase. However, this also means that more "C1 only" photons are detected with the Horizontal-Lamellae Collimator in the beam plane, as indicated by a C1 count value that is more than three times larger than that of other collimators. Finally, the significance of the signal is $Z = 6.9 \pm 1.2$, which is lower than that of the shifted Horizontal-Lamellae Collimator, whose significance is $Z = 9.5 \pm 2.1$.

Another collimator in the beam plane is the Vertical-Lamellae Collimator, which collimates more photons than the other lamellae-based collimators. In particular, "C1 only" photons are suppressed and reduced to only 8% compared to the Horizontal-Lamellae Collimator in the beam plane. This is due to the criteria chosen for the Vertical-Lamellae Collimator (Sec. 6.1.1), which only allows detection along the beam axis within the fluorescence target section between $z = -80\,\text{mm}$ and $z = -70\,\text{mm}$, as shown in Fig. 6.30. This is linked with a FWHM of 4.8 mm, resulting in a significance of 7.9±2.3.
Among all the collimators, the one with the highest significance is the shifted Horizontal-Lamellae Collimator attached to a detector at 180°. This setup has two main advantages. First, for a target at $z_{Au} = -75\,\text{mm}$, this detector location is associated with the most detected fluorescence photons. Second, the background is still strongly reduced due to the shorter distances of the background photons. This is due to the low collimator transmission outside the target, which is described by a FWHM of only 12.4 mm, being smaller than 20.9 mm in the case of the shifted Horizontal-Lamellae Collimator at 150° (Fig. 6.30). Additionally, the background is shifted to lower energies due to the location of the 180° detector, which decreases the probability to detect background photons in the K_β region (Sec. 5.3.2). Finally, the "C1 only" counts detected by the 180° detector are as large as those detected by the 150° detector and the multiply-scattered background is even lower, resulting in a significance of 13.3±2.8 for the $C_{L,h,180°}$ collimator.
These results demonstrate that the considered lamellae-based collimators achieve higher signal significances than the hole-based collimators. This is because hole-based collimators are subdivided in both the vertical and horizontal directions, whereas lamellae-based collimators are only subdivided in one dimension. Thus, hole-based collimators have a smaller angular acceptance and accept fewer fluorescence photon trajectories than lamellae-based collimators. Furthermore, it should be noted that the hole-based collimators are simulated with a length of 50 mm, in accordance with Jayarathna et al. [88], whereas the Horizontal-Lamellae collimators have the optimized length of 70 mm (Sec. 6.2.5). Consequently, the number of detected fluorescence photons is expected to decrease further for hole-based collimators with a length of 70 mm due to the decreasing opening angles per hole.

6.4 Discussion

Collimation with Backward Detector Geometry The collimator designs presented in Sec. 6 are all developed for backward detection. A detector located in the backward direction is associated with larger Compton scattering angles and, consequently, lower C1 photon energies. This reduces the background within the K_β energy range of gold, where the remaining background is predominantly caused by C1 photons that reach the K_β energy range due to Doppler broadening (Sec. 5). Therefore, the described intrinsic background problem of multiple Compton-scattered photons in the K_α energy range, as discussed by Grüner et al. [28], can be reduced. The lamellae-based collimators provide additional spatial filtering and improve the sensitivity (Sec. 6.1.6, 6.2.6, 6.2.7). To the best of the author's knowledge, placing the detector in the backward direction for spectral filtering and combining it with a collimator for spatial filtering in a more practical, non-4π

detector geometry represents a novel approach for imaging human-sized objects with a pencil beam. However, some of these strategies have been used separately in the literature. While Grüner et al. [28] focused on the Au-K_α fluorescence region in their paper and therefore faced the high background of the multiple Compton-scattered photons, Ungerer et al. [62] considered the Au-K_β signal range in addition and could therefore partly achieve a higher significance. Both papers also considered human-scale objects. However, they used a 4π-detector with a different, larger collimator design and applied a detector pixel selection algorithm for spectral filtering, allowing for improved sensitivity [28, 62]. Vernekohl et al. [29] analyzed human-sized phantoms as well. Specifically, they examined the thorax, containing four cylindrical gold targets, each with a diameter of 5 mm and a height of 1 mm. However, they used a fan beam with an energy of 82 keV and an opening angle of 2.6°, which corresponds to a beam width 45 times larger than that of a 1 mm-diameter pencil beam and results in lower spatial resolution [29, 11]. As in this thesis, the detectors were located in the backward direction, but they were larger (four detectors, each measuring $26 \times 16\,\mathrm{cm}^2$) [29].
In a different study by AL-Ghorabie [113], a cylindrical tumor phantom with a diameter of 36 mm and a height of 50 mm, containing platinum as a marker, was located inside a cylindrical neck phantom with a diameter of 160 mm and a height of 200 mm. As in one scenario with the shifted Horizontal-Lamellae Collimator, a detector was placed at 180°. However, they used the radioisotope ^{133}Xe as the beam source and instead of a pencil beam, this resulted in an isotropically emitting beam source. Therefore, the beam source was located at a different height than the detector and tumor and was additionally surrounded by a collimator that blocked photons emitted in the backward direction to protect the detector [113]. Consequently, this collimator also reduces the number of detected photons scattered within the neck phantom.
Other research groups have also considered backward detection in the context of XFI. However, this was mostly done for objects smaller than human size without a detector collimator, as in the studies referenced in [114, 115, 86, 116]. A detector collimator was often used when detecting at a 90° angle to determine the direction of the detected photons' origin, as in the studies cited in [117, 88, 93, 118]. Furthermore, a collimator was also sometimes used when considering a detector ring, as in the study by Mandot et al., which used a 96-pinhole collimator [119].

Collimator Design In Sec. 6, different collimator designs are presented to address the background problem for human-sized objects. Unlike the approach of Grüner et al. [28], these collimators are all based on the assumption that the target location must be known a priori along the incident beam in order to restrict the detector's FOV outside the target. Therefore, the collimators presented in this thesis (Sec. 6) can only be used in multimodal imaging contexts. The advantage of these collimators, however, is that they are much more compact than the collimator used by Grüner et al., which used a 4π-detector with 3,600 radially aligned molybdenum leaves [28]. Each leaf was 30 cm long and installed to shield the higher orders of Compton scattering. In contrast, the collimator designs presented in this thesis use nine lamellae per Vertical-Lamellae Collimator and 15 lamellae per Horizontal-Lamellae Collimator, in addition to the collimator housing.

Furthermore, the lamellae are much shorter, with the Horizontal-Lamellae Collimator having lamellae which are only 7 cm long. Moreover, a material analysis showed that, in the high energy range in which the K_β signal range of gold lies, tantalum is a more promising absorbing material compared to molybdenum, which was used by Grüner et al. [28].
However, in other studies, detector collimators are not necessarily used for background reduction. Instead, when a sheet or fan beam is used in XFCT to decrease imaging time, the detector collimator allows for improved spatial localization along the incident beam direction [120, 117, 121, 88]. One commonly used setup is the parallel-hole collimator used by Jayarathna et al. but it does not improve the significance of the gold signal as it blocks a substantial fraction of fluorescence photons (Sec. 6.3) [93, 88, 89]. The research group of Dunning et al. presented a detector collimator with short slits of 3.3 mm length and 0.4 mm spacing, resulting in a total opening angle of 7° [117]. As discussed in Sec. 6.2.5, short lamellae and, consequently, large opening angles are associated with a larger background and are less preferable due to lower significances. In comparison, the opening angles in the height of the Horizontal-Lamellae Collimator, with a spacing of 2.1 mm and a length of 70 mm, are all below 1.7° and are associated with much higher significances (Fig. 6.23, 6.25b). Hence, longer lamellae are preferable to reduce the opening angle. Alternatively, more lamellae could reduce the opening angle by decreasing the lamellae spacing. However, this would also reduce the effective detector area and cause fewer fluorescence photons to be detected.

Spatial Resolution In XFI, the spatial resolution in the transverse direction is only defined by the beam diameter and depth information can be obtained along the beam using XFCT by irradiating the object from different incident beam angles [62, 122]. However, attaching a collimator to the detector, such as one of those presented in this thesis, can restrict the detector's FOV, thereby achieving longitudinal resolution (Sec. 6.1.5, 6.2). In this thesis, restricted FOVs reduce the background, mainly the C1 photons which do not originate from the fluorescence target region. In this context, the longitudinal spatial resolution is not used to obtain depth information about the target location, but rather to increase the significance of the signal where it is mandatory to know the target position a priori in order to adjust the collimator. This allows the beam section outside the target to be shielded more strongly, while the section within the target is shielded less, achieving high fluorescence photon detection. Consequently, the FOV of the detector, and thus the longitudinal resolution of the beam, depends on the target position and the chosen collimator. In Tab. 8, the FOV values, described by the FWHM of the modeled collimator transmissions, are summarized for the Vertical-Lamellae Collimator and the shifted Horizontal-Lamellae Collimator at 150° and 180°.
In the context of a pencil beam and a human-sized object, the Parallel-Hole Collimator, as used by Jayarathna et al. [88] and Ahmed et al. [120], and a Parallel-Slit Collimator, as used by Dunning et al. [117], are less recommendable due to their large FOV and low fluorescence detection (Sec. 6.3). To achieve longitudinal resolution, Jayarathna et al. used the HEXITEC detector with 6,400 pixels (Sec. 3.4) in addition to the collimator. However, they performed their studies on a much smaller cylinder object with a height

and diameter of only 30 mm. Therefore, many more fluorescence photons are expected to be detected per pixel than with a human-sized cylinder. For a human-sized cylinder, with 10^{10} incident photons, the total number of detected fluorescence photons is well below 6,400 for a target position at $z_{Au} = -75$ mm (Sec. 6.3). The low number of detected counts would reduce detector effects such as charge sharing, but more pixels would have to be considered to achieve significant signals [95]. As discussed in Sec. 6.1.6, a target located at greater depth is associated with larger FOVs for the horizontal lamellae, while this only occurs for the Vertical-Lamellae Collimator for targets with a position of $z_{Au} \leq -50$ mm. In all cases, the FWHM of the Vertical-Lamellae Collimator is smaller than the FWHM when using horizontal lamellae due to their different alignments. The Vertical-Lamellae Collimator collimates as many C1 paths as possible outside the fluorescence target, whereas the Horizontal-Lamellae Collimator shields less of the incident beam, as indicated by the FWHM. However, more fluorescence photons are detected with the Horizontal-Lamellae Collimator (Sec. 6.3). Consequently, a smaller FWHM is associated not only with fewer background photons, but also with fewer fluorescence photons, which can result in a lower sensitivity. Furthermore, a higher longitudinal spatial resolution or a more restricted FOV of the detector would mean that the detectable target size would be more limited along the incident beam. Due to the restricted FOV, the lamellae collimators are not suitable for pharmacokinetic applications where the origin of the fluorescence photons is unknown. Instead, the lamellae-collimators are developed for monitoring the tumor during cancer treatment, for example, where the tumor's location is known a priori. For instance, CT images could provide information about the tumor localization, as this anatomical imaging technique is typically used for treatment planning [123, 124]. XFI could then be used for longitudinal studies to monitor the tumor response.

Collimator	FWHM [mm] for z_{Au} [mm]				
	-100	-75	-50	-25	0
$C_{L,v}$ collimator	4.7	4.7	6.3	8.3	10.5
$C_{L,h,s}$ collimator	14.1	16.3	20.3	24.8	30.3
$C_{L,h,180°}$ collimator	7.2	10.2	14.9	20.7	27.2

Table 8: The modeled FWHM of the collimator transmission distributions, depending on the collimator orientation and target position z_{Au}, are listed for the Vertical-Lamellae Collimator $C_{L,v}$, the shifted Horizontal-Lamellae Collimator $C_{L,h,s}$ at 150°, and the shifted Horizontal-Lamellae Collimator $C_{L,h,180°}$ at 180° with $y_s = 22$ mm.

Sensitivity Like the FOV, the sensitivity depends on the target position and the collimator used. The corresponding minimum detectable concentrations and masses of gold are summarized in Fig. 6.31. The minimum detectable mass is obtained by multiplying the minimum gold concentration by the target's volume, which is 7.85 µl. With greater depths and thus larger z_{Au}-values, the sensitivity decreases for all collimators, as reflected by the increasing minimum detectable concentrations and masses. However, the highest collimation effect is reached at deeper target depths, where the prominent background

at shallow depths can be collimated (Sec. 6.1.6, 6.2.6, 6.2.7). The Horizontal-Lamellae Collimator at 180° achieves the highest sensitivity compared to the other collimators for target locations up to z_{Au}=−50 mm, due to the short distance to the detector (Sec. 6.2.7). However, at greater depths with a target at −25 mm, the Horizontal-Lamellae Collimator at 150° is the most sensitive, while at 0 mm, the Vertical-Lamellae Collimator is the most sensitive. The Vertical-Lamellae Collimator collimates the background more strongly than collimators with horizontal lamellae, yet still allows enough fluorescence photons to be detected (Sec. 6.3). This is also reflected in the smaller FWHM, as discussed above. These results show that there is no universal best collimator for all depths. For compar-

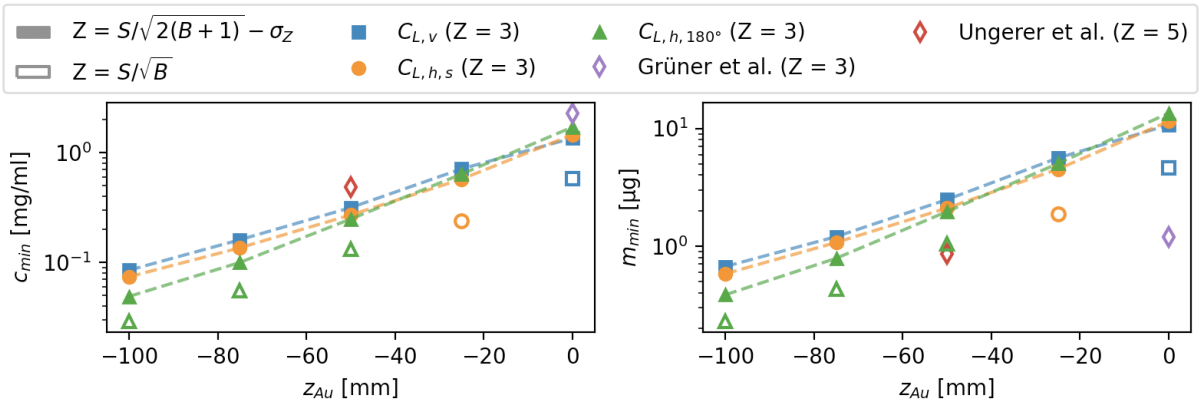

Figure 6.31: The minimum detectable concentrations c (left) and masses m (right) are shown as a function of the target position z_{Au} for the Vertical-Lamellae Collimator ($C_{L,v}$) (blue) and the shifted Horizontal-Lamellae Collimator at 150° ($C_{L,h,s}$) (orange) and at 180° ($C_{L,h,180°}$) (green). The mass is obtained by multiplying the concentrations by the irradiated target volume of 7.85 µl. For comparison, the results of Ungerer et al. [62] (red), with a gold target located in the lung within a human-sized voxel model, and Grüner et al. [28] (purple), with a gold target sphere located in the center of a soft-tissue sphere with a diameter of 30 cm, are shown. Note that the target volumes of Ungerer et al. and of Grüner et al. within the incident beam are 1.78 µl and 0.52 µl, respectively. Filled markers correspond to $Z = S/\sqrt{2B+2} - \sigma_Z = 3$ (Eq. 3.6) and unfilled markers correspond to $Z = S/\sqrt{B}$ (Eq. 3.3), for which Z = 3 holds, except for Ungerer et al., for whom Z = 5 was used.

ison, Fig. 6.31 shows reported sensitivities from the literature. A minimum detectable concentration of 2.3 mg/ml corresponds to the results published by Grüner et al. for a spherical gold target with a diameter of 1 mm located at the center of a soft-tissue sphere with a diameter of 30 cm [28]. Therefore, the minimum detectable gold concentration is higher than that in this thesis, where it is 1.36 mg/ml for a target in the object center at a depth of 150 mm, when $Z - \sigma_Z = 3$ (Eq. 3.6) holds, using Eq. 3.5 and Eq. 3.7. However, Grüner et al. considered a signal as detectable if $Z > 3$, according to Eq. 3.3. Therefore, the following comparison uses Eq. 3.3 for consistency. Under this condition, a gold concentration as low as 0.58 mg/ml is detectable, which is 25% of the 2.3 mg/ml gold concentration required in Grüner et al. However, the irradiated target volume of Grüner et al. is with 0.52 µl smaller than the one used in this thesis (7.85 µl). This is

accounted for by considering the minimum detectable masses, which are the product of the minimum concentrations and the irradiated volume. This results in detectable masses of a similar order of magnitude, but slightly lower, compared to the approach of Grüner et al., who detected 1.2 μg of gold. In contrast, in this thesis a gold mass of 4.6 μg is required according to the significance determination conditions in the paper (Eq. 3.3). Instead of using a cylinder as soft-tissue object, Grüner et al. used a sphere, which may partly explain the lower detectable masses. Due to the lower attenuation by a shorter path length within the smaller spherical object volume (2.12), the number of detected fluorescence photons is expected to increase. However, a cylinder better approximates the cross-section of a human body than a sphere does, though both are strong simplifications. Beyond comparing the object centers, it should be noted that the sensitivity is depth-dependent, and the target locations at the object centers are associated with the highest required concentrations and masses, thus the lowest sensitivity. For a target located at $z_{Au} = -50$ mm, at a depth of 100 mm, masses as low as 1.04 μg can be detected, and at a depth of 75 mm, a mass of 0.43 μg is necessary, both achieved with the Horizontal-Lamellae Collimator at 180°. Overall, the sensitivities of this thesis and that of Grüner et al. are of a similar order of magnitude, despite the fact that their approach uses a much larger detector area ($\approx 8\,\mathrm{m}^2$) compared to the setup presented here, which has a detector area of only 24 cm^2. In other words, Grüner et al.'s approach requires a detector area that is about three orders of magnitude larger, making the approach in this thesis much more practical and economical.

Ungerer et al. continued investigating the approach developed by Grüner et al. [28, 62]. In that study, however, the soft-tissue sphere was replaced by a human-voxel phantom and the minimum detectable gold concentrations were analyzed for a target within the lung, for example, at a depth of approximately 10 cm. A minimum detectable gold concentration of 0.49 mg/ml was achieved (Fig. 6.31). Therefore, the same equation (Eq. 3.3) as by Grüner et al. was used, but the significance limit was set to five instead of three to consider a signal significant. Under these conditions, the approach of this thesis achieves a minimum detectable gold concentration of 0.22 mg/ml, which is lower than the 0.49 mg/ml minimum reported by Ungerer et al. The 15.23 μl target volume used by Ungerer et al. is accounted for by considering the minimum detectable mass. This corresponds to a value of 7.31 μg, which exceeds the detectable mass for a 100 mm depth target when using the setup presented in this thesis. Unlike the case in the thesis, the target is not fully covered by the incident beam. Taking only the volume of 1.78 μl within the beam into account results in an irradiated mass of 0.86 μg. In the thesis scenario, under the same significance condition as Ungerer et al. using the Horizontal-Lamellae Collimator at 180°, a mass of 1.73 μg can be detected, which is slightly larger than the 0.86 μg detected by Ungerer et al. However, it is important to note that the minimum detectable concentrations are not directly comparable. In this thesis, the soft-tissue cylinder has a diameter of 30 cm, whereas Ungerer et al. considered a female human-voxel phantom with a maximum diameter of 24 cm [62]. The thorax slice that was examined to determine the minimum detectable concentration of a gold target in the lung is even smaller, with a diameter of approximately 18 cm. The incident beam propagated through this slice, resulting in a lower total attenuation compared to an object diameter of 30 cm.

Furthermore, unlike the cylindrical object in this thesis, the human-voxel phantom is inhomogeneous [62, 125]. This means that lower attenuation is expected in the lungs due to the air that is present. On the other hand, the human-voxel phantom also models bones, which are associated with higher densities and attenuation [125]. Nevertheless, the detectable masses in this thesis are of similar order of magnitude as those by Ungerer et al., and only slightly higher, even though they used a detector area about three orders of magnitude larger, as did Grüner et al. This underscores the potential of this thesis's approach.

In the setup used by Vernekohl et al. [29], a minimum gold concentration of 0.35 mg/ml was determined for a target being in the center of a lung phantom. The specific phantom diameter, and thus the actual depth of the target, are not mentioned. However, this corresponds to a concentration which is detectable at a depth of 100 mm within the approach presented in this thesis but not at a depth of 125 mm, since a concentration of 0.58 mg/ml is necessary at $z_{Au} = -25\,\text{mm}$ to obtain a detectable signal. The total target volume used, however, was about ten times larger (four targets of 19.6 μl each), the total detector area was almost seventy times larger (four detector panels of $26 \times 16\,\text{cm}^2$ each) and the dose in the lung center was almost ten times higher, at 30 mGy compared to 3.5 mGy in the center of the human-sized cylinder (Sec. 5.2). These factors, together with the use of a fan beam instead of a pencil beam, make a fair comparison difficult. Nevertheless, with the same dose of 30 mGy at the center of the cylinder object, the thesis approach could detect the same concentration within a target volume of 11.8 μl. Despite the smaller detector area in this thesis, this volume is still about 40% smaller than the one used by Vernekohl et al. [29] indicating that the approach in this thesis is more sensitive.

In the study by AL-Ghorabie [113], the cylindrical tumor phantom was placed inside a cylindrical neck phantom and photons were detected by a detector positioned at 180°. With a maximum total target depth of 30 mm, a minimum detectable concentration of approximately 50 ppm platinum was achieved, corresponding to 0.05 mg/ml platinum assuming a density of 1 g/ml. However, since AL-Ghorabie used a different target material (platinum), a different beam source (radioisotope ^{133}Xe) and a smaller detector area ($2\,\text{cm}^2$) compared to $24\,\text{cm}^2$ in this thesis, a direct comparison of the sensitivities is limited. Nevertheless, the detectable gold concentration of 0.049 mg/ml in this thesis is comparable to the platinum concentration of AL-Ghorabie, even at a greater depth of 50 mm, while the target volume (7.85 μl) is much smaller than the one used by AL-Ghorabie (1800 μl) [113].

The research group of Ahmed et al. also considered a lung phantom [120]. However, they simulated a 1.8 mm wide fan beam and two array detectors, containing 90 elements each with an area of 3 mm × 3 mm. Additionally, a parallel-hole collimator was attached to the detector and gold targets with dimensions of 9.3 mm × 9.3 mm × 5.0 mm, corresponding to a volume of $432\,\text{mm}^3$, were placed at various locations in the lung phantom. Finally, concentrations of about 3 mg/ml gold were detectable at depths up to 40-50 mm. This concentration is much higher than the 0.49 mg/ml achievable at a depth of 50 mm in this thesis. Furthermore, the target volume in the study by Ahmed et al. is much larger, resulting in a significantly higher total gold mass (1297 μg). Thus, the approach presented in this thesis suggests a much higher sensitivity, as demonstrated by Ahmed et al.

In a CT study by Oumano et al. [126], the minimum gold concentration was determined to be 1.35 mg/ml for an object with a diameter of 33 cm and a 1 mm thick CT slice using a conservative approach with a dose of 23.6 mGy. With a second approach, they estimated a lower detection limit corresponding to a detectable gold concentration of 0.32 mg/ml [126]. Furthermore, CT imaging achieves contrast through differently strong photon transmissions caused by different material densities within the object in the forward direction [11]. According to the Beer-Lambert law (2.11), the detected total attenuation of the incident beam is independent of the target position and no target-depth-dependent sensitivities are expected, unlike in XFI, where, at a depth of 100 mm ($z_{Au} = -50$ mm), concentrations as low as 0.25 mg/ml can be detected with the Horizontal-Lamellae Collimator at 180°. This is lower than the most optimistic detectable concentration reported for CT under the investigated conditions by Oumano et al., suggesting that XFI can achieve a higher sensitivity [126]. This is emphasized when considering a depth of 50 mm ($z_{Au} = -100$ mm), where the sensitivity in XFI with the thesis approach is at least seven times higher than the optimistic detection limit and about 27 times higher than the conservative detection limit in CT, which demonstrates the potential of XFI in comparison to CT. It should be noted, however, that a direct quantitative comparison with the sensitivities determined in this thesis is limited, as the imaging setups and the criteria used to define a significant signal differ between the CT study and this thesis.
Overall, the combination of spectral filtering by a detector in the backward direction and lamellae-based collimators shows comparable sensitivities to those in the literature and slightly lower ones compared to a 4π-detector. However, it should be mentioned that the required gold masses, particularly at deeper target positions, remain relatively high and further investigation is recommended to improve the sensitivity at greater depths. Therefore, this approach could be of particular interest for monitoring treatments of tumors at shallower depths, such as breast cancer, since the strategy presented in this thesis offers a more practicable and economical application than other XFI setups. Nevertheless, the necessary mass of 10.7 μg at $z_{Au} = 0$ mm would, for example, still be well below a gold mass of 0.35 mg or a systemic concentration of 0.005 mg/kg, at which some gene expression changes occurred in the liver (Sec. 3.5) [101].

Limitations The approach to reduce the background problem in human-sized objects has limitations and requires assumptions. First, the target location has to be known because the collimator has different geometries for different foci, and the lamellae have to be adjusted. Therefore, this approach is not applicable to pharmacokinetics. However, it could be used to monitor the response to a cancer treatment.
Second, a homogeneous soft-tissue cylinder was used as a human-sized phantom. Due to more complex inhomogeneities in the human body caused by different materials, such as bones, and the cylinder's simplified shape, the attenuation might differ. However, for targets located primarily within soft tissue, no major deviation is expected.
Furthermore, this method only considers a maximum depth up to the phantom's center and for deeper depths, the beam would be applied to a different side of the object. This means that either the location of the beam source would have to change or the object would have to be reoriented when imaging a target deeper within the object.

However, irradiating an object from different sides is a common approach in other imaging modalities [13]. Another limitation is the monochromatic beam with a diameter of 1 mm and with 1.3×10^9 incident photons. These properties can be provided by synchrotron light sources [11]. For example, the P21.1 beamline at PETRA III (DESY, Hamburg, Germany) can offer a beam size of about $1\,\mathrm{mm}^2$ with energies between 40-150 keV and a high photon flux of 10^{10} to 10^{12}, offering low scan times [62, 27]. However, the access to synchrotrons is limited and they are costly and large-scale. Therefore, alternative, laboratory-based beam sources are being developed, such as laser-driven X-ray sources [11, 81].
In the data analysis of the Geant4 simulations, the recorded counts were considered, taking into account the energy resolution of a realistic detector, as well as the detector material's intrinsic fluorescence. However, charge sharing which occurs in the HEXITEC detector, was neglected and could decrease the significance further.

7 Test Measurement for Experimental Validation

A test measurement for experimental validation of the collimator systems described in the previous section was conducted at the PETRA-III synchrotron (DESY, Hamburg, Germany) on beamline P21.1.

7.1 Setup

The test measurement was conducted with an incident energy of 101.4 keV and a flux of $3.3 \times 10^{10} \frac{photons}{s \cdot mm^2}$. Note that the incident energy used in the experiment is higher than 81 keV simulated in the previous scenarios. This is due to the limited possibility of changing the incident beam energy at the beamline P21.1. A human-sized object was mimicked by a cylinder made of polymethyl methacrylate (PMMA) with a radius of 150 mm and a height of 60 mm which was mounted on an aluminium base plate. Inside the cylinder, a 1.4 ml gold-water solution (Au target) was placed in an Eppendorf tube with a capacity of 1.5 ml and a maximum inner diameter of 9.85 mm, which is comparable to the previously simulated target size. This tube was inserted into the cylinder such that the tube's cap was at a distance of 18 mm from the upper circular cylinder base and was simultaneously located on the beam axis at a depth of 50 mm within the cylinder.
Based on the previous simulations, a collimator design consisting of 15 tantalum plates, each 0.2 mm thick and 64 mm long, was constructed to collimate the background. Contrary to Sec. 6.2, a shorter lamella length was chosen to ensure a safety distance to the detector chip of the planned detector. These lamellae were arranged horizontally and, for safety reasons, at a distance of 6 mm to the detector. The orientation of the plates

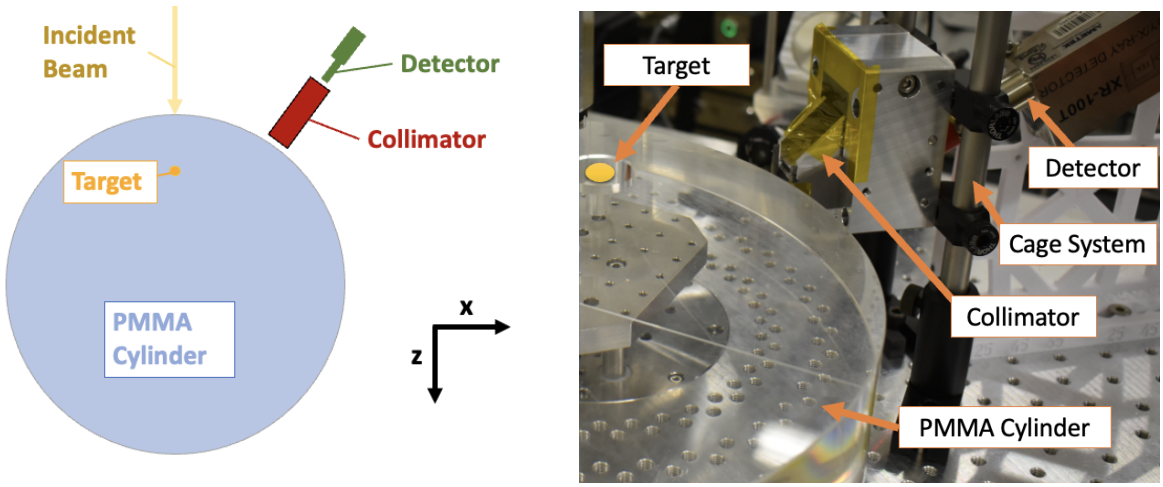

(a) Schematic setup (top view) (b) Photo of the setup

Figure 7.1: The experimental setup at the synchrotron beamline P21.1 is shown schematically (a) and via a photographic image (b). An Eppendorf tube (target) is inserted into a PMMA cylinder at a depth of 50 mm and is irradiated by the incident beam. A collimator is placed in front of the detector.

is designed in such a way that they point toward the center of the Au target, corresponding to the presented shifted Horizontal-Lamellae Collimator in Sec. 6.2. To mount the horizontal tantalum plates, a 3 mm thick aluminium holder was constructed on both sides. Additionally, to minimize background radiation, a 2 mm thick tantalum plate was attached at each side, at the top and bottom.
The detector was placed at an angle of about 150° to the incident beam and a distance of 225 mm to the PMMA cylinder. For detection, the HEXITEC detector was planned, as it provides both a larger detector area of 400 mm^2 and thus higher coverage, as well as spectral resolution due to its pixels, unlike the much smaller Amptek CdTe detector (Sec. 3.4). Due to technical issues with the HEXITEC detector, however, an Amptek detector equipped with a cadmium telluride detector chip was used instead on short notice. Consequently, the collimator could not be attached directly to the detector and was instead positioned using cage systems from Thorlabs, as shown in Figure 7.1, which did introduce some inaccuracies.
In a first measurement, a gold reference target was placed in the center of the beam to generate fluorescence counts. This allowed the alignment of both the collimator and the detector to be checked and corrected. The fine adjustments were completed as soon as a gold signal became visible in the spectrum. In this case, the signal from the Au-L_α line at 9.7 keV reached a significance of up to $Z = 9$ at 9.7 keV, while the signal from the Au-K_α line reached a maximum significance of $Z = 5$ (Eq. 3.9). After alignment, the gold reference target was replaced by the PMMA cylinder with an inserted Eppendorf tube containing a gold-water solution of 10.0 mg/ml. The target was located at the same position as the reference target in the alignment experiment, at a depth of 50 mm within the PMMA cylinder along the beam axis (Fig. 7.1). The efficiency of the collimator design was verified by comparing a measurement with the collimator to a measurement without the collimator.
To minimize statistical uncertainties and to prevent detector damage caused by a too-high input rate, four absorbers were used as a compromise in the experiment with the collimator, and measurements were taken for 35 minutes. In the second experiment, without the collimator, seven absorbers had to be used due to the higher input rate, and measurements were taken for 25 minutes. Here, one absorber corresponds to 0.1 mm of tantalum and reduces the incident photon beam intensity by about 50%, which can be calculated using the Beer-Lambert law of transmission. Accordingly, the transmission is 6.29% with four absorbers and 0.79% with seven absorbers. In order to compare these experiments, the recorded counts from the experiments with a collimator are finally multiplied by factors corresponding to the scenario with seven absorbers and a measurement time of 25 minutes.

7.2 Experimental Results

In Fig. 7.2, the experimentally recorded spectra of the cylindrical PMMA phantom are shown for both scenarios, with and without a collimator. The cylinder has a diameter of 300 mm along the beam axis, resulting in a high probability of interaction between photons and the phantom. In particular, as shown in the previous sections, Compton scattering is a dominant interaction in human-sized objects. It causes the broad spectra in both scenarios, with a C1 peak at 77.8 keV in the scenario without a collimator and at 77.2 keV in the scenario with a collimator. The high incident beam energy of 101.4 keV, compared to the simulated 81 keV in the previous sections, is responsible for the C1 peak being located at higher energies. In this case, it is located in the K_β energy range of gold. However, this is not the case for the recommended incident energy of 81 keV (Sec. 5.3.2). The effect of the collimator becomes clear when comparing both recorded spectra (Fig. 7.2) since the collimator enables a reduction of the total recorded counts to 6%, which corresponds well to the simulated photon count reduction to 5% (Appendix: Fig. A.3). The remaining 1% discrepancy is likely due to the alignment uncertainties in the experiment. While a maximum of 3.2×10^4 photons are detected at the C1 peak in the scenario with the collimator, more than an order of magnitude more photons (6.7×10^5 photons) are detected in the case without the collimator. This corresponds to a reduction of the background to about 4.8%. In the Au-K_α signal range, the background can even be further reduced to 3.7% at 69 keV. Note that the decreasing efficiency of the collimator for energies above 85 keV can be attributed to the collimator not being directly attached to the detector, allowing photons to enter from the side. With an ideal detector housing up to the collimator, however, these counts are minimized (Appendix: Fig. A.5).

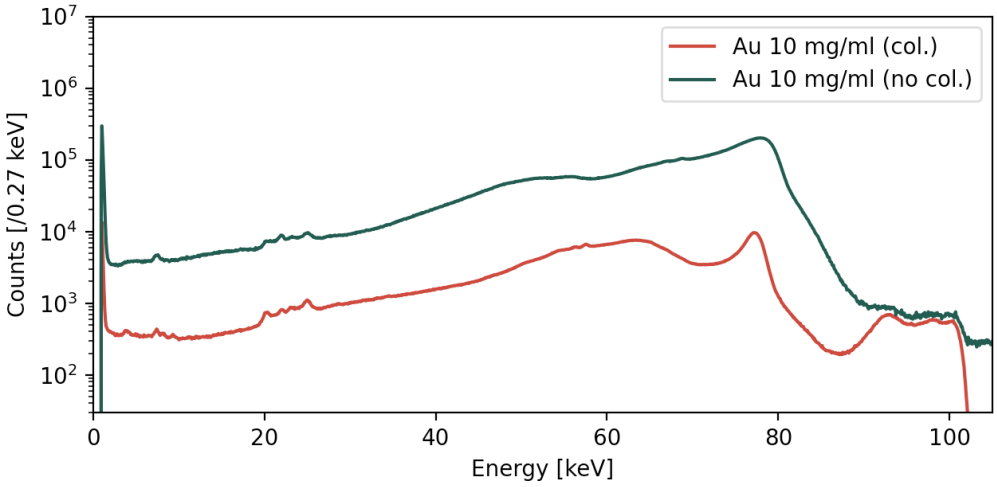

Figure 7.2: The experimentally recorded spectra of a PMMA cylinder with (red) and without the collimator (green) are shown for an incident beam energy of 101.4 keV. The target is a water-gold solution with a gold concentration of 10 mg/ml.

Nevertheless, many gold fluorescence photons do not pass through the collimator spaces but are absorbed by it, although some gold fluorescence photons were detected

in the previous alignment experiment. This can probably be attributed to an insufficiently precise alignment of the collimator and detector with respect to the fluorescence paths, once the original setup with the HEXITEC detector was no longer applicable. Due to the different shape of the Amptek detector used compared to the planned HEXITEC detector, the initially designed detector mounts could not be used, and the collimator could not be attached directly to the detector as intended for the HEXITEC detector. As a result, alignment inaccuracies likely arose, leading to the absorption of the signal photons. The impact of the alignment is discussed in more detail in the following Sec. 7.3.

It is also worth mentioning that in the experiments, counts are observed whose energies exceed the incident energy of 101.4 keV, which can be explained by the pile-up effect of the detector (Sec. 3.4). Another detector-related effect is the peak due to electronic noise, which occurs at low energies around 1 keV and is caused by the threshold set on the detector (Sec. 3.4).

7.3 Impact of the Alignment

The invisible gold signal in the experimental results shown in Fig. 7.2 can be understood by Fig. 7.3, which shows several simulations with the setup described in Sec. 7.1 but with altered collimator and detector alignments. For the simulations, 10^{11} incident photons and the Amptek's energy resolution are used. When the collimator is shifted in the positive y-direction by $\Delta y_L = 2\,\text{mm}$, the intensity of the C1 peak decreases and the peak appears at lower energies. Meanwhile, the lower-energy Compton continuum caused by multiple Compton scattering remains almost unchanged. This is due to the change in the FOV of the detector caused by the different collimator position. (The FOVs for all simulated alignments can be found in the Appendix (Fig. A.4)). The shift of 2 mm in the y-direction causes the collimator to focus on greater depths than the collimator with $\Delta y_L = 0\,\text{mm}$ and restricts the detection of photons from shallower depths. This results in a higher collimation of C1 photons from shallower depths, which are associated with higher energies, hence a lower-energetic C1 peak appears. The stronger attenuation at greater depths explains the intensity reduction of the C1 peak (Eq. 2.12). At the same time, the collimator's different focus along the beam axis results in more fluorescence photons being blocked by the collimator.

In addition to the collimator alignment, the position of the detector affects the recorded spectrum, as shown in Fig. 7.3. If the detector is not aligned with the center of the collimator, the spectrum changes. For instance, moving the detector to a lower y-position relative to the collimator center by changing the angle $\alpha_{D,y}$ increases in the multiple-Compton scattering background, yet the C1 peak remains at nearly the same energy with an almost identical simulated count rate. This can be observed by comparing the green curve ($\alpha_{D,y} = 8.0°$) with the blue curve ($\alpha_{D,y} = 6.5°$). Because the collimator is not positioned directly in front of the detector, background photons can reach the detector from the side without passing through the collimator. These photons are scattered primarily within the object first, then at the base plate of the P21 setup, and sometimes in the air before being detected. For example, a detector positioned at an angle of α_D=148.5°, lo-

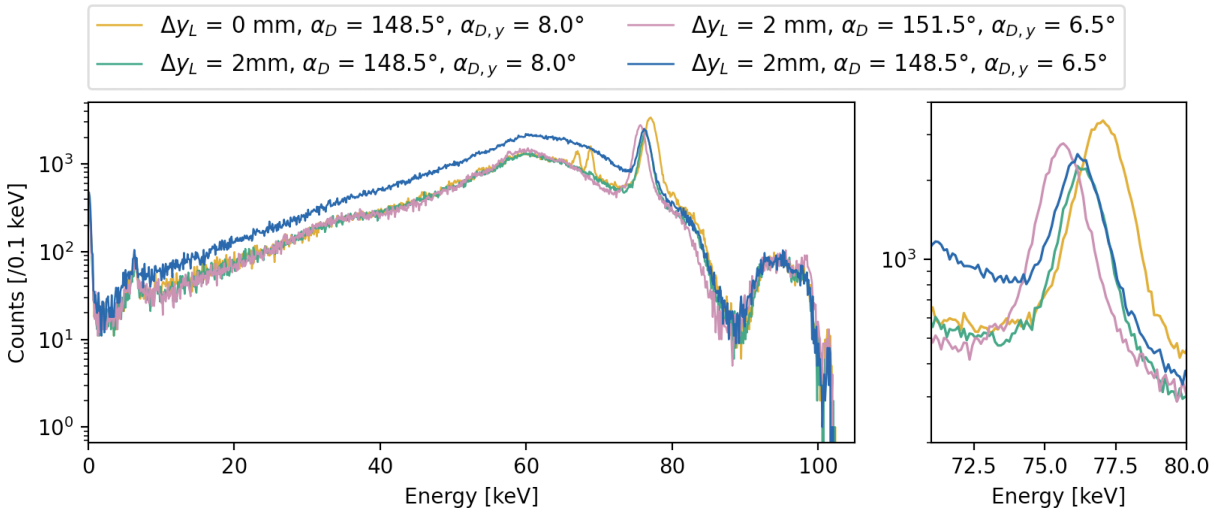

Figure 7.3: The simulated spectra for various detector and collimator alignments are shown. The parameter Δy_L describes the displacement of the collimator in the y-direction with respect to the planned position, α_D describes the angle of the detector in the equatorial xz-plane with respect to the phantom center, and $\alpha_{D,y}$ describes the angular position of the detector relative to the xz-plane. Note that the collimator is designed for the following parameter: $\Delta y_L = 0\,\text{mm}$, $\alpha_D = 150°$, $\alpha_{D,y} = 8°$. Furthermore, the collimator design remains fixed in these simulations, only the location of the collimator and detector vary. The detector area and resolution of the CdTe Amptek are considered. This plot shows that within the Au-K_β signal range (right), no gold signal is visible, and due to a displacement of the collimator by $\Delta y_L = 2\,\text{mm}$, the signal in the Au-$K_\alpha$ range (67 - 69 keV) vanishes.

cated lower at $\alpha_{D,y} = 6.5°$ rather than at $\alpha_{D,y} = 8.0°$, is closer to the base plate, resulting in the detection of more scattered photons. Furthermore, at a lower position, closer to the edge of the collimator, less shielding by the collimator is expected. However, adding a detector shield at the sides of the detector up to the collimator suppresses these photons, minimizing the difference in the simulated spectra for $\alpha_{D,y} = 6.5°$ and $\alpha_{D,y} = 8.0°$ (Appendix: Fig. A.5). For comparison, less background is detected when the detector is shifted from an angle of $\alpha_D = 148.5°$ to $\alpha_D = 151.5°$ with $\alpha_{D,y} = 6.5°$. In this case, the detector is located on the collimator side closer to the beam source, where fewer photons have undergone Compton scattering, and in addition, due to the orientation of the collimator, the detector is better shielded from the side where the main cylinder is located and where therefore most Compton photons are generated. Finally, fewer photons that do not pass the collimator are recorded, while the photons passing the detector define the background peak by C1 photons, which has a slightly lower energy at $\alpha_D = 151.5°$ compared to $\alpha_D = 148.5°$. This is due to the geometry of the collimator, which, at larger detector angles, only allows C1 photons from greater depths within the PMMA cylinder to pass through, resulting in larger scattering angles and thus lower energy.
Overall, these simulations demonstrate the importance of precisely aligning the detector and collimator because even slight inaccuracies can result in the loss of the fluorescence

signal. However, inaccuracies in the detector position relative to the collimator are expected to be minimized when using the HEXITEC detector, to which the collimator can be mounted directly, or when using the Amptek detector with a more precise collimator holder. Furthermore, the experimental data demonstrate the collimator's potential to significantly reduce background by up to 94%, leaving only 6% compared to the uncollimated case.

8 Conclusion and Outlook

The goal of this thesis was to study the spatial distribution of photons in human-sized objects and to find a collimation strategy that can reduce the high amount of background noise associated with such objects. Unlike previous studies, the aim was to find a more practical and economical solution, meaning a more compact setup, including a smaller detector area.

Using the numerical model, the spatial distribution of multiple Compton-scattered photons was studied, revealing that the solid angle considerably impacts the detection probability, as the paths with the highest probability are associated with large solid angles. Consequently, for a detector positioned at the edge of an object, paths that undergo their final scattering event near the detector are associated with high probabilities. Additionally, photon paths of double Compton scattering are more likely to undergo the final scattering close to the incident beam where the previous (first) scattering occurs. However, when the detector is located further away, the effect of high probabilities close to the edge of the object disappears.
In order to develop a collimation strategy, the behavior of the detected background and fluorescence photons was first studied, as well as their significance within the K_α and K_β energy ranges of gold, for different detector angles without a collimator. A backward detector in combination with the K_β energy range was identified as the most promising approach. Due to large scattering angles, most background photons are too low in energy to fall within the K_β energy range, and single Compton-scattered photons dominate the background due to Doppler broadening.
Based on the results from the uncollimated XFI scenario, a detector was chosen in the backward direction and collimators consisting of either vertical or horizontal lamellae were designed. These collimators restricted the FOV of the detector along the incident beam, which is the origin of the background photons that undergo one Compton scattering only and constitute the largest part of the background. The detector's FOV was more restricted along the beam axis by the Vertical-Lamellae collimator than by the Horizontal-Lamellae Collimator. However, shifting the detector with the Horizontal Lamellae Collimator out of the beam plane and positioning it in vertical direction reduces the FOV along the beam axis, thereby increasing the significance. Additionally, an optimum significance was found when varying the collimator parameters, including the material, thickness, number and length of the lamellae with tantalum being identified as an effective material due to its high absorption coefficient in the relevant energy range. It was discovered that using the shifted horizontal lamellae collimator at a detector angle of 180° instead of 150° further increased the sensitivity up to a depth of approximately 100 mm. For greater target depths, however, the shifted horizontal lamellae collimator at 150° provided a higher sensitivity. Nonetheless, the vertical lamellae collimator offered the best performance for targets at the object center at a depth of 150 mm and achieved higher sensitivities than the other collimators. These results demonstrate that there is no universally best collimator because performance depends on the target depth. Furthermore, a comparison with hole collimators (including parallel-hole and converging-hole collimators) revealed that lamellae-based

collimators more effectively increase the signal significance and, consequently, the sensitivity, because hole-based collimators have a smaller angular acceptance and therefore block a larger fraction of fluorescence photons. Moreover, an experimental test measurement revealed that precise alignment is required and that the collimator blocks a comparable amount of background photons as expected from simulations.
This study demonstrates that comparable sensitivities to those reported in the literature can be achieved, including achieving a similar order of magnitude as approaches using a detector approximately three orders of magnitude larger. Consequently, these results suggest that XFI could be a feasible option for imaging human-sized objects in the context of multimodal imaging using a smaller, more economical setup.
Based on the results of this thesis, the next step should be to simulate a more realistic scenario, such as a human voxel model. This would allow the different structures and inhomogeneities within the body to be taken into account, as the homogeneous soft-tissue cylinder analyzed in this study is simplified. For instance, the lower densities expected in the lungs and the higher densities in the bones would no longer be neglected. Additionally, a pixelated detector should be considered, as it could provide more information about the target location. The pixelated HEXITEC detector is a promising option for this purpose due to its larger size compared to the Amptek detector. Hence, charge sharing, a HEXITEC detector effect, should also be included in the simulations. Furthermore, it is recommended to validate the simulated results experimentally with a more precise alignment. Since the setup is less sensitive at greater depths due to fewer gold K_β fluorescence photons resulting from a larger path length, investigating the K_α energy range more precisely at those greater depths may be worthwhile, as more K_α fluorescence photons are present. One approach could be to collimate all photons originating from outside the beam plane because they form a large fraction of the background and originate from different locations than the fluorescence photons, as shown in the background analysis.

Bibliography

[1] World Health Organization. *Cancer*. 2026. URL: https://www.who.int/news-room/fact-sheets/detail/cancer (visited on 06/15/2026).

[2] World Health Organization. *Global cancer burden growing, amidst mounting need for services*. 2024. URL: https://www.who.int/news/item/01-02-2024-global-cancer-burden-growing--amidst-mounting-need-for-services (visited on 06/15/2026).

[3] NIH: National Cancer Institute. *What is Cancer*. 2021. URL: https://www.cancer.gov/about-cancer/understanding/what-is-cancer (visited on 06/15/2026).

[4] Paula A. Oliveira and Ana I. Faustino-Rocha. "Chemical Carcinogens". In: *Cancer and Surrounding Environment: Etiologies and Tumor Microenvironment*. Ed. by Nima Rezaei. Cham: Springer Nature Switzerland, 2025, pp. 519–541. DOI: 10.1007/978-3-032-00761-2_121. URL: https://doi.org/10.1007/978-3-032-00761-2_121.

[5] V. Butnari, P. Scantlebury, and T. Green. "The crucial role of early diagnosis for patients and the nation, understanding the costs of late-stage cancer diagnosis from a large district general hospital in England". In: *Cost Effectiveness and Resource Allocation* 23.60 (2025). DOI: https://doi.org/10.1186/s12962-025-00657-1.

[6] Leonard Fass. "Imaging and cancer: A review". In: *Molecular Oncology* 2.2 (2008), pp. 115–152. DOI: https://doi.org/10.1016/j.molonc.2008.04.001. eprint: https://febs.onlinelibrary.wiley.com/doi/pdf/10.1016/j.molonc.2008.04.001. URL: https://febs.onlinelibrary.wiley.com/doi/abs/10.1016/j.molonc.2008.04.001.

[7] Xiang Wang et al. "Current status and future prospects of molecular imaging in targeting the tumor immune microenvironment". In: *Frontiers in Immunology* 16 (2025). ISSN: 1664-3224. DOI: 10.3389/fimmu.2025.1518555. URL: https://www.frontiersin.org/journals/immunology/articles/10.3389/fimmu.2025.1518555.

[8] Johanna Bischof et al. "Multimodal bioimaging across disciplines and scales: challenges, opportunities and breaking down barriers". In: *npj Imaging* 2.1 (2024). DOI: 10.1038/s44303-024-00010-w.

[9] Dengwei Gan et al. "Advances in Functional and Metabolic Imaging for Early Tumor Treatment Response and Resistance Evaluation: A Review". In: *Cancers* 18.5 (2026). ISSN: 2072-6694. DOI: 10.3390/cancers18050858. URL: https://www.mdpi.com/2072-6694/18/5/858.

[10] Stephanie Histed et al. "Review of functional/anatomical imaging in oncology". In: *Nuclear medicine communications* 33 (Apr. 2012), pp. 349–61. DOI: 10.1097/MNM.0b013e32834ec8a5.

[11] Theresa Staufer and Florian Grüner. "Review of Development and Recent Advances in Biomedical X-ray Fluorescence Imaging". In: *International Journal of Molecular Sciences* 24.13 (2023). ISSN: 1422-0067. DOI: 10.3390/ijms241310990. URL: https://www.mdpi.com/1422-0067/24/13/10990.

[12] Xiangyu Ou et al. "Recent Development in X-Ray Imaging Technology: Future and Challenges". In: *Research* 2021 (2021). DOI: 10.34133/2021/9892152. eprint: https://spj.science.org/doi/pdf/10.34133/2021/9892152. URL: https://spj.science.org/doi/abs/10.34133/2021/9892152.

[13] Yoleidy Huérfano-Maldonado et al. "A comprehensive review of extreme learning machine on medical imaging". In: *Neurocomputing* 556 (2023), p. 126618. ISSN: 0925-2312. DOI: https://doi.org/10.1016/j.neucom.2023.126618. URL: https://www.sciencedirect.com/science/article/pii/S0925231223007415.

[14] Joanne D. Schuijf et al. "CT imaging with ultra-high-resolution: Opportunities for cardiovascular imaging in clinical practice". In: *Journal of Cardiovascular Computed Tomography* 16.5 (2022), pp. 388–396. ISSN: 1934-5925. DOI: https://doi.org/10.1016/j.jcct.2022.02.003. URL: https://www.sciencedirect.com/science/article/pii/S1934592522000235.

[15] Alan C. Kwan et al. "Next-Generation Hardware Advances in CT: Cardiac Applications". In: *Radiology* 298.1 (2021). PMID: 33201793, pp. 3–17. DOI: 10.1148/radiol.2020192791. eprint: https://doi.org/10.1148/radiol.2020192791. URL: https://doi.org/10.1148/radiol.2020192791.

[16] Ritse M. Mann, Nariya Cho, and Linda Moy. "Breast MRI: State of the Art". In: *Radiology* 292.3 (2019). PMID: 31361209, pp. 520–536. DOI: 10.1148/radiol.2019182947. eprint: https://doi.org/10.1148/radiol.2019182947. URL: https://doi.org/10.1148/radiol.2019182947.

[17] Jeff H. Duyn. "The future of ultra-high field MRI and fMRI for study of the human brain". In: *NeuroImage* 62.2 (2012). 20 YEARS OF fMRI, pp. 1241–1248. ISSN: 1053-8119. DOI: https://doi.org/10.1016/j.neuroimage.2011.10.065. URL: https://www.sciencedirect.com/science/article/pii/S1053811911012298.

[18] Clio Ribbens and Roland Hustinx. "Chapter 7 - NUCLEAR (SCINTIGRAPHIC) METHODS AND FDG-PET IN RHEUMATOID ARTHRITIS AND OSTEOARTHRITIS". In: *Arthritis in Color*. Philadelphia: W.B. Saunders, 2009, pp. 138–149. ISBN: 978-1-4160-4722-3. DOI: https://doi.org/10.1016/B978-1-4160-4722-3.00007-0. URL: https://www.sciencedirect.com/science/article/pii/B9781416047223000070.

[19] Timothy G. Turkington. "Introduction to PET Instrumentation". In: *Journal of Nuclear Medicine Technology* 29.1 (2001), pp. 4–11. ISSN: 0091-4916. eprint: https://tech.snmjournals.org/content/29/1/4.full.pdf. URL: https://tech.snmjournals.org/content/29/1/4.

[20] Yaser Gholami. "Positron annihilation localization by nanoscale magnetization". In: *Scientific Reports* 10 (Nov. 2020), p. 20262. DOI: 10.1038/s41598-020-76980-9.

[21] Dale L. Bailey and Kathy P. Willowson. "An Evidence-Based Review of Quantitative SPECT Imaging and Potential Clinical Applications". In: *Journal of Nuclear Medicine* 54.1 (2013), pp. 83–89. ISSN: 0161-5505. DOI: 10.2967/jnumed.112.111476. eprint: https://jnm.snmjournals.org/content/54/1/83.full.pdf. URL: https://jnm.snmjournals.org/content/54/1/83.

[22] Carolin von der Osten-Sacken et al. "Numerical Study towards In Vivo Tracking of Micro-/Nanoplastic Based on X-ray Fluorescence Imaging". In: 12.7 (2024). DOI: 10.3390/biomedicines12071500. URL: https://www.mdpi.com/2227-9059/12/7/1500.

[23] Valentin Lider. "X-ray fluorescence imaging". In: *Physics-Uspekhi* 61 (July 2017). DOI: 10.3367/UFNe.2017.07.038174.

[24] Kunal Kumar, Melanie Fachet, and Christoph Hoeschen. "High-Spatial-Resolution Benchtop X-ray Fluorescence Imaging through Bragg-Diffraction-Based Focusing with Bent Mosaic Graphite Crystals: A Simulation Study". In: *International Journal of Molecular Sciences* 25.9 (2024). ISSN: 1422-0067. DOI: 10.3390/ijms25094733. URL: https://www.mdpi.com/1422-0067/25/9/4733.

[25] Florian Grüner et al. "Comparing the Achievable Sensitivity Limits of Synchrotron-based X-ray Fluorescence Imaging versus conventional X-ray absorption imaging and comparing absorbed dose levels including PET/SPECT". In: *Zeitschrift für Medizinische Physik* (2025). ISSN: 0939-3889. DOI: https://doi.org/10.1016/j.zemedi.2025.04.001. URL: https://www.sciencedirect.com/science/article/pii/S0939388925000704.

[26] Katarina Vogel-Mikus. "Synchrotron X-Ray Fluorescence Imaging and Recent Developments". In: Oct. 2025, pp. 77–112. ISBN: 978-3-031-98374-0. DOI: 10.1007/978-3-031-98375-7_4.

[27] Deutsches Elektronen-Synchrotron DESY. A Research Center of the Helmholtz Association. *PHOTON SCIENCE: PETRA III Beamlines*. 2026. URL: https://photon-science.desy.de/facilities/petra_iii/beamlines/index_eng.html (visited on 06/16/2026).

[28] Florian Grüner et al. "Localising functionalised gold-nanoparticles in murine spinal cords by X-ray fluorescence imaging and background-reduction through spatial filtering for human-sized objects". In: *Scientific Reports* 8 (Nov. 2018). DOI: 10.1038/s41598-018-34925-3.

[29] Don Vernekohl et al. "Feasibility study of Compton cameras for x-ray fluorescence computed tomography with humans". In: *Physics in medicine and biology* 61.24 (Nov. 2016), pp. 8521–8540. ISSN: 0031-9155. DOI: 10.1088/0031-9155/61/24/8521.

[30] Quantum Detectors. *HEXITEC*. 2022. URL: https://quantumdetectors.com/wp-content/uploads/2024/02/HEXITEC-Application-Note-DIGITAL.pdf (visited on 03/23/2026).

[31] Amptek. *XR100 CdTe: X-Ray and Gamma Ray Detector and Preamplifier*. URL: https://www.amptek.com/-/media/ametekamptek/documents/resources/products/specs/xr100cdte-specs.pdf?la=en&revision=ddade6a1-e35a-4143-88b4-ce1eb2a035eb (visited on 03/23/2026).

[32] patent application filed by UHH, August 2026.

[33] Godfrey N. Hounsfield. "Computed Medical Imaging". In: *Science* 210 (4465 1980), pp. 22–28. DOI: 10.1126/science.6997993. URL: https://www.science.org/doi/10.1126/science.6997993.

[34] Hanno Krieger. *Grundlagen der Strahlungsphysik und des Strahlenschutzes*. 7th ed. Springer Spektrum, 2023. ISBN: 978-3-662-67609-7.

[35] Birgit Dörschel, Volkmar Schuricht, and Joachim Steuer. *Praktische Strahlenschutzphysik*. Spektrum Akademischer Verlag Heidelberg Berlin New York, 1992. ISBN: 3-86025-013-2.

[36] Tom Schoonjans. *The xraylib API list of all functions*. 2024. URL: https://github.com/tschoonj/xraylib/wiki/The-xraylib-API-list-of-all-functions#cross-sections (visited on 11/19/2025).

[37] Jens Falta and Thomas Möller. *Forschung mit Synchrotronstrahlung: Eine Einführung in die Grundlagen und Anwendungen*. 1st ed. Vieweg+Teubner Verlag, 2010. ISBN: 978-3-519-00357-1.

[38] David Halliday, Robert Resnick, and Jearl Walker. *Physik: Bachelor-Edition*. 2nd ed. WILEY-VCH Verlag GmbH & Co. KGaA, 2013. ISBN: 978-3-527-41181-8.

[39] W. S. C. Williams. *Nuclear and Particle Physics*. Oxford Science Publications, 1991.

[40] Claude Cohen-Tannoudji, Jacques Dupont-Roc, and Gilbert Grynberg. *Atom-Photon Interactions*. Wiley-VCH Verlag GmbH & Co. KGaA, 2004.

[41] Bernd Crasemann. *ATOMIC INNER-SHELL PHYSICS*. 1st ed. Plenum Press, New York, 1985. ISBN: 978-1-4612-9472-6.

[42] Wolfgang Demtroeder. *Atoms, Molecules and Photons: An Introduction to Atomic-, Molecular- and Quantum Physics*. 3rd ed. Springerxf-Verlag GmbH, 2018. ISBN: 978-3-662-55521-7.

[43] Donald T. Graham, Paul Cloke, and Martin Vosper. *PRINCIPLES AND APPLICATIONS OF RADIOLOGICAL PHYSICS*. 6th ed. CHURCHILL LIVINGSTONE ELSEVIER, 2011. ISBN: 978-0-7020-5215-6.

[44] Cosimo Bambi and Andrea Santangelo. *Handbook of X-ray and Gamma-ray Astrophysics*. Springer Nature Singapore Pte Ltd., 2024. ISBN: 9789811969607.

[45] Frank Herbert Attix. *Introduction to Radiological Physics and Radiation Dosimetry*. WILEY-VCH Verlag GmbH &Co. KGaA, 2004. ISBN: 978-0-471-01146-0.

[46] Eva Bezak et al. *THE PHYSICS OF RADIOLOGY*. 6th ed. Charles C Thomas, Publisher, LTD, 2021. ISBN: 978-0-398-09294-8.

[47] "Insight into the Bouguer-Beer-Lambert Law: A review". In: *Sustainable Chemical Engineering* (2024). DOI: 10.37256/sce.5220245325.

[48] Iliyasu Usman, Mukhtar Bature, and Muttaka Umar et al. "Photon attenuation properties of samarium-doped zinc bismuth silicate glass: A study using Cs-137, Co-60, and Na-22 Radiation Sources". In: *Caliphate Journal of Science and Technology* 6.3 (2024), pp. 281–288. DOI: 10.4314/cajost.v6i3.5.

[49] Volodymyr Mosorov. "The Lambert-Beer law in time domain form and its application". In: *Applied Radiation and Isotopes* 128 (2017), pp. 1–5. ISSN: 0969-8043. DOI: https://doi.org/10.1016/j.apradiso.2017.06.039. URL: https://www.sciencedirect.com/science/article/pii/S0969804317300878.

[50] U.S. Department of Commerce. *Select a material:* URL: https://physics.nist.gov/cgi-bin/Star/compos.pl (visited on 12/01/2025).

[51] Jacob Beutel, Harold L. Kundel, and Richard L. Van Metter. *Handbook of Medical Imaging: Volume 1. Physics and Psychophysics*. 2nd ed. SPIE-The International Society for Optical Engineering, 2000. ISBN: 9780819481184. DOI: https://doi.org/10.1117/3.832716.

[52] Harry E. Martz Jr, Clint M. Logan, and Daniel J. Schnerberk. *X-RAY IMAGING: Fundamentals, Industrial Techniques and Applications*. CRC Press Taylor and Francis Group, 2017. ISBN: 978-0-8493-9772-1.

[53] Syed Naeem Ahmed. *Physics and Engineering of Radiation Detection*. 2nd ed. Elsevier, 2015. ISBN: 978-0-12-801363-2. DOI: https://doi.org/10.1016/C2013-0-15270-1.

[54] David J. Dowsett, Patrick A. Kenny, and R. Eugene Johnston. *The Physics of Diagnostic Imaging*. 2nd ed. Hodder Arnold, 2006. ISBN: 978 0 340 80891 7.

[55] J. Anthony Seibert. "X-ray imaging physics for nuclear medicine technologists. Part 1: Basic principles of x-ray production." In: *Journal of nuclear medicine technology* 32.3 (2004), pp. 139–47. URL: https://api.semanticscholar.org/CorpusID:2637912.

[56] Daniele Funaro. *FORM PHOTONS TO ATOMS: The Electromagnetic Nature of Matter*. World Scientific Publishing Co. Pte. Ltd., 2020. ISBN: 978-981-120-423-4.

[57] David Halliday, Robert Resnick, and Jearl Walker. *Halliday Physik für natur- und ingenieurwissenschaftliche Studiengänge*. John Wiley & Sons, Incorporated, 2019, p. 25. ISBN: 9783527822645.

[58] R Lewis. "Medical applications of synchrotron radiation x-rays". In: *Physics in Medicine & Biology* 42.7 (1997), p. 1213. DOI: 10.1088/0031-9155/42/7/001.

[59] J. Als-Nielsen et al. "Multiple station beamline at an undulator X-ray source". In: *Nuclear Instruments and Methods in Physics Research Section B: Beam Interactions with Materials and Atoms* 94.3 (1994), pp. 306–318. ISSN: 0168-583X. DOI: https://doi.org/10.1016/0168-583X(94)95370-8. URL: https://www.sciencedirect.com/science/article/pii/0168583X94953708.

[60] Oliver Schmutzler et al. “X-ray Fluorescence Uptake Measurement of Functionalized Gold Nanoparticles in Tumor Cell Microsamples”. In: *International Journal of Molecular Sciences* 22.7 (2021). ISSN: 1422-0067. DOI: 10.3390/ijms22073691. URL: https://www.mdpi.com/1422-0067/22/7/3691.

[61] Komang G. Y. Arsana et al. “Laboratory Liquid-Jet X-ray Microscopy and X-ray Fluorescence Imaging for Biomedical Applications”. In: *International Journal of Molecular Sciences* 25.2 (2024). ISSN: 1422-0067. DOI: 10.3390/ijms25020920. URL: https://www.mdpi.com/1422-0067/25/2/920.

[62] Arthur Ungerer et al. “X-ray-Fluorescence Imaging for In Vivo Detection of Gold-Nanoparticle-Labeled Immune Cells: A GEANT4 Based Feasibility Study”. In: *Cancers* 13.22 (2021). ISSN: 2072-6694. DOI: 10.3390/cancers13225759. URL: https://www.mdpi.com/2072-6694/13/22/5759.

[63] Sakshi Dudhe et al. “Radiation Dose Optimization in Radiology: A Comprehensive Review of Safeguarding Patients and Preserving Image Fidelity”. In: *Cureus* (May 2024). DOI: 10.7759/cureus.60846.

[64] Dilshad Ahmad et al. “Radiation Dose Absorption In The Human Body: A Comprehensive Analysis”. In: *Journal for ReAttach Therapy and Developmental Diversities* (Dec. 2023), pp. 1762–1770. DOI: 10.53555/jrtdd.v6i10s(2).2286.

[65] Frank Herbert Attix. *Introduction to Radiological Physics and Radiation Dosimetry*. WILEY-VCH Verlag GmbH & Co. KGaA, Weinheim, 2004. ISBN: 978-0-471-01146-0.

[66] Penelope Allisy-Roberts and Jerry Williams. “Farr’s Physics for Medical Imaging (Second Edition)”. In: Second Edition. W.B. Saunders, 2008, pp. 1–21. ISBN: 978-0-7020-2844-1. DOI: https://doi.org/10.1016/B978-0-7020-2844-1.50005-3. URL: https://www.sciencedirect.com/science/article/pii/B9780702028441500053.

[67] Christian Gabriel Körnig. “Pilot Studies for Quantitative 2D and 3D X-Ray Fluorescence Imaging”. PhD thesis. Universität Hamburg, 2022.

[68] S. Agostinelli et al. “Geant4—a simulation toolkit”. In: *Nuclear Instruments and Methods in Physics Research Section A: Accelerators, Spectrometers, Detectors and Associated Equipment* 506.3 (2003), pp. 250–303. ISSN: 0168-9002. DOI: https://doi.org/10.1016/S0168-9002(03)01368-8. URL: https://www.sciencedirect.com/science/article/pii/S0168900203013688.

[69] Carrier JF et al. “Validation of GEANT4, an object-oriented Monte Carlo toolkit, for simulations in medical physics”. In: *Med Phys.* 31.3 (2004), pp. 484–92. DOI: 10.1118/1.1644532. URL: https://pubmed.ncbi.nlm.nih.gov/15070244/.

[70] J. Allison et al. “Recent developments in Geant4”. In: *Nuclear Instruments and Methods in Physics Research Section A: Accelerators, Spectrometers, Detectors and Associated Equipment* 835 (2016), pp. 186–225. ISSN: 0168-9002. DOI: https://doi.org/10.1016/j.nima.2016.06.125. URL: https://www.sciencedirect.com/science/article/pii/S0168900216306957.

[71] Geant4. *Overview*. 2025. URL: https://geant4.web.cern.ch/about/ (visited on 11/14/2025).

[72] Geant4. *Introduction to Geant4*. Version 11.3. 2025. URL: https://geant4-userdoc.web.cern.ch/UsersGuides/IntroductionToGeant4/fo/IntroductionToGeant4.pdf (visited on 11/14/2025).

[73] Geant4. *Physics Processes*. 2024. URL: https://geant4-userdoc.web.cern.ch/UsersGuides/AllGuides/html/ForApplicationDevelopers/TrackingAndPhysics/physicsProcess.html (visited on 11/17/2025).

[74] Geant4. *EM Liv*. 2025. URL: https://geant4-userdoc.web.cern.ch/UsersGuides/PhysicsListGuide/html/electromagnetic/Opt1.html (visited on 11/16/2025).

[75] Geant4. *Tracking*. 2024. URL: https://geant4-userdoc.web.cern.ch/UsersGuides/AllGuides/html/ForApplicationDevelopers/TrackingAndPhysics/tracking.html (visited on 11/17/2025).

[76] R. Brun and F. Rademakers. "ROOT: An object oriented data analysis framework". In: *Nucl. Instrum. Meth. A* 389 (1997). Ed. by M. Werlen and D. Perret-Gallix, pp. 81–86. DOI: 10.1016/S0168-9002(97)00048-X.

[77] Norbert Henze. *Die Poisson—Verteilung*. Wiesbaden: Vieweg+Teubner Verlag, 2004. ISBN: 978-3-663-11525-0. DOI: 10.1007/978-3-663-11525-0_25. URL: https://doi.org/10.1007/978-3-663-11525-0_25.

[78] P. Fornasini. *The Uncertainty in Physical Measurements: An Introduction to Data Analysis in the Physics Laboratory*. Springer New York, 2008. ISBN: 9780387786506. URL: https://books.google.de/books?id=PBJgvPgf2NkC.

[79] Joseph Alvarez. "Poisson-based detection limit and signal confidence intervals for few total counts". In: *Health physics* 93 (Sept. 2007), pp. 120–6. DOI: 10.1097/01.HP.0000261331.73389.bd.

[80] Jonas Joachim Kreidelmeyer. "Bayesian Methods for XFI". PhD thesis. Universität Hamburg, 2026. URL: https://ediss.sub.uni-hamburg.de/handle/ediss/12351.

[81] Theresa Staufer et al. "Enabling X-ray fluorescence imaging for in vivo immune cell tracking". In: *Scientific Reports* 13 (2023). DOI: https://doi.org/10.1038/s41598-023-38536-5. URL: https://doi.org/10.1038/s41598-023-38536-5.

[82] Nilanjana Kumar and Stephen P. Martin. "Vectorlike leptons at the Large Hadron Collider". In: *Physical Review D* 92.11 (Dec. 2015). ISSN: 1550-2368. DOI: 10.1103/physrevd.92.115018. URL: http://dx.doi.org/10.1103/PhysRevD.92.115018.

[83] Glen Cowan et al. "Asymptotic formulae for likelihood-based tests of new physics". In: *European Physical Journal C* 71 (July 2011), p. 1554. DOI: 10.1140/epjc/s10052-013-2501-z.

[84] Robert Redus et al. "Characterization of CdTe Detectors for Quantitative X-ray Spectroscopy". In: *Nuclear Science, IEEE Transactions on* 56 (Sept. 2009), pp. 2524–2532. DOI: 10.1109/TNS.2009.2024149.

[85] Amptek. *User Operating Manual XR-100CdTe X-Ray Detector & Preamplifier*. 2017. URL: https://www.amptek.com/-/media/ametekamptek/documents/resources/products/user-manuals/xr100-cdte-user-manual-b2.pdf?la=en&revision=c7533c8d-5c70-4172-a1e0-3582edb70d5e (visited on 03/24/2026).

[86] Min Woo Kim et al. "The early development of a combined micro- and full-field X-ray fluorescence analysis system using white X-rays at PLS-II". In: *Journal of Synchrotron Radiation* 32.1 (Jan. 2025), pp. 254–260. DOI: 10.1107/S1600577524011111. URL: https://doi.org/10.1107/S1600577524011111.

[87] Cindy Le Loirec, Dominique Chambellan, and David Tisseur. "IMAGE-GUIDED TREATMENT USING AN X-RAY THERAPY UNIT AND GOLD NANOPARTICLES: TEST OF CONCEPT". In: *Radiation Protection Dosimetry* 169.1-4 (2016), pp. 331–335. DOI: https://doi.org/10.1093/rpd/ncw013.

[88] Sandun Jayarathna, Hem Moktan, and Sang Hyun Cho. "Use of the Fully Spectroscopic Pixelated Cadmium Telluride Detector for Benchtop X-Ray Fluorescence Computed Tomography". In: *IEEE Access* 10 (2022), pp. 105074–105083. DOI: 10.1109/ACCESS.2022.3210590.

[89] Amrit Kaphle, Sandun Jayrathna, and Sang Hyun Cho. "Deep learning based rapid X-ray fluorescence signal extraction and image reconstruction for preclinical benchtop X-ray fluorescence computed tomography applications". In: *Scientific Reports* 15 (June 2025). DOI: https://doi.org/10.1038/s41598-025-03900-0.

[90] Amptek. *XR-100CdTe X-Ray & Gamma Ray Detector*. 2026. URL: https://www.amptek.com/internal-products/xr-100cdte-x-ray-and-gamma-ray-detector (visited on 03/24/2026).

[91] Amptek. *Digital Pulse Processor: User's Guide and Operating Instructions*. 2015. URL: https://www.yumpu.com/en/document/view/36213819/digital-pulse-processor-users-guide-and-operating-instructions (visited on 03/24/2026).

[92] Nivedh Manohar, Francisco J. Reynoso, and Sang Hyun Cho. "Technical Note: A benchtop cone-beam x-ray fluorescence computed tomography (XFCT) system with a high-power x-ray source and transmission CT imaging capability". In: *Medical Physics* 45.10 (2018), pp. 4652–4659. DOI: https://doi.org/10.1002/mp.13138. URL: https://aapm.onlinelibrary.wiley.com/doi/abs/10.1002/mp.13138.

[93] Sandun Jayarathna et al. "Characterization of a Pixelated Cadmium Telluride Detector System Using a Polychromatic X-Ray Source and Gold Nanoparticle-Loaded Phantoms for Benchtop X-Ray Fluorescence Imaging". In: *IEEE access : practical innovations, open solutions* 9 (2021), pp. 49912–49919. DOI: doi:10.1109/access.2021.3069368.

[94] M.C. Veale et al. "Measurements of charge sharing in small pixel CdTe detectors". In: *Nuclear Instruments and Methods in Physics Research Section A: Accelerators, Spectrometers, Detectors and Associated Equipment* 767 (2014), pp. 218–226. ISSN: 0168-9002. DOI: https://doi.org/10.1016/j.nima.2014.08.036. URL: https://www.sciencedirect.com/science/article/pii/S0168900214009711.

[95] Matthew Veale et al. "HEXITEC: A High-Energy X-ray Spectroscopic Imaging Detector for Synchrotron Applications". In: *Synchrotron Radiation News* 31 (Nov. 2018), pp. 28–32. DOI: 10.1080/08940886.2018.1528431.

[96] J. Kenneth McGregor Douglas and Shultis. *Radiation Detection: Concepts, Methods, and Devices*. CRC Press, 2020. ISBN: 9781000038583.

[97] Leeann Yao, Dejan Bojic, and Mingyao Liu. "Applications and safety of gold nanoparticles as therapeutic devices in clinical trials". In: *Journal of Pharmaceutical Analysis* 13.9 (2023), pp. 960–967. ISSN: 2095-1779. DOI: https://doi.org/10.1016/j.jpha.2023.06.001. URL: https://www.sciencedirect.com/science/article/pii/S2095177923001132.

[98] Xiao-Dong Zhang et al. "Toxicologic effects of gold nanoparticles in vivo by different administration routes". In: *Int J Nanomedicine* 5 (2010), pp. 771–781. DOI: 10.2147/IJN.S8428.

[99] Phuc van Nguyen et al. "Long-term, Non-invasive in Vivo Tracking of Progenitor Cells Using Multimodality Photoacoustic, Optical Coherence Tomography, and Fluorescence Imaging". In: *ACS Nano* 15.8 (2022), pp. 13289–13306. DOI: 10.1021/acsnano.1c03035.

[100] Chenjie Xu, Glenn A Tung, and Shouheng Sun. "Size and Concentration Effect of Gold Nanoparticles on X-ray Attenuation As Measured on Computed Tomography". In: *Chemistry of materials : a publication of the American Chemical Society* 20.13 (2008), pp. 4167–4169. DOI: 10.1021/cm8008418.

[101] Yi-Hsien Cheng et al. "Probabilistic risk assessment of gold nanoparticles after intravenous administration by integrating in vitro and in vivo toxicity with physiologically based pharmacokinetic modeling". In: *Nanotoxicology* 12.5 (2018), pp. 453–469. DOI: 10.1080/17435390.2018.1459922.

[102] Łukasz Niźnik et al. "Gold Nanoparticles (AuNPs)-Toxicity, Safety and Green Synthesis: A Critical Review". In: *International journal of molecular sciences* 25.7 (2024), p. 4057. DOI: 10.3390/ijms25074057.

[103] Regina Garmatter. "Numerical study on the spatial distribution of photons in X-ray fluorescence imaging of human-sized objects". Master's thesis. Universität Hamburg, 2023.

[104] Moiz Ahmad, Magdalena Bazalova-Carter, and Lei Xing. "Order of Magnitude Sensitivity Increase in X-ray Fluorescence Computed Tomography (XFCT) Imaging With an Optimized Spectro-Spatial Detector Configuration: Theory and Simulation". In: *IEEE transactions on medical imaging* 33 (May 2014), pp. 1119–28. DOI: 10.1109/TMI.2014.2305101.

[105] Florian Blumendorf. "Background Reduction for XFI with Human-Sized Phantoms". PhD thesis. Universität Hamburg, 2018.

[106] Krzysztof Iniewski. *Semiconductor Radiation Detection Systems*. USA: CRC Press, 2010. ISBN: 9781439803868.

[107] Jan S. Iwanczyk. *Radiation Detectors for Medical Imaging*. USA: CRC Press, 2015. ISBN: 9781498766821.

[108] J.M.C. Brown et al. "A low energy bound atomic electron Compton scattering model for Geant4". In: *Nuclear Instruments and Methods in Physics Research Section B: Beam Interactions with Materials and Atoms* 338 (2014), pp. 77–88. ISSN: 0168-583X. DOI: https://doi.org/10.1016/j.nimb.2014.07.042. URL: https://www.sciencedirect.com/science/article/pii/S0168583X14006934.

[109] M. Pushie et al. "Elemental and Chemically Specific X-ray Fluorescence Imaging of Biological Systems". In: *Chemical reviews* 114 (Aug. 2014). DOI: 10.1021/cr4007297.

[110] A.L.M. Silva et al. "Characterization of an energy dispersive X-ray fluorescence imaging system based on a Micropattern Gaseous Detector". In: *Spectrochimica Acta Part B: Atomic Spectroscopy* 66.5 (2011). Thematic Issue 11th Rio Symposium on Atomic Spectrometry, pp. 308–313. ISSN: 0584-8547. DOI: https://doi.org/10.1016/j.sab.2011.03.002. URL: https://www.sciencedirect.com/science/article/pii/S058485471100053X.

[111] Nivedh Manohar, Francisco J. Reynoso, and Sang Hyun Cho. "Experimental demonstration of direct L-shell x-ray fluorescence imaging of gold nanoparticles using a benchtop x-ray source". In: *Medical Physics* 40.8 (2013), p. 080702. DOI: https://doi.org/10.1118/1.4816297. URL: https://aapm.onlinelibrary.wiley.com/doi/abs/10.1118/1.4816297.

[112] D. Loshin. *The Geometrical Optics Workbook*. USA: Elsevier Health Sciences., 2015. ISBN: 9781483293653.

[113] Fayez H.H AL-Ghorabie. "Computer simulation of a backscattered x-ray fluorescence system". In: *Journal of X-Ray Science and Technology* 23.1 (2015). PMID: 25567407, pp. 57–64. DOI: 10.3233/XST-140470. eprint: https://journals.sagepub.com/doi/pdf/10.3233/XST-140470. URL: https://journals.sagepub.com/doi/abs/10.3233/XST-140470.

[114] Yue Sun et al. "Optimizing detector geometry for trace element mapping by X-ray fluorescence". In: *Ultramicroscopy* 152 (2015), pp. 44–56. ISSN: 0304-3991. DOI: https://doi.org/10.1016/j.ultramic.2014.12.014. URL: https://www.sciencedirect.com/science/article/pii/S030439911400271X.

[115] C G Ryan et al. "Maia X-ray fluorescence imaging: Capturing detail in complex natural samples". In: *Journal of Physics: Conference Series* 499.1 (Apr. 2014), p. 012002. DOI: 10.1088/1742-6596/499/1/012002. URL: https://doi.org/10.1088/1742-6596/499/1/012002.

[116] Akio Yoneyama, Masahide Kawamoto, and Rika Baba. "Novel Zeff imaging method for deep internal areas using back-scattered X-rays". In: *Scientific Reports* 9 (Dec. 2019), p. 18831. DOI: 10.1038/s41598-019-54907-3.

[117] Chelsea A. S. Dunning and Magdalena Bazalova-Carter. "Sheet beam x-ray fluorescence computed tomography (XFCT) imaging of gold nanoparticles". In: *Medical Physics* 45.6 (2018), pp. 2572–2582. DOI: https://doi.org/10.1002/mp.12893. eprint: https://aapm.onlinelibrary.wiley.com/doi/pdf/10.1002/mp.12893. URL: https://aapm.onlinelibrary.wiley.com/doi/abs/10.1002/mp.12893.

[118] Luzhen Deng et al. "A detector's eye view (DEV)-based OSEM algorithm for benchtop x-ray fluorescence computed tomography (XFCT) image reconstruction". In: *Physics in Medicine & Biology* 64.8 (Apr. 2019), 08NT02. DOI: 10.1088/1361-6560/ab0e9d. URL: https://doi.org/10.1088/1361-6560/ab0e9d.

[119] Shubham Mandot et al. "A High-Sensitivity Benchtop X-Ray Fluorescence Emission Tomography (XFET) System With a Full-Ring of X-Ray Imaging-Spectrometers and a Compound-Eye Collimation Aperture". In: *IEEE Transactions on Medical Imaging* 43.5 (2024), pp. 1782–1791. DOI: 10.1109/TMI.2023.3348791.

[120] Md Foiez Ahmed, Sandun Jayarathna, and Sang Hyun Cho. "Feasibility of X-ray Fluorescence Computed Tomography (XFCT) Imaging of Human Lung Tumors loaded with Gold Nanoparticles: A Monte Carlo Study". In: *2018 IEEE 12th International Conference on Nano/Molecular Medicine and Engineering (NANOMED)*. 2018, pp. 250–254. DOI: 10.1109/NANOMED.2018.8641551.

[121] Ling Jian Meng, Nan Li, and Patrick J. La Riviere. "X-Ray Fluorescence Emission Tomography (XFET) With Novel Imaging Geometries— A Monte Carlo Study". In: *IEEE Transactions on Nuclear Science* 58.6 (2011), pp. 3359–3369. DOI: 10.1109/TNS.2011.2167632.

[122] Kunal Kumar et al. "Characterization of a polychromatic microfocus X-ray fluorescence imaging setup with metallic contrast agents in a microphysiological tumor model". In: *Frontiers in Physics* 11 (2023). ISSN: 2296-424X. DOI: 10.3389/fphy.2023.1125143. URL: https://www.frontiersin.org/journals/physics/articles/10.3389/fphy.2023.1125143.

[123] Shreekripa Rao et al. "Advanced Computational Methods for Radiation Dose Optimization in CT". In: *Diagnostics* 14.9 (2024). ISSN: 2075-4418. DOI: 10.3390/diagnostics14090921. URL: https://www.mdpi.com/2075-4418/14/9/921.

[124] Gisele C. Pereira, Melanie Traughber, and Raymond F. Muzic Jr. "The Role of Imaging in Radiation Therapy Planning: Past, Present, and Future". In: *BioMed Research International* 2014.1 (2014), p. 231090. DOI: https://doi.org/10.1155/2014/231090. eprint: https://onlinelibrary.wiley.com/doi/pdf/10.1155/2014/231090. URL: https://onlinelibrary.wiley.com/doi/abs/10.1155/2014/231090.

[125] Maria ZANKL. "Adult Male and Female Reference Computational Phantoms (ICRP Publication 110)". In: *Jpn. J. Health Phys.* 45.4 (2010), pp. 357–369. DOI: 10.5453/jhps.45.357.

[126] Michael Oumano et al. "CT imaging of gold nanoparticles in a human-sized phantom". In: *Journal of Applied Clinical Medical Physics* 22.1 (2021), pp. 337–342. DOI: https://doi.org/10.1002/acm2.13155. eprint: https://aapm.onlinelibrary.wiley.com/doi/pdf/10.1002/acm2.13155. URL: https://aapm.onlinelibrary.wiley.com/doi/abs/10.1002/acm2.13155.

A Appendix

A.1 Compton1 and Compton3 Model

Compton1 Model The numerical model for single Compton-scattered photons works similarly to the fluorescence model, since both interactions occur only along the z-axis, with the difference that Compton photons are supposed to be generated within the object (from (0, 0, $z_{Obj,min}$) to (0, 0, $z_{Obj,max}$)) and not only in the typically smaller fluorescence target inside the object. However, the basic principle remains the same: in order to estimate the detected once Compton-scattered photons (Compton1), it is assumed that Compton scattering occurs in the object along the z-axis with a step size d_z. The step size or the distance between possible Compton1 scattering locations impacts the number of possible Compton1 paths $\left(\frac{z_{Obj,max}-z_{Obj,min}}{d_z}\right)$, which in the case of the standing cylinder scenario would be $\frac{2R_{Obj}}{d_z}$ Compton1 paths.
The probability p_{C_1} of each possible Compton path i can be calculated similarly to the fluorescence model, whereby the Compton model considers the scattering location O_{C_1} = (0, 0, z_{C_1}) with $z_{C_1} = z_{Obj,min} + i \cdot d_z$ instead of the fluorescence origin (0, 0, z_{Au}) from the fluorescence model. As in the fluorescence model, the probability p_{C_1} of each possible Compton path i is determined by a number of factors. These factors include the transmission T_{in} (Eq. 3.12) from the beam source to the interaction location (i.e., the Compton scattering location) and the transmission T_{out} (Eq. 3.14) from the scattering location to the detector, as well as the solid angle G (Eq. 3.15) of the detector area in relation to the distance between the Compton scattering origin and the detector center and at last the projection P (Eq. 3.16):

$$(p_{C_1})_i = (T_{in} Y_{C_1} T_{out} G P)_i \quad \text{with} \quad i \in \left\{1, 2, \cdots, \frac{z_{Obj_{max}} - z_{Obj_{min}}}{d_z}\right\}. \tag{A.1}$$

The yield of once Compton-scattered photons in the interval d_z is given by Y_{C_1}:

$$Y_{C_1} = \mu_C \cdot d_z = \mu_{m,C_1} \cdot \rho_{Obj} \cdot d_z. \tag{A.2}$$

Unlike fluorescence, Compton scattering is not isotropic but anisotropic. This is taken into account by the Compton interaction coefficient μ_C, which is calculated by a function from xraylib depending on the material, the incident energy of the photons before Compton scattering E_{in}, and finally the scattering angle θ_{C_1} of the Compton photon, which depends only on the scattering position when the end of the Compton scattering path is considered at the center of a fixed detector. Moreover, the scattering angle θ_{C_1} affects the energy E_1 after one Compton scattering, which is calculated according to Eq. 2.7, assuming that the electrons are free and at rest before interacting with the photon:

$$E_1 = \frac{E_0}{1 + \frac{E_0}{m_0 c^2}(1 - cos(\theta_{C_1}))}. \tag{A.3}$$

The number of expected once-scattered Compton photons C_1 can be estimated using the following equation:

$$C_1 = \sum_i C_{1_i} = \sum_i N_0 \cdot p_{C_{1_i}} \quad \text{with} \quad i \in \left\{1, 2, \cdots, \frac{z_{Obj_{max}} - z_{Obj_{min}}}{d_z}\right\}. \tag{A.4}$$

It is the sum over all probabilities $p_{C_{1_i}}$ of all possible Compton1 paths multiplied by the number of photons N_0 from the incident beam.

Compton3 Model For clarification, and since this thesis also focuses on triple Compton-scattered photons, the path probability of a triple scattered photon is explained in more detail below as an example.
The path of a triple Compton-scattered photon begins at the beam source $O_S = (0,0,z_S)$, from where the photon proceeds to its first scattering site somewhere on the z-axis ($O_{C_1} = (0,0,z_1) = (0,0,z_{min} + k \cdot d_{z_1})$) within the object (with $z_{Obj_{min}} < z_1 < z_{Obj_{max}}$). The

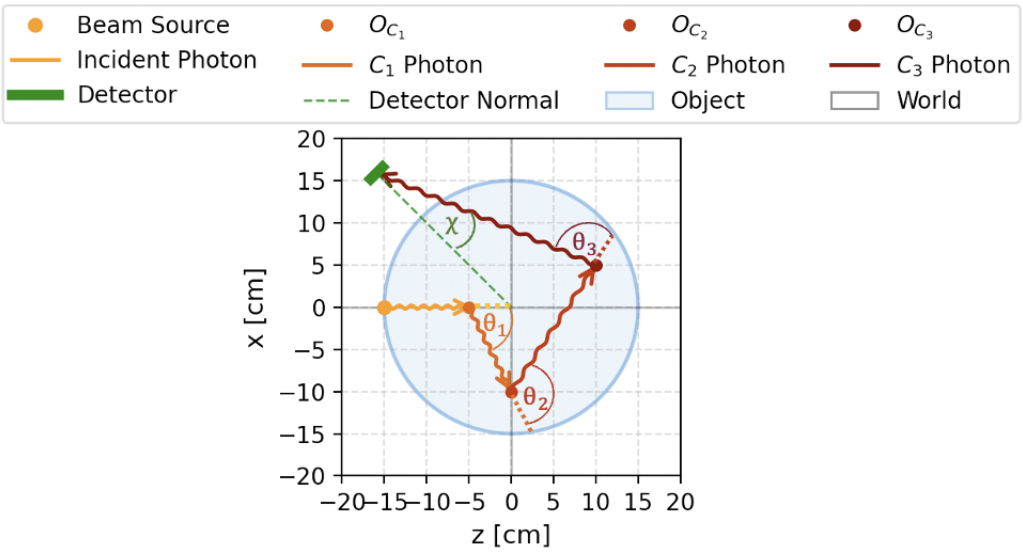

Figure A.1: A possible path of a detected Compton3 photon is shown in the beam plane ($y = 0$). A beam source on the z-axis at the edge of an object emits photons that travel along the z-axis until they scatter at O_{C_1} with a scattering angle of θ_1. Then, the C_1 photon scatters at O_{C_2} with an angle of θ_2 and subsequently, the double Compton-scattered C_2 photon scatters at O_{C_3} with θ_3. Finally, the triple-scattered C_3 photon is detected with a projection angle of χ with respect to the detector normal. In this example, the detector normal is oriented toward the center of the object, and only scattering locations with step sizes of d_x and d_z are modeled within the beam plane, as visualized by the grid crosses.

transmission of the incident beam during this distance $r_{in} = |\overrightarrow{O_S O_{C_1}}| = z_1 - z_S$ is described by T_{in}:

$$T_{in} = e^{-\mu_{Obj} r_{in}} = e^{-\mu_{m,Obj} \rho_{Obj} r_{in}}, \; r_{in} = |\overrightarrow{O_S O_{C_1}}|. \tag{A.5}$$

The possible scattering sites are considered separated by a distance d_{z_1} from each other, so that $z_1 = z_{Obj_{min}} + k \cdot d_{z_1}$ holds, whereby the index k represents the considered Compton path. Consequently, as already mentioned above, there are $\frac{z_{Obj_{max}} - z_{Obj_{min}}}{d_{z_1}}$ possible Compton1 scattering places.
The probability that Compton scattering occurs during this interval d_{z_1} is described by the yield Y_{C_1} according to equation A.2.
Afterwards, the once Compton-scattered photon transmits to the second Compton scattering place O_{C_2}, which is described by T_1:

$$T_1 = e^{-\mu_{Obj} r_1} = e^{-\mu_{m,Obj} \rho_{Obj} r_1},\ r_1 = |\overrightarrow{O_{C_1} O_{C_2}}|. \tag{A.6}$$

However, the second Compton scattering site $O_{C_2} = (x_2,\ y_2,\ z_2)$ can now be located anywhere within the entire cylinder and is not restricted to the z-axis. For this purpose, the model iterates over l, m, n, and the second Compton scattering place can also be described by $O_{C_2} = (x_{min} + l \cdot d_{x_2},\ y_{min} + m \cdot d_{y_2},\ z_{min} + n \cdot d_{z_2})$.
To determine the geometrical factor G_1, we imagine a pixel around the origin of Compton scattering with the step sizes $(d_{x_2},\ d_{y_2},\ d_{z_2})$ as the length in the x, y, and z directions. Then the geometrical factor G_1 is the solid angle of the pixel of the second Compton scattering relative to the distance r_1 between the first and second Compton scattering sites. Note that for the numerical model, a step-size $d_s = d_{x_2} = d_{y_2} = d_{z_2}$ was always chosen, so that the pixel around the scattering origin is a cube with equal lengths, allowing the pixel area considered for the solid angle to be described by $d_{z_2}^2$:

$$G_1 = \frac{d_{z_2}^2}{4\pi r_1^2}. \tag{A.7}$$

The resulting Compton yield of the double Compton-scattered photon is calculated according to equation A.2 with the step size d_{z_2} and the Compton interaction coefficient $\mu_{C_2}(material, E_1, \theta_2)$:

$$Y_{C_2} = \mu_{C_2} \cdot d_{z_2} = \mu_{m,C_2} \cdot \rho_{Obj} \cdot d_{z_2}. \tag{A.8}$$

The Compton interaction coefficient μ_{C_2} depends on the material of the object, the energy of the once-scattered photon E_1 and the angle of the second Compton scattering θ_2 and can be calculated with xraylib according to equation A.2.
Then the transmission of the twice Compton-scattered photon from the spot O_{C_2} to the third Compton scattering spot $O_{C_3} = (x_3,\ y_3,\ z_3) = (x_{min} + r \cdot d_{x_3},\ y_{min} + s \cdot d_{y_3},\ z_{min} + t \cdot d_{z_3})$ is described by T_2:

$$T_2 = e^{-\mu_{Obj} r_2} = e^{-\mu_{m,Obj} \rho_{Obj} r_2},\ r_2 = |\overrightarrow{O_{C_2} O_{C_3}}|. \tag{A.9}$$

As with G_1, the geometrical factor G_2 describes the solid angle of the pixel around the third Compton scattering site with lengths $d_{x_3} = d_{y_3} = d_{z_3}$ with respect to the distance between the second and third scattering origins r_2:

$$G_2 = \frac{d_{z_3}^2}{4\pi r_2^2}. \tag{A.10}$$

The yield of the triple Compton-scattered photon can subsequently be calculated according to equations A.2 and A.8 using the energy of the double Compton-scattered photon E_2 and the angle of the third Compton scattering θ_3 for the Compton interaction coefficient and the step size d_{z_3}.
Afterwards, the triple Compton-scattered photons transmit to the detector (O_D), which is described by T_3:

$$T_3 = e^{-\mu_{Obj} r_{3,Obj}} e^{-\mu_{world} r_{3,world}},\ r_3 = |\overrightarrow{O_{C_3} O_D}|. \tag{A.11}$$

Here, it is important to consider that the detector is located in the world where the material and, therefore, the attenuation coefficient μ_{world} are usually different from those in the object. This means that the attenuation must be considered separately for distances within the object ($r_{3,Obj}$) and within the world ($r_{3,world}$).
Since the triple Compton-scattered photons now transmit to the detector, the detector area A_D has to be used for the solid angle or geometrical factor:

$$G_3 = \frac{A_D^2}{4\pi r_3^2}. \tag{A.12}$$

Lastly, the projection of the photon path (from the third Compton scattering spot to the detector) has to be taken into account with respect to the detector normal, which can be calculated like in equation 3.16.
Finally, according to equation (3.18), the number of triple Compton-scattered photons for n modeled paths is composed of all these components:

$$C_3 = \sum_{i=1}^{n} C_{3_i} = \sum_{i=1}^{n} N_0 \cdot p_{C_{3_i}} \ \text{ with } \ (p_{C_3})_i = (T_{in} Y_{C_1} T_1 G_1 Y_{C_2} T_2 G_2 Y_{C_3} T_3 G_3 P)_i. \tag{A.13}$$

Note, that the $(p_{C_3})_i$ describes the probability of a single path i and there are in total $i = k \cdot l \cdot m \cdot n \cdot r \cdot s \cdot t$ different paths.

A.2 Collimators Used for the Comparison in Section 6.3

In Sec. 6.3 different collimator designs are compared. This includes the Parallel-Hole Collimator described in the literature by the research group of Jayarathna et al. [88], the Parallel-Lamellae Collimator, the Cone-Hole Collimator, the Vertical-Lamellae Collimator and the Horizontal-Lamellae Collimator in the beam plane for a detector at 150°, as well as the Horizontal-Lamellae Collimator shifted out of the beam plane at 150° and 180°. Based on the setup used by Jayarathna et al., the collimators were designed for use with the HEXITEC detector with a detector-chip area of 20 x 20 mm^2 [88]. It should be noted that all collimators have an area of 35 × 35 mm^2 at the detector, however, the holes or lamellae openings only cover the detector area. The surrounding collimator is solid tantalum. Details of the hole collimators are listed in Tab. 9 and of the lamellae collimators in Tab. 10.

Collimator	Description
$C_{H,P,7}$	• Parallel-Hole Collimator with 7 × 7 parallel holes corresponding to the setup of Jayarathna et al. [88] • Collimator length: 50 mm • Hole spacing: 3.0 mm (distance between the hole center) • Septum thickness: 1.0 mm • Detector location: 150°, center at (112.5, 0, −194.9) mm
$C_{H,P,9}$	• Parallel-Hole Collimator with 9 × 9 parallel holes • Collimator length: 50 mm • Hole spacing: 2.2 mm (distance between the hole center) • Septum thickness: 0.2 mm • Detector location: 150°, center at (112.5, 0, −194.9) mm
$C_{H,C}$	• Cone-Hole Collimator with 9 × 9 converging holes • Collimator length: 50 mm • Hole Spacing: 2.2 mm (distance between the hole center at the detector) • Septum thickness: 0.2 mm • Detector location: 150°, center at (112.5, 0, −194.9) mm

Table 9: The parameters of the different hole collimators are listed. Note that the hole spacing refers to the spacing at the detector. For the converging Cone-Hole collimator, the cone holes focus on the target, with the hole diameter decreasing proportionally with increasing distance from the detecor.

Collimator	Description
$C_{L,\parallel}$	• Parallel-Lamellae Collimator with 10 parallel horizontal lamellae • Collimator length: 70 mm • Lamella spacing: 2.2 mm • Lamella thickness: 0.2 mm • Detector location: 150°, center at (112.5, 0, −194.9) mm
$C_{L,h}$	• Horizontal-Lamellae Collimator with 10 horizontal lamellae focusing on the target • Collimator length: 70 mm • Lamella spacing: 2.2 mm • Lamella thickness: 0.2 mm • Detector location: 150°, center at (112.5, 0, −194.9) mm
$C_{L,h,s}$	• shifted Horizontal-Lamellae Collimator with 10 horizontal lamellae focusing on the target • Collimator length: 70 mm • Lamella spacing: 2.2 mm • Lamella thickness: 0.2 mm • Detector location: 150°, center at (112.5, 32.0, −194.9) mm with the detector edge at $y_s = 22$ mm above the beam plane
$C_{L,h,180°}$	• shifted Horizontal-Lamellae Collimator with 10 horizontal lamellae focusing on the target • Collimator length: 70 mm • Lamella spacing: 2.2 mm • Lamella thickness: 0.2 mm • Detector location: 180°, center at (0, 32.0, −225.0) mm with the detector edge at $y_s = 22$ mm above the beam plane
$C_{L,v}$	• Vertical-Lamellae Collimator with 9 vertical lamellae • Collimator length: 70 mm • Lamella spacing: 2.5 mm • Lamella thickness: 0.2 mm • Detector location: 150°, center at (112.5, 0, −194.9) mm

Table 10: The parameters of the different lamellae collimators are listed. Note that the lamella spacing refers to the spacing at the detector. In case of non-parallel lamellae, the spacing changes for a longer distance to the detector (Sec. 6.1.1, Sec. 6.2.1).

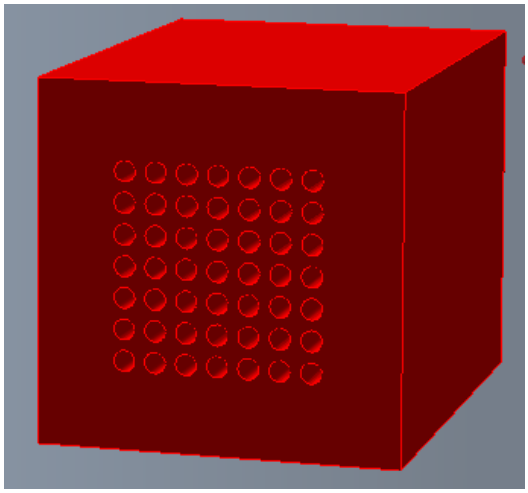

(a) Parallel-Hole Collimator with 7 × 7 parallel holes

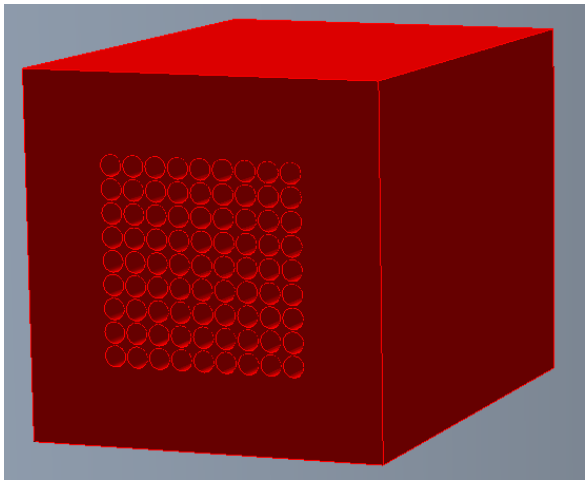

(b) Parallel-Hole Collimator with 9 × 9 parallel holes

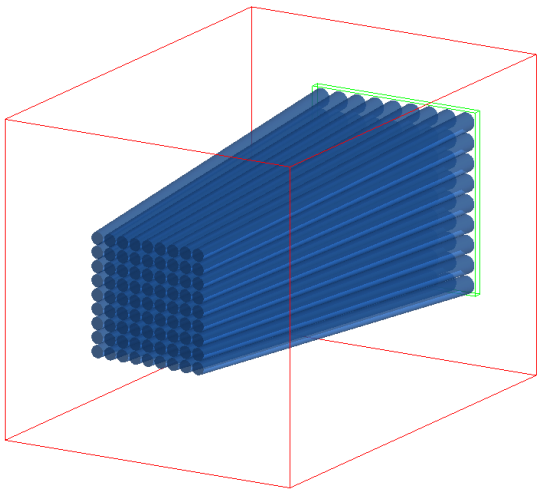

(c) Cone-Hole Collimator with 9 × 9 converging holes

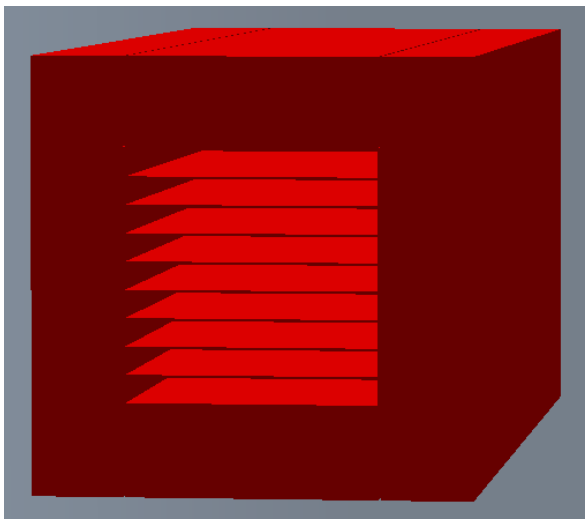

(d) Lamellae Collimator

Figure A.2: Visualizations of the following collimators are presented: the Parallel-Hole Collimator with 7 × 7 parallel holes (a), the Parallel-Hole Collimator with 9 × 9 parallel holes (b), the Cone-Hole Collimator with 9 × 9 converging holes (c) and a Lamellae Collimator with horizontal lamellae resulting in nine free spaces (d).

A.3 Simulations for the Test Measurement

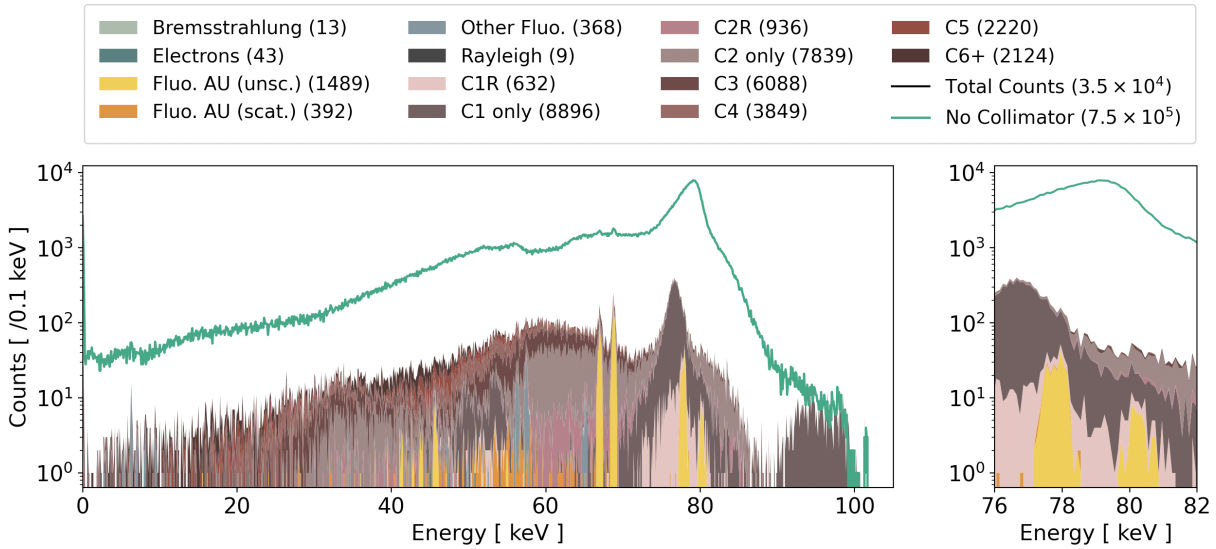

Figure A.3: The simulated stacked spectrum for 10^{11} incident photons with an incident energy of $E_0 = 101.4\,\text{keV}$ is shown for a PMMA cylinder detected by a CdTe detector with the energy resolution and size of the Amptek detector chip. The detector is placed at a 150° angle relative to the incident beam, with respect to the phantom center. A Horizontal-Lamellae Collimator is added and shifted out of the xz-plane to an angular position $\alpha_{D,y} = 8°$ relative to the xz-plane. Additionally, the simulated spectrum without a collimator (green) is shown. This plot demonstrates that the simulated counts decrease to 6% when a collimator is used.

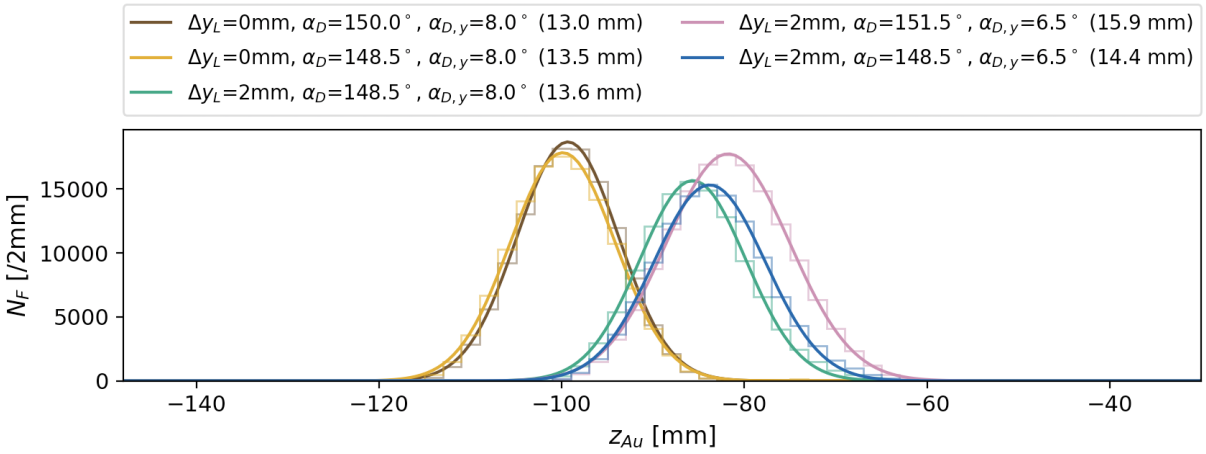

Figure A.4: The simulated fluorescence counts N_F for 10^{10} incident photons with an incident energy of 101.4 keV are shown as a function of the target position z_{Au}, indicating the detector FOV. A 10 mm-long gold target with a gold concentration of 10 mg/ml is shifted along the z-axis in a vacuum. The detector, matching the size of the Amptek detector chip, is positioned at an angle α_D in the xz-plane and has an angular position $\alpha_{D,y}$ relative to the xz-plane. The collimator is shifted by Δy_L with respect to the detector center. The FWHM values are indicated in the brackets. Note that the collimator design remains fixed in these simulations, only the location of the collimator and detector changes. This plot explains the invisible gold signal in the experimental spectra since the FOV is shifted to different z-sections when the collimator is displaced by Δy_L.

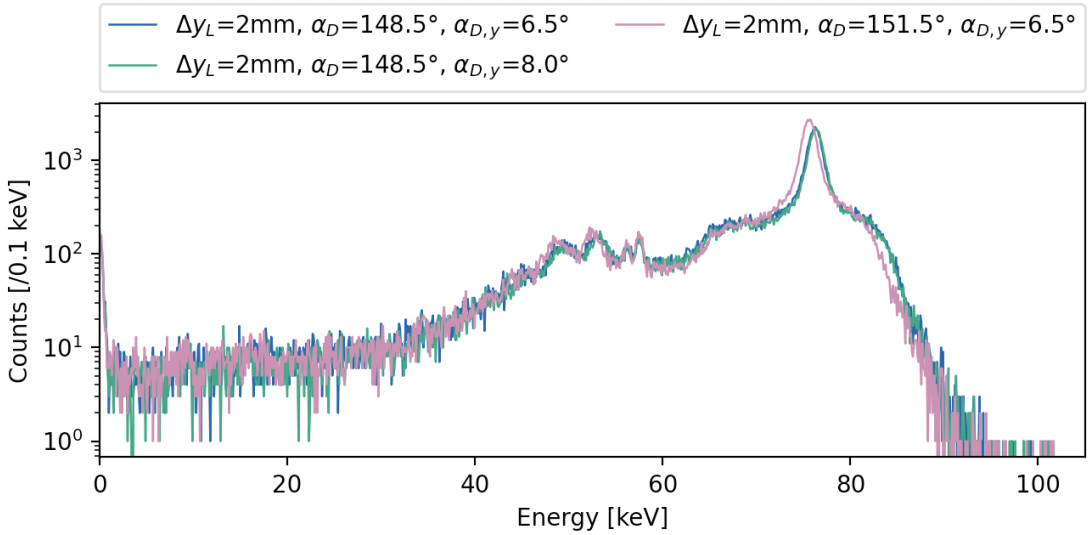

Figure A.5: Simulated spectra ($N_0 = 10^{11}$, $E_0 = 101.4\,\text{keV}$) with additional ideal shielding around the back of the detector up to the collimator are shown for various detector positions. The angle α_D describes the detector location in the equatorial xz-plane relative to the incident beam and the phantom center. The CdTe detector, which has the same size as the Amptek detector chip, has an angular position $\alpha_{D,y}$ relative to the xz-plane. The collimator is displaced by $\Delta y_L = 2\,\text{mm}$ in the y-direction relative to its planned position with respect to the detector center. Note that the collimator design remains fixed in these simulations, only the location of the collimator and detector changes. This plot shows that the additional detector shielding minimizes the number of photons above 90 keV that enter the detector from the side of the beam source. Furthermore, positioning the detector at different angles $\alpha_{D,y}$ reduces discrepancies of the Compton continuum in the spectrum, which occurs without shielding.

List of Figures

2.1 Mass-attenuation coefficient of the photoelectric effect for iodine, tantalum and gold. . . . 5
2.2 Schematic of the photoelectric effect, Auger process and fluorescence process. 6
2.3 Schematic of Compton scattering. . . . 7
2.4 Angular dependence of the Compton energy. . . . 8
2.5 Angular dependence of the Klein-Nishina cross sections. . . . 9
2.6 Photon attenuation in air, soft tissue, tantalum and gold. . . . 10
2.7 Total mass-attenuation coefficients and components (photoelectric effect, Rayleigh scattering, Compton scattering) in soft tissue and gold. . . . 11
3.1 Principle of the Fluorescence Model. . . . 19
3.2 Comparison of true and recorded counts. . . . 25
4.1 Setup for the numerical analysis of multiple Compton scattering background. 27
4.2 Background spectrum for a detector at 60°. . . . 28
4.3 Validation of the numerical model. . . . 29
4.4 Spatial distributions for C2 and C3 photons with a detector close to the object edge. . . . 31
4.5 Impact of the distance on solid angle and attenuation, and impact of the Compton energy dependence on scattering angles. . . . 32
4.6 y-distribution of C2 and C3 photons for a detector at the object edge. . . . 33
4.7 Spatial distributions for C2 and C3 photons with an increased detector distance. . . . 34
4.8 y-distribution of C2 and C3 photons for an increased detector distance. . . . 35
5.1 Setup for uncollimated XFI. . . . 38
5.2 Radiation dose as a function of depth in a human-sized object. . . . 39
5.3 Detector angle and target location dependency of detected fluorescence counts. . . . 40
5.4 Background spectra for different detector angles and incident energies. . . . 42
5.5 Background counts in the K_α and K_β signal ranges for different detector angles. . . . 43
5.6 Significance depending on the target depth and the detector angle. . . . 44
5.7 Uncollimated spectrum for a detector angle at 150°. . . . 45
5.8 Impact of the Doppler broadening for C1 photons. . . . 46
6.1 Principle of the Vertical-Lamellae Collimator. . . . 50
6.2 Setup for collimation studies with a Vertical-Lamellae Collimator. . . . 52
6.3 Impact of an ideal Vertical-Lamellae Collimator on the energy spectrum. . . . 53
6.4 Modeled energy distribution for C1 and C2 photons. . . . 54
6.5 Effect of collimator material on the spectrum. . . . 57
6.6 Mass-attenuation coefficients for molybdenum and tantalum. . . . 58
6.7 Effect of lamella thickness on the spectrum. . . . 60
6.8 Attenuation within tantalum depending on the depth and energy. . . . 61
6.9 Effect of lamella thickness on fluorescence, background and significance. . . . 62
6.10 Collimator transmission for the Vertical-Lamellae Collimator. . . . 64

6.11 Effect of the target position on fluorescence, background and significance for a Vertical-Lamellae Collimator. . . . 65
6.12 Collimator transmission of the Vertical-Lamellae Collimator for different foci. . . . 66
6.13 Setup for collimation studies with a Horizontal-Lamellae Collimator. . . . 68
6.14 Opening angle geometry of a lamella collimator. . . . 69
6.15 Effect of the detector displacement in y-direction on fluorescence, background and significance for a Vertical-Lamellae Collimator. . . . 71
6.16 FOV volumes of a Horizontal-Lamellae Collimator for different shifts in y-direction. . . . 71
6.17 FOV intersections in the beam plane for different detector shifts. . . . 72
6.18 Dependence of the collimator transmission for different detector shifts. . . . 73
6.19 Effect of the lamella number on fluorescence, background and significance for a shifted Horizontal-Lamellae Collimator. . . . 76
6.20 FOV volumes of a Horizontal-Lamellae Collimator for different lamella numbers. . . . 76
6.21 FOV intersections in the vertical beam plane and normalized FOV height, background and lamella spacing for different lamella numbers. . . . 77
6.22 FOV intersections in the horizontal beam plane and modeled collimator transmissions for different lamella numbers. . . . 78
6.23 Effect of the lamella length on fluorescence, background and significance for a shifted Horizontal-Lamellae Collimator. . . . 80
6.24 FOV volumes of a Horizontal-Lamellae Collimator for different lamella lengths. . . . 81
6.25 Dependence of opening angles, FOV and background on the lamella length. 82
6.26 FOV intersections in the horizontal beam plane and modeled collimator transmissions for different lamella lengths. . . . 84
6.27 Effect of the target location on fluorescence, background and significance for a shifted Horizontal-Lamellae Collimator and a 150° detector. . . . 86
6.28 Effect of the target location on fluorescence, background and significance for a shifted Horizontal-Lamellae Collimator and a 180° detector compared to no collimator. . . . 88
6.29 Effect of different collimator designs on fluorescence, background and significance. . . . 91
6.30 Comparison of collimator transmissions for different collimator designs. . . . 92
6.31 Comparison of the depth-dependent sensitivity for different lamellae-based collimators with literature. . . . 97
7.1 Experimental setup for test measurements. . . . 102
7.2 Experimentally recorded spectra with and without collimator. . . . 104
7.3 Impact of the collimator and detector alignment on recorded spectra. . . . 106
A.1 Schematic for the Compton3 photon model. . . . 123
A.2 Collimator designs for comparison. . . . 128
A.3 Simulated spectra of the test measurement scenario. . . . 129
A.4 Impact of the alignment in the test measurement shown by FOV distributions. 130

A.5 Simulated spectra of the test measurement scenario with varying alignments. 131

List of Tables

1 Gold fluorescence line energies. 26
2 Fluorescence, background and significance within the gold K_α range for different collimator materials. 58
3 Fluorescence, background and significance within the gold K_β and K_γ range for different collimator materials. 59
4 Minimum detectable gold concentrations for different depths with and without the Vertical-Lamellae Collimator at 150°. 67
5 Minimum detectable gold concentrations for different depths with and without the Horizontal-Lamellae Collimator at 150°. 87
6 Minimum detectable gold concentrations for different depths with and without the Horizontal-Lamellae Collimator at 180°. 89
7 Parameters of different collimators for comparison. 90
8 Dependence of FWHM for lamellae-based collimators on the depth. 96
9 Descriptions of hole-based Collimators. 126
10 Descriptions of lamellae-based Collimators. 127

Acknowledgements

First, I would like to thank my supervisor, Prof. Dr. Florian Grüner for his ongoing guidance and advice throughout this research project over the past few years. His consistent support was crucial to completing this thesis.
I would also like to thank Dr. Theresa Staufer for always being available to answer question, provide support, and proofread my thesis.
I would also like to thank the examination committee for taking the time to engage with this topic.
Furthermore, I would like to thank all the team members for always providing a positive and supportive atmosphere and for helping whenever questions arose.
Finally, I would like to express my gratitude to my family, friends and Quentin for their support, patience, and motivation throughout this entire journey.

Use of Artificial Intelligence Tools

For proofreading and language refinement, DeepL (2025-2026), Claude (Anthropic, 2025-2026) and ChatGPT (OpenAI, 2025-2026) were used. Furthermore, Claude (Anthropic, 2025-2026) and ChatGPT (OpenAI, 2025-2026) were used to identify potentially relevant literature for subsequent independent research and evaluation. The large language model Claude (Anthropic, 2025-2026) was used for code assistance. All AI-generated suggestions, including code, language refinements, and literature recommendations, were critically reviewed and verified by the author. The AI tools were used solely as supporting tools and did not replace the author's own scientific work.

Eidesstattliche Versicherung

Hiermit versichere ich an Eides statt, die vorliegende Dissertationsschrift selbst verfasst und keine anderen als die angegebenen Hilfsmittel und Quellen benutzt zu haben.

Sofern im Zuge der Erstellung der vorliegenden Dissertationsschrift generative Künstliche Intelligenz (gKI) basierte elektronische Hilfsmittel verwendet wurden, versichere ich, dass meine eigene Leistung im Vordergrund stand und dass eine vollständige Dokumentation aller verwendeten Hilfsmittel gemäß der Guten wissenschaftlichen Praxis vorliegt. Ich trage die Verantwortung für eventuell durch die gKI generierte fehlerhafte oder verzerrte Inhalte, fehlerhafte Referenzen, Verstöße gegen das Datenschutz- und Urheberrecht oder Plagiate.

Datum	Unterschrift